# ON THE MULTISCALE MODELLING OF HYDRODYNAMICS, MASS TRANSFER AND CHEMICAL REACTIONS IN BUBBLE COLUMNS

**Samenstelling promotiecommissie:**

| | |
|---|---|
| Prof. dr. ir. A. Bliek, voorzitter | Universiteit Twente |
| Prof. dr. ir. J.A.M. Kuipers, promotor | Universiteit Twente |
| Dr. ir. N.G. Deen, assistent-promotor | Universiteit Twente |
| Prof. dr. D. Bothe | Rheinisch-Westfälische T.H. Aachen |
| Prof. dr. S.T. Johansen | SINTEF Trondheim |
| Prof. dr. D. Lohse | Universiteit Twente |
| Prof. dr. R.F. Mudde | Technische Universiteit Delft |
| Prof. A. Tomiyama | Kobe University |
| Prof. dr. ir. G.F. Versteeg | Universiteit Twente |

This work is financially supported by DSM and the Institute of Mechanics, Processes and Control-Twente (IMPACT).
This work was sponsored by the Stichting Nationale Computerfaciliteiten (National Computing Facilities Foundation, NCF) for the use of supercomputer facilities, with financial support from the Nederlandse Organisatie voor Wetenschappelijk Onderzoek (Netherlands Organization for Scientific Research, NWO).



Printed by:
PrintPartners Ipskamp, Enschede, The Netherlands.
The summary was translated to Dutch by Niels Deen.

ISBN: 90-365-2425-3

# ON THE MULTISCALE MODELLING OF HYDRODYNAMICS, MASS TRANSFER AND CHEMICAL REACTIONS IN BUBBLE COLUMNS

**PROEFSCHRIFT**

ter verkrijging van
de graad van doctor aan de Universiteit Twente,
op gezag van de rector magnificus,
prof. dr. W.H.M. Zijm,
volgens besluit van het College van Promoties,
in het openbaar te verdedigen
op donderdag 26 oktober 2006 om 15.00 uur

door

**Dadan Darmana**

geboren op 24 juli 1976
te Jakarta, Indonesië

Dit proefschrift is goedgekeurd door de promotor

**Prof. dr. ir. J.A.M. Kuipers**

en de assistent-promotor

**Dr. ir. N.G. Deen**

For my parents:
*Mimih* and *Bapak* in Jakarta
*Mamah* and *Bapak* in Kuningan

For my beloved wife:
*Rini Farida Rosdiany*

# Contents

# Summary

Despite their widespread use for various (chemical) processes and a vast amount of research devoted to understand their behavior, detailed knowledge of bubble column reactors is still lacking. The highly complex interactions between hydrodynamics, mass transfer and chemical reaction as well as the wide range of both time and spatial scales prevailing in the reactor make bubble column reactors challenging from a modelling point of view. In this thesis, a multi-scale modelling approach in combination with an advanced parallel computing strategy is used to study the phenomena prevailing at different scales. Two CFD models, namely a front tracking model and an Eulerian-Lagrangian model are used to study the relevant phenomena at different scales. The interactions between hydrodynamics, mass transfer and chemical reactions are treated directly in each model taking into account the relevant coupling.

In order to study detailed hydrodynamics and mass transfer phenomena on the level of individual bubbles, a three-dimensional front tracking model in combination with an immersed boundary technique that explicitly accounts for the bubble-liquid mass transfer process is developed. The model allows us to a priori calculate mass transfer coefficients for bubbles (droplets) that can be used as a closure to more coarse modelling techniques, such as the Eulerian-Eulerian or Eulerian-Lagrangian techniques. Simulations are carried out to demonstrate capabilities of the developed model to predict bubble shape, flow field as well as transport of a species from the bubble to the liquid phase. Furthermore, in a simulation employing multiple bubbles, we found that bubbles rising in the wake of other bubbles will experience an increase of rise velocity, while the mass transfer rate is decreased.

A three-dimensional discrete bubble model (DBM) is adopted to investigate complex behavior involving hydrodynamics, mass transfer and chemical reactions in a gas-liquid bubble column reactor. In this model a continuum description is adopted for the liquid phase and additionally each individual bubble is tracked in a Lagrangian framework, while accounting for bubble-bubble and bubble-wall interactions via an encounter model. The mass transfer rate is calculated for each individual bubble using a surface renewal model accounting for the instantaneous and local properties of the liquid phase in its vicinity. The spatial distributions of chemical species residing in the liquid phase are computed from the coupled species balances considering the mass transfer from bubbles and reactions between the species. The hydrodynamics part of the developed model is validated with the experimental data of Deen et al. [*Chem. Eng. Sci.*, 2001, **56**, 6341]

and is found to be in good agreement. Furthermore, the model is applied to study the mixing and physical absorption of $CO_2$ bubbles in water until saturation of the liquid prevails.
For the purpose of validating the DBM to predict the hydrodynamics, mass transfer and chemical reactions, a dedicated experimental setup consisting of a pseudo-2D lab-scale bubble column reactor was constructed. A reversible two-step reaction system found in the chemisorption process of $CO_2$ in an aqueous $NaOH$ solution was studied both experimentally and numerically using the developed DBM. The computational results are compared with experimental data of bubble velocities, which were obtained with the use of Particle Image Velocimetry. Furthermore, the influence of the mass transfer and chemical reaction on the hydrodynamics, bubble size distribution and gas hold-up is also studied and compared with the experiment. It is found that the model is able to predict the entire reaction process. The prediction of the hydrodynamics without mass transfer is found to be accurate. The model however seems to underpredict the overall mass transfer process, which we believe, can be attributed to an inaccuracy of the mass transfer closure being used in the present study. Nevertheless, the trends of the influence of the mass transfer rate on the hydrodynamics have been successfully captured by the present model.
As the simulations of bubble column reactors using the DBM taking into account mass transfer and chemical reaction with relatively high gas hold-up require excessive computer power, parallelization of the model is necessary. A parallel algorithm applicable to the DBM was thus developed. The model describing the dispersed phase dynamics accounts for bubble-bubble collisions and is parallelized using a *'mirror domain'* technique while the pressure Poisson equation for the continuous phase is solved using a domain decomposition technique implemented in the PETSc library [Ref. http://www.mcs.anl.gov/petsc]. The parallel algorithm is verified and it is found that it gives the same results for both phases as compared to the serial algorithm. Furthermore, the algorithm shows good scalability up to $32$ processors. Using the proposed method, a homogeneous bubbly flow in a laboratory scale bubble column can be simulated at very high gas hold-up (up to $37\%$) while consuming a reasonable amount of calculation wall time.
Using the parallel version of the model, the role of the gas injection pattern on the large scale structures in a homogeneous pseudo-2D bubble column operated at relatively high gas hold-up is studied. Seven cases with different inlet configurations have been studied experimentally by Harteveld et al. [In *Proc. CHISA*, 2004]. Each of these cases has been simulated using the parallel version of DBM. The presence of coherent structures for both uniform and non-uniform gas injection is studied. Furthermore, the influence of the gas injection pattern on the dynamics is investigated, while the statistical (average and fluctuating) quantities are compared with the PIV/PTV and LDA measurement data of Harteveld et al. The results show that the model resembles the observed experimental flow structures to a large extent.

# Samenvatting

Gedetailleerde kennis van bellenkolom reactoren ontbreekt nog steeds ondanks het feit dat bellenkolommen in een grote verscheidenheid aan (chemische) processen worden toegepast en er uitgebreid onderzoek is verricht aan het gedrag in deze apparaten. De zeer complexe interacties tussen de hydrodynamica, stofoverdracht en chemische reacties in combinatie met de grote variatie in tijd- en lengteschalen die in de reactor voorkomen, maakt het modelleren van bellenkolom reactoren tot een uitdaging. In dit proefschrift wordt een aanpak van modellen op verschillende schalen in combinatie met een geavanceerde parallellisatie strategie gebruikt om de stromingsverschijnselen op verschillende schalen te bestuderen. Twee numerieke stromingsmodellen, namelijk een "front-tracking" model en een Euler-Lagrange model, worden gebruikt om de relevante fenomenen op verschillende schalen te bestuderen. De interactie tussen de hydrodynamica, stofoverdracht en chemische reacties worden op een deterministische wijze in het model verdisconteerd, waarbij de relevante koppeling in acht wordt genomen.

Een drie-dimensionaal "front tracking" model gecombineerd met een "immersed boundary" techniek is ontwikkeld om de hydrodynamica en stofoverdracht op het niveau van individuele bellen in detail te bestuderen. Het gecombineerde model beschrijft op expliciete wijze de bel-vloeistof stofoverdracht. Het model stelt ons in staat om a priori de stofoverdrachtscoëfficiënten voor bellen (of druppels) te berekenen, welke gebruikt kunnen worden om sluitingsrelaties op te stellen voor meer grofstoffelijke modeleertechnieken, zoals Euler-Euler of Euler-Lagrange technieken. De mogelijkheden van het model voor het voorspellen van de belvorm, het stromingsveld en het gas-vloeistof stoftransport zijn aan de hand van een aantal simulaties gedemonstreerd. Uit de simulatieresultaten van een systeem met meerdere bellen bleek dat bellen die in de zog van andere bellen stijgen, een hogere stijgsnelheid en een lagere stofoverdrachtssnelheid vertonen.

Een drie-dimensionaal "discrete bubble model" (DBM) is gebruikt om het ingewikkelde gedrag van gas-vloeistof bellenkolommen ten aanzien van hydrodynamica, stofoverdracht en chemische reacties te onderzoeken. In dit model wordt een continuë beschrijving van de vloeistoffase gebruikt. Verder wordt iedere individuele bel op een Lagrangiaanse wijze gevolgd, waarbij rekening wordt gehouden met bel-bel en bel-wand interacties door middel van een botsingsmodel. De stofoverdrachtssnelheid wordt voor elke individuele bel berekend met behulp van een "surface renewal

model" dat gebruik maakt van de lokale instantane eigenschappen van de vloeistoffase in de nabijheid van de bel. De ruimtelijke verdeling van de chemische componenten in de vloeistoffase wordt berekend uit de gekoppelde componentbalansen waarin rekening wordt gehouden met de stofoverdracht van de bellen naar de vloeistof en de chemische reacties tussen de componenten. Het hydrodynamische gedeelte van het ontwikkelde model is gevalideerd aan de hand van experimentele data van Deen et al. [*Chem. Eng. Sci.*, 2001, **56**, 6341] en blijkt goed overeen te komen. Voorts is het model toegepast om menging en fysische absorptie van $CO_2$ bellen in water te bestuderen, totdat verzadiging van de vloeistof optreedt.
Om de kwaliteiten van het DBM voor het voorspellen van de hydrodynamica, stofoverdracht en chemische reacties te valideren is een experimentele opstelling gebouwd, bestaande uit een quasi-2D lab-schaal bellenkolom. Het reversibele twee-staps reactiesysteem van de chemisorptie van $CO_2$ in een waterige $NaOH$ oplossing werd zowel experimenteel als numeriek bestudeerd met behulp van het DBM. De numerieke resultaten zijn vergeleken met de experimenteel bepaalde belsnelheden, welke werden gemeten met behulp van "Particle Image Velocimetry". Verder is de invloed van de stofoverdracht en chemische reactie op de hydrodynamica, belgrootteverdeling en gas volumefractie bestudeerd en vergeleken met de experimentele observaties. Het blijkt dat het model goed in staat is om het gehele reactieve proces te voorspellen. De berekende simulatieresultaten van de hydrodynamica in afwezigheid van stofoverdracht zijn zeer accuraat. Het model lijkt daarentegen het gehele stofoverdrachtsproces te onderschatten, wat naar alle waarschijnlijkheid kan worden toegedicht aan de onzekerheid in het sluitingsmodel voor de stofoverdracht die in deze studie is gebruikt. Desondanks is de invloed van de stofoverdracht en chemische reactie op de hydrodynamica op succesvolle wijze door het model voorspeld.
Parallelisatie van het DBM is noodzakelijk voor het uitvoeren van bellenkolom simulaties inclusief stofoverdracht en chemische reactie bij een relatief hoge gas volumefractie, aangezien deze simulaties een excessieve hoeveelheid rekenkracht vergen. Om deze reden is een parallel algoritme voor het DBM ontwikkeld. Het model voor de beschrijving van de dynamica van de gedispergeerde fase houdt rekening met bel-bel botsingen en is geparalleliseerd met een zogenaamde "mirror domain" techniek, terwijl de Poisson vergelijking voor de drukcorrectie van de continuë fase wordt opgelost met een domein decompositie techniek die is geïmplementeerd in de PETSc bibliotheek [Ref. http://www.mcs.anl.gov/petsc]. Het parallelle algoritme is geverifieerd en blijkt voor beide fasen dezelfde resultaten te geven als het seriële algoritme. Verder vertoont het algoritme een goede schaalbaarheid tot $32$ processoren. Met behulp van de voorgestelde methode kan de homogene stroming in een lab-schaal bellenkolom voor zeer hoge gas volume fracties (tot $37\%$) worden gesimuleerd in een

aanvaardbare rekentijd.
Met behulp van een parallelle versie van het model is de invloed van de gas inlaat configuratie op grootschalige structuren in een homogene quasi-2D bellenkolom bij relatief hoge gas volumefracties bestudeerd. Zeven cases met verschillende inlaat configuraties zijn experimenteel door Harteveld et al. [In *Proc. CHISA*, 2004] bestudeerd. Elk van deze cases is gesimuleerd met behulp van de parallelle versie van het DBM. De aanwezigheid van coherente structuren bij zowel uniforme als niet-uniforme begassing is bestudeerd. Verder is de invloed van de inlaat configuratie op de stromingsdynamica bestudeerd, waarbij de statistische (tijdsgemiddelde en fluctuerende) grootheden zijn vergeleken met PIV/PTV en LDA metingen van Harteveld et al. De resultaten laten zien dat de modelresultaten in grote mate overeenstemmen met de experimentele stromingsstructuren.

# Ringkasan

Meski telah banyak di gunakan pada berbagai proses (kimia) dan telah banyak penelitian ditujukan untuk mengerti kelakuannya, informasi detil tentang kolom gelembung masih sangat terbatas. Interaksi yang rumit antara hidrodinamika, perpindahan masa dan reaksi kimia ditambah dengan rentang waktu dan jarak yang lebar yang terdapat di dalam reaktor membuat kolom gelembung sangat menantang ditinjau dari segi pemodelan.

Di dalam disertasi ini pendekatan pemodelan bertingkat yang di kombinasikan dengan strategi perhitungan paralel lanjut digunakan untuk mempelajari fenomena yang terdapat di dalam kolom gelembung. Dua model numerik dinamika aliran yakni "front tracking" dan "Eulerian-Lagrangian" digunakan untuk mempelajari fenomena yang terkait. Interaksi yang relevan di antara hidrodinamika, perpindahan masa dan reaksi kimia diperlakukan secara langsung pada setiap model.

Dalam rangka mempelajari fenomena hidrodinamika dan perpindahan masa secara detil di tingkat individu gelembung, model front tracking tiga dimensi yang dikombinasikan dengan teknik "immersed boundary" telah dikembangkan. Model ini secara eksplisit menyertakan proses perpindahan masa antara gelembung dan fasa cairan. Dengan model ini, perhitungan koefisien perpindahan masa (yang dibutuhkan pada model yang lebih kasar seperti pada model "Eulerian-Lagrangian" atau "Eulerian-Eulerian") secara apriori telah dimungkinkan. Beberapa simulasi dilakukan untuk mendemonstrasikan kemampuan dari model yang dikembangkan dalam memprediksi bentuk gelembung, medan aliran dan juga perpindahan komponen kimia dari gelembung ke fasa cairan. Lebih lanjut dalam simulasi menggunakan beberapa gelembung, kita telah menemukan bahwa gelembung yang berjalan di riak yang dihasilkan oleh gelembung lain akan mengalami peningkatan kecepatan sedangkan laju perpindahan masa akan berkurang.

Model gelembung diskrit tiga dimensi ("discrete bubble model", DBM) dipakai untuk menyelidiki kelakuan rumit yang melingkupi hidrodinamika, perpindahan masa dan reaksi kimia di dalam reaktor kolom gelembung gas-cairan. Dalam model ini fasa cairan dideskripsikan sebagai kontinu dan properti gelembung ditelusuri dalam kerangka Lagrangian dengan mengikutsertakan interaksi antar gelembung dan gelembung-dinding melalui model perjumpaan. Laju perpindahan masa dihitung untuk setiap gelembung dengan menggunakan model pembaruan lapisan yang mengikutsertakan karakteristik lokal sesaat dari fasa cair di sekitar

gelembung. Distribusi ruang dari komponen kimia yang terdapat di dalam fasa cair dihitung menggunakan persamaan kesetimbangan komponen kimia dengan mengikutsertakan perpindahan masa dari gelembung ke fasa cairan dan reaksi antar komponen. Model hidrodinamika yang di kembangkan divalidasi dengan menggunakan data eksperimen dari Deen et al. [*Chem. Eng. Sci.*, 2001, **56**, 6341] dan kita menemukan tingkat keselarasan yang tinggi. Lebih jauh model yang dikembangkan juga diaplikasikan untuk mempelajari proses pencampuran dan serapan fisik dari gelembung $CO_2$ di dalam air hingga fasa cair mencapai kondisi jenuh.
Untuk memvalidasi DBM dalam memprediksi hidrodinamika, perpindahan masa dan reaksi kimia, instalasi eksperimen yang melingkupi reaktor kolom gelembung kuasi dua dimensi dalam skala laboratorium telah dibangun. Sistem reaksi dua tingkat dan dua arah yang terdapat di dalam proses absorpsi kimia dari gas $CO_2$ di dalam larutan $NaOH$ telah dipelajari secara eksperimen dan numerik menggunakan DBM yang telah dikembangkan sebelumnya. Hasil perhitungan dibandingkan dengan data eksperimen dari kecepatan gelembung yang diperoleh dengan menggunakan teknik pengukuran kecepatan berbasis citra partikel ("particle image velocimetry", PIV). Lebih jauh, pengaruh dari perpindahan masa dan reaksi kimia terhadap hidrodinamika, distribusi ukuran gelembung dan gas hold-up juga dipelajari dan dibandingkan dengan data eksperimen. Hasil penelitian menyimpulkan model yang dikembangkan mampu untuk memperkirakan proses reaksi secara keseluruhan. Perkiraan hidrodinamika tanpa mengikutsertakan perpindahan masa terbukti akurat. Sedangkan hasil simulasi dengan mengikutsertakan perpindahan masa menunjukkan total laju perpindahan masa yang lebih rendah dibandingkan dengan data eksperimen. Ketidakakuratan ini diperkirakan berasal dari ketidakakuratan koefisien perpindahan masa yang digunakan. Meskipun demikian, kecenderungan dari pengaruh laju perpindahan masa terhadap karakteristik hidrodinamika telah dapat diperoleh dengan model yang dikembangkan pada penelitian ini.
Karena simulasi DBM dari kolom gelembung dengan mengikutsertakan perpindahan masa dan reaksi kimia pada kondisi gas hold-up yang tinggi membutuhkan kapasitas komputer yang besar, teknik perhitungan secara paralel dibutuhkan. Algoritma paralel untuk DBM telah dikembangkan. Model yang menerangkan dinamika dari fasa terdispersi yang menyertakan prediksi dari tumbukan antar gelembung dipecahkan secara paralel dengan menggunakan teknik "*mirror domain*" sedangkan persamaan tekanan Poisson untuk fasa kontinu dipecahkan dengan menggunakan teknik pemisahan domain dengan menggunakan paket perangkat lunak PETSc [Ref. http://www.mcs.anl.gov/petsc]. Algoritma paralel yang dikembangkan telah diverifikasi dengan membandingkan hasil yang diperoleh dengan algoritma serial. Lebih jauh algoritma paralel juga menunjukkan skalabilitas yang baik hingga menggunakan 32 prosessor. Dengan menggunakan algoritma yang dikembangkan, kolom gelembung

yang beroperasi pada regim homogen sampai dengan gas hold-up 37% dapat disimulasikan dengan menggunakan waktu perhitungan yang relatif singkat.

Algoritma paralel yang dikembangkan telah diaplikasikan untuk menyelidiki pengaruh dari pola injeksi gelembung terhadap struktur aliran pada sebuah kolom gelembung kuasi dua dimensi yang beroperasi pada regim homogen dengan gas hold-up yang cukup tinggi. Tujuh kasus dengan pola injeksi yang berbeda telah dipelajari secara eksperimen oleh Harteveld et al. [*Proc. CHISA*, 2004]. Setiap kasus telah disimulasikan dengan menggunakan versi paralel dari DBM. Keberadaan struktur koheren untuk pola inlet seragam dan terbatas dipelajari. Selanjutnya, pengaruh dari pola injeksi gas terhadap dinamika aliran dipelajari, sedangkan kuantitas statistik (rata-rata dan fluktuasi) dibandingkan dengan pengukuran PIV/PTV dan LDA dari Harteveld et al. Hasil yang di peroleh menunjukkan model yang dikembangkan dapat memprediksi hasil eksperimen secara luas.

# Acknowledgements

This thesis is the result of a four-year research project which was conducted at the research group Fundamentals of Chemical Reaction Engineering, Faculty of Science and Technology, University of Twente. Here I would like to express my sincere thanks to those who have contributed in accomplishing the research reported in this thesis.
First of all, I would like to thank DSM and IMPACT for their financial support to the project. Support from the National Computing Facilities Foundation, NCF for the use of supercomputer facilities, with financial support from the Netherlands Organization for Scientific Research (Nederlandse Organisatie voor Wetenschappelijk Onderzoek, NWO) is also acknowledged.
I owe my gratitude to all of my teachers who have tought me up to this point. In particular for the current project, I would like to express many thanks to my promotor *Hans Kuipers* and assistant promotor *Niels Deen* who acted as my daily supervisor, for giving me the opportunity to work on this project and for their dedication in guiding me during the entire PhD project. Especially regarding *Niels*, I will long remember our weekly meetings which proceeded with intense discussions about the research activities but frequently filled with a non-research related topic which was equally interesting to discuss. I also would like to thank you for helping me to process the PIV data, for all the grammatical correction work of the papers and for making the Dutch translation of the summary and all other things that you did for me, which would require more than 10 pages of acknowledgement if I would list it all. But most of all, thank you for always being there for helping me. My sincere thanks also for *Martin van Sint Annaland*, *Martin van der Hoef* and *Bernard Geurts* (Faculty of EEMCS) for the discussions that we had during the project.
Having no chemical engineering background, doing experiments involving reactions (even for a very simple system) proved to be challenging and impossible to realize without help of many people. Here I would like to thank all persons involved in the experimental part of the thesis: *Robert Brouwer* for building a wonderful experimental setup with help from *Robert Meijer* and *Mousa Al-Tarazi* for the electronics part. Thanks also to *Wouter Harteveld* (currectly at Shell Global Solutions, Amsterdam) for valuable discussions about the bubble inlet during the early development of the experimental setup. Many thanks also to *Wim Leppink* and *Gerrit Schorfhaar* who always were ready to help if technical problems were encountered. Also my master student, *Roy Henket* who did the experiments

reported in Chapter 4 of this thesis, thank you very much.
I wish to express my thanks to *Nicole Haitjema* for her help in many administrative matters. A warm thanks to *Liesbeth Kuipers* for our conversation every now and then and for the group annual event at the *Waarbeek* which I will always miss. I am very grateful to all my fellow (former) PhD students for a friendly and pleasant working environment experienced in the group, *Chris*, *Jeroen*, *Renske*, *Albert*, *Esther*, *Salim*, *Charu*, *Dhaneswar*, *Mousa*, *Mr. Zhang*, *Mao*, *Tymen*, *Sanders*, *Joris*, *Wouter*, *Jan Albert*, *Bai*, *Willem*, *Sabita* and *Sebastian*. Special thanks to Wouter for our discussions mostly regarding the front tracking model; *Mao* for the LaTeX template use for this thesis and *Jan Albert* for becoming my paranimf. *Terima kasih banyak* for the entire Indonesian community in Enschede, especially *Agung*, *Agoes*, *Pak Drajat*, *Rajesh*, *Reza*, *Eko*, *Syaiful*, *Hadi*, *Vita* and *Budi*. All of you have made my stay in the Netherlands feels like home.
Many thanks to my parents: *Mimih* and *Bapak* in Jakarta; *Mamah* and *Bapak* in Kuningan who give invaluable support for me to finish my study. Also for all my brothers and sisters: *Kak Enang*, *Teh Dewi*, *Kak Ato*, *Una* for your support. For *Rika*, *Lina*, and *Andri* thanks a lot for taking care of your sister for me.
Finally, my special gratitude is directed to my lovely wife, *Neng Rini*, for your never ending love, prayers, patience, understanding and support which kept me holding on even in the most difficult time. To you I especially dedicated this thesis and for you I come home now.

*Enschede, September* $27^{th}$ 2006

# 1

# Introduction

*"Nothing is too small to know, and nothing is too big to attempt."*
- William Van Horne


## Abstract

*In this chapter a brief introduction to bubble columns, with emphasis on modelling is given. Despite their widespread use for various (chemical) processes and a vast amount of research devoted to understand their behavior, detailed knowledge of bubble column reactors is still lacking. The highly complex interactions between hydrodynamics, mass transfer and chemical reaction as well as the wide range of both time and spatial scales prevailing in the reactor make bubble column reactors challenging from a modelling point of view. In this thesis a multi-scale modelling approach in combination with an advanced parallel computing technique is used to study the phenomena prevailing at different scales. Two CFD models, namely an Eulerian-Lagrangian model and a front tracking model are used to study the relevant phenomena at different scales. The interactions between hydrodynamics, mass transfer and chemical reactions are treated directly in each model taking into account the relevant coupling.*

## 1.1 Bubble column reactors

Gas-liquid bubble column reactors refer to (cylindrical) vessels filled with a liquid through which the gas is rising in the form of bubbles. The reactor usually has one or more gas feeds, one of which is normally located at the bottom of the column, and additional channels to distribute the liquid phase (see illustration in Fig. 1.1). Bubble columns are encountered in a wide range of applications such as the Fischer-Tropsch process for hydrocarbon synthesis, hydrogenation of unsaturated oil, oxidation of hydrocarbons, fermentation and (biological) wastewater treatment (see Table 1.1 for more examples). Approximately $10^7$ to $10^8$ tons of products are obtained through reactions in bubble columns per year [1].
Bubble column reactors offer distinct advantages over other gas-liquid contactors. Two characteristic aspects of bubble columns are their simple construction and the absence of complex (moving) mechanical parts. The bubble column is a relatively cheap reactor and can be built in large sizes. The aspect ratio (the ratio between length and diameter), may vary enormously. However the most common aspect ratios being used are in between $3$ to $6$ where the column height can easily exceed $20\,\mathrm{m}$.
In bubble column reactors the flow is buoyancy driven, i.e. by differences in the local density of the gas-liquid mixture or difference in the local gas holdup. The flow structure can easily become highly dynamic or chaotic. In

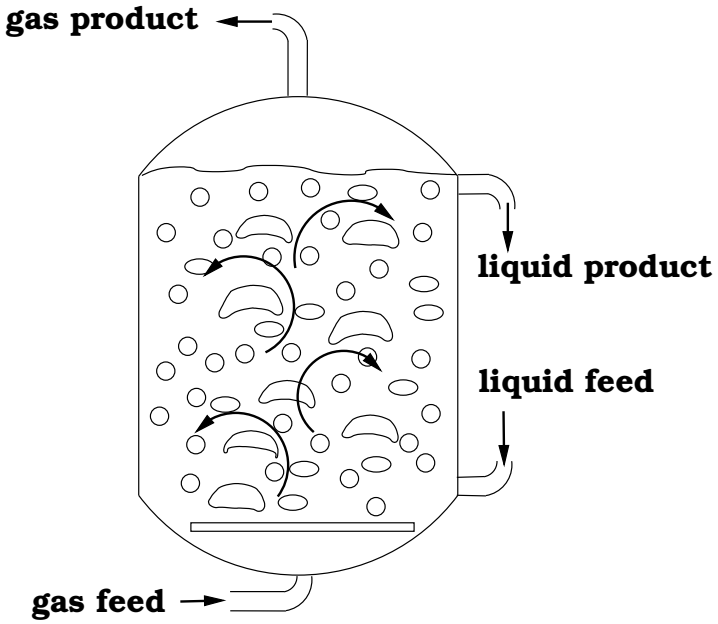


**Figure 1.1:** *Sketch of a bubble column reactor.*

**Table 1.1:** *Some examples of reaction products obtained in bubble column reactors [1].*

| **purpose / product** | **reactants** |
|---|---|
| waste water purification | waste water, air |
| wet oxidation of sludge | sludge, air |
| protein from single cell organisms | methanol, ammonia, air |
| margarine | fatty acid, hydrogen |
| acetaldehyde | ethylene, oxygen |
| cyclohexane | benzene, hydrogen |
| cyclohexanol /-on | cyclohexane, air |
| acetic acid | acetaldehyde, oxygen or n-butane, air |
| ethyl benzene | benzene, ethylene |
| methanol | hydrogen, carbon monoxide / carbon dioxide |
| propylene oxide | propylene, per acetic acid |
| Fischer-Tropsch synthesis | hydrogen, carbon monoxide |

particular in "empty" bubble columns where internals like draft tubes are absent, an overall circulation pattern can prevail. The bubbles are primarily responsible for the good mixing characteristics of the column and excellent heat transfer characteristics marked by a nearly uniform temperature distribution everywhere even under strong exothermic reaction conditions.
Three different flow regimes are encountered in bubble column operations (see Fig. 1.2). These flow regimes affect the hydrodynamics, transport and mixing properties in the column. When the gas flow rate is low, the bubble size is relatively small and its distribution is narrow; spherical gas bubbles are uniformly rising in the column. This is known as the homogeneous regime. The rise velocity of the bubbles in this regime is about $0.18 - 0.3\ \mathrm{m/s}$ [2]. Liquid up-flow is observed in the wake of the bubbles and liquid down-flow in between the bubbles and near the walls.
When the superficial gas velocity is increased, bubble coalescence and break-up occur more frequently resulting in bubbles of different sizes and shapes. This regime, which is known as the heterogeneous regime, has distinct characteristics where big bubbles rise in the center of the column and smaller bubbles are moving along the walls of the column or in the wakes of the larger bubbles. The liquid flow field is unsteady and dominated by a variety of vortical turbulent structures. Industrial bubble columns are commonly operated in this regime.
At even higher superficial gas velocity and in particular when the column diameter is smaller than $0.15\ \mathrm{m}$, the slug flow regime can be observed. In this regime very large bubbles, the so-called slugs, span the entire cross section of the bubble column. The slug behavior is normally undesirable for bubble column operation due to its excessive gas by-pass effect. This regime can however, be encountered in pipelines used to transport

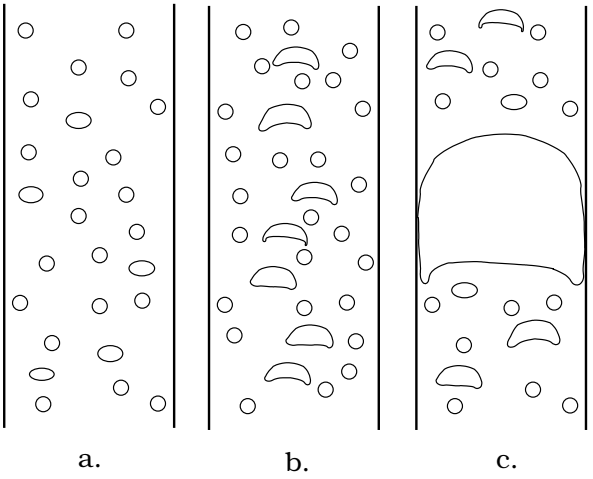


**Figure 1.2:** *The flow regimes observed in gas-liquid bubble column reactors; a. bubbly flow or homogeneous regime; b. heterogeneous regime; c. slug flow regime.*

mixtures of oil and gas from offshore oilrigs to coastal processing facilities. In this thesis only the first two regimes will be considered.

## 1.2 Modelling of bubble column reactors

The performance of the bubble column reactor relies on the combined outcome of multiphase fluid dynamics, interfacial mass transfer and chemical reactions. The interaction between these phenomena is illustrated in Fig. 1.3. The chemical reaction rate depends on the local availability of the species, which is determined by the interphase mass transfer process and the mixing induced by the bubbles. The interphase mass transfer depends on the mass transfer coefficient, the specific interfacial area and chemical reaction rate. The mass transfer parameters are a function of the local prevailing hydrodynamics, which in its turn is affected by the bubble behavior and variation of physical properties due to in-homogeneous chemical species distributions. Most of these phenomena are non-linear, and empirical models cannot be extrapolated too far from the set of design parameters and operating conditions under which they were extracted. As a result, bubble column reaction engineering is still confronted with major challenges from a modelling point of view.

Danckwerts [4, 5] was one of the first to investigate the mixing behavior in bubble column reactors. A major step was taken by introducing the concept of residence time distribution (RTD). The RTD arising from tracer experiments can be used to identify situations that exist between the two extremes of plug flow and complete mixing, and a variety of compartmental models,

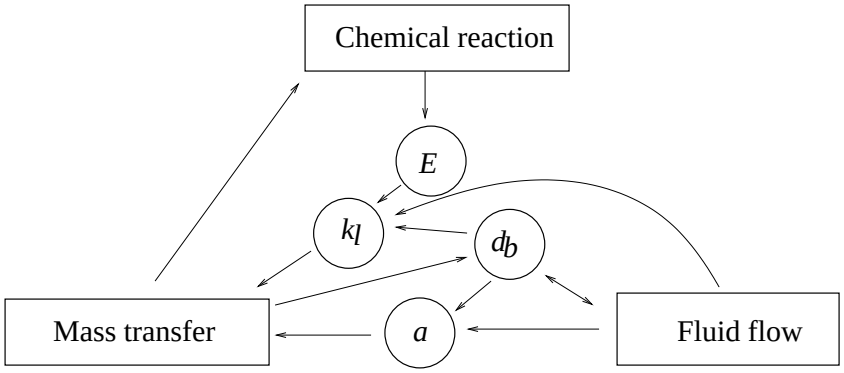


**Figure 1.3:** *Inter-dependency diagram of fluid flow, mass transfer and chemical reaction (from Darmana et al. [3]).*

such as the tanks-in series and the cell model with backflow (or its continuous equivalent, the axial dispersion model) have been used to include a more or less detailed description of reaction and mass transfer [6–9]. Many different empirical correlations for integral gas holdup, $k_l a$ values, and mixing parameters in the column are available as a function of superficial gas velocity [10]. The validity of these correlations with respect to e.g. reactor geometry, the viscosity of the phases and the reactive gas consumption is often questionable [11].

With the continuous development of computer power, scientists have investigated the hydrodynamics of the bubble column reactor using Computational Fluid Dynamics (CFD), where detailed models that describe the phenomena at various scales are derived from first principles and solved numerically. Depending on the scale of interest, several modelling techniques are available, and summarized in Table 1.2. In modelling multiple bubbles rising in a bubble column, two approaches are commonly used: the Euler-Euler formulation, based on the concept of interpenetrating continua, i.e. the two-fluid model, and the Euler-Lagrange approach. In the former approach the Navier-Stokes equations are ensemble averaged using the approach of Drew [12]. Expressions for all interphase interaction terms (i.e. closures) are then required, and these mainly consist of models for the drag, lift and virtual (added) mass forces. The number of bubbles present in a computational cell is represented by a volume fraction and the information of the bubble size distribution is often obtained by incorporating population balance model which take into account break-up and coalescence of bubbles as well as growth or shrinkage of bubbles as a consequence of mass transfer. The Euler-Lagrange model on the other hand adopts a continuum description for the liquid phase and additionally tracks each individual bubble using Newtonian equations of motion. This allows for a direct consideration of additional effects related to bubble-bubble and bubble-liquid interaction.

Table 1.2: *Overview of the available modelling techniques based on the first principles*

| **Model** | **Equations** | **Spatial resolution** | **Applicability** |
|---|---|---|---|
| Two fluid model (Euler-Euler) | Ensemble averaged mass- and momentum conservation equations for both phases | Low $\Delta \gg d_b$ | Full size reactor |
| Discrete bubble model (Euler-Lagrange) | Equation of motion for each bubble; volume averaged mass- and momentum conservation equation for liquid phase | Medium $\Delta \approx d_b$ | Lab-scale bubble columns, bubble plumes |
| Volume tracking / front tracking model | Navier stokes equations for both phases; advanced volume tracking or front tracking scheme | High $\Delta \ll d_b$ | Small systems; $\mathcal{O}\left(10^2\right)$ bubbles |

Mass transfer with and without chemical reaction, bubble coalescence and re-dispersion can be incorporated directly [13–15]. Unlike the Euler-Euler model, the Euler-Lagrange model does not require (computationally expensive) population balance model to predict the bubble size distribution since the bubble size are tracked individually. However, closure for breakage and coalescence is still required to account for the phenomena.
In addition to the above-described methods, several models have been developed to investigate in detail hydrodynamics and the interface deformation of a limited number of individual gas bubbles (i.e. up to $\mathcal{O}\left(10^2\right)$ bubbles). Hirt and Nichols [16] followed by Youngs [17] developed the volume-of-fluid (VOF) method which is able to account for substantial changes in the topology of the gas-liquid interface induced by the relative liquid motion. This particular capability allows a detailed study of bubble formation, coalescence and breakup. Sankaranarayan et al. [18] implemented the VOF technique in the lattice Boltzman method (LBM) to simulate the flow of a single rising bubble. They showed that the great potential of the LBM can also be applied to resolve the details of multiphase flows. Delnoij et al. [19] and Van Sint Annaland et al. [20] respectively used a 2D and 3D VOF showed that this technique is able to predict the interactive behavior and subsequent coalescence of two trailing bubbles, rising in a quiescent liquid remarkably well.
Unverdi and Tryggvason [21] developed the front tracking method, which describes the interface by additional computational elements, usually a connected set of points or a separate unstructured grid that forms a moving boundary. The method describes and tracks the time-dependent behavior of the interface itself. Front tracking methods are extremely accurate but also very complex. This complexity arises from the interaction between the moving boundary and the Eulerian mesh employed to solve the flow field. Major difficulties arise when multiple interfaces interact with each other as in bubble coalescence or breakup. These cases require additional algorithms governing the merger or breakup of interfaces.

One of the major benefits of a very detailed model mentioned above is that parameters (closure) are not needed apart from the physical properties governing the system. Instead, these methods can provide the closures needed by a less detailed model such as the Euler-Euler or Euler-Lagrange models. Some work in this direction has been done for instance by Dijkhuizen et al. [22] who obtained drag and virtual mass closures for a single bubble rising in quiescent liquid from both volume-of-fluid and front tracking simulations and Deen et al. [23] who used front tracking model to simulate the hydrodynamics of bubble motion on a small scale and subsequently derived closure information from the model to be used on a larger scale model (i.e. the Euler-Lagrange model).
Reaction and mass transfer are usually not included in detailed hydrodynamics models of bubble columns. This is mainly because chemical reactions normally employ a large set of chemical species which requires extra computer memory on top of the big memory needed to solve the hydrodynamics model. Furthermore, the coupling between fluid dynamics with complex and often non-linear chemical reaction systems results in a prohibitively steep increase of computational time, whereas the full reaction evolution process can take minutes or even hours, which is very long from a computational point of view.
Recently some authors tried to solve the problem by disassembling the interaction between hydrodynamics, mass transfer, chemical reactions and solve each aspect in a separate model. In those models, CFD is employed only for hydrodynamic simulation, while the chemical phenomena are resolved in a custom-build compartmental model (similar with the one used in the early modelling of bubble columns). Bauer and Eigenberger [1, 11, 24] used a multi-scale modelling approach where parameters obtained from small scale simulation, "frozen" detailed hydrodynamics resulting from CFD and population balances are fed to a simplified reactor model where mass transfer and chemical reaction is treated. Similarly, Rigopolous and Jones [25] mapped a CFD solution into a compartmental model, which was applied to study $CO_2$ absorption into an alkali solution.
Since these methods essentially form compromising techniques to cope with the necessity to get insight information about the mass transfer and chemical reaction process and the prohibitively expensive direct CFD calculation, it does not necessarily resolve the interaction between hydrodynamics, mass transfer and chemical reactions as shown in Fig. 1.3. For example, the method does not have back coupling from the mass transfer and chemical reaction phenomena to the hydrodynamics. This means a.o., a fixed mean bubble size is used to calculate the specific surface area for mass transfer calculation. By assuming an incorrect bubble size, the CFD prediction of other parameters needed in hybrid methods such as the integral gas holdup and the slip velocity would not be accurate either, which eventually will deteriorate the prediction accuracy of the mass transfer and chemical reaction process. Therefore, it is realized that direct coupling between CFD,

mass transfer and chemical reaction is indispensable despite the excessive calculation power needed to solve it and more research effort has to be given in this direction.

## 1.3 Multiscale modelling approach

Apart from its complex interaction, bubble column reactors cover a wide range of spatial scales which span about 7 orders of magnitude. Resolving all scales is not possible in the present or even in the foreseeable future due to excessive requirements in computer power. As an illustration, consider a simple air-water system in a lab-scale bubble column reactor. The largest possible length-scale $\lambda_R$ is introduced as the characteristic of the mean flow, which depends on the scale of the reactor geometry $R$. In order to predict the size of the computational cells required to properly resolve all the relevant hydrodynamics scale, one for example, can use the Kolmogorov length scale $\lambda_K$ ($\lambda_K \ll \lambda_R$), which is given by:

$$\lambda_k = \left(\frac{\nu^3}{\epsilon}\right)^{1/4} \tag{1.1}$$

where $\nu$ is the kinematic viscosity of the respective phase and $\epsilon$ denotes the energy dissipation rate per unit mass, which can be estimated as [26]: $\epsilon = \mathbf{v} \cdot \mathbf{g}$, where $\mathbf{v}$ is the bubble rise velocity and $\mathbf{g}$ the gravity constant. For a $4\,\mathrm{mm}$ air bubble rising in water with a rise velocity of $30\,\mathrm{cm/s}$, this leads to a length scale $\Delta \approx 0.04\,\mathrm{mm}$ inside the liquid phase and $0.2\,\mathrm{mm}$ inside the gas phase.
It has meanwhile been well accepted that the two-phase hydrodynamics of bubble column reactors can only be simulated reasonably well, if a fully dynamic (transient) 3D model is used [14, 15, 27]. Neither steady state nor dynamic 2D simulations with circular symmetry are able to represent the essential features of the buoyancy driven bubbly flow to a reasonable extent. Hence, for a lab-scale bubble column with size of $0.2 \times 0.03 \times 1\,\mathrm{m}$, a 3D hydrodynamics simulation would require about $10^{11}$ computational cells.
The amount of computational cells needed can even be increased if transfer and transport of a chemical species is taken into account. In such cases the smallest relevant length scale is determined by the Bachelor length scale $\lambda_B$, which is given by:

$$\lambda_B = \frac{\lambda_K}{\sqrt{\mathrm{Sc}}} \tag{1.2}$$

where $\mathrm{Sc}$ denotes the Schmidt number, i.e.

$$\mathrm{Sc} = \nu/D \tag{1.3}$$

In the case of gas-water systems with absorption of the gas phase into the liquid, typical values of $\mathrm{Sc}$ are about $10^3$ which makes the computational

cells required to resolve our lab-scale bubble column rise into a staggering $3.3 \times 10^{15}$ cells, a number which cannot be handled even by the next foreseeable computational power.
To cope with this problem, a multi-scale modelling strategy is adopted to properly simulate different aspects of the reactor within a reasonable amount of computational time without loosing too much detail. Within this strategy, the wide range of spatial scales prevailing in the bubble column is split into two or more sub ranges in which for each sub-range an appropriate CFD model tailored to study the phenomena at a certain scale is used. For a small lab scale bubble column, one for instance, can adopt a front tracking model to resolve all the relevant phenomena (hydrodynamics, mass transfer and chemical reaction) up to the bubble length scale $\lambda_d\left(\mathcal{O}\left(d_b\right)\right)$ while an Euler-Lagrange model is used to resolve all scales from the bubble scale $\lambda_d$ up to the integral scale $\lambda_R$ (see Fig. 1.4).
The key of this computational strategy is the exchange of information between the different scales of modelling that constitute our multiscale models. For example, the detailed front tracking model requires no empirical closure laws at all, but it does provide us with extremely detailed information on the flow as well as the species concentration field in and around a deforming gas bubble. The Euler-Lagrange model on the other hand is able to simulate multiple bubbles rising and resolving the (geometry dependent) mean flow field, however it does require a set of closures to describe the bubble dynamics. By performing front tracking simulations with the condition dictated by the bulk flow configuration resulting from an Euler-Lagrange simulation, we can derive sets of empirical closures as a function of various mean flow conditions and bulk concentrations, which later on are fed back to the Euler-Lagrange model.
The small scale that is being "trimmed" away from the Euler-Lagrange modelling (i.e. the subgrid phenomena) is recovered via an additional turbulence model such as the $k-\epsilon$ model or a large eddy simulation (LES) model. This turbulence modelling is very important as early laminar numerical simulations by Delnoij et al. [14] suggested that without a proper turbulence modeling the predicted oscillation period will be too short compared to experimental findings. Several authors like Mudde and Simonin [28], Sokolichin and Eigenberger [29] and Pfleger et al. [30] showed that, in order to get a grid independent quasi periodic solution, a 3-dimensional simulation, employing a $k-\epsilon$ model should be used. In this case, the effective viscosity gets a realistic value.
Recently the use of large eddy simulations as an alternative to the standard $k-\epsilon$ model is suggested by Kuipers and Van Swaaij [31]; Jakobsen et al. [32] and Van den Akker [33]. An article by Deen et al. [27] shows that contrary to the simulations using the standard $k-\epsilon$ model, the LES simulations captured the strong transient movement of a bubble plume, which were observed in the experiment. This gives indication of the superiority of the LES compared to the $k-\epsilon$ in predicting the dynamics of

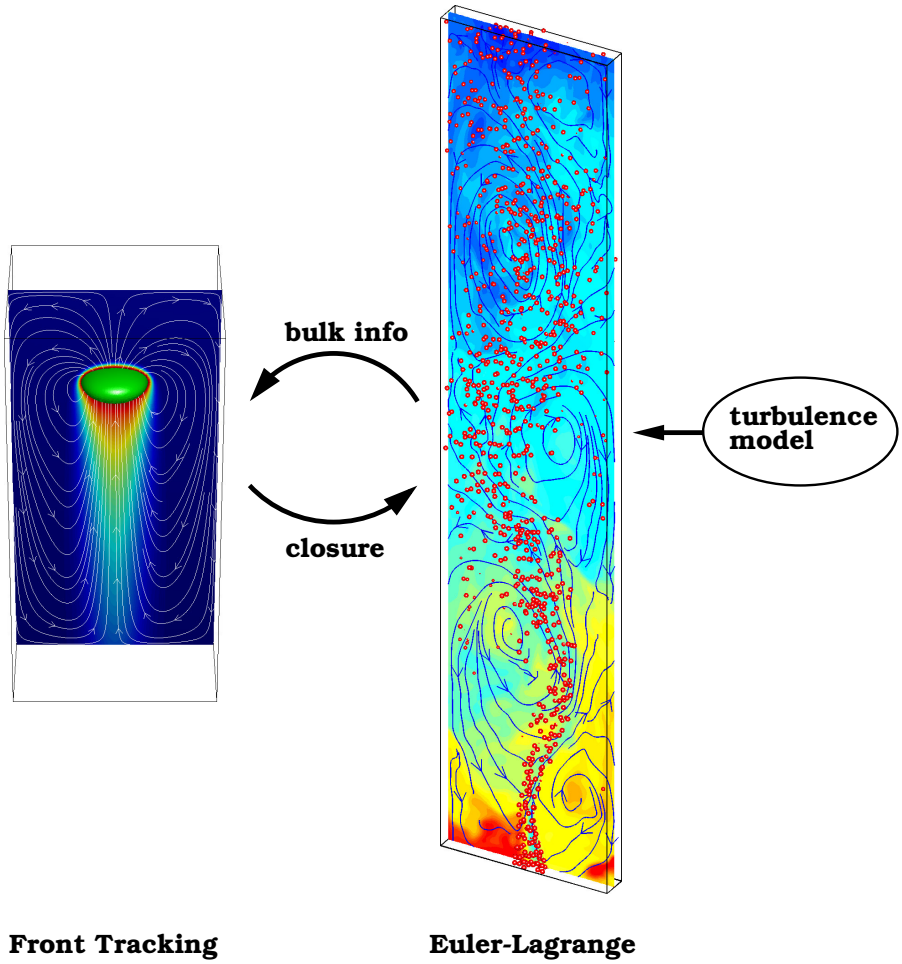


**Figure 1.4:** *Concept of the multiscale modelling applied to a lab-scale bubble column. A three dimensional Euler-Lagrange model supplemented with a turbulence model is used to predict the (geometry dependent) bulk properties such as the liquid velocity* $\mathbf{u}_\infty$*, void fraction* $\varepsilon$*, pressure field* $p$ *and concentration* $c_\infty$ *with the closures* $(C_D, C_L, C_{VM}, C_W, k_l, E)$ *that are provided by a 3D front tracking model simulation.*

multiphase flows. It should be noted that LES is computationally more expensive than the more simple turbulence model such as the $k-\epsilon$ model, because it requires a much higher spatial resolution.

## 1.4 The role of parallel computing

By employing a multiscale modelling approach the astronomical size of the required computational grid can be reduced significantly. Nevertheless the computational requirements are sometimes still bigger than a normal personal computer (PC) can provide. Using a grid size of $\Delta \approx 0.5 d_b$ for example, a total of $7.5 \times 10^5$ computational cells is required for the Euler-Lagrange simulation of our lab-scale bubble column, while the corresponding front tracking model with a typical computational size of $4d_b \times 4d_b \times 8d_b$ would require $\approx 10^8$ computational grid to resolve the Kolmogorov length scale. These computational requirements might fit into a state of the art PC, however it would take years to finish one calculation.
Recently parallelization strategies have received considerable attention in the CFD community. By solving a problem in parallel, not only the time required to solve the problem can be reduced significantly, also the problem size that can be handled is increased, since the memory requirements can be distributed.
Parallel algorithms can be constructed by redesigning serial algorithms to make effective use of parallel hardware. However, not all algorithms can be parallelized. This is summed up in a famous saying [34]:

> *"One woman can have a baby in nine months, but nine women can't have a baby in one month."*

By incorporating a standard parallel communication protocol such as message passing interface (MPI) and carefully writing the code to make it less platform dependent, the parallel code can be run on various platforms from a true massive parallel system such as the National Science Foundations Aster system, down to an in-house PC-cluster consisting of various normal commodity PCs, which are connected through a fast network to perform a single (parallel) task (see Fig. 1.5.). The latter has become increasingly popular in the CFD community as a cheap solution to enter the world of parallel computing.
The performance of a parallel code is measured by its speed-up and efficiency. In practice, linear speedup (i.e., speedup proportional to the number of processors) is very difficult to achieve. This is because many algorithms are essentially sequential in nature, which is reflected by Amdahl's law: *"it is the algorithm that decides the speedup not the number of processors"*.
To develop parallel algorithms that are highly efficient and can be used to solve bigger problems that are otherwise impossible to carry out on a single


(a) National Science Foundation's Aster system

(b) Part of FAP Oscar cluster (left) and FAP Citra parallel cluster

**Figure 1.5:** *Computational platform used in this project. (a) Aster supercomputer, a massively parallel system consisting of SGI Altix 3700 with 416 CPUs (Intel Itanium 2, 1,3 GHz, 3 Mbyte cache each), 832 Gbyte of memory and 2.8 Tbyte of scratch disk space with a total peak performance of 2.2 Teraflop/sec (b) In-house PC cluster built by the author during the project. Oscar cluster consisting of 60 commodity PCs, used mainly for serial calculation. Citra parallel cluster, consisting of 8-processor AMD Opteron 1.8GHz dualcore with 2GB of RAM for each core and infiniband interconnect dedicated for parallel code development and calculations.*

computer thus becomes the central interest in research of parallel computing.

## 1.5 Experimental validation

Experimental validation of the CFD model remains a crucial step in order to gain widespread acceptance of the model as an aided design tool in the engineering community as well as for the development of more sophisticated and refined CFD models.
For the purpose of validation of the flow field calculations, non-intrusive (laser based) experimental techniques such as particle image velocimetry (PIV) and laser Doppler anemometry (LDA) are preferred. PIV is the measurement technique developed in the field of experimental fluid dynamics to study fluid motion using tracer particles. It can be used to measure whole field information of the mean and fluctuating velocities. The LDA technique on the other hand can only provide velocity information in a single point, however the data rate is generally higher, which make it useful to measure intense turbulent flow.
For validation of the bubble size distribution, imaging techniques can be used. With such techniques, bubbles moving inside the reactor are recorded using a digital camera. The images are processed using bubble identifier software to measure the size of the bubbles. A disadvantage of this technique is that it can only be applied in pseudo 2D systems at relatively low gas hold-ups. Despite this disadvantage imaging techniques are applied in many studies.
To obtain high quality experimental data, especially using advanced experimental techniques as mentioned above, is very difficult and requires dedicated research activities, hence in this thesis the experimental data used for model validation is mostly obtained from literature and supplemented with data resulting from our dedicated experiments.

## 1.6 Objective and contributions

The objective of this thesis is to further develop and improve computational models in the research of fluid dynamics in gas-liquid bubble column reactors in the framework of multiscale modelling. The emphasis will be given to incorporate mass transfer and chemical reactions on top of the fluid dynamics models which have been previously developed. The model is then used to gain insight in the phenomena prevailing in a bubble column reactor under reactive conditions especially to achieve a better understanding on how to model the complex interaction between hydrodynamics, mass transfer and chemical reaction.
The contributions to these topics are arranged in chapters as follows:

- *Chapter 2* discusses the modelling of mass transfer using a front tracking model. The model is used to predict the mass transfer coefficient for different flow regimes selected from the Grace diagram. Furthermore, the cases of single and multiple bubbles rising in an initially quiescent flow are considered.
- *Chapter 3* will discuss detailed modelling of hydrodynamics, mass transfer and chemical reaction based on a three dimensional Euler-Lagrange model. The model is used to study the hydrodynamics, mixing, mass transfer and chemical reaction in a square 3D bubble column.
- *Chapter 4* discusses the application of the model developed in chapter 3 to simulate chemisorption of $CO_2$ gas into $NaOH$ solutions in a pseudo 2D lab-scale bubble column. Full evolution of the reactions is considered. Both quantitative and qualitative comparison with experimental observations is given.
- *Chapter 5* describes the parallelization effort applied into the three dimensional Euler-Lagrange model with four-way coupling. A new parallel algorithm called the *mirror domain technique* is developed to solve the model in parallel. Several test cases are presented ranging from a homogeneous bubbly flow simulation to the investigation of the influence of bubble coalescence on the hydrodynamics.
- *Chapter 6* is meant to further validate the Euler-Lagrange hydrodynamics model with experimental data. A pseudo-2D bubble column with relatively high gas hold-up is modeled with emphasis on the effect of the inlet onto the hydrodynamics behavior.

## Notation

| | |
|---|---|
| $a$ | reactor specific area, $\mathrm{m}^2\,\mathrm{m}^{-3}$ |
| $c_\infty$ | bulk species concentration, $\mathrm{kmol}\,\mathrm{m}^{-3}$ |
| $C_D$ | drag force coefficient, dimensionless |
| $C_L$ | lift force coefficient, dimensionless |
| $C_W$ | wall force coefficient, dimensionless |
| $C_{VM}$ | added mass force coefficient, dimensionless |
| $d_b$ | bubble diameter , $m$ |
| $D$ | species diffusion coefficient, $\mathrm{m}^2\,\mathrm{s}^{-1}$ |
| $E$ | enhancement factor, dimensionless |
| g | gravitational acceleration, $\mathrm{m}\,\mathrm{s}^{-1}$ |
| $k_l$ | liquid side mass transfer coefficient, $\mathrm{m}\,\mathrm{s}^{-1}$ |
| $p$ | pressure, $\mathrm{N}\,\mathrm{m}^{-2}$ |
| Sc | Schmidt number, dimensionless |

| | |
|---|---|
| $\mathbf{u}$ | liquid velocity vector, $\mathrm{m\,s^{-1}}$ |
| $\mathbf{v}$ | bubble velocity vector, $\mathrm{m\,s^{-1}}$ |

### Greek letters

| | |
|---|---|
| $\Delta$ | grid size, $\mathrm{m}$ |
| $\epsilon$ | energy dissipation rate per unit mass, $\mathrm{m}$ |
| $\lambda_B$ | Bachelor length scale, $\mathrm{m}$ |
| $\lambda_K$ | Kolmogorov length scale, $\mathrm{m}$ |
| $\lambda_R$ | reactor integral length scale, $\mathrm{m}$ |
| $\nu$ | kinematic viscosity, $\mathrm{m^2\,s^{-1}}$ |

## References

[1] M. Bauer. *On the multiscale modeling of bubble column reactors*. PhD thesis, University of Stuttgart, Germany, 2001.

[2] V. G. Levich. *Physicochemical hydrodynamics*. Prentice Hall, Engelewood Cliff, NJ., 1962.

[3] D. Darmana, N. G. Deen, and J. A. M. Kuipers. Detailed modeling of hydrodynamics, mass transfer and chemical reactions in a bubble column using a discrete bubble model. *Chemical Engineering Science*, 60:3383–3404, 2005.

[4] P. V. Danckwerts. Continuous systems: Distribution of residence times. *Chemical Engineering Science*, 2:1–13, 1953.

[5] P. V. Danckwerts. The efffect of incomplete mixing on homogenous reactions. *Chemical Engineering Science*, 8:93–100, 1958.

[6] J. C. Mecklenburgh and S. Hartland. *Theory of backmixing*. Wiley-Interscience, New York, 1975.

[7] E. B. Nauman and B. A. Buffham. *Mixing in continuous flow systems*. Wiley, New York, 1983.

[8] J. B. Joshi and M. M. Sharma. A circulation cell model for bubble columns. *Transaction of the Institute of Chemical Engineers*, 57:244–251, 1979.

[9] K. Ueyma and T. Miauchi. Properties of recirculating turbulent two phase flow in gas bubble columns. *A.I.Ch.E. Journal*, 25:258, 1979.

[10] W. D. Deckwer. *Reactionstechnik in Blasensäulen*. Otto Salle Verlag, Frankfurt, 1985.

[11] M. Bauer and G. Eigenberger. A concept for multi-scale modeling of bubble columns and loop reactors. *Chemical Engineering Science*, 54:5109–5117, 1999.

[12] D. A. Drew. Mathematical modeling of two-phase flow. *Annual Review of Fluid Mechanics*, 15:261, 1983.

[13] A. Tomiyama, H. Higaki I. Zun, Y. Makino, and T. Sakaguchi. A three-dimensional particle tracking method for bubbly flow simulation. *Nuclear Engineering and Design*, 175:77–86, 1997.

[14] E. Delnoij, F. A. Lammers, J. A. M. Kuipers, and W. P. M. van Swaaij. Dynamic simulation of dispersed gas-liquid two-phase flow using a discrete bubble model. *Chemical Engineering Science*, 52:1429–1458, 1997.

[15] A. Sokolichin and G. Eigenberger. Gas-liquid flow in buble columns and loop reactors: Part i. detailed modelling and numerical simulation. *Chemical Engineering Science*, 49:5735–5746, 1994.

[16] C. W. Hirt and B. D. Nichols. Volume of fluid (VOF) method for the dynamics of free boundaries. *Journal of Computational Physics*, 39:201, 1981.

[17] D. L. Youngs. *Numerical methods for fluid dynamics*, chapter Time-dependent multi-material flow with large fluid distortion, page 273. Academic Press, New York, 1982.

[18] K. Sankaranayan, X. Shan, I. G. Kevrekidis, and S. Sundaresan. Bubble flow simulations with the lattice boltzmann method. *Chemical Engineering Science*, 54:4817–4823, 1999.

[19] E. Delnoij, J. A. M. Kuipers, and W. P. M. Van Swaaij. Numerical simulation of bubble coalescence using volume of fluid (VOF) model. Lyon, France, 1998. Third International Conference on Multiphase Flow, ICMF'98.

[20] M. van Sint Annaland, N. G. Deen, and J. A. M. Kuipers. Numerical simulation of gas bubbles behaviour using a three-dimensional volume of fluid method. *Chemical Engineering Science*, 60:2999–3011, 2005.

[21] S. O. Unverdi and G. A. Tryggvason. A front-tracking method for viscous, incompressible multi-fluid flows. *Journal of Computational Physics*, 100:25–37, 1992.

[22] W. Dijkhuizen, E. I. V. van den Hengel, N. G. Deen, M. van Sint Annaland, and J. A. M. Kuipers. Numerical investigation of closures for interface forces acting on single air-bubbles in water using volume of fluid and front tracking models. *Chemical Engineering Science*, 60:6169–6175, 2005.

[23] N. G. Deen, M. van Sint Annaland, and J. A. M. Kuipers. Multiscale modeling of dispersed gasliquid two-phase flow. *Chemical Engineering Science*, 59:1853–1861, 2004.

[24] M. Bauer and G. Eigenberger. Multiscale modeling of hydrodynamics, mass transfer and reaction in bubble column reactors. *Chemical Engi-*

*neering Science*, 56:1067–1074, 2001.

[25] S. Rigopoulos and A. Jones. A hybrid cfd-reaction engineering framework for multiphase reactor modeling: basic concept and application to bubble column reactors. *Chemical Engineering Science*, 58:3077–3089, 2003.

[26] D. Bothe, M. Koebe, K. Wielage, and H. J. Warnecke. VOF-Simulations of mass transfer from single bubbles and bubble chains rising in aqueous solutions. In *Proceedings of FEDSM'03*, Honolulu, Hawaii, USA, July 6-11 2003. 4th ASME-JSME Joint Fluids Engineering Conference.

[27] N. G. Deen, T. Solberg, and B. H. Hjertager. Large eddy simulation of the gas-liquid flow in a square cross-sectioned bubble column. *Chemical Engineering Science*, 56:6341–6349, 2001.

[28] R. F. Mudde and O. Simonin. Two- and three-dimensional simulations of bubble plume using a two-fluid model. *Chemical Engineering Science*, 54:5061–5069, 1999.

[29] A. Sokolichin and G. Eigenberger. Applicability of the scandard $k-\epsilon$ turbulence model to the dynamic simulation of bubble columns: Part I. detailed numerical simulations. *Chemical Engineering Science*, 54:2273–2284, 1999.

[30] D. Pfleger, S. Gomes, N. Gilbert, and H. G. Wagner. Hydrodynamics simulations of laboratory scale bubble columns: fundamental studies of the Eulerian-Eulerian modelling approach. *Chemical Engineering Science*, 54:5091–5099, 1999.

[31] J. A. M. Kuipers and W. P. M. Van Swaaij. Computer fluid dynamics applied to chemical reaction engineering. *Reviews in Chemical Engineering*, 13:3, 1997.

[32] H. A. Jakobsen, B. H. Sannæs, S. Grevskott, and H. F. Svendsen. Reviews: Modeling of vertical bubble-driven flows. *Industrial and Engineering Chemical Research*, 36:4052–4074, 1997.

[33] H. E. A. Van Den Akker. The Euler-Euler approach to dispersed two-phase flows in the turbulent regime. *ERCOFTAC Bulletin*, 36:30–33, 1998.

[34] Wikipedia, the free encyclopedia. Parallel computing. *http://en.wikipedia.org/wiki/Parallel-computing*, 2006.

# 2

# Detailed 3D Modelling of Mass Transfer Processes in Two Phase Flows With Dynamics Interfaces[§]

*"We think in generalities, but we live in details."* - Alfred North Whitehead


## Abstract

*In this chapter a model is presented which allows us to a priori compute mass transfer coefficients for bubbles (droplets) rising in quiescent Newtonian fluids. Our model is based on the front tracking technique and explicitly accounts for the bubble-liquid mass transfer process. The dissolved species concentration in the liquid phase is computed from a species conservation equation while the value of the concentration at the interface is imposed via an immersed boundary technique. In the present study, simulations are carried out to demonstrate the capabilities of the model to predict bubble shape, flow field as well as transport of a species from bubble to the liquid phase. Finally, we also show that bubbles rising in the wake of other bubbles will experience an increase of rise velocity, while the mass transfer rate is decreased.*


[§]Based on: Darmana et al. [1, 2]

## 2.1 Introduction

Gas-liquid chemical reactors have been studied extensively, both experimentally and computationally. However, because of the complex hydrodynamics, mass transfer and chemical transformations, as well as their mutual interactions, there is still a lack of fundamental understanding of these industrially important reactors.
Due to recent advances in computer power, it has become possible to simulate three dimensional gas-liquid chemical reactors adopting either the Euler-Euler or Euler-Lagrange approach. With these models, large scale processes involving hydrodynamics, mass transfer and chemical reaction can be studied in detail. However, as both models require a set of closures to specifically describe a particular system, the reliability of the results strongly depends on the accuracy of the provided closures.
Traditionally the closures are obtained via experimental routes in well-controlled systems. Only recently scientists have embarked to obtain the required closures from detailed numerical simulations. As an example, using front tracking and volume of fluid models, Dijkhuizen et al. [3] obtained hydrodynamic (drag, lift and virtual mass) closures and found good agreement with experimental data reported in the literature. Furthermore, based on two-dimensional front tracking modelling with additional mass balance equations, Koynov et al. [4] showed that the mass transfer coefficient can also be extracted from such detailed numerical simulations.
From experimental data published by Grace [5] it is known that the physical properties of a gas-liquid system will determine the bubble shape as well as its rise velocity. These parameters, in turn affect the flow field in the vicinity of the bubbles and consequently the gas-liquid mass-transfer and the transport (mixing) in the liquid phase. It has become evident that, in order to accurately predict the mass transfer coefficient, a model should be able to render correctly the shape of the bubble as well as its rise velocity for a given set of physical properties.
In the past decade several techniques have been developed to simulate multifluid flow problems. The most popular techniques have been summarized by Van Sint Annaland et al. [6] and are given in Table 2.1 along with their main advantages and disadvantages. Each of the presented methods will be briefly described here.
*Level set* methods [7–13] are designed to minimize the numerical diffusion hampering shock-capturing methods and typically define the interface as the zero level set of a distance function from the interface. The advection of this distance function evolves through the solution of the following equation:

$$\frac{DF}{Dt} = \frac{\partial F}{\partial t} + (\mathbf{u} \cdot \nabla F) = 0 \tag{2.1}$$

Table 2.1: *Overview of techniques for multifluid flows with sharp interfaces (from Van Sint Annaland et al. [6])*

| Method | Advantages | Disadvantages |
|---|---|---|
| Level set | Conceptually simple | Limited accuracy |
| | Easy to implement | Loss of mass (volume) |
| Shock-capturing | Straightforward implementation | Numerical diffusion |
| | Abundance of advection schemes are available | Limited to small discontinuities |
| Marker particle | Extremely accurate | Computationally expensive |
| | Robust | Redistribution of marker particles required |
| | Accounts for substantial topology change in interface | |
| SLIC VOF | Conceptually simple | Numerical diffusion |
| | Straightforward extension to three dimensions | Limited accuracy |
| | | Merging and breakage of interface occurs automatically |
| PLIC VOF | Relatively simple | Difficult to implement in three dimensions |
| | Accurate | Merging and breakage of interface occurs automatically |
| | Accounts for substantial topology change in interface | |
| Lattice Boltzmann | Accurate | Difficult to implement |
| | Accounts for substantial topology changes in interface | Merging and breakage of interface occurs automatically |
| Front-tracking | Extremely accurate | Mapping of interface mesh onto Eulerian mesh |
| | Robust | Dynamic remeshing required |
| | Accounts for substantial topology changes in interface | Merging and breakage of interfaces requires subgrid model |

expressing that the interface property is advected with the local fluid velocity. Level set methods are conceptually simple and relatively easy to implement and yield accurate results when the interface is advected parallel to one of the coordinate axes. However, in flow fields with appreciable vorticity or in cases where the interface is significantly deformed, level set methods suffer from loss of mass (volume) and thus loss of accuracy.

*Shock-capturing* methods [14] employ high-order shock-capturing schemes to treat the convective terms in the governing equations. The advantage of this method is that explicit reconstruction of the interface is circumvented, which offers advantages for unstructured grids. Although state of the art shock-capturing methods are quite sophisticated, they work less well for the sharp discontinuities usually encountered in multifluid flows. Moreover, they require relatively fine grids to obtain accurate solutions. Rider and Kothe used a high-order Godunov method and conducted several numerical tests and concluded that "in all cases the use of shock-capturing methods was inadequate".

*Marker particle* methods [15, 16] use marker particles that are assigned to a particular fluid and are used to track the motion (and thus the interface) of this fluid. From the instantaneous positions of the marker particles the relevant Eulerian fluid properties, required to solve the Navier-Stokes equations, are retrieved. Marker particle methods are extremely accurate and robust and can be used successfully to predict the topology of an interface subjected to considerable shear and vorticity in the fluids sharing the interface. However, this method is computationally very expensive, especially in three dimensions. Moreover, difficulties arise when the interface stretches considerably, which necessitates the addition of fresh marker particles during the flow simulation. Similar difficulties arise when the interface shrinks. Also merging and breakup of interfaces constitute a problem; again a proper subgrid model needs to be invoked.

*Volume of fluid (VOF)* methods [17–23] use a color function $F(x, y, z, t)$ that indicates the fractional amount of fluid present at a certain position $(x, y, z)$ at time $t$. The evolution equation for $F$ is again Eq. 2.1, which is usually solved using special advection schemes (such as geometrical advection, a pseudo-Lagrangian technique), to minimize numerical diffusion. In addition to the value of the color function the interface orientation needs to be determined, which follows from the gradient of the color function. Roughly two important classes of VOF methods can be distinguished with respect to the representation of the interface: simple line interface calculation (SLIC) and piecewise linear interface calculation (PLIC). Earlier work is generally typified by the SLIC algorithm attributed to Noh and Woodward [24] and the donoracceptor algorithm published by Hirt and Nichols [18]. Modern VOF techniques include the PLIC method ascribed to Youngs [19]. The accuracy and capabilities of the modern PLIC VOF algorithms greatly exceeds that of the older VOF algorithms such as the Hirt and Nichols [20] VOF method. A drawback of VOF methods is the so-called artificial (or numerical) merging

of interfaces (that is, coalescence of gas bubbles), which occurs when their mutual distance is less than the size of a computational cell. On the other hand, when coalescence is known to prevail, the VOF method, contrary to the Front Tracking method does not require specific algorithms for the merging (or breakage) of the interface. Recently, van Sint Annaland et al. [25] successfully applied their three-dimensional (3D) VOF model, based on Youngs's method, to simulate the coaxial and oblique coalescence of two rising gas bubbles.

*Lattice Boltzmann methods (LBM)* can be viewed as a special, particle-based discretization method to solve the Boltzmann equation. This method is particularly attractive in case multiple moving objects (particles, bubbles, or droplets) have to be treated and avoids, contrary to the classical finite-difference and finite-element methods, the dynamic remeshing that becomes prohibitive for a large number of moving objects. Ladd has used the LBM successfully to compute the effective gas-particle drag in particulate suspensions whereas Sundaresan and coworkers [26, 27] recently extended this technique to deformable interfaces and successfully applied this technique to study the dynamics of isolated gas bubbles rising in quiescent liquids. However, in this method problems may arise similar to those in VOF methods as a result of the artificial coalescence of the dispersed elements (gas bubbles).

*Front-tracking* methods [28–31] make use of markers (such as triangles), connected to a set of points, to track the interface, whereas a fixed or Eulerian grid is used to solve the Navier-Stokes equations. These methods are extremely accurate but also rather complex to implement because dynamic remeshing of the Lagrangian interface mesh is required and mapping of the Lagrangian data onto the Eulerian mesh has to be carried out. Difficulties arise when multiple interfaces interact with each other as in coalescence and breakup, both of which require a proper subgrid model. Contrary to LBM and VOF, the automatic merging of interfaces does not occur in front-tracking techniques because a separate mesh is used to track the interface. This property is advantageous in case swarm effects in dispersed flows need to be studied. Because of the Lagrangian representation of the interface this technique offers considerable flexibility to assign different properties (such as the surface tension coefficient) to separate dispersed elements.

Study of mass or heat transfer taking into account a deforming interface has been carried out by several authors. Wohak and Beer [32], used VOF to study heat transfer from a spherical drop in a uniform stream. Davidson and Rudman [33] developed a new method to treat diffusion at the interface based on the VOF model and used it to study heat transfer from a rising bubble with toroidal shape and mass transfer from a rising drop with intra-droplet mass transfer limitation. Bothe et al. [34] used a VOF based method to study mass transfer and transport of oxygen for single bubbles as well as bubble chains rising in aqueous solutions.

Recently, Koynov et al. [4] used a 2D front tracking based method to study mass transfer and chemical reactions for single bubbles and clusters of bubbles. It is found that the VOF method has been mostly used to model mass transfer processes. However, as the interface resolved by the VOF model is less detailed compared to the front tracking model and the fact that front tracking does not suffer from automatic merging in the case of bubble-bubble encounters, we believe that front tracking is more promising to serve as a base model to study mass transfer, especially in the case of bubble swarms.
A three dimensional Front Tracking code (FT3D) has been developed in our group and validated by Van Sint Annaland et al. [6] by conducting extensive numerical tests. They showed that the model can predict shapes of bubbles as well as their rise velocities in accordance with the Grace diagram over a wide range of physical properties. In the present study, FT3D is extended by adding species transport equations to allow simulation of systems with mass transfer and chemical reaction. Three simulations are carried out to demonstrate the capabilities of the model to predict the mass transfer coefficient of a single bubble rising in a quiescent liquid. Furthermore, a simulation with a cluster of bubbles is also carried out to investigate the influence of neighboring bubbles on the mass transfer process. The ultimate goal of this study is the prediction of the bubble-liquid mass transfer coefficient for bubbles rising in isolation or dense swarms required to simulate gas-liquid chemical reactors using large scale models such as the Euler-Euler model or the Euler-Lagrange model.

## 2.2 Governing equations

The front tracking model makes use of markers (such as triangles), connected to a set of points, to track the interface, whereas a fixed or Eulerian grid is used to solve the Navier-Stokes equations (see Fig. 2.1). Furthermore, the interface markers are translated using the interpolated velocity field while the surface tension is calculated for every marker, which is then coupled to the Navier-Stokes equations.
For incompressible media the Navier-Stokes equations can be written as (one field formulation):

$$\nabla \cdot \mathbf{u} = 0 \tag{2.2}$$

$$\frac{\partial \rho \mathbf{u}}{\partial t} + \nabla \cdot \rho \mathbf{u}\mathbf{u} = -\nabla p + \rho \mathbf{g} + \nabla \cdot \mu \left[ (\nabla \mathbf{u}) + (\nabla \mathbf{u})^T \right] + \mathbf{F}_\sigma \tag{2.3}$$

where $\mathbf{F}_\sigma$ is the local volumetric surface force accounting for the presence of the dispersed phase.
The local averaged density $\rho$ and viscosity $\mu$ are evaluated from the local distribution of the phase indicator or colour function $F$ which is governed

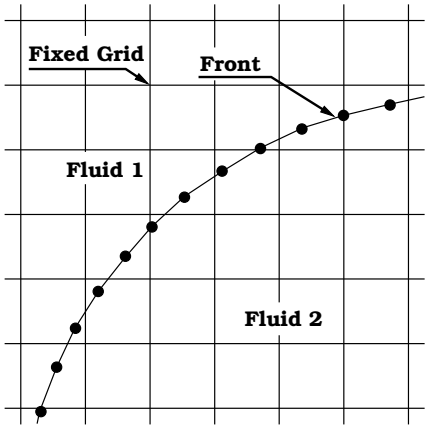


**Figure 2.1:** *Front tracking concept. The governing equations are solved on a fixed grid while the phase boundary is represented by a moving "front", consisting of connected marker points.*

by a Poisson equation given as:

$$\nabla^2 F = \nabla \cdot \mathbf{G} \tag{2.4}$$

where the vector quantity $\mathbf{G}$ contains the information of the spatial distribution of the interface.
For the density $\rho$ linear weighing of the density of the continuous $(\ell)$ and disperse phased $(g)$ is used:

$$\rho = F\rho_\ell + (1 - F)\rho_g \tag{2.5}$$

The local average viscosity is calculated via harmonic averaging of the kinematic viscosities of the involved phases following the approach proposed by Prosperetti [35]:

$$\frac{\rho}{\mu} = F\frac{\rho_\ell}{\mu_\ell} + (1 - F)\frac{\rho_g}{\mu_g} \tag{2.6}$$

The mass balance equations for a chemical species present in the liquid can be written as:

$$\frac{\partial}{\partial t}(c) + \nabla \cdot (\mathbf{u}c) - \mathcal{D}\nabla^2 (c) = \mathrm{F}_s \tag{2.7}$$

where $\mathrm{F}_s$ is a species volumetric forcing term, which will ensure that the value of the species concentration at the interface is equal to the value prescribed by Henry's law. In this study a single mass balance is used to describe the species quantity inside and outside the bubble. The depletion of the gas inside the bubble is neglected given the fact that for the purpose of obtaining mass transfer closure, the residence time of simulation is generally short compared to the mass-transfer time scale. Thus, by assuming

that the bubble only contains a single species and by neglecting pressure gradients inside the bubble, the concentration of the dissolved gas within the area enclosed by the interface must stay constant which is achieved via the forcing term at the interface.

## 2.3 Numerical solution method

### 2.3.1 Flow field

In order to handle systems with very large density ratios such as air-water or vapor-water system (see Dijkhuizen et al. [3]), the Navier-Stokes equations are rewritten in the non-conservative form using the continuity equation:

$$\rho\left[\frac{\partial \mathbf{u}}{\partial t} + (\nabla \cdot \mathbf{uu})\right] = -\nabla p + \rho \mathbf{g} + \nabla \cdot \mu\left[(\nabla \mathbf{u}) + (\nabla \mathbf{u})^T\right] + \mathbf{F}_\sigma \tag{2.8}$$

where the density on the left hand side is evaluated at the old time level.
Eq. 2.8 is solved with a standard finite difference technique on a staggered rectangular three-dimensional grid using a two-step projection-correction method with an implicit treatment of the pressure gradient and explicit treatment of the convection and diffusion terms. A second order flux delimited Barton-scheme is used for the discretization of the convective terms and standard second order central finite difference for the diffusion terms. The resulting pressure Poisson equation (PPE) is solved using the conjugate gradient method with the block Jacobi method selected as preconditioner implemented in the PETSc package [36–38].

### 2.3.2 Interface tracking and phase indicator

The corner points of the surface elements (markers) are moved with an interpolated velocity field using a first order Euler time integration:

$$\mathbf{r}^{n+1} = \mathbf{r}^n + \mathbf{u}_m^{n+1}\Delta t \tag{2.9}$$

where $\mathbf{r}^n$ and $\mathbf{r}^{n+1}$ represent the position vector of the marker points at respectively the old ($n$) and new ($n+1$) time level, whereas $\mathbf{u}_m^{n+1}$ represents the interpolated velocity field at the new time level.
The spatial distribution of the phase indicator $F$ is solved by first calculating the spatial interface vectors $\mathbf{G}$ using the method proposed by Unverdi and Tryggvason [28]:

$$\mathbf{G} = \sum_m D\left(\mathbf{x} - \mathbf{x}_m\right)\mathbf{n}_m \Delta s_m \tag{2.10}$$

where $D\left(\mathbf{x} - \mathbf{x}_m\right)$ represent a numerical approximation of the Dirac-function normalized to the cell volume. In the present model, volume weighing is used and proofed to be sufficiently stable [39].

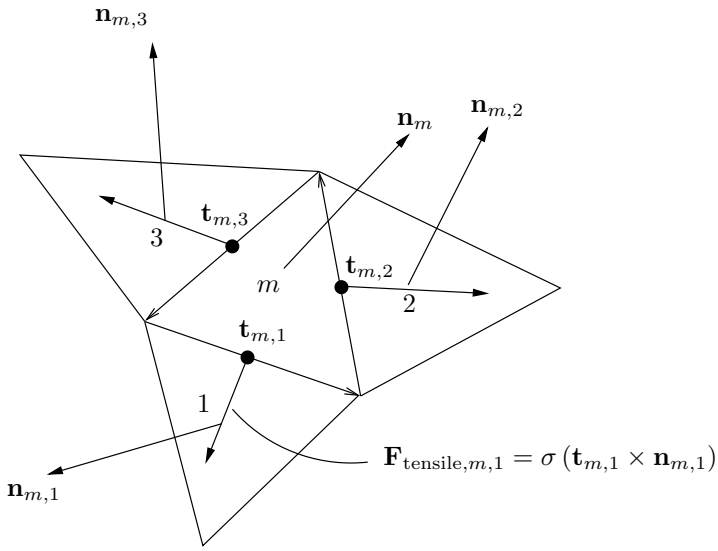


**Figure 2.2:** *Surface tension force exerted by three neighboring surface elements on the central surface element.*

Using $\mathbf{G}$ given by Eq. 2.10, the Poisson-equation for the colour function $F$ (Eq. 2.4) is discretized using a standard finite difference method. The resulting set of linear equations is solved using the incomplete Cholesky conjugate gradient (ICCG) algorithm.

### 2.3.3 Surface force

The net surface force acting on a single surface element $m$ is calculated as:

$$\mathbf{F}_{m,s} = \oint \sigma\left(\mathbf{t} \times \mathbf{n}\right) \mathrm{ds} \tag{2.11}$$

where $\mathbf{t}$ is the unit tangent vector (or edge) of element $m$, $s$ the tangent coordinate and $\mathbf{n}$ is the unit normal vector.
In the discrete form (see Fig. 2.2), Eq. 2.11 is written as:

$$\mathbf{F}_{m,s} = \sum_k \sigma\left(\mathbf{t}_k \times \mathbf{n}_k\right) \tag{2.12}$$

where $\mathbf{t}_k$ is the length of the edge shared by element $m$ and neighboring element $k$ and $\mathbf{n}_k$ is its unit normal vector. The tangent vectors are directly calculated form the known positions of the three corner points of the element. The volumetric surface force in the Eulerian grid is obtained by mapping individual net surface force from all elements:

$$\mathbf{F}_\sigma\left(\mathbf{x}\right) = \frac{\sum_m \sum_k \rho_{m,k} D\left(\mathbf{x} - \mathbf{x}_{m,k}\right) \sigma\left(\mathbf{t}_{m,k} \times \mathbf{n}_{m,k}\right)}{\sum_m \sum_k \rho_{m,k} D\left(\mathbf{x} - \mathbf{x}_{m,k}\right)} \tag{2.13}$$

where, additional density weighing is used to avoid distribution of the surface force to cells that have a very low liquid volume fraction.

### 2.3.4 Mass transfer

The species balance given in Eq. 2.7 is solved by a two-step prediction correction method. The value of the concentration at the interface is imposed using the immersed boundary technique described by Uhlmann [40]. In this technique a volumetric forcing term $\mathrm{F}_s$ is determined in such a way that the resulting solution of Eq. 2.7 gives the desired value of the concentration at the interface in an interpolated manner.
In the prediction step, the effect of the species forcing term is ignored to obtain an explicit expression for the intermediate solution $c^*$:

$$\frac{c^* - c^n}{\Delta t} = -\nabla \cdot \left(\mathbf{u}^{n+1} c^n\right) + \mathcal{D}\nabla^2 \left(c^n\right) \tag{2.14}$$

Here, $n$ denotes the old time level and $n+1$ the new time level.
The species volumetric forcing term $\mathrm{F}_s$ is determined by first calculating the total forcing term for computational cell $i$, $f_i^*$, by making use of the intermediate solution for the concentration:

$$f_i^* = \frac{H c_0 - c_i^*}{\Delta t} \tag{2.15}$$

where $H$ and $c_0$ respectively represent the Henry constant and species concentration inside the bubble.
Since we only want to force the value of the concentration at the interface, the volumetric forcing term is calculated by taking into account the influence from each marker $m$ as:

$$\mathrm{F}_{s,i}^* = \omega_i \cdot f_i^* \tag{2.16}$$

with $\omega_i$ is a distribution function for a computational cell $i$ calculated as:

$$\omega_i = \sum_m D\left(\mathbf{x}_i - \mathbf{x}_m\right) \frac{\Delta V_m}{V_{cell}} \tag{2.17}$$

where $\Delta V_m$ is the volume associated with marker $m$ defined as:

$$\Delta V_m = A_m (V_{cell})^{1/3} \tag{2.18}$$

where $A_m$ and $V_{cell}$ respectively are the area of marker $m$ and the volume of the associated computational cell, $V_{cell} = \Delta x \cdot \Delta y \cdot \Delta z$. Here we use a Peskin like function for the numerical approximation of the Dirac function $D\left(\mathbf{x}_i - \mathbf{x}_m\right)$ which we believe can provide a smoother function over the standard volume weighing as described in more detail in Chapter 5.

The second step in the solution of Eq. 2.7 is a correction step, where the species forcing term is added:

$$\frac{c^{n+1}-c^{n}}{\Delta t} = -\nabla\cdot\left(\mathbf{u}^{n+1}c^{n+1}\right) + \mathcal{D}\nabla^{2}\left(c^{n+1}\right) + \mathrm{F}_{s}^{*} \tag{2.19}$$

For both Eqs 2.14 and 2.19, a standard central scheme is applied to the diffusive term, while a second order Barton scheme [41] is used to evaluate the convective term. Furthermore, a first order Euler scheme is used for the time integration.
Since $\omega$ only depends on the interface position, one can first calculate $\omega$ for all markers $m$ and proceed by solving Eq. 2.14 only for the computational cells where $\omega_i \neq 0$. Meanwhile, in the solution of Eq. 2.19, for each chemical species involved in the system (including the background liquid) a species balance equation is used. The resulting discretized equations for all species are solved simultaneously using an algorithm similar to that used by Hjertager [42] in solving the mass conservation equations in a multi-fluid model. This algorithm has also been used by Darmana et al. [43] for solving chemical species balances in their discrete bubble model (see chapter 3).

### 2.3.5 Velocity interpolation for the species balance equation

To improve accuracy, the species balance is solved on a grid that is finer than the grid employed for the hydrodynamics. The fluid velocities defined on the (coarse) hydrodynamics grid are interpolated on the fine grid using a simple (divergence free) piecewise linear interpolation technique following the work of Rudman [20], which is illustrated in Fig. 2.3 and can be explained as follows: for the $x-$component of the fine-grid velocity $u$, piecewise linear interpolation of the coarse grid velocity $U$ is used in the $x-$ direction and piecewise constant interpolation in the $y-$direction (and vice versa for the $y-$direction velocity $v$). For $\frac{\Delta_c}{\Delta_f} = 2$ for example, the $x-$velocity fields on the fine grid are consequently calculated as:

$$u_{i,j-\frac{1}{4}} = u_{i,j+\frac{1}{4}} = \frac{U_{i-\frac{1}{2},j} + U_{i+\frac{1}{2},j}}{2} \tag{2.20}$$

$$u_{i-\frac{1}{2},j-\frac{1}{4}} = u_{i-\frac{1}{2},j+\frac{1}{4}} = U_{i-\frac{1}{2},j} \tag{2.21}$$

$$u_{i+\frac{1}{2},j-\frac{1}{4}} = u_{i+\frac{1}{2},j+\frac{1}{4}} = U_{i+\frac{1}{2},j} \tag{2.22}$$

For typical cases investigated in the present study, a grid dependence test revealed that a species balance grid of at least three times smaller size than the hydrodynamics grid is required.

### 2.3.6 Computational sequence

The phenomena involving detailed hydrodynamics and mass transfer are solved with the front tracking technique in a sequential manner. A diagram

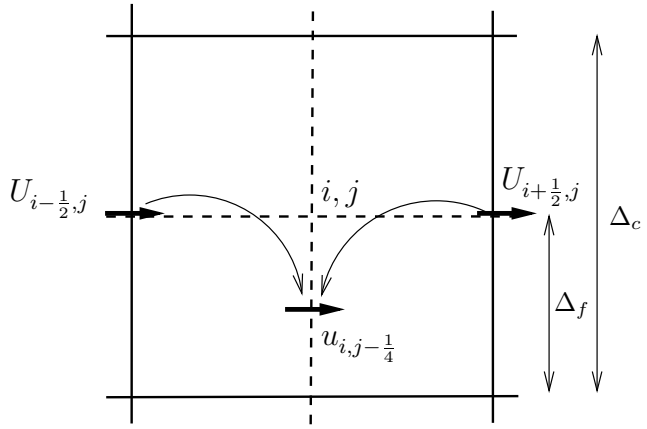


**Figure 2.3:** *Illustration of the velocity interpolation technique used in the present study for* $\frac{\Delta_c}{\Delta_f} = 2$. *The velocity at coarse cells is denoted by* $U$ *while the interpolated velocity on the fine grid is denoted by* $u$.

of the computational sequence is presented in Fig. 2.4. For every flow time step $\delta t_{flow}$, first, the front is moved using the interpolated velocity at the corner position of the marker followed by the remeshing procedure if necessary. With the new front position, the spatial distribution of the $F$ indicator is updated by solving Eq. 2.10. Calculation of the new density and viscosity fields is carried out afterwards. The pressure and velocity field are determined next by solving the Navier-Stokes equations using the new surface force. Subsequently, with the new velocity field and old species concentration, the intermediate concentration is determined explicitly. The intermediate concentration is then used to calculate the species forcing term. Finally the concentration field for the whole computational domain is determined by solving Eq. 2.19 implicitly. This sequential procedure is repeated until a specified simulation end time is reached.

## 2.4 Parallelization

To properly resolve the flow field, relatively large computational grids are required. For most practical purposes the hydrodynamics grid can easily exceeded $100^3$ cells while the corresponding species grid is then $300^3$ cells. Simulations with this amount of computational grid cells are not possible on a single processor due to limitation of computational power and memory. The method described in the previous section has been implemented for calculations on distributed memory parallel computers using the message passing interface (MPI) library [44, 45].
Parallelization of the method was carried out by identifying the parts

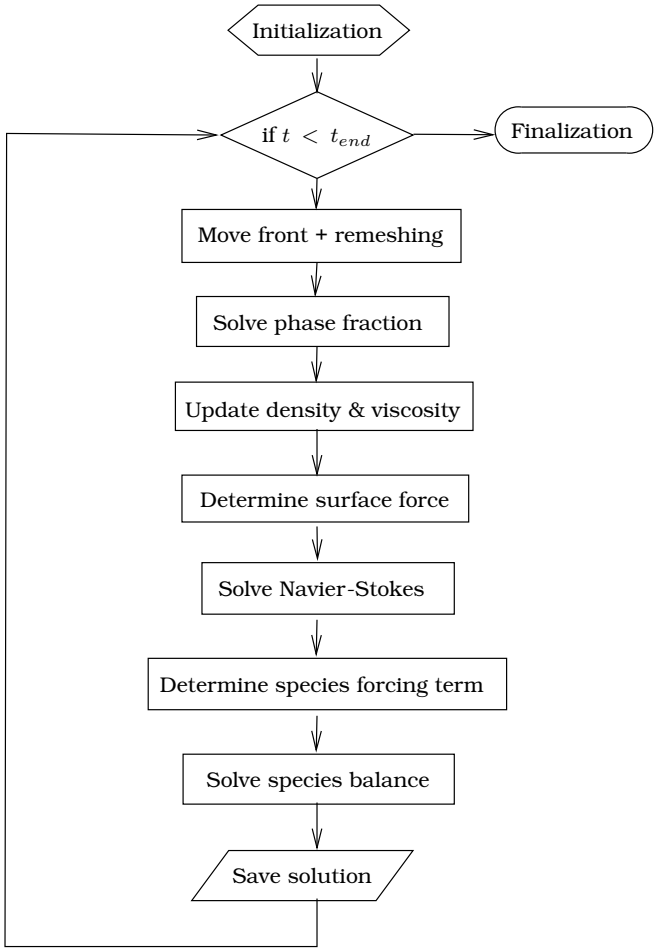


**Figure 2.4:** *Computational sequence diagram for the front tracking model.*

of the model that are related to the front and the liquid (see Table 2.2). For the liquid and the front related computational tasks, two different parallelization strategies are implemented. For the liquid, domain decomposition is used. Here the rectangular, three-dimensional domain is partitioned into even-sized subdomains and the task in each subdomain is processed on a different processor. The data consistency is maintained by interchanging data in each subdomain boundary with their corresponding subdomain neighbor.

For the bubble front, the computational task is distributed by spreading the set of bubbles evenly over the processors. The front element data is structured independently for each bubble hence the front related operations such as moving the front, remeshing, calculating the phase fraction and the species forcing term can directly be calculated in parallel.

For the calculation which requires interaction (coupling) between bubble front data and the Eulerian data an additional procedure is required. This is because the bubble front data might require (or is required by) Eulerian cells that belong to other processors. Here we use a multipurpose buffer variable that is available on each processor. The local value of a Eulerian quantity is copied to the buffer and by using the *gather all* operator available in MPI, the local buffer is collected and redistributed to all processors. Through this procedure, a Eulerian quantity for the complete domain is available on each processor locally, which can be used by a front element regardless which processor is holding the front data. The exact opposite procedure is applied to map front bubble quantities to the Eulerian cells.

The parallel procedure described here is simple and easy to implement. However it has a drawback that processors can have an uneven load due to an uneven number of bubbles on every processor. Also, in the case where multiple sizes of bubbles are present in the system, a processor holding a big bubble will have a higher load due to the higher number of elements present in big bubbles compared to a small bubble. Nevertheless, since the front related computations generally take a relatively small fraction of the total computational time, the time penalty will be minor in many cases.

Table 2.2: *Separation of the computational tasks for parallelization purposes.*

| **Bubble front** | **Liquid** |
|---|---|
| Moving front + remeshing | Navier-Stokes solver |
| Phase fraction solver | Species balance solver |
| Calculation of surface force | Density & viscosity calculation |
| Calculation of species forcing term | |

## 2.5 Validation

Validation of the hydrodynamics part of the model has been reported by Van Sint Annaland et al. [6] by comparing simulation results from the present model with experimental data contained in the Grace diagram [5]. They showed that the computed Reynolds number and bubble shape for various bubble regimes compare very well with data obtained from the bubble diagram.
The validation of the numerical method for the species balance equation is presented here by comparing simulation results of a stationary spherical bubble immersed in a large quiescent liquid pool with the analytical solution. The species balance equation in spherical coordinates is given by:

$$\frac{\partial c}{\partial t} = \frac{\mathcal{D}}{r^2}\frac{\partial}{\partial r}\left(r^2\frac{\partial c}{\partial r}\right) \tag{2.23}$$

with the initial condition $c = 0$ for $r\ R$ and boundary conditions $c = c_0$ for $r = R$ and $c = 0$ for $r = \infty$ which has the following analytical solution involving an error function:

$$\frac{c}{c_0}(r) = \frac{R}{r}\left(1 - \text{erf}\left(\frac{r-R}{\sqrt{4\mathcal{D}t}}\right)\right) \tag{2.24}$$

where $R$ is the bubble radius.
In the numerical simulation, a bubble is fixed exactly in the center of a cubic computational domain which has a diameter equal to $3.2d_b$. The liquid velocities are set to zero throughout the entire simulation domain. An initial concentration of $1.0$ is set inside the bubble and zero otherwise. Neumann boundary conditions are applied on all confining walls. A computational grid of $64^3$ cells is used for the hydrodynamics, while $192^3$ cells are used for solving the species balance equations. Furthermore a time step of $10^{-4}\,\text{s}$ and species diffusivity of $1 \times 10^{-4}\,\text{m}^2/\text{s}$ are used.
Figure 2.5 (top) shows instantaneous species concentration profiles in the vicinity of the bubble at $t = 7 \times 10^{-2}$ s. It can be seen that, due to the concentration gradient present at the bubble-liquid interface, the species diffuses from the bubble into the surrounding liquid. As the time advances, the species diffuses from the interface and the amount of species present in the liquid continually increases. Comparison between the computed radial concentration profile and the analytical solution is presented in Fig. 2.5 (bottom). As we can see for the four different times, the agreement between the numerical and the analytical solution is very good, which indicates that the method has been properly implemented and is able to resolve the species distribution as well as its evolution correctly. Further validation by comparing the mass transfer coefficient obtained with the present model and a potential flow model will be addressed in the next section.

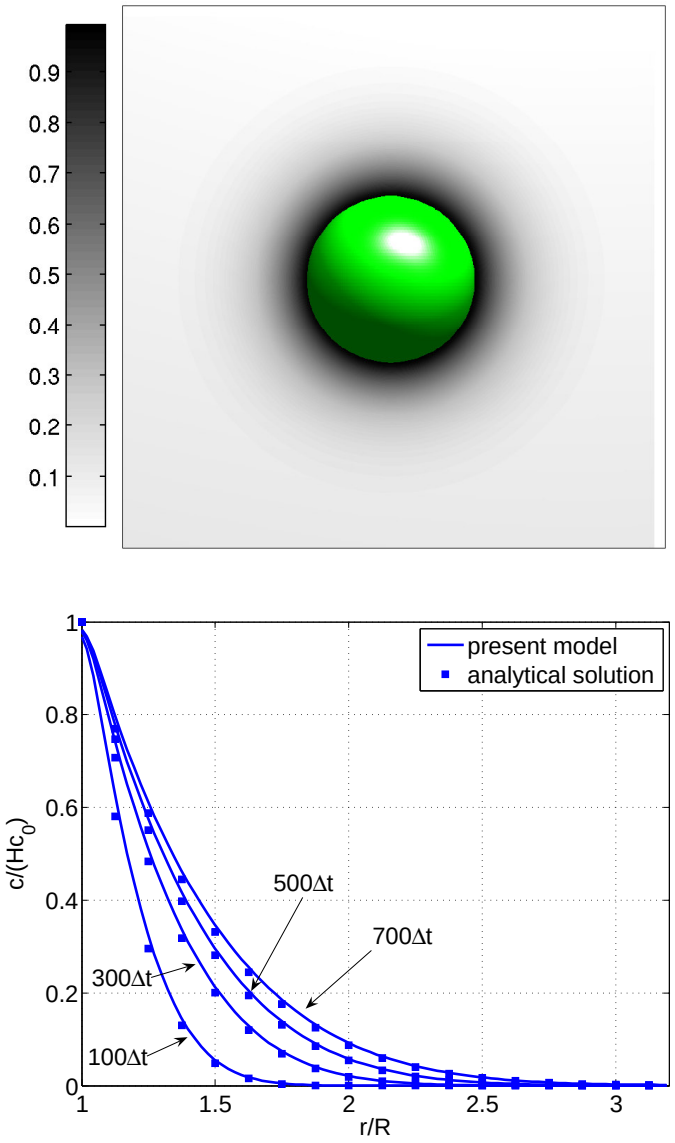


**Figure 2.5:** *Mass transfer from a stationary spherical bubble with* $\mathcal{D} = 1 \times 10^{-4}\,\mathrm{m}^2/\mathrm{s}$. *(top) Normalized concentration distribution after* $7 \times 10^{-2}\,\mathrm{s}$. *(bottom) Radial concentration profiles. Comparison between numerical and analytical solutions.*

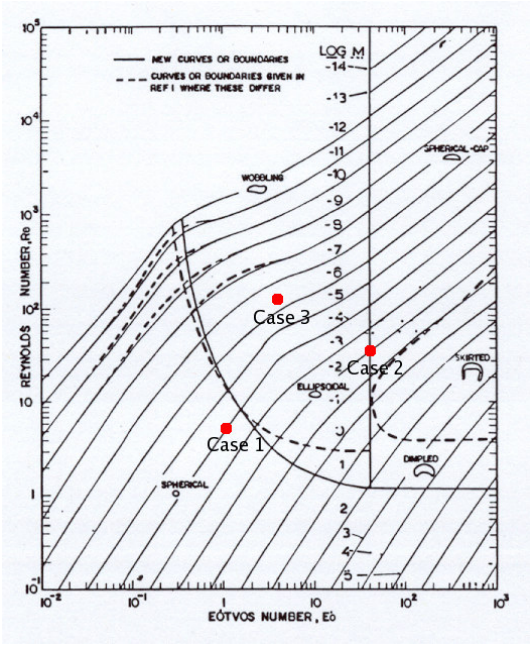


**Figure 2.6:** *Bubble diagram of Grace [5] for the shape and terminal rise velocity of gas bubbles in quiescent viscous liquids. The simulated cases are indicated with circles (see Table 2.3).*

## 2.6 Simulations

Grace [5] showed that the bubble shape and rise velocities in quiescent viscous liquids can be represented in a single diagram provided that an appropriate set of dimensionless number is used. To demonstrate the capabilities of the model in predicting bubble shape, flow field as well as the corresponding dissolved species concentration distribution, three simulations for three different bubble regimes are presented. The Grace diagram is used as our reference for the bubble shape and rise velocities while the mass transfer coefficients are compared with the potential flow model reported in Clift et. al. [46].

A representation of the Grace diagram taken from [5] is shown in Fig. 2.6. The simulation cases carried out in the present study are shown in the diagram as dots (see Table 2.3 for precise numbers). The dimensionless parameters used are Morton (Mo), Eötvös (Eo) and Reynolds (Re) which respectively are given by:

$$\mathrm{Mo} = \frac{g\mu_\ell^4 \Delta\rho}{\rho_\ell^3 \sigma^3} \tag{2.25}$$

**Table 2.3:** *Morton (*Mo*) and Eötvos (*Eo*) numbers for the three cases. For all cases the Schmidt number is set to unity.*

| **Case** | **Mo** | **Eo** |
|---|---|---|
| 1 | $1 \times 10^{-4}$ | 1 |
| 2 | $9.2 \times 10^{-3}$ | 40 |
| 3 | $5 \times 10^{-7}$ | 3.125 |

$$\mathrm{Eo} = \frac{g\Delta\rho d_e^2}{\sigma} \tag{2.26}$$

$$\mathrm{Re} = \frac{\rho_\ell v_\infty d_e}{\mu_\ell} \tag{2.27}$$

Here $d_e$ is defined as the equivalent diameter of a spherical bubble with the same volume as the bubble under consideration, moreover $v_\infty$ represents the terminal rise velocity of the bubble.
In addition three dimensionless number are used to describe the mass transfer, namely Schmidt (Sc), Sherwood (Sh) and Peclet (Pe) number, which are respectively defined as:

$$\mathrm{Sc} = \frac{\mu_\ell}{\rho_\ell \mathcal{D}} \tag{2.28}$$

$$\mathrm{Sh} = \frac{k_l d_e}{\mathcal{D}} \tag{2.29}$$

$$\mathrm{Pe} = \frac{v_\infty d_e}{\mathcal{D}} \tag{2.30}$$

The computational domain used in our simulations is a rectangular box with dimension of $4d_b \times 4d_b \times 8d_b$. The computational grids used for the flow field and species distribution are respectively $80 \times 80 \times 160$ and $240 \times 240 \times 480$ grid cells. Using these grid settings, twenty computational cells in each direction were used inside the bubble for the flow field at its initial state. Furthermore, a time step of $2 \times 10^{-5}$ s was taken for case 1 while $1 \times 10^{-4}$ s was used for case 2 and 3. The size of the computational domain has been checked carefully to warrant that it is large enough to mimic the conditions of an infinite quiescent liquid while the grid resolution was tested to verify that the computed rise velocities were not grid dependent.
For the Navier-Stokes equations, free slip boundary conditions were applied at the domain walls, while for the species balance the Neumann boundary is imposed on all boundaries. A fixed density and viscosity ratio of 100 was used. This density and viscosity ratio is believed to be high enough to mimic gas-liquid systems with sufficient accuracy. The bubble initially has a spherical shape and is positioned at $(x_0, y_0, z_0) = (2d_b, 2d_b, 6d_b)$ in an initially quiescent liquid. To reduce the number of required computational cells, a window shifting technique is used to maintain the bubble at its original position [3].

Table 2.4: *Comparison of the bubble regime and Reynolds numbers obtained from the Grace diagram and simulation results.*

| Case | Bubble regime | Re | |
|---|---|---|---|
| | | **Grace** | **Simulations** |
| 1 | Spherical | 5 | 5.05 |
| 2 | Spherical cap | 33 | 31.4 |
| 3 | Ellipsoidal | 103 | 108 |

The simulations for the single bubble cases were carried out in parallel on a 12-processor Linux cluster (AMD Opteron 1.8GHz dualcore with 2GB of RAM for each core and infiniband interconnect). For these cases, computational times of about 10 days are required to calculate $15,000$ time steps.

## 2.7 Results and discussion

### 2.7.1 Single bubble

Figure 2.7, 2.8 and 2.9 show series of snapshots of the bubble shape, velocity field and the normalized dissolved species concentration at different times. It can be seen that, depending on the physical parameters that were used, bubbles that originally have a spherical shape gradually evolve into different shapes except for case 1 where the bubble remains in its original shape. A spherical cap bubble is found in Case 2 while in Case 3, the spherical bubble has transformed into an ellipsoidal bubble. Comparison between the simulation results and the Grace diagram are presented in Table 2.4. It can be seen that for the three cases, the computed Reynolds numbers compare very well with the data obtained from the Grace diagram with discrepancy less than $6\%$.
As the bubble starts to rise, the flow field in the vicinity of bubble starts to develop and transports the dissolved species downstream. Transport of the species near the bubble surface in general can be divided into two regions, a roof and a wake region. For the three simulations presented in this work the shape of the roof region is similar with only slight variation in the radius of curvature. This shape similarity generates an akin species distribution at the roof region of the bubble. As the Reynolds number increases, the convective transport is becoming more dominant. As a result, the thickness of the species boundary layer at the roof region will decrease as the Reynolds number increases, generating higher interphase mass transfer due to a higher concentration gradient (driving force).
In the wake region the shapes of the bubbles are different for the three cases, generating different flow characteristics as well as species distribution. In case 1, the bubble has a closed wake at the center bottom region of the bubble. Due to the less pronounced convective transport, in this case the

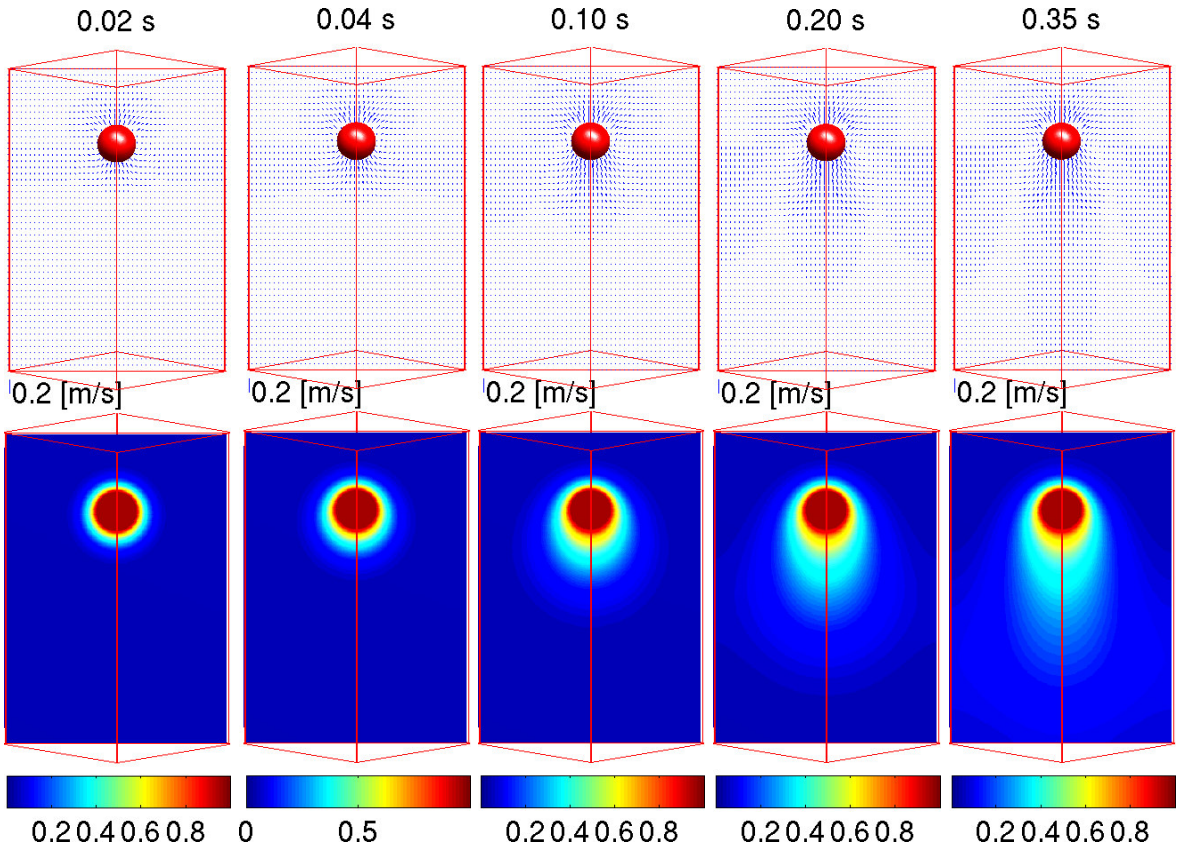


**Figure 2.7:** *Case 1: Spherical bubble,* $\mathrm{Mo} = 1.0 \times 10^{-4}$, $\mathrm{Eo} = 1$, $\mathrm{Sc} = 1$. *Bubble shape and velocity vector (top); Normalized dissolved species concentration (bottom).*

**Figure 2.8:** *Case 2: Spherical cap bubble,* $\mathrm{Mo} = 9.2 \times 10^{-3}$, $\mathrm{Eo} = 40$, $\mathrm{Sc} = 1$. *Bubble shape and velocity vector (top); Normalized dissolved species concentration (bottom).*

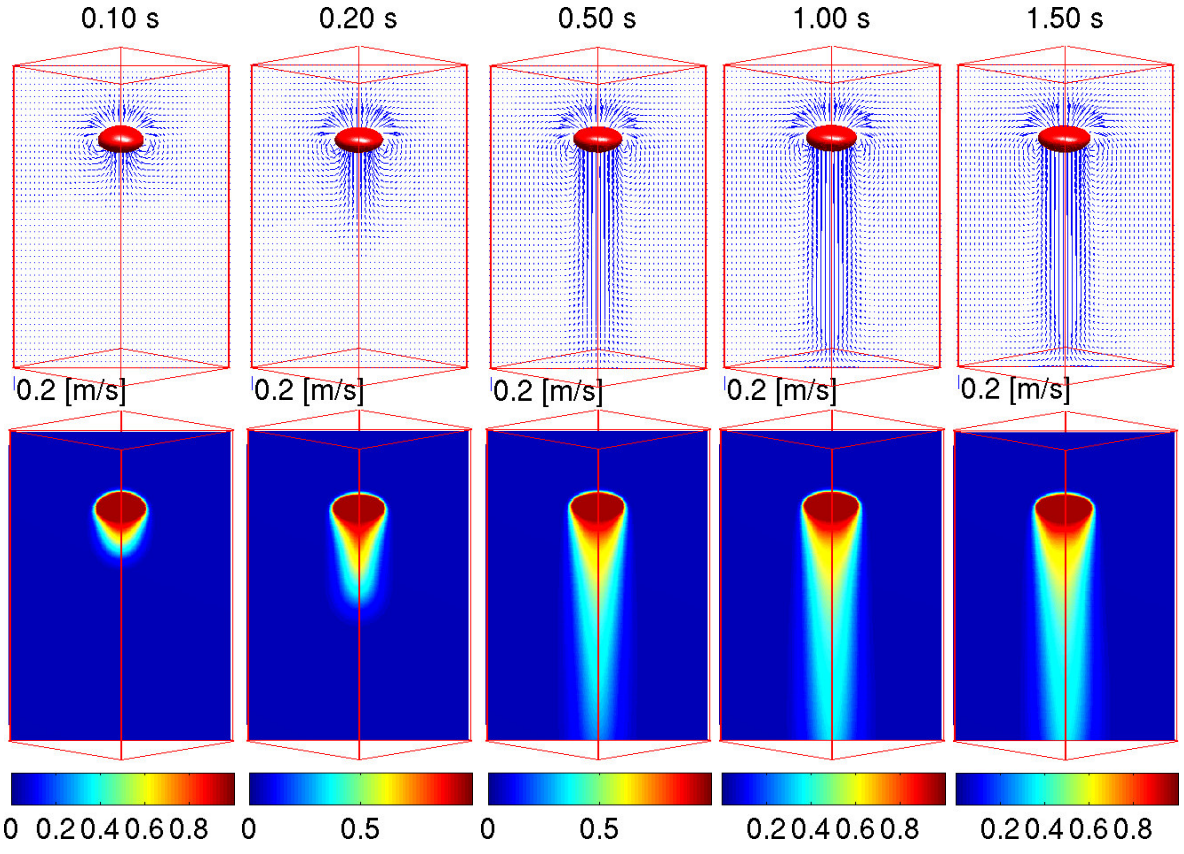


**Figure 2.9:** *Case 3: Ellipsoidal bubble,* $\mathrm{Mo} = 5 \times 10^{-7}$, $\mathrm{Eo} = 3.125$, $\mathrm{Sc} = 1$. *Bubble shape and velocity vector (top); Normalized dissolved species concentration (bottom).*

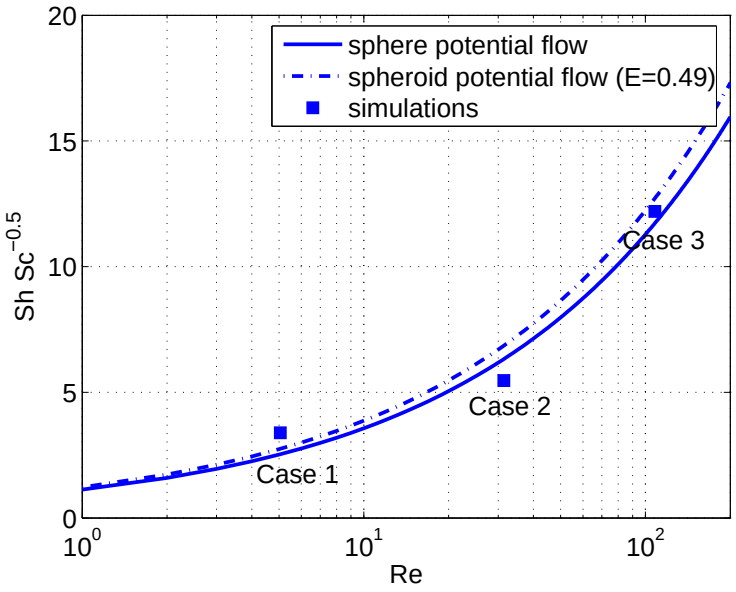


**Figure 2.10:** *Mass transfer factor,* $\mathrm{Sh}/\sqrt{\mathrm{Sc}}$*, obtained with the present model in comparison with the potential flow model [46].*

dissolved gas is found also outside the wake region. In case 2, the bubble possesses a recirculation wake at the edge of the spherical cap bubble. The high concentration of dissolved gas that is trapped below the bubble is flowing through this edge generating a tubular region rich with dissolved gas while the central region has a relatively low concentration of dissolved gas. Finally in case 3, the concentration distribution shows a pattern similar to case 1 where a closed wake at the center bottom region of the bubble is found. However due to the higher Reynolds number, the wake region is somewhat bigger with the dissolved gas almost solely contained in it.
To describe the influence of Reynolds number on the mass transfer process, mass transfer coefficients are calculated from the numerical results by means of the following relation:

$$k_l \approx \frac{V_{cell}}{a\Delta t H c_0} \Sigma_{\forall i \in cell} \left( c_i^{n+1} - c_i^n \right) \tag{2.31}$$

where $a$ denotes the total instantaneous interfacial area, i.e. $a = \Sigma_{\forall m} A_m$.

The mass transfer coefficient is compared with the potential flow model in terms of the Sherwood number, which for a spherical bubble is given by [46]:

$$\mathrm{Sh} = \frac{2}{\sqrt{\pi}} \mathrm{Pe}^{1/2} \tag{2.32}$$

For oblate spheroidal bubbles, Eq. 2.32 is modified taking into account the shape factor [47]:

$$\mathrm{Sh} = \frac{2}{\sqrt{\pi}}\mathrm{Pe}^{1/2}\left[\frac{8e^3E^{1/3}}{3\left(\sin^{-1}e - eE\right)}\right]^{1/2} / \left[1 + \frac{E^2}{2e}\ln\left(\frac{1+e}{1-e}\right)\right] \tag{2.33}$$

where $E$ is the bubble aspect ratio and $e$ is the corresponding eccentricity calculated as:

$$e = (1 - E^2)^{1/2} \tag{2.34}$$

Figure 2.10 shows the comparison between the mass transfer factor ($\mathrm{Sh}/\sqrt{\mathrm{Sc}}$) obtained from the simulations along with both the potential flow model (spherical and spheroidal bubbles) using the actual eccentricity obtained from the simulation. As can be seen the mass transfer rate indeed increases as the Reynolds number increases. Comparison of both the potential flow models shows that the effect of bubble shape is minor in this Reynolds number range. By comparing our result with the potential flow model we can conclude that the match is very good, nevertheless further validation by comparing simulation results for a broader parameter range (Eötvös, Morton, Reynolds and Schmidt number) is essential.

### 2.7.2 Multiple bubbles

In the previous section we have investigated the mass transfer process from a single bubble rising in a quiescent liquid. A real bubble column reactor however, contains multiple bubbles that move collectively as swarms of bubbles. It is well known that bubbles that move in a group behave differently than a single bubble. The interaction between the bubble and the liquid phase is perturbed by the bubbles motion influencing the hydrodynamic behavior of individual bubbles. One could expect that this phenomenon will also influence the mass transfer behavior, where the species dissolved in the liquid surrounding a bubble might not come from the bubble itself but also from neighboring bubbles. As a first step to have a better understanding on how neighboring bubbles influence mass transfer, a simulation with a cluster of bubbles is carried out.

The configuration of case 3 is used as a base for this simulation. The cluster of bubbles is arranged in a $2 \times 2 \times 3$ array with a center to center distance between the bubbles of $2d_b$. A computational domain of $6.4d_b \times 6.4d_b \times 11.2d_b$ is used to accommodate the bubbles present in the domain. The computational grids used for this case are $128 \times 128 \times 224$ and $384 \times 384 \times 672$ grid cells respectively for the hydrodynamics and species grid. With this configuration the same grid per bubble density is used for both the single and multiple bubble case, furthermore the distance between the bubble and the wall is also similar. For this case, the simulation was carried out using $32$ processors in NSF Aster system (Intel Itanium 2, 1.3 GHz). The simulation time for

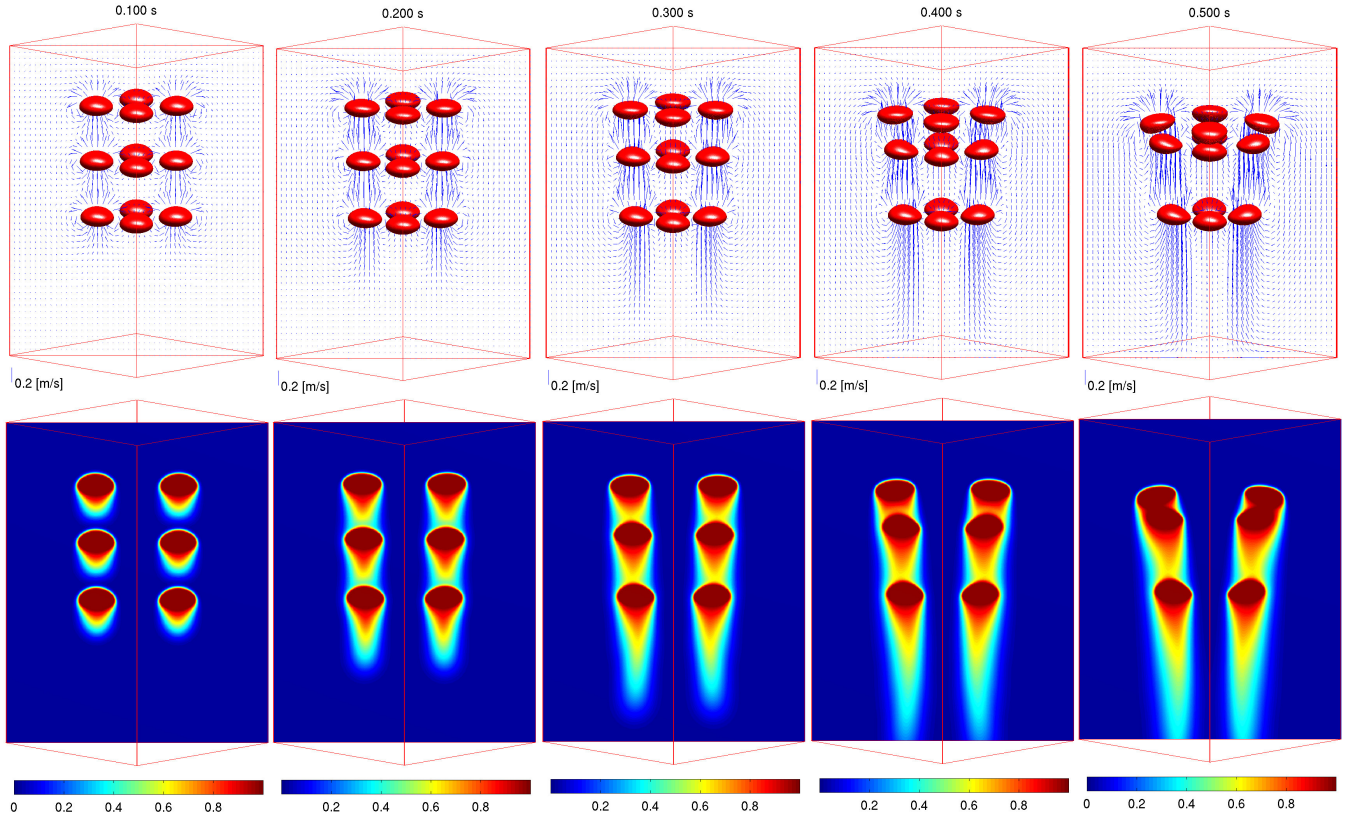


**Figure 2.11:** *Multiple bubble cases: Ellipsoidal bubble,* $\mathrm{Mo} = 5 \times 10^{-7}$, $\mathrm{Eo} = 3.125$, $\mathrm{Sc} = 1$. *Twelve bubbles are initially arranged in a* $2 \times 2 \times 3$ *array with distance pitch of* $2d_b$. *Bubbles shape and velocity vector (top); Normalized dissolved species concentration (bottom).*

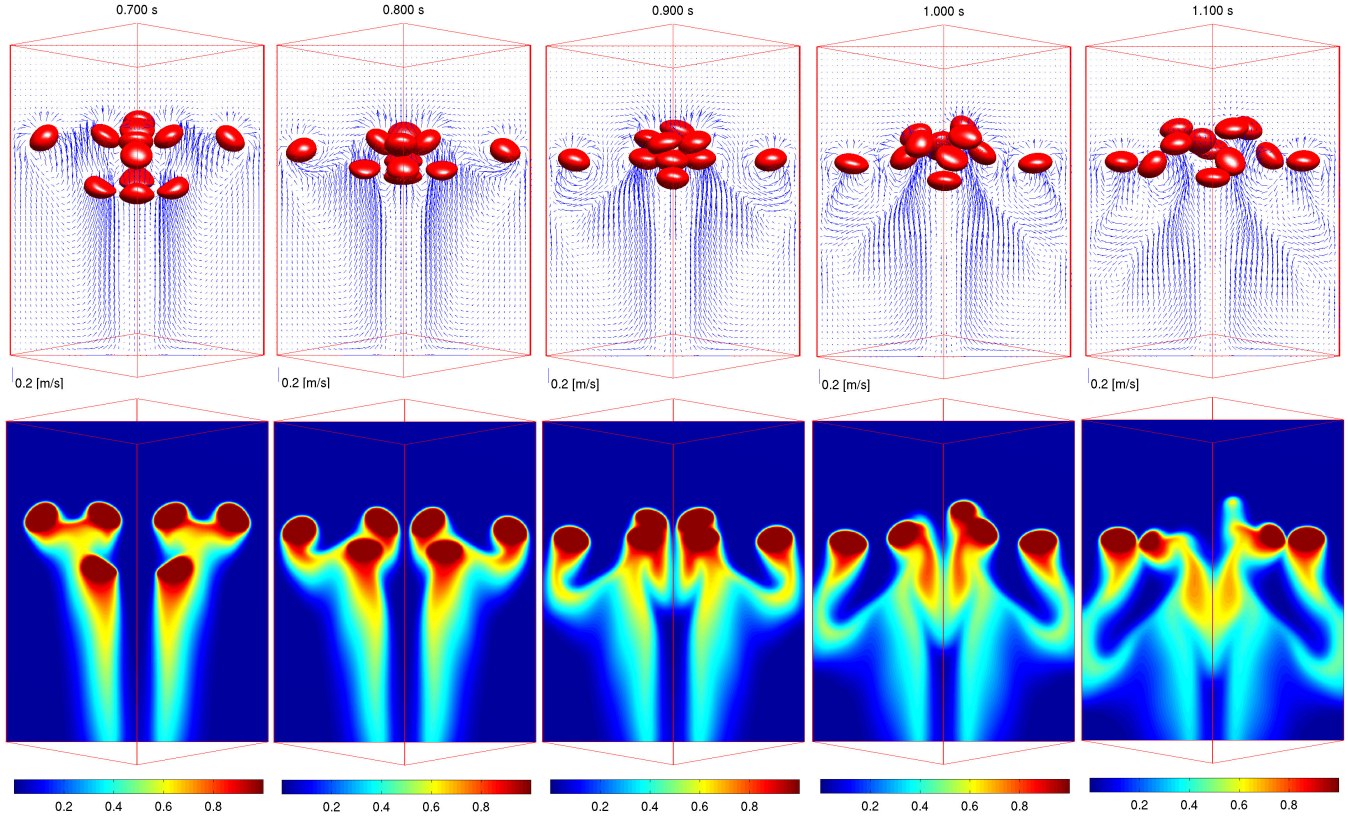


**Figure 2.12:** *Multiple bubble cases (continued): Ellipsoidal bubble,* $\mathrm{Mo} = 5 \times 10^{-7}$, $\mathrm{Eo} = 3.125$, $\mathrm{Sc} = 1$. *Twelve bubbles are initially arranged in a* $2 \times 2 \times 3$ *array with distance pitch of* $2d_b$. *Bubbles shape and velocity vector (top); Normalized dissolved species concentration (bottom).*

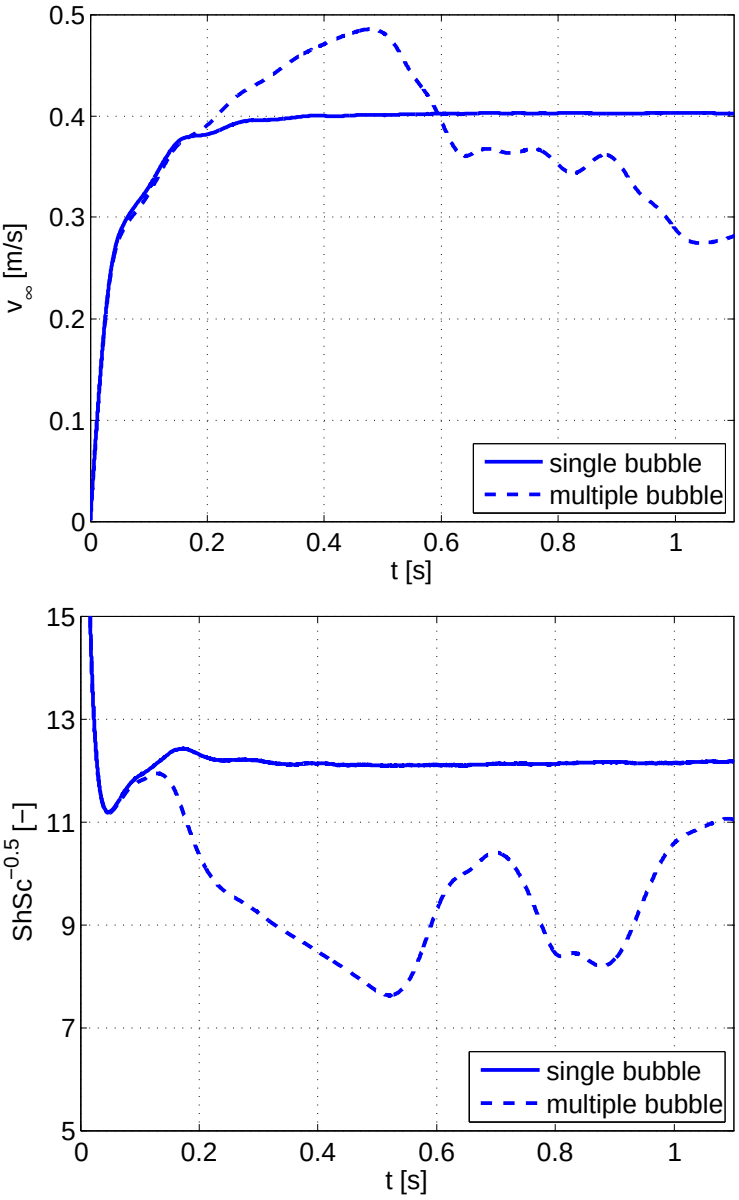


**Figure 2.13:** *Evolution of Velocity (top) and mass transfer (bottom) over time. Comparison between single bubble and cluster of bubbles.*

this case is about $3$ days for every $1000$ time steps.
Figures 2.11 and 2.12 shows series of snapshots of the bubble cluster simulation consisting of bubble shape, velocity field and the normalized dissolved species concentration at different times while Fig. 2.13 shows the time history of velocity and mass transfer of the bubble cluster in comparison with the single bubble case. Note that for the bubble cluster, mass transfer is calculated using $a$ as the total instantaneous interfacial area from all bubbles while the velocity is the cluster velocity.
Just like in its single bubble counterpart, at the beginning all the bubbles that originally have a spherical shape gradually evolve into ellipsoidal bubbles. Trailing of dissolved gas concentration starts to appear behind each bubble. In this stage both rise velocity and mass transfer coefficient is similar for the single bubble case and the bubble cluster. At about $t = 0.15\,\mathrm{s}$ the wakes from the leading bubbles start to reach the trailing bubbles. Subsequently the trailing bubbles are accelerated in the wake of the leading bubbles while the dissolved concentration from the leading bubbles starts to cover the roof region of the trailing bubbles. Because of this situation, the bubble cluster rise velocity starts to increase while the mass transfer coefficient starts to decrease due to the lower driving force.
For the single bubble case, the terminal values for velocity and mass transfer are reached after $t = 0.3\,\mathrm{s}$. However for the bubble cluster, the velocity keeps increasing while the mass transfer keeps decreasing after this period, indicating that the trailing bubbles are still accelerating while receiving higher dissolved gas concentration from the leading bubbles. At $t = 0.5\,\mathrm{s}$ the second row of the bubbles catches up with the first row; here the bubbles experience shape distortion and start to change their course. Later on, the bubbles in the second row move towards the walls next to the bubbles of the first row. Meanwhile, the bubbles from the third row start to catch up with the bubbles from the first and second rows, which eventually makes all the bubbles reside at a similar vertical position at $t = 1.1\,\mathrm{s}$.
The dynamic behavior of the bubbles is affecting the mass transfer coefficient as the mass transfer is significantly decreased when the bubbles are located in the wake of other bubbles. When the second row of bubbles is exposed to fresh liquid, the overall mass transfer starts to increase. However, when the bubbles from the third row are approaching the leading bubbles, the overall mass transfer decreases again. Eventually, the mass transfer coefficient starts to increase again when all the bubbles are arranged around the same vertical position, which makes that all bubbles are exposed to fresh liquid.
It is important to notice that even when the bubbles are nearly touching, they do not automatically merge due to the distinct Lagrangian interface representation. Instead, the pressure will start to build between the bubbles, which eventually will lead to a repulsion force pushing the bubbles away from each other. This feature is a crucial advantage of front tracking compared to the lattice Boltzmann or VOF techniques in case swarm effects

need to be investigated.
From the simulation of the cluster of bubbles, it is clear that both the rise velocity and mass transfer coefficient are different compared with the single bubble counterpart. Hence, in order to use the front tracking method properly to derive closures that can be used for more coarse grained models such as the Euler-Euler or the Euler-Lagrange model, simulations with multiple bubbles are necessary. Only by considering multiple bubbles, we can include swarm effects to our closures.

## 2.8 Conclusions

In this chapter a three-dimensional Front Tracking model, taking into account mass transfer calculated with an immersed boundary technique, has been presented. Simulations for three different physical properties have been conducted to demonstrate the capabilities of the model. The computed terminal Reynolds numbers and shapes of the bubbles rising in quiescent liquids are compared with data taken from the bubble diagram of Grace. It was demonstrated that the computed shapes and rise velocities agree very well with the data taken from this diagram. We found that different bubble shapes lead to different flow fields in the vicinity of the bubble, which influences the transport of the dissolved gas in the liquid. It is also found that the mass transfer coefficient agrees very well with the potential flow theory. Finally from a simulation with a cluster of bubbles, we have observed bubbles rising in the wake of other bubbles will experience an increase in the terminal rise velocity while in the same time the mass transfer is significantly decreased compared to the single bubble case.

## Acknowledgements

The author would like to thank Ir. W. Dijkhuizen and Dr. ir. M. Van Sint Annaland for the initial version of the front tracking code and intense discussions on the topic.

## Notation

| | |
|---|---|
| $A_m$ | area of marker $m$, $\mathrm{m}^2$ |
| $c$ | species concentration, $\mathrm{kmol\,m}^{-3}$ |
| $c_0$ | concentration inside the bubble, $\mathrm{kmol\,m}^{-3}$ |
| $d$ | diameter, $\mathrm{m}$ |
| $D$ | distribution (mapping) function, dimensionless |
| $\mathcal{D}$ | species diffusion coefficient, $\mathrm{m}^2\,\mathrm{s}^{-1}$ |
| $\mathrm{e}$ | bubble eccentricity, dimensionless |

| | |
|---|---|
| E | bubble aspect ratio, dimensionless |
| Eo | Eötvös number, dimensionless |
| $F$ | phase indicator function, dimensionless |
| $\mathbf{G}$ | vector containing information of the interface, $\mathrm{m}^{-1}$ |
| $f$ | total volumetric forcing term, $\mathrm{kmol\,m^{-3}s^{-1}}$ |
| $\mathrm{F}_s$ | volumetric forcing term, $\mathrm{kmol\,m^{-3}s^{-1}}$ |
| $\mathbf{F}_\sigma$ | volumetric surface force, $\mathrm{N\,m^{-3}}$ |
| $\mathbf{g}$ | gravitational acceleration, $\mathrm{m\,s^{-1}}$ |
| $H$ | Henry constant, dimensionless |
| Mo | Morton number, dimensionless |
| $\mathbf{n}$ | unit normal vector |
| $k_l$ | liquid side mass transfer coefficient, $\mathrm{m\,s^{-1}}$ |
| $p$ | pressure, $\mathrm{N\,m^{-2}}$ |
| Pe | Peclet number, dimensionless |
| $r$ | radial coordinate, $\mathrm{m}$ |
| $\mathbf{r}$ | position vector, $\mathrm{m}$ |
| $R$ | bubble radius, $\mathrm{m}$ |
| Re | Reynolds number, dimensionless |
| Sc | Schmidt number, dimensionless |
| Sh | Sherwood number, dimensionless |
| $t$ | time, $\mathrm{s}$ |
| $T$ | transpose of a tensor |
| $\mathbf{t}$ | tangent vector, dimensionless |
| $\mathbf{t}_k$ | length of marker edge, $\mathrm{m}$ |
| $\mathbf{u}$ | velocity vector, $\mathrm{m\,s^{-1}}$ |
| $V_{cell}$ | volume of computational cell, $\mathrm{m}^3$ |
| $\mathbf{x}$ | position vector, $\mathrm{m}$ |
| $x$ | Cartesian coordinate, $\mathrm{m}$ |
| $y$ | Cartesian coordinate, $\mathrm{m}$ |
| $z$ | Cartesian coordinate, $\mathrm{m}$ |

## Greek letters

| | |
|---|---|
| $\Delta t$ | time step, $\mathrm{s}$ |
| $\Delta V_m$ | volume associated with marker $m$, $\mathrm{m}^3$ |
| $\mu$ | viscosity, $\mathrm{kg\,m^{-1}\,s^{-1}}$ |
| $\omega_i$ | distribution function for computational cell $i$, dimensionless |
| $\rho$ | density, $\mathrm{kg\,m^{-3}}$ |
| $\sigma$ | interfacial surface tension, $\mathrm{N\,m^{-1}}$ |

## Indices

| | |
|---|---|
| $b$ | bubble |
| $e$ | equivalent |
| $g$ | gas |

$i$ the $i-th$ computational cell
$\ell$ liquid
$m$ surface element or marker
$n$ time level

## References

[1] D. Darmana, N. G. Deen, and J. A. M. Kuipers. Detailed 3D modelling of mass transfer processes in two phase flows with dynamics interfaces. *Chemical Engineering and Technology Journal*, 29(9):1027–1033, 2006.

[2] D. Darmana, N. G. Deen, and J. A. M. Kuipers. Detailed 3D modelling of mass transfer processes in two phase flows with dynamics interfaces. In *Proceedings of the 7th German-Japanese Symposium on bubble column*, Goslar, Germany, May 20-23 2006.

[3] W. Dijkhuizen, E. I. V. van den Hengel, N. G. Deen, M. van Sint Annaland, and J. A. M. Kuipers. Numerical investigation of closures for interface forces acting on single air-bubbles in water using volume of fluid and front tracking models. *Chemical Engineering Science*, 60:6169–6175, 2005.

[4] A. Koynov, J. G. Khinast, and G. Tryggvason. Mass transfer and chemical reactions in bubble swarms with dynamic interfaces. *AIChE Journal*, 51(10):2786–2800, October 2005.

[5] J. R. Grace. Shapes and velocities of bubbles rising in infinite liquids. *Trans. Instn. Chem. Eng*, 51:116–120, 1973.

[6] M. van Sint Annaland, W. Dijkhuizen, N. G. Deen, and J. A. M. Kuipers. Numerical simulation of gas bubbles behaviour using a 3D front tracking method. *AIChE Journal*, 52:99–110, 2006.

[7] M. Sussman, P. Smereka, and S. Osher. A level set approach for computing solutions to incompressible two-phase flow. *Journal of Computational Physics*, 114:146–159, 1994.

[8] M. Sussman, A. S. Almgren, J. B. Bell, P. Colella, L. H. Howell, and M. L. Welcome. An adaptive level set approach for incompressible two-phase flows. *Journal of Computational Physics*, 148:81–124, 1999.

[9] J. A. Sethian. *Level Set Methods*. Cambridge Univ. Press, Cambridge, UK, 1996.

[10] Y. C. Chang, T. Y. Hou, B. Merriman, and S. Osher. A level set formulation of eulerian interface capturing methods for incompressible fluid flows. *Journal of Computational Physics*, 124:449–464, 1996.

[11] M. Sussman and P. Smereka. Axi-symmetric free boundary problems. *Journal of Fluid Mechanics*, 341:269–294, 1997.

[12] M. Sussman and E. Fatemi. An efficient interface-preserving level set redistancing algorithm and its application to interfacial incompressible fluid flow. *SIAM Journal on Scientific Computing*, 20:1165–1191, 1999.

[13] R. P. Fedkiw and S. Osher. Level-set methods: An overview and some recent results. *Journal of Computational Physics*, 169:463, 2001.

[14] M. Ida. An improved unified solver for compressible and incompressible fluids involving free surfaces: Part I. convection. *Computational Physics Communnications*, 132:44–65, 2000.

[15] W. J. Rider and D. B. Kothe. Stretching and tearing interface tracking methods. Technical report, Los Alamos National Laboratory., 1995. http://laws.lanl.gov/XHM/personnel/wjr/Web-papers/pubs.html.

[16] J. E. Welch, F. H. Harlow, J. P. Shannon, and B. J. Daly. The mac method: A computing technique for solving viscous incompressible transient fluid flow problems involving free surfaces. Technical report, Los Alamos Scientific Laboratory, Emeryville, CA, 1965. Report LA-3425.

[17] S. Scardovelli and S. Zaleski. Direct numerical simulation of free-surface and interfacial flow. *Annual Review of Fluid Mechanics*, 31:567–603, 1999.

[18] C. W. Hirt and B. D. Nichols. Volume of fluid (VOF) method for the dynamics of free boundaries. *Journal of Computational Physics*, 39:201, 1981.

[19] D. L. Youngs. *Numerical Methods for Fluid Dynamics.*, chapter Time-dependent multi-material flow with large fluid distortion, pages 273–285. Academic Press, New York, NY, 1982.

[20] M. Rudman. A volume-tracking method for incompressible multifluid flows with large density variations. *International Journal For Numerical Methods In Fluids*, 28:357–378, 1998.

[21] W. J. Rider and D. B. Kothe. Reconstructing volume tracking. *Journal of Computational Physics*, 141:112–152, 1998.

[22] S. Popinet and S. Zaleski. A front-tracking algorithm for accurate representation of surface tension. *International Journal on Numerical Methods in Fluids*, 30:775–793, 1999.

[23] M. Bussman, J. Mostaghimi, and S. Chandra. On a three-dimensional volume tracking model of droplet impact. *Physics of Fluids*, 11:1406–1417, 1999.

[24] W. F. Noh and P. R. Woodward. *Lecture Notes in Physics. Vol. 59.*, chapter SLIC (Simple Line Interface Calculation) method, page 330. Springer-Verlag, Berlin, 1976.

[25] M. Van Sint Annaland, N. G. Deen, and J. A. M. Kuipers. Numerical

simulation of gas bubbles behaviour using a three-dimensional volume of fluid method. *Chemical Engineering Science*, 60:2999–3011, 2005.

[26] K. Sankaranarayanan, X. Shah, I. G. Kevrekidis, and S. Sundaresan. Analysis of drag and added mass forces in bubbly suspensions using an implicit formulation of the lattice Boltzmann method. *Journal of Fluid Mechanics*, 452:61–96, 2002.

[27] K. Sankaranarayanan and S. Sundaresan. Lift force in bubble suspensions. *Chemical Engineering Science*, 57:3521–3542, 2002.

[28] S. O. Unverdi and G. A. Tryggvason. A front-tracking method for viscous, incompressible multi-fluid flows. *Journal of Computational Physics*, 100:25–37, 1992.

[29] A. Esmaeeli and G. Tryggvason. Direct numerical simulation of bubble flows. part I. low reynolds number arrays. *Journal of Fluid Mechanics*, 377:313–345, 1998.

[30] A. Esmaeeli and G. Tryggvason. Direct numerical simulation of bubble flows. part II. moderate reynolds number arrays. *Journal of Fluid Mechanics*, 385:325–358, 1998.

[31] G. Tryggvasson and B. Bunner A. Esmaeeli. A front tracking method for the computations of multiphase flow. *Journal of Computational Physics*, 169:708–759, 2001.

[32] M. G. Wohak and H. Beer. Numerical simulation of direct-contact evaporation of a drop rising in a hot, less volatile immiscible liquid of higher density–possibilities and limits of the SOLA-VOF/CSF algorithm. *Numerical Heat Transfer A*, 33:561–582, 1998.

[33] M. R. Davidson and M. Rudman. Volume-of-fluid calculations of heat or mass transfer across deforming interfaces in two-fluid flow. *Numerical Heat Transfer, Part B*, 41:291–308, 2002.

[34] D. Bothe, M. Koebe, K. Wielage, and H. J. Warnecke. Vof-simulations of mass transfer from single bubbles and bubble chains rising in auqueous solutions. In *Proceedings of FEDSM'03*, Honolulu, Hawaii, USA, July 6-11 2003. 4th ASME-JSME Joint Fluids Engineering Conference.

[35] A. Prosperetti. *Drop-surface interaction*, chapter A Navier-Stokes numerical algorithms for free-surface flow computations: An overview, pages 237–257. Wien: Springer, 2002.

[36] S. Balay, K. Buschelman, W. D. Gropp, D. Kaushik, M. G. Knepley, L. C. McInnes, B. F. Smith, and H. Zhang. PETSc Web page, 2001. http://www.mcs.anl.gov/petsc.

[37] S. Balay, K. Buschelman, V. Eijkhout, W. D. Gropp, D. Kaushik, M. G. Knepley, L. C. McInnes, B. F. Smith, and H. Zhang. PETSc users manual. Technical Report ANL-95/11 - Revision 2.1.5, Argonne National

Laboratory, 2004.

[38] S. Balay, V. Eijkhout, W. D. Gropp, L. C. McInnes, and B. F. Smith. Efficient management of parallelism in object oriented numerical software libraries. In E. Arge, A. M. Bruaset, and H. P. Langtangen, editors, *Modern Software Tools in Scientific Computing*, pages 163–202. Birkhäuser Press, 1997.

[39] M. Van Sint Annaland, N. G. Deen, and J. A. M. Kuipers. *Series: Heat and Mass Transfer*, chapter Multi-Level Modelling of Dispersed Gas-Liquid Two-Phase Flows, pages 139–157. Springer-Verlag, 2003.

[40] M. Uhlmann. An immersed boundary method with direct forcing for the simulation of particulate flows. *Journal of Computational Physics*, 209:448–476, 2005.

[41] J. Centrella and J. R. Wilson. Planar numerical cosmology. II. the difference equations and numerical tests. *Astronomy & Astrophysics Journal Supplement Series*, 54:229–249, 1984.

[42] B. H. Hjertager. Computational fluid dynamics (CFD) analysis of multiphase chemical reactors. *Trends in Chemical Engineering*, 4:44–92, 1998.

[43] D. Darmana, N. G. Deen, and J. A. M. Kuipers. Detailed modeling of hydrodynamics, mass transfer and chemical reactions in a bubble column using a discrete bubble model. *Chemical Engineering Science*, 60:3383–3404, 2005.

[44] G. Burns, R. Daoud, and J. Vaigl. LAM: An Open Cluster Environment for MPI. In *Proceedings of Supercomputing Symposium*, pages 379–386, 1994.

[45] J. M. Squyres and A. Lumsdaine. A Component Architecture for LAM/MPI. In *Proceedings, 10th European PVM/MPI Users' Group Meeting*, number 2840 in Lecture Notes in Computer Science, pages 379–387, Venice, Italy, September / October 2003. Springer-Verlag.

[46] R. Clift, J. R. Grace, and M. E. Weber. *Bubbles, Drops, and Particles*. Academic Press, Inc., 1978.

[47] A. C. Lochiel and P. H. Calderbank. Mass transfer in the continuous phase around axisymmetric bodies of revolution. *Chemical Engineering Science*, 19:471–484, 1964.

# 3

# Discrete Bubble Model: From hydrodynamics to mass transfer and chemical reaction[§]

*"To manage a system effectively, you might focus on the interactions of the parts rather than their behavior taken separately."* - Russell L. Ackoff

## Abstract

*A 3D discrete bubble model is adopted to investigate complex behavior involving hydrodynamics, mass transfer and chemical reactions in a gas-liquid bubble column reactor. In this model a continuum description is adopted for the liquid phase and additionally each individual bubble is tracked in a Lagrangian framework, while accounting for bubble-bubble and bubble-wall interactions via an encounter model. The mass transfer rate is calculated for each individual bubble using a surface renewal model accounting for the instantaneous and local properties of the liquid phase in its vicinity. The distributions in space of chemical species residing in the liquid phase are computed from the coupled species balances considering the mass transfer from bubbles and reactions between the species. The model has been applied to simulate chemisorption of $CO_2$ bubbles in $NaOH$ solutions. Our results show that apart from hydrodynamics behavior, the model is able to predict the bubble size distribution as well as temporal and spatial variations of each chemical species involved.*

[§]This chapter is based on: Darmana et al. [1, 2]

## 3.1 Introduction

Bubble columns are used in a variety of industrial processes including large-scale production of base chemicals and synthetic fuels. Many processes involve gas-liquid mass transfer with accompanying reactions between the gas and the liquid phase itself or with components dissolved or suspended in it. Despite the widespread application of bubble columns and substantial research efforts devoted to understand their behavior, detailed knowledge on the fluid flow, mass transfer and chemical reactions as well as their interactions are still lacking.

The coupling between these phenomena is illustrated in Fig. 3.1. The chemical reaction rate depends on the local availability of the species which is determined by the interphase mass transfer process and the mixing induced by the bubbles. The interphase mass transfer depends on the mass transfer coefficient, the specific interfacial area and chemical reaction rate. The mass transfer parameters are a function of the local prevailing hydrodynamics [3], which in its turn are affected by the bubble behavior and variation of physical properties due to in-homogeneous chemical species distributions. It is these complex interactions that make the overall prediction of performance and scale-up of this type of reactor very difficult.

In recent years, computational fluid dynamics (CFD) has emerged as a powerful tool for both scientists and engineers. CFD modelling of dispersed gas-liquid two-phase flows has shown remarkable progress over the last decade. Two models are widely used for describing hydrodynamics of bubble columns, i.e. the (E-E) model and (E-L) model. The E-E model employs the volume-averaged mass and momentum conservation equations to describe the time dependent motion of both phases [4–6]. The number of bubbles present in a computational cell is represented by a volume fraction and the information of the bubble size distribution is often obtained by incorporating

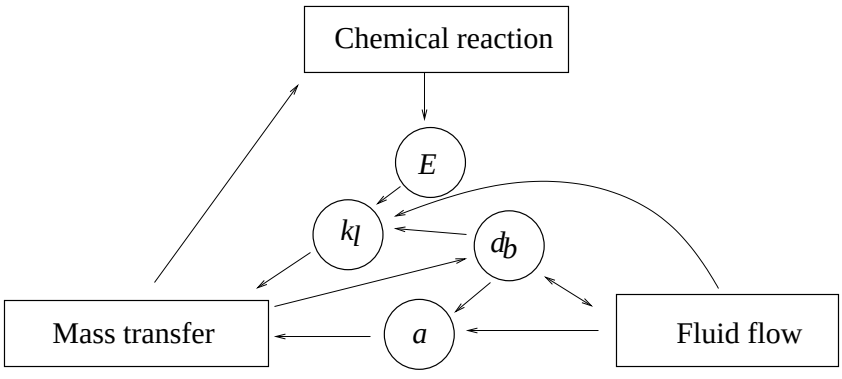


**Figure 3.1:** *Inter-dependency diagram of fluid flow, mass transfer and chemical reaction.*

population balance equations which take into account break-up and coalescence of bubbles as well as growth or shrinkage of bubbles as a consequence of mass transfer. The E-L model on the other hand adopts a continuum description for the liquid phase and additionally tracks each individual bubble using Newtonian equations of motion. This allows for a direct consideration of additional effects related to bubble-bubble and bubble-liquid interaction. Mass transfer with and without chemical reaction, bubble coalescence and re-dispersion can be incorporated directly [6–8]. Unlike the E-E model, the E-L model does not require additional models to predict the bubble size distribution since this information is already part of the solution. A drawback of the E-L model compared to the E-E model is its limitation on the number of bubbles that can be handled (i.e. less than $\mathcal{O}\left(10^5\right)$) since for each individual bubble one equation of motion needs to be solved. This makes this method less attractive in handling large scale bubble columns.

Based on the E-E model, Fleischer et al. [9] have pioneered to combine hydrodynamics, mass transfer and chemical reactions into a one-dimensional plug flow model accounting for axial dispersion and heat effects. The model consists of a liquid mass balance for each chemical species involved and momentum and energy balances for the liquid phase. The mass transfer rate is calculated from the two film theory based on the bubble size predicted by a population balance model. This model has been used to predict transient behavior of chemisorption of carbon dioxide into an aqueous solution of sodium hydroxide in a gas-lift reactor. A similar method was used by Márquez et al. [10, 11] to study the coupling between hydrodynamics and chemical reaction without mass transfer in an external-loop gas liquid reactor. This model also has been adopted in several CFD software packages, which are used to solve a wide variety of practical two phase problems [12–14].

The model of Fleischer is able to qualitatively predict the transient behavior of a chemisorption process in a slender cylindrical bubble column. However, for more general geometries, experimental investigations by Becker et al. [15] and Chen et al. [16] indicate that bubble columns generally show an unsteady flow with considerable spatial variation of the key hydrodynamic quantities. Numerical simulations reported by Delnoij et al. [17], Sokolichin and Eigenberger [6] and Deen et al. [4] also show that unsteady vortical structures appear in 2D and 3D simulations. These results suggest that a 1D plug flow model as was used in Fleischers model is not able to capture the unsteady hydrodynamics behavior of a bubble column.

In this chapter we present a detailed 3D model for the hydrodynamics, mass transfer and chemical reactions in an isothermal bubble column operated in the homogeneous regime. The Euler-Lagrange model is adopted to solve the hydrodynamics since incorporation of the bubble size distribution and interphase mass transfer calculation is relatively straightforward. The model is applied to study the coupling of hydrodynamics, gas-liquid mass transfer and chemical reactions in a square bubble column. First we will focus on the

hydrodynamics of the column and compare our results with experimental and numerical results obtained by Deen et al. [4]. The mixing characteristics of the column will subsequently be studied with the use of hydrodynamics and species tracking models. Next the physical absorption of $CO_2$ into water will be addressed and finally the complete model will be used to investigate chemisorption of $CO_2$ bubbles into an aqueous solution of sodium hydroxide.

## 3.2 Model formulation

The three-dimensional model described in this chapter is an extension of the hydrodynamic Euler-Lagrange model of Delnoij et al. [17], which is applicable to disperse (homogeneous) regimes, which are characterized by low gas velocities and relatively small spherical bubbles that do not coalesce nor break-up. The interphase mass transfer is calculated for each bubble using the surface renewal theory which takes into account both physical and chemically enhanced mass transfer. The spatial distributions of chemical species residing in the liquid phase are computed from the coupled species conservation equations formulated in the Eulerian framework. Moreover, the numerical implementation of direct bubble-bubble interaction and the two-way coupling between phases will be addressed in section 3.3.

### 3.2.1 Bubble dynamics

The motion of each individual bubble is computed from the bubble mass and momentum equations. The liquid phase contributions are taken into account by the interphase mass transfer rate $\dot{m}$ and the net force $\sum F$ experienced by each individual bubble. For an incompressible bubble, the equations can be written as:

$$\rho_b \frac{d\left(V_b\right)}{dt} = \left(\dot{m}_{l\to b} - \dot{m}_{b\to l}\right) \tag{3.1}$$

$$\rho_b V_b \frac{d\mathbf{v}}{dt} = \sum \mathbf{F} - \left(\rho_b \frac{dV_b}{dt}\right)\mathbf{v} \tag{3.2}$$

Here the gas density $\rho_b$ is assumed to be constant considering the limited height of the simulated column. The interphase mass transfer term $\dot{m}$ is calculated using a method, which will be describe in section 3.2.4. The net force acting on each individual bubble is calculated by considering all the relevant forces. It is composed of separate, uncoupled contributions such as: gravity, pressure, drag, lift and virtual mass:

$$\sum \mathbf{F} = \mathbf{F}_G + \mathbf{F}_P + \mathbf{F}_D + \mathbf{F}_L + \mathbf{F}_{VM} \tag{3.3}$$

Table 3.1: *Overview of forces acting on a bubble.*

| Force | Closure |
|---|---|
| $\mathbf{F}_G = \rho_b V_b \mathbf{g}$ | $-$ |
| $\mathbf{F}_P = -V_b \nabla P$ | $-$ |
| $\mathbf{F}_D = -\frac{1}{2} C_D \rho_l \pi R_b^2 \lvert\mathbf{v}-\mathbf{u}\rvert (\mathbf{v}-\mathbf{u})$ | $C_D = \frac{2}{3}\sqrt{E\ddot{o}}$ |
| $\mathbf{F}_L = -C_L \rho_l V_b (\mathbf{v}-\mathbf{u}) \times \nabla \times \mathbf{u}$ | $C_L = 0.5$ |
| $\mathbf{F}_{VM} = -C_{VM} \rho_l V_b \left(\frac{D_b \mathbf{v}}{D_b t} - \frac{D_l \mathbf{u}}{D_l t}\right)$ | $C_{VM} = 0.5$ |

Expressions for each of these forces can be found in Table 3.1 (see [8] for a discussion on the forces experienced by a bubble). Note that the closure models used in this chapter is for model demonstration only, more sophisticated closure models may be used to obtain better results.

### 3.2.2 Liquid phase hydrodynamics

The liquid phase hydrodynamics is represented by the volume-averaged Navier-Stokes equation, which consists of continuity and momentum equations. The presence of bubbles is reflected by the liquid phase volume fraction $\varepsilon_l$, the source term that accounts for the interphase mass transfer $\dot{M}$, and the total interphase momentum transfer due to forces and mass transfer $\Phi$:

$$\frac{\partial}{\partial t}(\varepsilon_l \rho_l) + \nabla \cdot \varepsilon_l \rho_l \mathbf{u} = \left(\dot{M}_{b\to l} - \dot{M}_{l\to b}\right) \tag{3.4}$$

$$\frac{\partial}{\partial t}(\varepsilon_l \rho_l \mathbf{u}) + \nabla \cdot \varepsilon_l \rho_l \mathbf{u}\mathbf{u} = -\varepsilon_l \nabla P - \nabla \cdot \varepsilon_l \tau_l + \varepsilon_l \rho_l \mathbf{g} + \Phi \tag{3.5}$$

The liquid phase flow is assumed to be Newtonian, thus the stress tensor $\tau_l$ can be represented as:

$$\tau_l = -\mu_{\text{eff},l}\left[\left((\nabla \mathbf{u}) + (\nabla \mathbf{u})^T\right) - \frac{2}{3}\mathbf{I}(\nabla \cdot \mathbf{u})\right] \tag{3.6}$$

where $\mu_{\text{eff},l}$ is the effective viscosity. In the present model the effective viscosity is composed of two contributions, the molecular viscosity and the turbulent viscosity:

$$\mu_{\text{eff},l} = \mu_{L,l} + \mu_{T,l} \tag{3.7}$$

Deen et al. [4] did extensive work on the implementation and verification of a model that could account for the sub-grid scale turbulence. They concluded that the Large Eddy Simulation (LES) turbulence model implemented in the Euler-Euler framework outperformes the $k-\epsilon$ model in predicting the experimentally observed dynamic behavior of the flow in a square bubble column.

Recently van den Hengel et al. [18] and Láin and Sommerfeld [19] have successfully employed LES in combination with the Euler-Lagrange model and obtained good agreement with experimental data in a square and cylindrical bubble column. Following them, the turbulent viscosity $\mu_{T,l}$ represents the contribution of the subgrid scales. In the present study $\mu_{T,l}$ is described by the Smagorinsky [20] model, which is expressed as:

$$\mu_{T,l} = \rho_l \left(C_S \triangle\right)^2 |\mathbf{S}| \tag{3.8}$$

where $C_S$ is a model constant with a typical value of $0.1$, $\mathbf{S}$ the characteristic filtered strain rate and $\triangle = (V_{cell})^{1/3}$ the SGS length scale.

### 3.2.3 Chemical species

The fraction of a chemical species $j$ in the liquid mixture is represented by mass fraction $Y_l^j$. The presence of various chemical species are modeled through a transport equation for each species given by:

$$\frac{\partial}{\partial t}\left(\varepsilon_l \rho_l Y_l^j\right) + \nabla \cdot \left(\varepsilon_l \left(\rho_l \mathbf{u}_l Y_l^j - \Gamma_{\text{eff}}^j \nabla Y_l^j\right)\right) = \left(\dot{M}_{b\to l}^j - \dot{M}_{l\to b}^j\right) + \varepsilon_l S^j \tag{3.9}$$

where $S^j$ is the source term accounting for production or consumption of species $j$ due to homogeneous chemical reaction and

$$\Gamma_{\text{eff}}^j = \frac{\mu_{\text{eff,l}}}{\text{Sc}^j} \tag{3.10}$$

For a mixture, which consists of $N_S$ chemical species, we only have to solve $N_S - 1$ transport equations represented by eq. (3.9). The remaining species mass fraction can be calculated from the overall species balance using the following relation:

$$\sum_{j=1}^{N_S} Y_j = 1 \tag{3.11}$$

For a mixture consisting of $N_S$ species, the liquid density and viscosity are taken as the average of properties of each species as follow:

$$\frac{1}{\rho_l} = \sum_{j=1}^{N_S} \frac{Y_l^j}{\rho_l^j} \tag{3.12}$$

$$\mu_{L,l} = \sum_{j=1}^{N_S} Y_l^j \mu_l^j \tag{3.13}$$

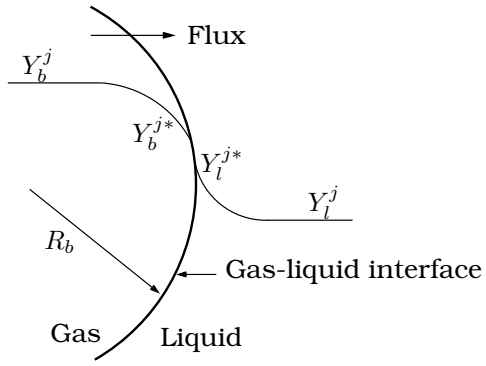


**Figure 3.2:** *Schematic representation of gas-liquid mass transfer.*

### 3.2.4 Mass transfer

The interphase mass transfer in a bubble with radius $R_b$ is considered to be driven by mass fraction gradients. The mass fraction of a chemical species $j$ in the liquid phase and bubble are represented by $Y_l^j$ and $Y_b^j$ respectively, while the value of both quantities at each side of the bubble-liquid interface is given by $Y_l^{j*}$ and $Y_b^{j*}$ (see Fig. 3.2).
The mass transfer in a bubble due to a mass fraction gradient of species $j$ is represented as:

$$\dot{m}_b^j = E k_l^j A_b \rho_l \left( Y_l^{j*} - Y_l^j \right) \tag{3.14}$$

where $E$ is the due to chemical reactions, $A_b$ is the surface area of the bubble and $k_l^j$ is the mass transfer coefficient for species $j$, which is determined using a Sherwood relation for a moving bubble [21]:

$$\mathrm{Sh} = 2 + 0.6415 \left( \mathrm{ReSc}^j \right)^{1/2} \tag{3.15}$$

When the mass transfer resistance lies in the liquid phase, the mass fraction on the liquid side of the interface can be determined using a Henry constant:

$$Y_l^{j*} = H^j Y_b^j \frac{\rho_b}{\rho_l} \tag{3.16}$$

where $H^j$ is the Henry constant for the species $j$.
The total mass transfer rate is the sum of the mass transfer rates of all species $j$, thus:

$$\dot{m}_b = \sum_{j=1}^{N_S} \dot{m}_b^j \tag{3.17}$$

The mass transfer from the liquid to a bubble can be written as $\dot{m}_{l\to b} = \max(\dot{m}_b, 0)$, while the mass transfer from a bubble into the liquid is $\dot{m}_{b\to l} = \max(-\dot{m}_b, 0)$.

## 3.3 Numerical implementation

In this section the numerical implementation of the model described in section 3.2 will be described briefly.

### 3.3.1 Time marching

To resolve the time-dependent motion of the bubbles and the liquid phase, as well as the chemical species, four different time scales are considered. The biggest time step ($\delta t_{flow}$) is employed in solving the Navier-Stokes equations to obtain the macroscopic liquid flow field. The interphase mass and momentum transfer are resolved on the scale of the bubble time step ($\delta t_{bub}$). To account for the possible encounters (collisions) between bubbles and the displacement of the bubbles an even smaller time step ($\delta t_{ab}$) is used. The chemical species transport equation is solved using a time step $\delta t_{spec}$ similar to the $\delta t_{flow}$. However, for chemical species, which undergo fast chemical reactions a smaller time step is required, in order to prevent numerical instability.

### 3.3.2 Bubble tracking and direct bubble-bubble interaction

The mass and momentum conservation equation of the bubbles are ordinary differential equations. These equations are integrated numerically using a first order explicit scheme. For a general time integrable variable $\xi$ the formula can be written as:

$$\xi^{t+1} = \xi^t + \left(\frac{d\xi}{dt}\right)^t \delta t_{bub} \tag{3.18}$$

The mass and momentum balance equations for each bubble are solved sequentially. First the mass transfer rate is calculated explicitly using the method describe in section 3.2.4 to obtain the bubble volume rate of change. Using the numerical scheme described in eq. 3.18, the bubble volume rate of change is integrated to obtain a new bubble size.
Subsequently the bubble momentum equation is solved by first calculating the interphase momentum and mass transfer term explicitly. The acceleration of each individual bubble is obtained in a straight forward manner using eq. 3.2. The new bubble velocity is obtained by integrating the acceleration using eq. 3.18.
The collision between bubbles is modeled using a so called hard sphere model following the work of Hoomans et al. [22]. In this method a constant time step $\delta t_{bub}$ is used to account for the forces acting on a bubble. Within this time step, the velocity of bubbles is assumed to change only due to binary collisions between the bubbles. A sequence of collisions is then processed, one collision at a time.

To predict the collision between bubbles, we extend the model that is widely used in the field of molecular dynamics [23] by taking into account the rate of change of the bubble size. Consider two bubbles, $a$ and $b$, of radius $R_a$ and $R_b$ respectively. At time $t$ the bubbles are located at $\mathbf{r}_a$ and $\mathbf{r}_b$ with velocity $\mathbf{v}_a$ and $\mathbf{v}_b$ and bubble growth rates (in terms of bubble radius growth rate) $\dot{R}_a$ and $\dot{R}_b$. If those bubbles are to collide at time $t + \delta t_{ab}$ then the following equation must be satisfied:

$$|\mathbf{r}_{ab}\,(t + \delta t_{ab})| = |\mathbf{r}_{ab} + \mathbf{v}_{ab}\delta t_{ab}| = (R_a + R_b) + (\dot{R}_a + \dot{R}_b)\delta t_{ab} \tag{3.19}$$

where $\mathbf{r}_{ab} = \mathbf{r}_a - \mathbf{r}_b$ and $\mathbf{v}_{ab} = \mathbf{v}_a - \mathbf{v}_b$ and $\delta t_{ab}$ is the time until the collision. The second and third term in eq. (3.19) can be written in the quadratic equation in $\delta t_{ab}$ as follow:

$$A\delta t_{ab}^2 + 2B\delta t_{ab} + C = 0 \tag{3.20}$$

with

$$\begin{aligned} A &= \mathbf{v}_{ab}^2 - (\dot{R}_a + \dot{R}_b)^2 \\ B &= \mathbf{r}_{ab} \cdot \mathbf{v}_{ab} - (R_a + R_b)(\dot{R}_a + \dot{R}_b) \\ C &= \mathbf{r}_{ab}^2 - (R_a + R_b)^2 \end{aligned}$$

If $B > 0$ then the two bubbles are moving away from each other and they will not collide. Otherwise (if $B < 0$) there is a chance in a certain period that the bubbles will be collide. Provided that eq. (3.20) has a positive discriminant, two positive roots will arise and the smaller will correspond to the impact:

$$\delta t_{ab=}\frac{-B - \sqrt{B^2 - AC}}{A} \tag{3.21}$$

In order to calculate the collision time efficiently we use a so called bubble neighbor region. Only bubbles located inside this region are considered to be possible collision partners. Hoomans et al. [22] and Delnoij et al. [17] use a rectangular shape to represent the neighbor region, however in this work we choose a spherical shaped neighbor region since this shape is more natural with respect to the bubble shape. For all the bubbles inside the neighbor area of a certain bubble $a$ (see Fig. 3.3), we calculate the collision time $\delta t_{ab}$ between bubble $a$ and the possible collision partner $b$ using eq. (3.20) . Note that the collision partner may also be one of the column walls or the top surface.

For all the possible collision pairs, the smallest $\delta t_{ab}$ is selected. This $\delta t_{ab}$ will be used to update both size and position of all bubbles. However for bubbles $a$ and $b$, which correspond to the smallest $\delta t_{ab}$, a collision procedure is carried out and new velocities are determined.

A pair of colliding bubbles will bounce during the collision event. The velocities of both bubbles after the bounce are determined by splitting the initial

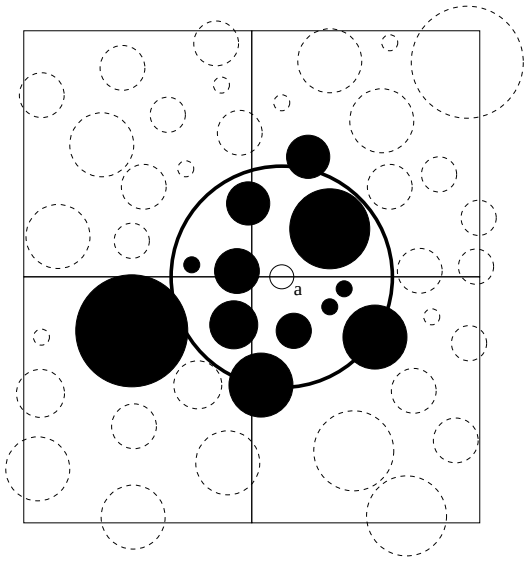


**Figure 3.3:** *When the skin-to-skin distance between bubble $a$ and neighbouring bubble $b$ is less than the boundary parameters, than bubble $b$ belongs to the neighbour list of bubble $a$.*

velocities into a normal and tangential component with respect to the line connecting the centers of mass of both bubbles. The tangential component does not change due to a collision, while the new normal component is calculated from:

$$v_{n,a}^{aftercollision} = 2\frac{m_a v_{n,a} + m_b v_{n,b}}{m_a + m_b} - v_{n,a} \tag{3.22}$$

where the new velocity of bubble $b$ is calculated in a similar way.

### 3.3.3 Liquid flow field

A finite difference technique was adopted to discretize the governing equations of the liquid phase. The volume-averaged Navier-Stokes equations have been solved with a semi-implicit method for pressure linked equations (SIMPLE-algorithm). A staggered grid is employed to prevent numerical instability. First order explicit time differencing is applied for the time derivative. The convective terms of the mass and momentum conservation equations are treated implicitly using a second order accurate Barton scheme [24]. Moreover the pressure gradient is treated implicitly, while the interphase mass and momentum transfer and all other terms are treated explicitly. The resulting set of linear equations yields a discretized pressure-Poisson equation, which is solved iteratively using the incomplete Choleski

conjugate gradient (ICCG) method, which is incorporated in the PETSc library [25].

### 3.3.4 Chemical reactions and species transport equations

All the terms in the species transport equation are discretized using a fully implicit method, except for the interphase mass transfer and chemical reaction rate, which appear as source terms and are treated explicitly. The convective flux is treated using a first order accurate upwind scheme which is corrected using deferred correction method [26] in order to be consistent with the second order Barton scheme method, which is used in solving the Navier-Stokes equation. The resulting discretized equations for all species are solved simultaneously using an algorithm similar to that used by Hjertager [27] in solving the mass conservation equations in a multi-fluid model. Using this technique, the algebraic constraint for the species equation (eq. 3.11) is automatically imposed, yielding mass fractions for each species which are bounded between 0 and 1.

### 3.3.5 Interphase coupling

The coupling between the liquid phase and the bubbles is accomplished through the liquid phase volume fraction $\varepsilon_l$, the interphase momentum transfer rate $\Phi$, as well as the mass transfer rate from and to the bubbles. Since the liquid phase and the bubbles are defined in different reference frames (i.e. Lagrangian and Eulerian), a mapping technique which correlates the two reference frames is required. This mapping technique translates the Lagrangian bubble quantities to the Eulerian grid, which are required as closure for the liquid phase equations and vice versa.
Most of the mapping techniques in literature are developed for bubbles, which are much smaller than the grid size [7, 17]. However, in order to allow for changes in bubble size due to coalescence and mass transfer processes, it is desirable that bubbles can become larger than the computational grid size.
In this section we propose a new mapping technique, which allows us to simulate bubbles, which can be smaller as well as bigger than the Eulerian grid size.

#### Porosity mapping

The bubble volume fraction $\varepsilon_b$ in a computational cell is calculated from the volume occupied by the bubbles present in the cell under consideration:

$$\varepsilon_b = \frac{1}{V_{cell}} \sum_{\forall i \in cell} \zeta^i_{cell} V^i_b \tag{3.23}$$

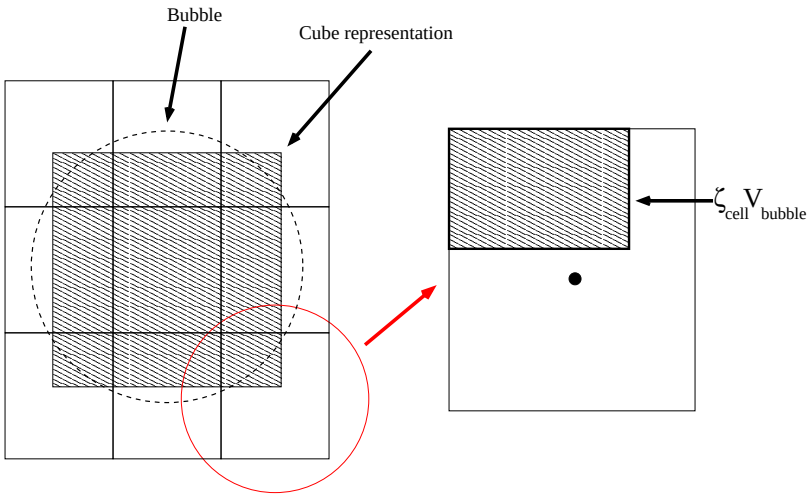


**Figure 3.4:** *Schematic representation of the porosity mapping technique.*

with $\zeta^i_{cell}$ is the volume fraction of the $i-$th bubble included in the cell under consideration.
The liquid volume fraction $\varepsilon_l$ is calculated using the algebraic expression:

$$\varepsilon_l = 1 - \varepsilon_b \tag{3.24}$$

Equation (3.23) requires a value $\zeta^i_{cell}$ which unfortunately depends on the shape of the bubbles. The prediction of the bubble shape is a tedious task, since it depends on various parameters such as fluid properties, bubble size and the time-dependent flow field around the bubble. Even for a simple shape such as a sphere or ellipsoid, the calculation of $\zeta^i_{cell}$ requires significant computational effort, especially if the size of bubble is larger than the size of the computational grid. For this reason, we use a cubic shape to represent the bubble following the work of Tomiyama et al. [7] with the arguments: (1) the calculation of $\zeta^i_{cell}$ is easy and takes little CPU time; and (2) since the actual bubbles take time-dependent complex shapes, there may be little difference between the cubic approximation and other, more sophisticated approximations such as spherical and ellipsoidal shapes.
Figure 3.4 shows how we can map portion of a bubble into the involved computational cells. Special attention should be given to cells, which are entirely occupied by a bubble and do not allow for the solution of the liquid phase conservation equations. To overcome this problem the liquid phase porosity has been forced to have the lowest value $\varepsilon_l = \varepsilon_{low}$. The value of $\varepsilon_{low}$ that we choose will influence the accuracy as well as the computational cost to solve the problem. We found that by taking $\varepsilon_{low} = 0.05$ both aspects are treated in a satisfactory manner.

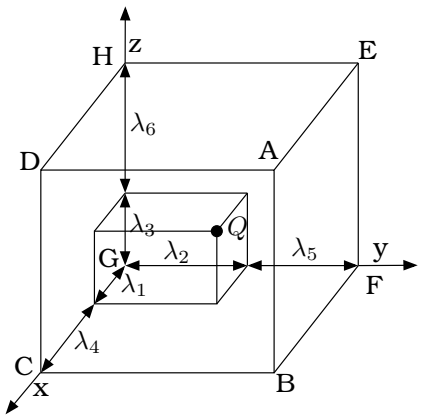


**Figure 3.5:** *Notation used for mapping Eulerian data at points $A - H$ to Lagrangian point $Q$ (after Tomiyama et al. [7]).*

### Lagrange to Euler mapping

In order to close eqs. (3.4) - (3.9) a relation between a Lagrangian quantity of bubbles $\omega$ and the respective Eulerian value $\Omega$ is required. Since $\Omega$ is given as a volume-averaged value of $\omega$ in a unit volume, let us consider a computational cell in 3D Cartesian coordinates which has volume $V_{cell}$. For all bubbles $i$ in this cell, the relation between $\omega$ and $\Omega$ can be written as:

$$\Omega = \frac{1}{V_{cell}} \sum_{\forall i \in cell} \zeta_{cell}^{i} V_b^i \omega \tag{3.25}$$

where $\zeta_{cell}^{i}$ is calculated with the cubic shape representation, which was introduced earlier.

### Euler to Lagrange mapping

To evaluate forces experienced by each bubble, we need information of liquid quantities which are defined on the Eulerian grid. For this purpose we adopt the volume weighing method, which was used by Delnoij et al. [17] and Tomiyama et al. [7]. As shown in Figure 3.5, the value of any physical quantities $\Omega$ at point $Q$ (denotes as $\omega$) can be calculated as:

$$\begin{aligned} \omega \quad = \quad & \lambda_1\lambda_2\lambda_3\Omega_A + \lambda_1\lambda_2\lambda_6\Omega_B + \lambda_1\lambda_5\lambda_6\Omega_C + \lambda_1\lambda_5\lambda_3\Omega_D \\ & + \lambda_4\lambda_2\lambda_3\Omega_E + \lambda_4\lambda_2\lambda_6\Omega_F + \lambda_4\lambda_5\lambda_6\Omega_G + \lambda_4\lambda_5\lambda_3\Omega_H \end{aligned} \tag{3.26}$$

where $0 \leq \lambda_k \leq 1$ and $\lambda_1 + \lambda_4 = \lambda_2 + \lambda_5 = \lambda_3 + \lambda_6 = 1$

### 3.3.6 Computational sequence

The complex phenomena involving hydrodynamics, mass transfer and chemical reactions are solved in a sequential manner. A diagram of the computational sequence is presented in Fig. 3.6. For every flow time step $\delta t_{flow}$, first, the interphase mass and momentum transfer are calculated explicitly for each individual bubble. The liquid quantities required to calculate these terms are obtained from the Euler to Lagrange mapping technique (section 3.3.5). Using the interphase mass and momentum transfer, the bubbles size and position are updated taking into account direct bubble-bubble and bubble-wall interaction (section 3.3.2).
The available bubble size and positions are mapped to the Eulerian mesh using the porosity mapping method (section 3.3.5) to obtain the liquid phase porosity in every Eulerian computational cell. The interphase mass and momentum transfer rate, which was previously calculated from every individual bubble is also mapped to the Eulerian cell using the Lagrangian to Eulerian mapping technique (section 3.3.5). Using the new liquid porosity as well as the interphase mass and momentum transfer rate, the liquid hydrodynamics are solved to obtain the liquid phase hydrodynamics at the new time level (section 3.3.3). Finally, the chemical reactions and species transport equation are solved to obtain a chemical species distribution at the new time level (section 3.3.4). This sequential procedure is repeated until a specified simulation end time is reached.

## 3.4 Geometry and boundary condition

Deen et al. [4] performed particle image velocimetry (PIV) measurements in a 3D bubble column filled with distilled water. The column has a square cross-section $(W \times D)$ of $0.15 \times 0.15\,\mathrm{m}^2$ and a height $(L)$ of $0.45\,\mathrm{m}$. Air with a superficial gas velocity of $4.9\,\mathrm{mm/s}$ was introduced into the system through a perforated plate. The plate contained 49 holes with a diameter of $1\,\mathrm{mm}$, which were positioned in the middle of the plate at a square pitch of $6.25\,\mathrm{mm}$. The column is modeled using the DBM code, which was described in the preceding section. The computational grid consists of $30 \times 30 \times 90$ cells and the flow time step $(\delta t_{flow})$ is $1.0 \times 10^{-3}\,\mathrm{s}$. Preliminary calculations revealed that this configuration gives a grid and time step independent solution. The boundary conditions are imposed to the column using the flag matrix concept of Kuipers et al. [28] as can be seen in Fig. 3.7. The definition of each boundary condition can be seen in Table 3.2. The configuration of boundary conditions used in the simulations has been carefully investigated. The prescribed pressure cells close to the column surface wall are required as inlet as well as outlet channel to compensate for the change of liquid volume due to bubbles entering and leaving the column. The width of this pressure cell slit is one third of the total width of the column and located in the mid-

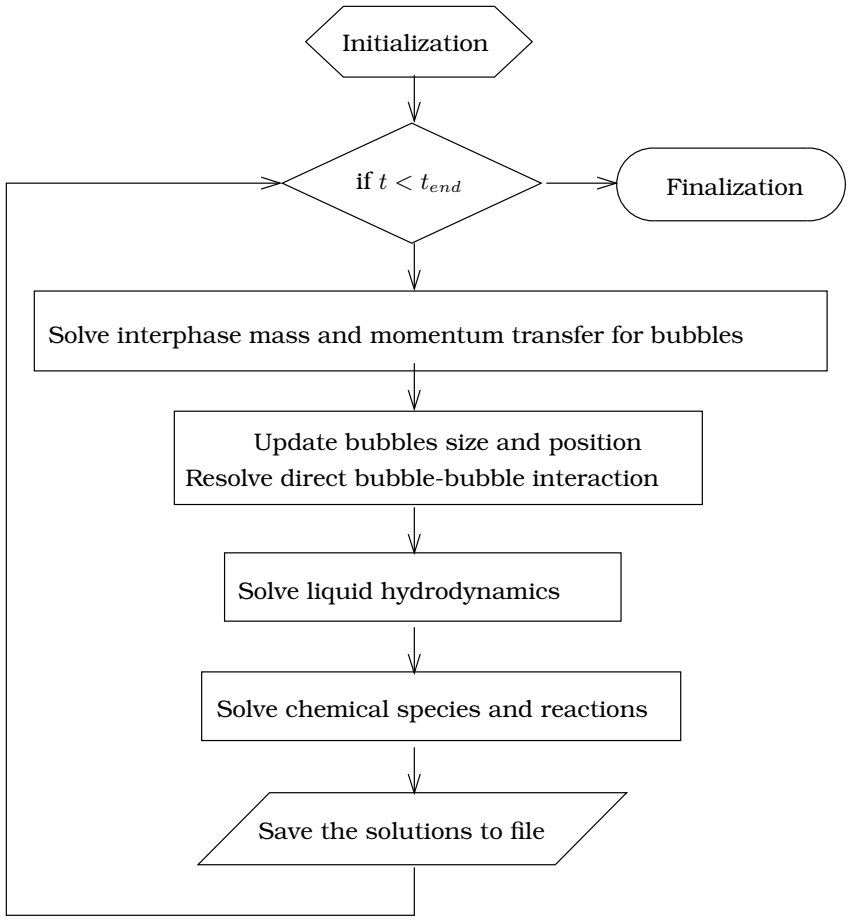


**Figure 3.6:** *Computational sequence diagram of the DBM.*

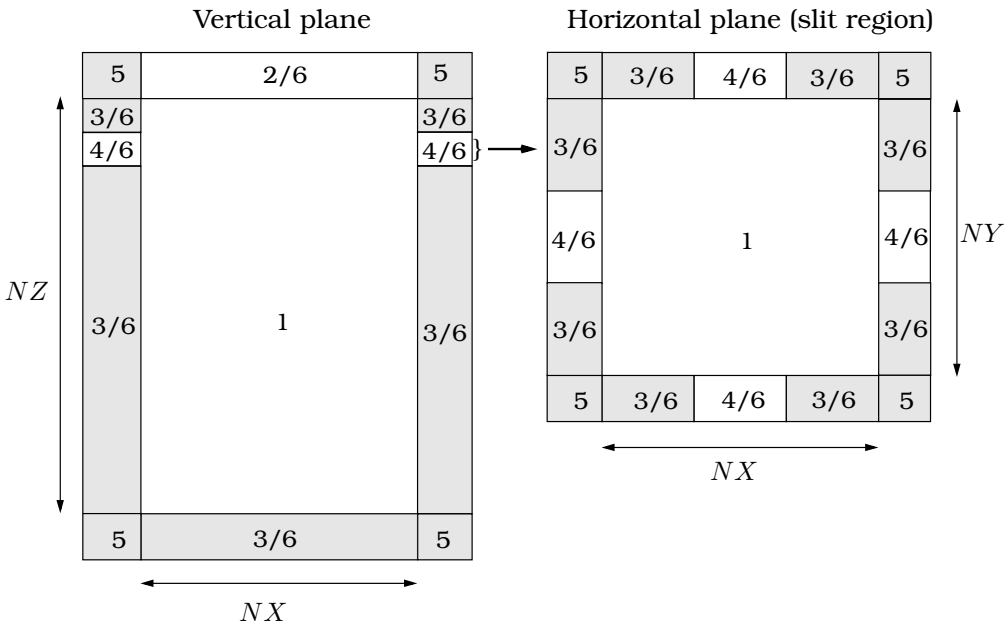


**Figure 3.7:** *Typical boundary conditions used in simulations with the discrete bubble model. The vertical plane is at $j = NY/2$ while a slit is defined at $k = NZ - 1$*

**Table 3.2:** *Cell flags and corresponding cell types used in defining boundary conditions.*

| flag | Boundary conditions |
|---|---|
| 1 | Interior cell, no boundary conditions specified |
| 2 | Impermeable wall, free slip boundary |
| 3 | Impermeable wall, no slip boundary |
| 4 | Prescribed pressure cell, free slip boundary |
| 5 | Corner cell, no boundary conditions specified |
| 6 | Neumann boundary for species transport equation ($\nabla Y^j \cdot \vec{n} = 0$) |

dle. It was found that this configuration avoids hydrodynamic instabilities developing at the top surface of the column. Furthermore for the species transport equations, a Neumann boundary condition is used in all of the boundary cells.

Each hole in the perforated plate is modeled as a position in the bottom of the column where bubbles with specific size enter the column with a fixed velocity. All the bubbles entering the column have a diameter of $4\,\mathrm{mm}$ as has been experimentally observed by Deen et al. [4]. The distance between the center of two consecutive bubbles released from a single hole $\delta_b$ is set to $2.5 \times R_b$. This arrangement is made to avoid unnecessary collisions between two consecutive bubbles immediately after they enter the column. The

velocity of bubbles entering the column is determined from the superficial velocity through the following formula:

$$v_{z,enter} = \frac{v_s \delta_b W \times D}{N_h V_b} \tag{3.27}$$

with $\mathbf{v}_s$ the superficial gas velocity, $W \times D$ the cross sectional area of the column and $N_h$ is number of holes.
For all of the holes, the vertical position of the bubbles underneath the bottom plate is generated in such way that none of the bubbles enters the column at the same time. This was implemented in order to prevent (artificial) pulsing behavior of the incoming bubbles, which would occur if bubbles enter the column through all holes simultaneously. By doing so, the occurrence of undesired pressure fluctuations at the top of the column was prevented.
When a bubble hits the top boundary of the column, the bubble is marked to be removed from the column. The removal procedure is very important since it can influence the overall flow inside the column and in some case may induce instabilities in the numerical solution. When a bubble is marked to be removed from the column, its velocity and interphase mass and momentum transfer to the liquid phase are no longer updated. The bubble is still however, moving with a constant velocity using the last velocity value calculated immediately before it touches the top boundary. Using this velocity, the bubble is passing the top boundary according to the normal bubble time step. The portion of bubble which still resides in the column is still accounted for in the calculation of the liquid phase volume fraction. When the entire bubble is completely above the top boundary, the bubble is disposed from the bubble list which concludes the bubble removal procedure.
For a typical bubble size used in the simulation, the whole process of removing a bubble takes around $10^{-2}$ s and within this interval the liquid phase gradually adapts the change in the volume fraction. Compared with the instantaneous bubble removing technique used by Delnoij et al. [17], the method presented here can eliminate numerical instabilities at the top boundary especially when removing a bubble which has bigger size than the computational grid cell.

## 3.5 Verification

To verify the method for calculating liquid phase porosity, the Lagrangian to Eulerian mapping as well as the Eulerian to Lagrangian mapping, we consider a case in which a bubble rises through a quiescent liquid. The terminal rise velocity of the bubble resulting from our simulations is compared with the analytical solution. For a bubble rising with a constant velocity through

a quiescent liquid the buoyancy force equals the drag force. The drag coefficient is calculated based on Eötvös number as given in table 3.1.
When the terminal rise velocity is reached, the buoyancy force is equal to the drag force hence the terminal rise velocity can be determined as:

$$\mathbf{v}_{terminal} = \left( \frac{8(\rho_l - \rho_b) R_b \mathbf{g}}{3 C_D \rho_l} \right)^{1/2} = \left( \frac{4\,(\rho_l - \rho_b)\,\sigma \mathbf{g}}{\rho_l^2} \right)^{1/4} \tag{3.28}$$

Using $\rho_l = 1000\,\mathrm{kg/m^3}$ , $\rho_b = 1\,\mathrm{kg/m^3}$, $\mathbf{g} = 9.81\,\mathrm{m/s^2}$ and $\sigma = 0.073\,\mathrm{N/m}$ we obtain a terminal rise velocity of $0.2312\,\mathrm{m/s}$. Note that by calculating the drag coefficient using relation reported in table 3.1, the terminal rise velocity of the bubble is independent of its size.
In the simulation, a bubble is released at the bottom of the column and because of the buoyancy, the bubble will start to rise. Simulations were conducted for bubble diameters of $4$ and $10\,\mathrm{mm}$, with computational cells of $5$ and $10\,\mathrm{mm}$.
The comparison between the analytical terminal rise velocity and the simulations are shown in Fig. 3.8. As we can see from this figure, the model can reproduce the terminal rise velocity accurately. For the $10\,\mathrm{mm}$ bubble however, the terminal rise velocity shows small wiggles. These (very small) wiggles can be attributed to the mapping technique and occur when the bubble crosses the face of a computational cell. The order of this wiggle however is very small compared to the magnitude of the terminal rise velocity, thus we can conclude that the proposed mapping method performs satisfactory and can be used for further simulations.
Another simulation was performed to verify the time integration procedure that has been implemented to track the bubble size as well as bubble mass due to mass transfer. The verification was carried out by simulating the rise of a single bubble with mass transfer. The mass transfer rate was set to be constant by selecting the initial conditions of the species $Y_l^j$, $k_l$ and $Y_l^{j*}$ in such a way that $k_l \left( Y_l^j - Y_l^{j*} \right) = 4 \cdot 10^{-6}\,\mathrm{m/s}$. With this arrangement, the analytical solution of the bubble size becomes:

$$R_b(t) = k_l \left( Y_l^j - Y_l^{j*} \right) \frac{\rho_l}{\rho_b} t + R_b(0) \tag{3.29}$$

A bubble with an initial diameter of $4\,\mathrm{mm}$ is released at the bottom of the column. The bubble size is tracked in time and the result is compared with the analytical solution. Fig. 3.9 shows the comparison of the analytical solution and single bubble simulation with grid sizes of $5$ and $10\,\mathrm{mm}$. This figure shows that the simulation results and the analytical solution practically coincide. These results verify that the time integration of the bubble size is correctly implemented and can be used for further simulations.
As mentioned in the previous section, the terminal rise velocity is independent of the bubble size. This fact can also be observed in Fig. 3.10. As can

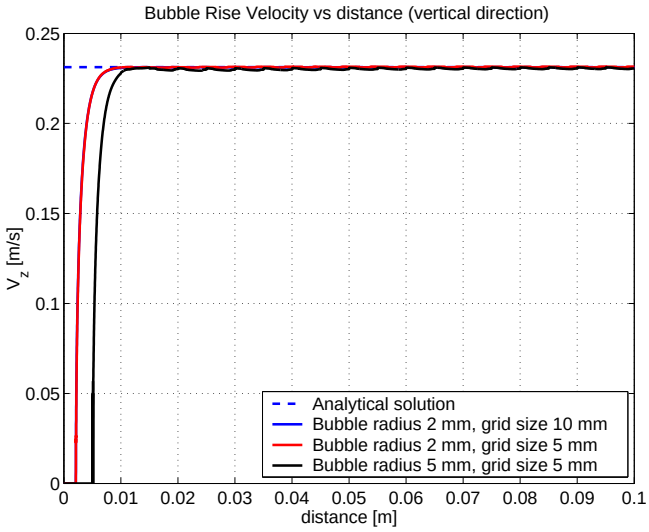


**Figure 3.8:** *Single air bubble rise velocity in an initially quiescent column filled with water. Several combinations of bubble and grid size as compared with the analytical solution.*

be seen from this figure, after the bubble reaches its terminal velocity, the velocity remains constant, despite the fact that the bubble size is increasing. When the bubble diameter exceeds the size of the computational cell, small wiggles start to develop. However the order of these wiggles is again very small and does not increase as the bubble size increases.

## 3.6 Results

In order to demonstrate the capabilities of the model four case studies are presented in this section. The square bubble column introduced in section 3.4 is used as a base configuration. The hydrodynamics part of the model is compared with PIV measurements of Deen et al. [4].

### 3.6.1 Hydrodynamics

In this case study, the hydrodynamics of an air-water system is investigated. The gas-liquid flow in a square bubble column is simulated using the hydrodynamic model as described in section 3.2.1 and 3.2.2. Air is injected into an initially quiescent liquid as indicated in Fig. 3.11. Shortly after the bubbles are released into the column, a bubble plume rises through the column and creates a typical mushroom like shape. Due to the gas-liquid momentum coupling, some motion is induced in the liquid phase, and after

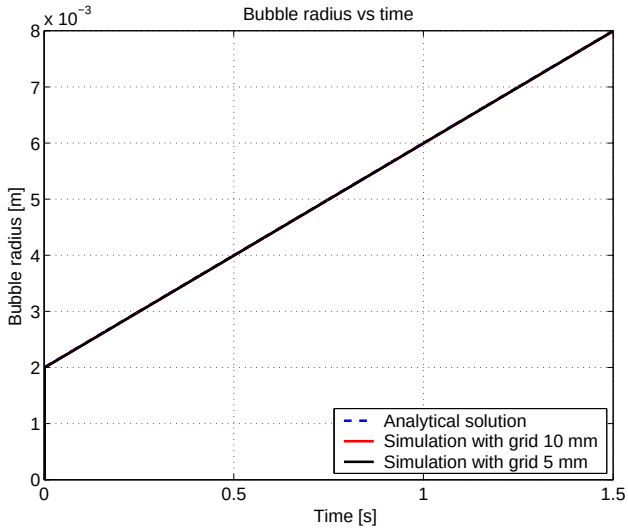


**Figure 3.9:** *Time integration verification of a single air bubble size rising in an initially quiescence water. Bubble initial diameter* $4\mathrm{mm}$*;* $k_l(Y_l^j - Y_l^{j*}) = 4{\cdot}10^{-6}\mathrm{m/s}$*. Simulation results with two different grid size practically coincide with the analytical solution.*

a while the entire bulk liquid starts to move. The first bubbles escape from the column after $1.5\,\mathrm{s}$ simulations. After some time the motion inside the bubble becomes unstable. Strong circulation patterns appear with up flow in the center region and down flow in the corners of the column. Due to the liquid down flow, some bubbles close to the wall are dragged downwards to the lower region of the column before being dragged again to the column surface by the upward flow.

The bubble plume is meandering in a random fashion. Using animation representation of our simulation results as suggested by Delnoij et al. [8] we can see that this meandering behavior is due to random formation of vortices close to the column surface. The vortices generate strong down flow, which pushes the bubbles near the inlet region to one side when they reach the bottom of the column. The bubble plume will then move close to one side of the column. This process is repeated, but the vortex formation appears in another location, which will make the bubble plume move in another direction.

A time history plot of the vertical liquid velocity at one point in the column is shown in Fig. 3.12. As can be seen in this figure, the DBM simulation is able to reveal the highly dynamic nature of the bubble column hydrodynamics. As compared to the experimental measurements using laser Doppler anemometry (LDA) technique by Deen et al. [4], the DBM results are in agreement for both time and velocity scales.

A more quantitative comparison with the experimental measurement is ob-

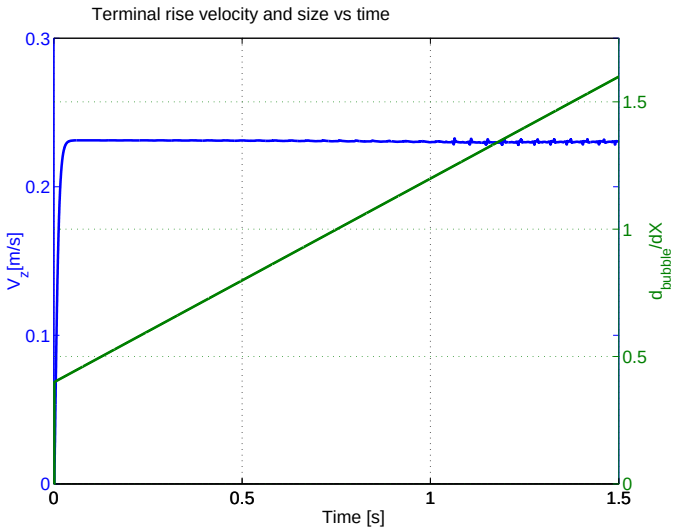


**Figure 3.10:** *Bubble terminal rise velocity for an air bubble experienced constant radius rate. Bubble initial diameter* $4\,\mathrm{mm}$*;* $k_l(Y_l^j - Y_l^{j*}) = 4 \cdot 10^{-6}\,\mathrm{m/s}$*; grid size* $10\,\mathrm{mm}$

tained through the long term (i.e. the statistical averaged) quantities. In the present study the time-averaged mean velocity and velocity fluctuations of the simulation are calculated during a $10 - 120\,\mathrm{s}$ interval. The mean velocity is calculated as follow:

$$\overline{\mathbf{u}} = \frac{1}{N_t} \sum_{i=1}^{N_t} \mathbf{u}_i \tag{3.30}$$

where $N_t$ is the number of time steps used in the averaging.
The large scale velocity fluctuation is calculated as:

$$\mathbf{u}' = \frac{1}{N_t} \sqrt{\sum_{i=1}^{N_t} (\mathbf{u}_i - \overline{\mathbf{u}})^2} \tag{3.31}$$

The time averaged quantities are compared with the PIV measurements of Deen et al. [4], who also conducted two fluid simulations of this column with a two fluid model using the commercial CFD package CFX. Fig. 3.13 shows the profile of the average liquid velocity in the vertical direction while the liquid phase vertical and horizontal velocity fluctuations can be seen in Fig. 3.14. As can be seen in these figures, the simulation results show good agreement with the experimental data. The average velocity profile gives a maximum value in the center of the column and a negative value close to the wall, which resembles a liquid flow pattern with liquid up-flow in the center region of the column and down flow near the walls.

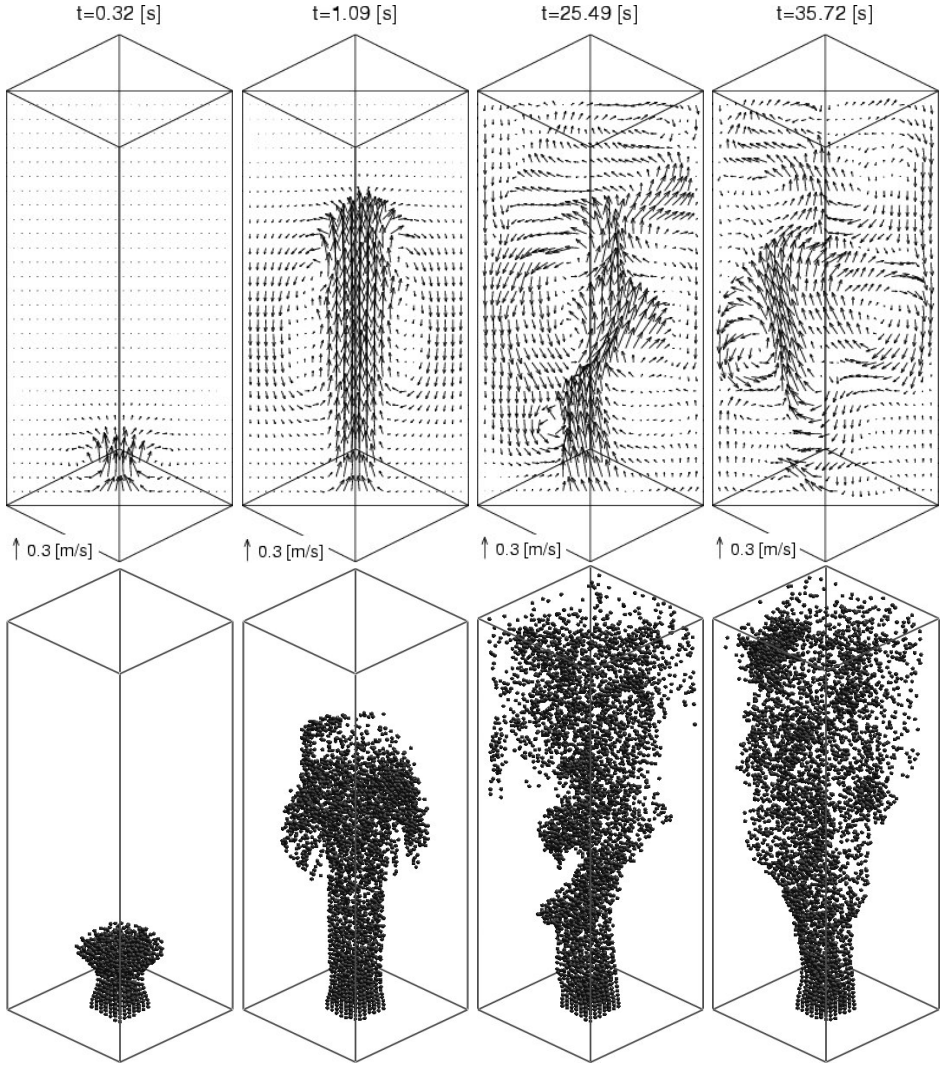


**Figure 3.11:** *Series of corresponding velocity fields and bubble position obtained from simulation of air-water bubble column at different time after the air was switched on. Gas superficial velocity=* $4.9\,\mathrm{mm/s}$.

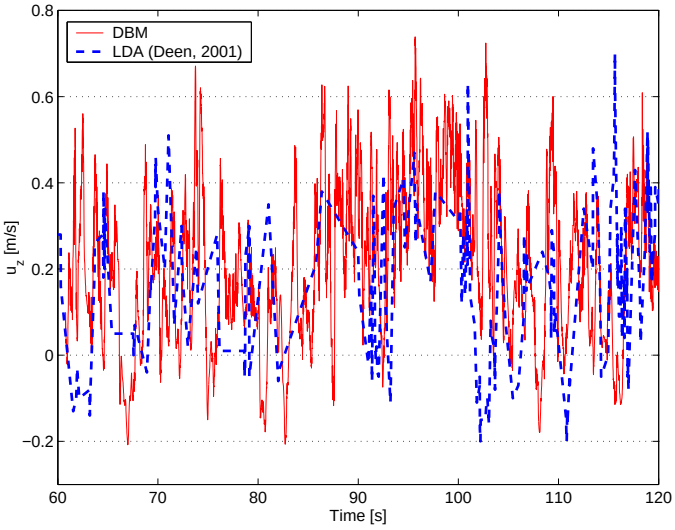


**Figure 3.12:** *Time history of the vertical liquid velocity at the centreline of the column and at a height of* $z/H = 0.56$.

Compared to the PIV measurements, the DBM simulations generally slightly overpredict the average and fluctuation velocities in the center region of the column, while the two-fluid simulation shows the opposite tendency. The vertical velocity fluctuations, measured with PIV, show a local minimum in the middle, which is also predicted nicely in the DBM simulation. The velocity fluctuations predicted by the two fluid model, however, do not show this feature.

### 3.6.2 Mixing

The liquid velocity induced by the motion of the bubbles generates mixing in the bubble column. The characteristics of the mixing is very important, since it will determine the homogeneity of chemical species present in the reactor. The mixing rate is normally determined by injecting a pulse of tracer containing a specified amount of tracer and by monitoring tracer concentrations within the reactor at single or multiple points [14].
In the present study, the mixing mechanism of the air-water bubble column system is investigated immediately after bubbles are injected by making use of three different tracers. The column is divided into three equal regions in the vertical direction. Initially, only one tracer is present in each region as can be seen in Fig. 3.15. The tracer is treated as a passive scalar, which is described by Eq. 3.9, where the source terms are all set to zero.
Fig. 3.16 shows the mixing sequence immediately after bubbles are intro-

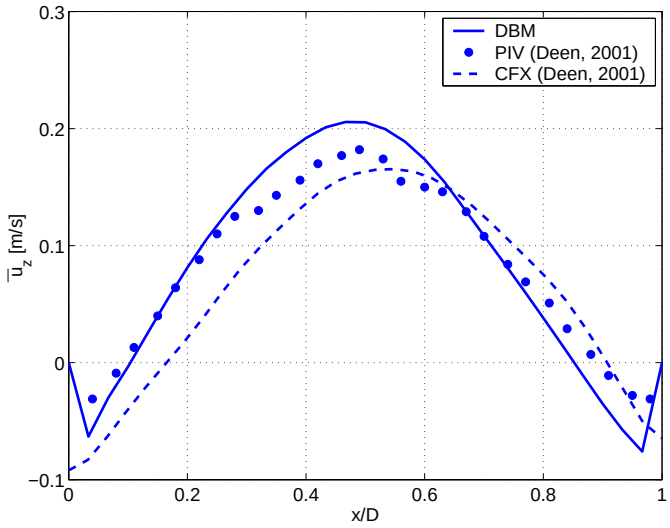


**Figure 3.13:** *Comparison of simulated and experimental profiles of the liquid vertical average velocity* ($\overline{u}_z$)*, at a height of* $z/H = 0.56$ *and a depth* $y/W = 0.5$*.*

duced into the column. As can be seen, the tracers that are initially separated are pushed upward in the center region of column, because of the bubble motion. This upward motion is balanced by downward motion close to the column wall. The tracers, which come from the three regions then hit the top and bottom part of the column. The vortices present in these regions mix the tracers even further. The process is continued until all the tracer is mixed evenly.
The mixing time is quantified by monitoring the mass fractions of the three tracers at the centerline axis, at a height of $z/H = 0.5$ (see Fig. 3.17). As can be seen from this figure, a homogeneous mixture is reached after $8\ s$. This figure also shows that the mass fraction is bounded between $0 - 1$ and the sum of all species is conserved during the simulation.

### 3.6.3 Physical absorption

In this case study the physical absorption of $CO_2$ in water is simulated. $CO_2$ gas is fed into the column filled with water. A species transport equation is utilized to track the mass fractions of $CO_2$ in the liquid phase. Initially there is no dissolved $CO_2$ present in the column. During the process of the physical absorption, a relatively low mass transfer rate is experienced by the bubbles.
Fig. 3.18 shows the transient behavior in the column after the $CO_2$ bubbles are injected into the column. As can be seen, the hydrodynamics are relatively similar to the air-water case as described in the previous test cases.

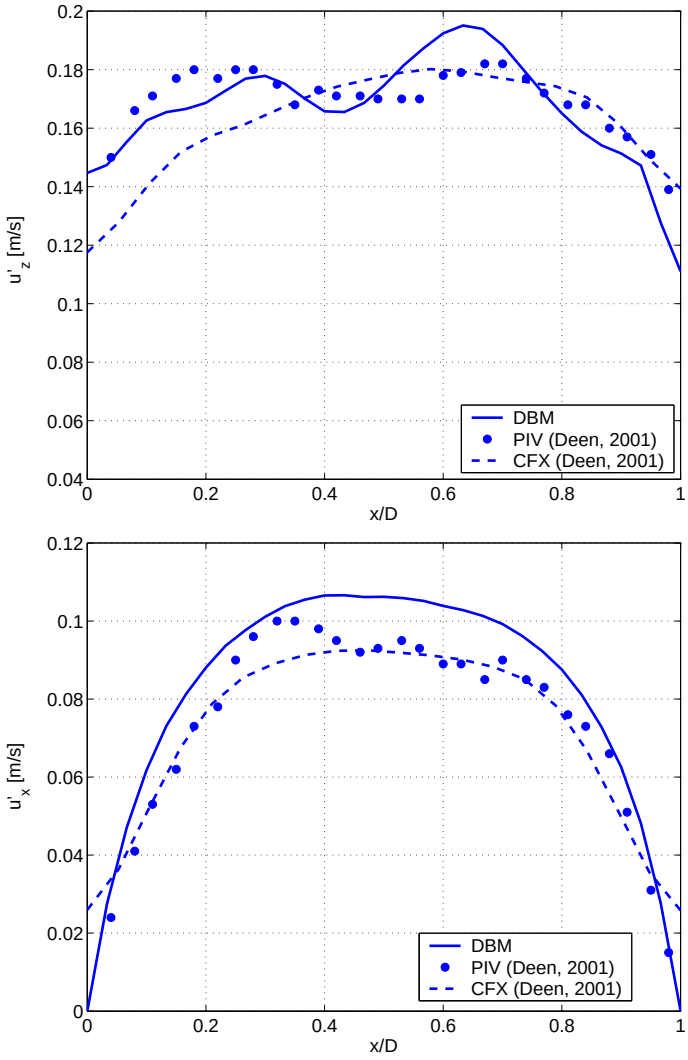


**Figure 3.14:** *Comparison of simulated and experimental profiles of the liquid velocity fluctuations, at a height of* $z/H = 0.56$ *and a depth* $y/W = 0.5$*. Top: vertical fluctuations* $(u'_z)$*, bottom: horizontal fluctuations* $(u'_x)$*.*

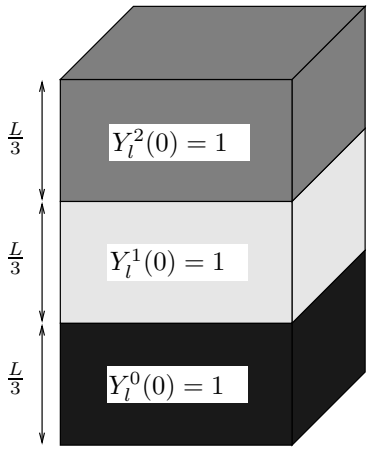


**Figure 3.15:** *Initial condition used for the mixing study. The column is divided into three different regions. Only one species is initially present in each region.*

The size of the bubbles is only slightly changed during their presence in the column. A high fraction of dissolved $CO_2$ can be found in the vicinity of the bubbles. The dissolved $CO_2$ is convected by the liquid to other parts of the column.
The overall mass transfer rate can also be estimated by integrating eq. 3.14 over the entire column. In the case of no mass transfer enhancement, this yields the following expression for the mean dissolved $CO_2$ concentration in the column at time $t$:

$$\frac{[CO_2(aq)]\,(t)}{H\,[CO_2(g)]} = 1 - \exp\frac{-tN_b k_l A_b}{V_l} \tag{3.32}$$

with $N_b$ the (averaged) total number of bubble and $V_l$ the (averaged) liquid volume of the column. The mass transfer coefficient $k_l$ is calculated using the theoretical terminal rise velocity as explained in sect. 3.5 while the interfacial area $A_b$ is calculated by assuming constant bubble size.
According to eq. 3.32, the dissolved $CO_2$ is accumulated exponentially in time. The interphase mass transfer decreases as the dissolved $CO_2$ concentration increases and eventually diminished when the equilibrium condition as prescribed by the Henry constant is reached.
Fig. 3.19 shows the concentration of $CO_2$ at the centreline of the column, at a height of $z/H = 0.5$ resulting from the DBM simulation compared with the macro balance calculation given by eq. 3.32 within the time interval $0 - 500\mathrm{s}$. As can be seen in this figure, the macro balance shows good agreement with the DBM results. The discrepancy observed is less than $5\%$, which might come from the fact that DBM employs the exact number of bubbles as well as the bubbles and liquid properties in calculating the mass transfer, in contrast with the average value and constant size used in the macro balance

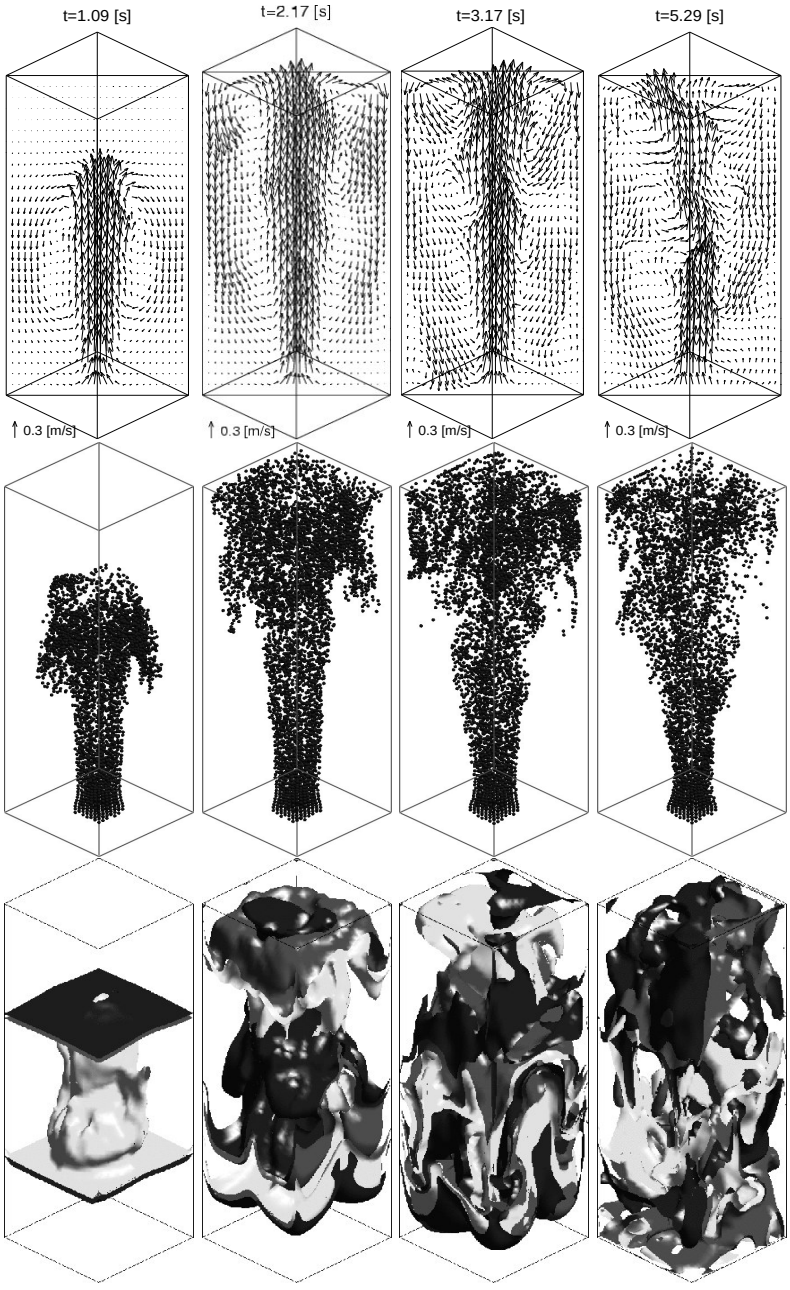


**Figure 3.16:** *Set of corresponding velocity fields (top), bubble position (middle) and isosurface of 30% tracer mass fraction (bottom) obtained from simulation of air-water bubble column with additional three passive scalar act as tracer at different time after the air was switched on. Gas superficial velocity=* $4.9\ \mathrm{mm/s}$.

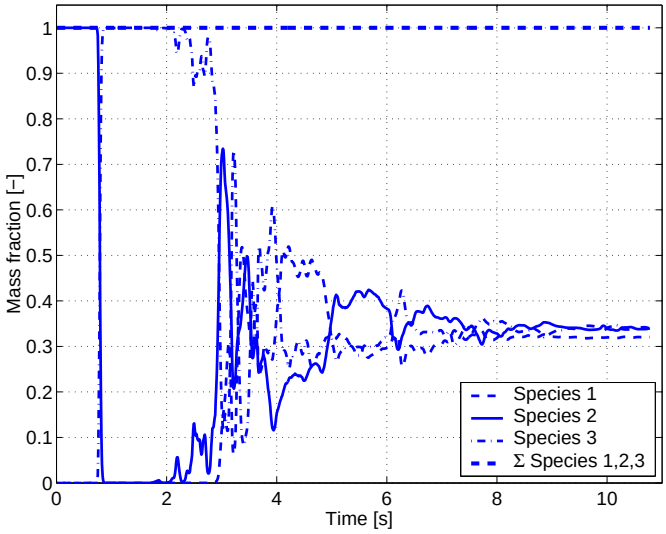


**Figure 3.17:** *Variation of the tracer during the mixing sequence at the centreline of the column and at a height of* $z/H = 0.5$.

model. Furthermore, in the macro balance model it is assumed that the transferred components are ideally mixed in the liquid, which is in contrast to the findings of the DBM.

### 3.6.4 Bubble column under reactive conditions

In this case study, we combine all the models described in section 3.2 to obtain a complete, comprehensive model for a bubble column under reactive conditions. The chemisorption of $CO_2$ into aqueous $NaOH$ solution is chosen as a test case, since it accounts for important phenomena that are encountered in practice.
The overall reaction mechanism of the chemisorption of carbon dioxide in an aqueous solution of sodium hydroxide is well understood and the reaction kinetics is well documented. The reaction sequence comprises several steps, which are given below:

$$CO_2(g) \longrightarrow CO_2(aq) \tag{3.33}$$

$$CO_2(aq) + OH^- \rightleftharpoons HCO_3^- \tag{3.34}$$

$$HCO_3^- + OH^- \rightleftharpoons CO_3^{2-} + H_2O \tag{3.35}$$

At high pH the second reaction is considered to be instantaneous. Thus in the present study the overall reaction can be simplified into:

$$CO_2(aq) + 2OH^- \rightleftharpoons CO_3^{2-} + H_2O \tag{3.36}$$

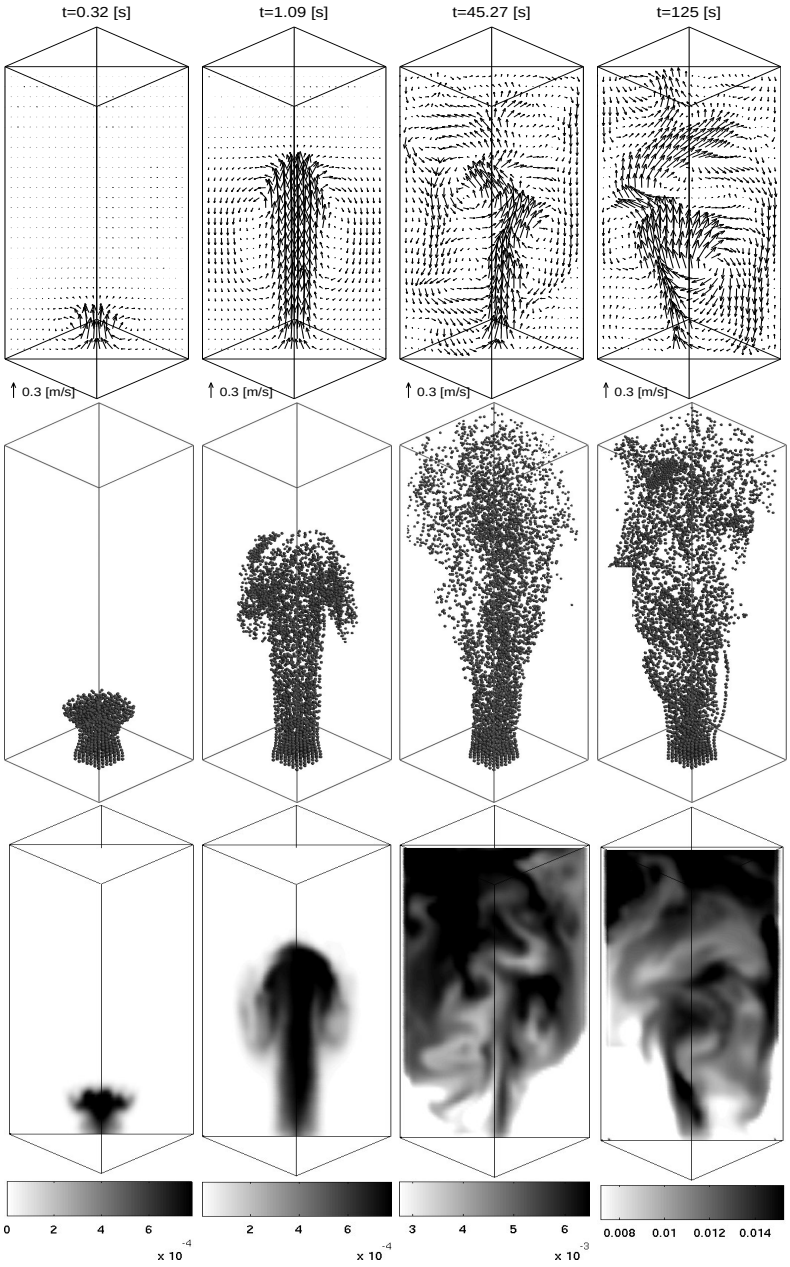


**Figure 3.18:** *Set of corresponding velocity fields (top), bubble position (middle) and distribution of dissolved $CO_2$ concentration* $[\mathrm{mol/l}]$ *(bottom) obtained from simulation of the physical absorption of $CO_2$ gas in water at various time after the $CO_2$ gas was switched on. $CO_2$ gas superficial velocity=* $4.9\,\mathrm{mm/s}$.

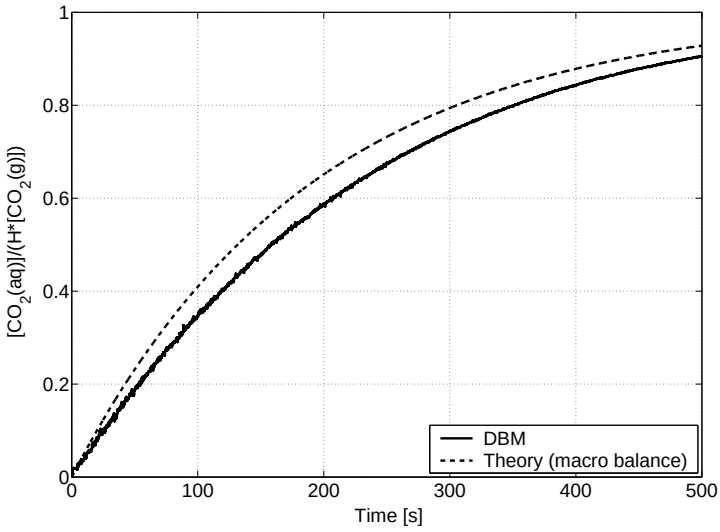


**Figure 3.19:** *Normalized dissolved $CO_2$ concentration at the centreline of the column and at a height of $z/H = 0.5$ compared with macro balance model. Simulation result of physical absorption of $CO_2$ bubbles in water. $CO_2$ gas superficial velocity=* $4.9\,\mathrm{mm/s}$. $N_b = 4643$.

Since the first reaction is rate determining, the rate of the overall reaction is taken from the first reaction. The forward and backward reaction rate can respectively be formulated as:

$$R_{1,1} = k_{1,1}\left[CO_2(aq)\right]\left[OH^-\right] \tag{3.37}$$

$$R_{1,2} = k_{1,2}\left[HCO_3^-\right] \tag{3.38}$$

where $k_{1,1}$ and $k_{1,2}$ are the forward and backward reaction rate constants respectively.
The influence of the chemical reaction on the gas absorption process is usually accounted for by an enhancement factor, $E$. This factor can be calculated numerically by solving the (coupled) diffusion equations in the boundary layer surrounding the bubbles. The equations should be solved for each individual bubble, hence in the case where a large number of bubbles is present this method becomes impractical. In the present study, an approximate solution of the enhancement factor is used. The enhancement factor takes a simple algebraic form as a function of the Hatta number [29]:

$$E = \begin{cases} -\frac{\mathrm{Ha}^2}{2(E_\infty - 1)} + \sqrt{\frac{\mathrm{Ha}^4}{4(E_\infty - 1)^2} + E_\infty \frac{\mathrm{Ha}^2}{E_\infty - 1} + 1} & ; \quad E_\infty > 1 \\ 1 & ; \quad E_\infty \leq 1 \end{cases} \tag{3.39}$$

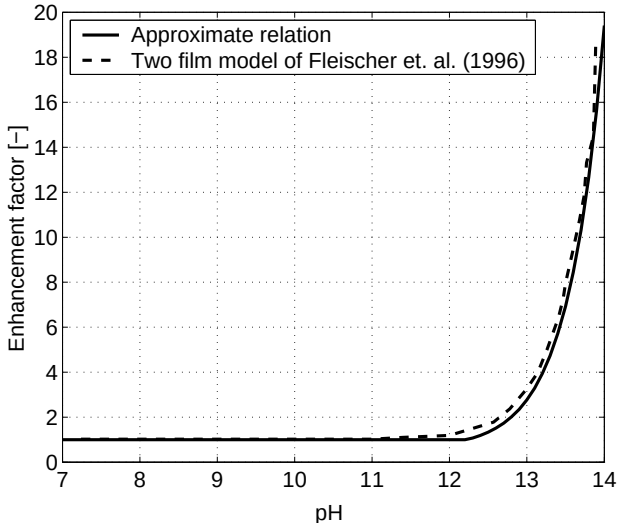


**Figure 3.20:** *pH-dependence of the enhancement factor $E$ determined using approximate relation compared with with the detailed simulation with the two-film model of Fleischer et al. [9].*

where

$$E_\infty = \left(1 + \frac{D_{OH^-}\left[OH^-\right]}{2D_{CO_2}H\left[CO_2\left(g\right)\right]}\right)\sqrt{\frac{D_{CO_2}}{D_{OH^-}}} \tag{3.40}$$

$$\mathrm{Ha} = \frac{\sqrt{k_{1,1}D_{CO_2}\left[OH^-\right]}}{k_l} \tag{3.41}$$

This approach provides a much cheaper solution for the enhancement factor for each individual bubble. The variation of the enhancement factor, $E$, for $pH$ ranging from $7$ to $14$ can be seen in Fig. 3.20. As we can see the physical mass transfer rate is significantly enhanced by the chemical reaction at pH $>$ $12$. Compared to the detailed simulation result using the two-film model by Fleischer et al. [9], the approximate relation can represent the enhancement factor quite well. Small discrepancy is observed at high pH range. However since this is only a test case to demonstrate the capabilities of the Euler-Lagrange model, the approximate relation for the enhancement factor given by eq. 3.39 is considered to be adequate to describe the physical phenomena.

During the chemisorption process, due to the high interphase mass transfer rate, it is possible that bubbles are completely dissolved in the liquid. In our model a bubble is considered to be completely dissolved in the liquid when the bubble radius is less than $1$ $\mu$m, while the bubble growth rate is negative (i.e. the bubble is still dissolving). If a bubble meets this

**Table 3.3:** *Initial conditions and source terms used in the species transport equations.*

| j | **Species** | $\mathbf{Y_l^j\,(t=0)}$ | $\mathbf{S^j/M_w^j}$ $\left[\frac{\mathbf{kmol}}{\mathbf{m^3 s}}\right]$ |
|---|---|---|---|
| 0 | $CO_2(aq)$ | $1\times10^{-50}$ | $-R_{1,1}+R_{1,2}$ |
| 1 | $OH^-$ | $Y_1\,(pH)$ | $2\,(-R_{1,1}+R_{1,2})$ |
| 2 | $CO_3^{2-}$ | $1\times10^{-50}$ | $R_{1,1}-R_{1,2}$ |

criterion, it will be disposed from the column and no longer being tracked.
The chemisorption problem is simulated using the DBM model. $CO_2$ gas is feed into the column filled with $NaOH$ solution with an initial pH of 14. Three species transport equation are utilized to track mass fractions of $CO_2(aq)$, $OH^-$ and $CO_3^{2-}$. A summary of the initial conditions and the source terms used in each transport equation is presented in Table 3.3.
Fig. 3.21 shows the transient behavior in the column immediately after the $CO_2$ bubbles are injected into the column. Shortly after bubbles are released into the column, a typical mushroom like shape appears. This shape is however, less pronounced compared to the case without absorption as described in section 3.6.1. Due to the chemically enhanced mass transfer, the bubbles are completely dissolved within $0.15\,\mathrm{m}$ from the bottom and remain in that position for quite a while. Although the bubbles only appear in the lower part of the column, the liquid circulation induced by the bubbles extends to the top portion of the column. Compared to the case without absorption, the liquid phase oscillation is only observed in the higher part of the column. Since no bubbles are present in this region, these oscillations do not interact with bubbles, which makes them less pronounced.
Fig. 3.22 shows the transient behavior of chemical species distribution in the column. Since bubbles are only present in the lower part of the column, the mass transfer and reactions only take place close to the gas inlet. $CO_2$ gas, which dissolves into the liquid from the bubbles immediately reacts with hydroxide to produce carbonate, hence only very small traces of dissolved $CO_2$ can be found in the vicinity of the bubbles. The hydroxide ions that have been consumed by the reaction as well as the newly formed carbonate ions will be transported by the circulation flow to the top of the column in the center region and return back again through the downflow zone close to the column walls. This behavior suggests that the reactions taking place in the bottom part of the column are always supplied with relatively fresh reactant, since the product of the reaction is immediately transported by the liquid flow.
With time, the pH is decreasing and the carbonate concentration is continuously increasing. As the pH decreases, the enhancement factor, as shown in Fig. 3.20, also decreases, resulting in a lower mass transfer rate. In time the position where the bubbles are completely dissolved will slowly move upward. This behavior has been experimentally observed by

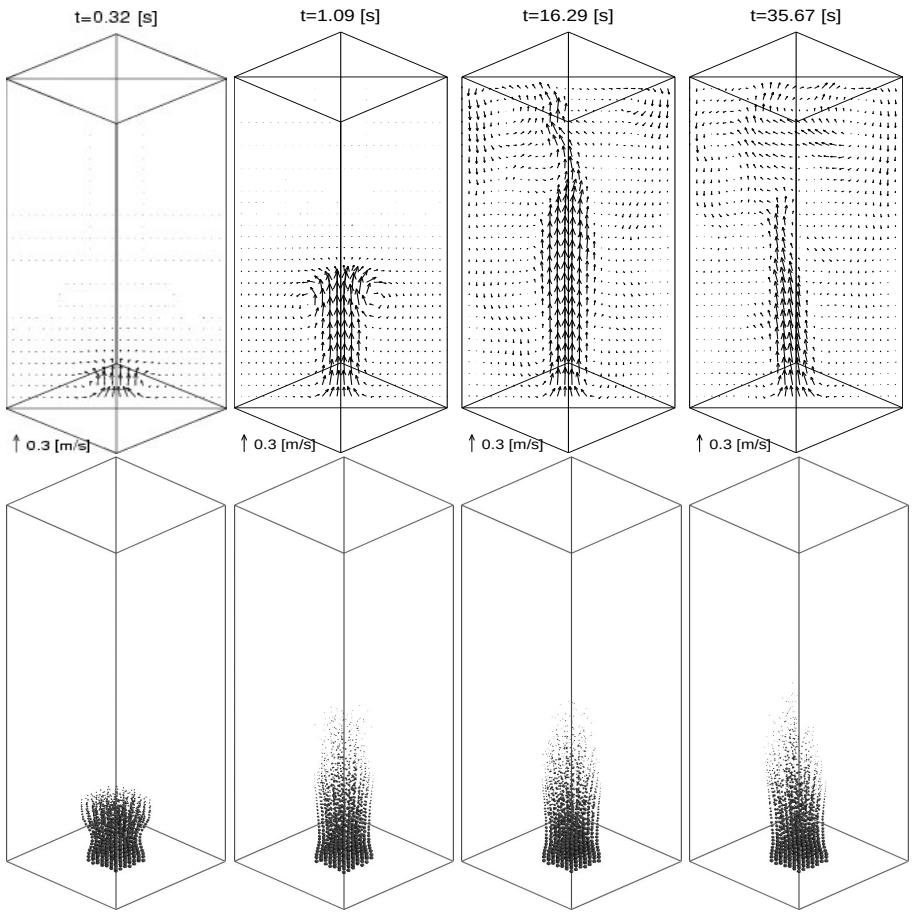


**Figure 3.21:** *Set of corresponding velocity fields (top), bubble position (bottom) obtained from simulation of the chemisorption of $CO_2$ gas in liquid $NaOH$ at various time after the $CO_2$ gas was switched on. Initial $NaOH$ $pH = 14$, $CO_2$ gas superficial velocity=* $4.9\,\mathrm{mm/s}$.

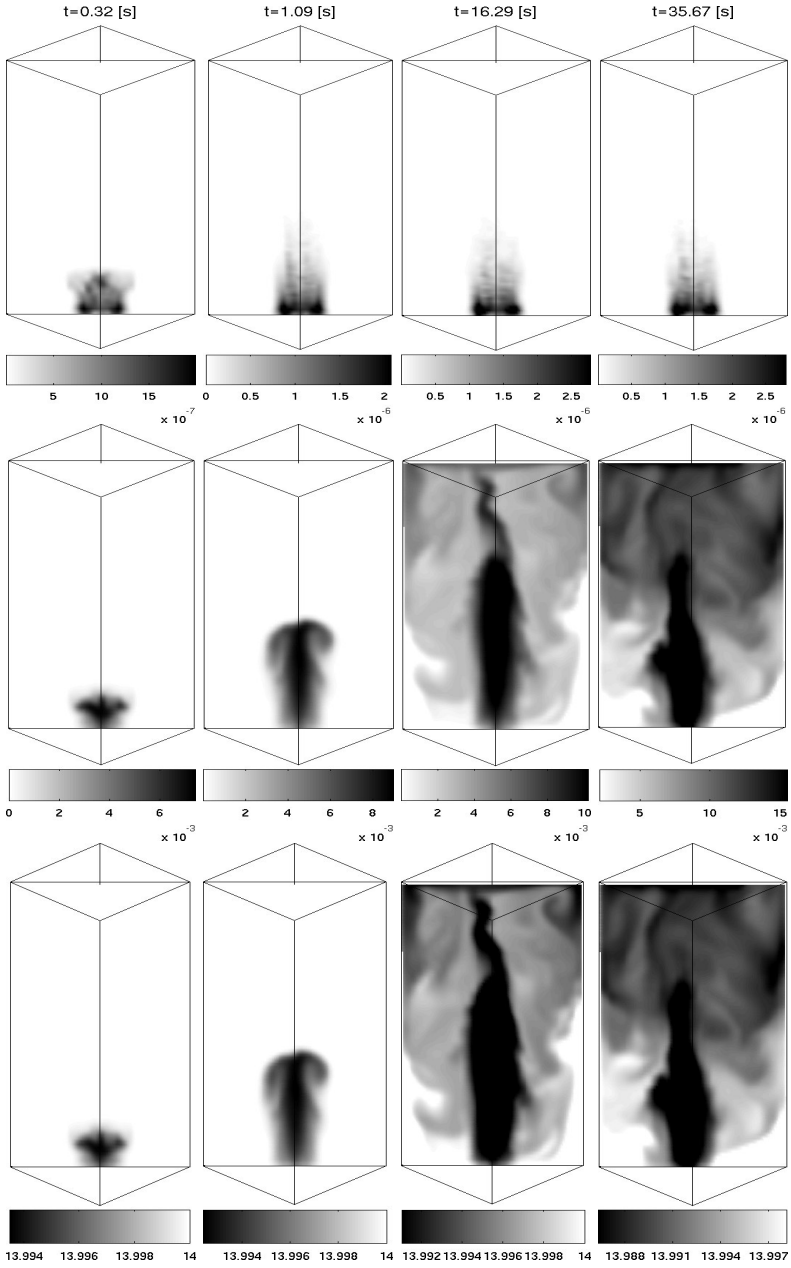


**Figure 3.22:** *Set of corresponding dissolved $CO_2$ concentration* $[\mathrm{mol/l}]$ *(top), $CO_3^{2-}$ concentration* $[\mathrm{mol/l}]$ *(middle) and liquid phase $pH$* $[-]$ *(bottom) obtained from simulation of the chemisorption of $CO_2$ gas in liquid $NaOH$ at various time after the $CO_2$ gas was switched on. $pH_0 = 14$; pure $CO_2$ gas superficial velocity=* $4.9\,\mathrm{mm/s}$.

Fleischer et al. [9]. To investigate whether our model is capable to predict such behavior, a series of simulations with an initial pH varying from 13 up to 14 has been conducted. This technique is used to save calculation time, since the rate of change of pH is very low. Fig. 3.23 shows that the afore mentioned behavior is nicely predicted by the current model. As the pH decreases the position where bubbles are completely dissolved moves upward and since the model is also able to predict the decrease of pH in time we can conclude that this behavior can also be captured if we would proceed the simulation for a sufficiently long period.

## 3.7 Conclusions

A model that combines hydrodynamics, mass transfer and chemical reaction in a bubble column has been successfully formulated and implemented. The simulation results obtained shows that the model can be used to investigate those phenomena in more detail than before.
Simulation of a single rising bubble in a quiescent liquid shows that the model is able to predict the terminal rise velocity correctly. In combination with a constant mass transfer rate, the model also accurately produces the bubble size as a function of time.
The hydrodynamics model has been validated using the experimental data of Deen et al. [4]. Both instantaneous and time-averaged liquid velocities predicted by the model are in good agreement with the experimental data. The experimentally observed meandering of the bubble plume is also nicely predicted by the present model.
By combining the hydrodynamics and chemical species transport equations, the mixing mechanism in the column can be studied in more detail. Our simulations indicate that intense mixing prevails at regions where sudden changes in flow direction occur.
One of the key features of the model presented in this chapter is its capability to track individual bubbles in time. By calculating the mass transfer rate for each individual bubble and combining this information with a chemical species transport equation, gas absorption in reactive liquids can be described.
In the case of the physical absorption of $CO_2$ bubbles is water, it was found that the distribution of dissolved $CO_2$ is not uniform. Relatively high dissolved $CO_2$ was found in the vicinity of bubbles. In time the dissolved $CO_2$ is accumulated in the water until the equilibrium is attained. This behavior shows good agreement compared with theoretical calculations.
The model was also used to investigate the chemisorption of $CO_2$ gas in $NaOH$ solution. This process has been studied experimentally by Fleischer et al. [9]. The model is able to reveal liquid phase hydrodynamics, bubble size and position as well as chemical species distribution involves in the reaction. In simulations with initial pH=14, bubbles are only present close to

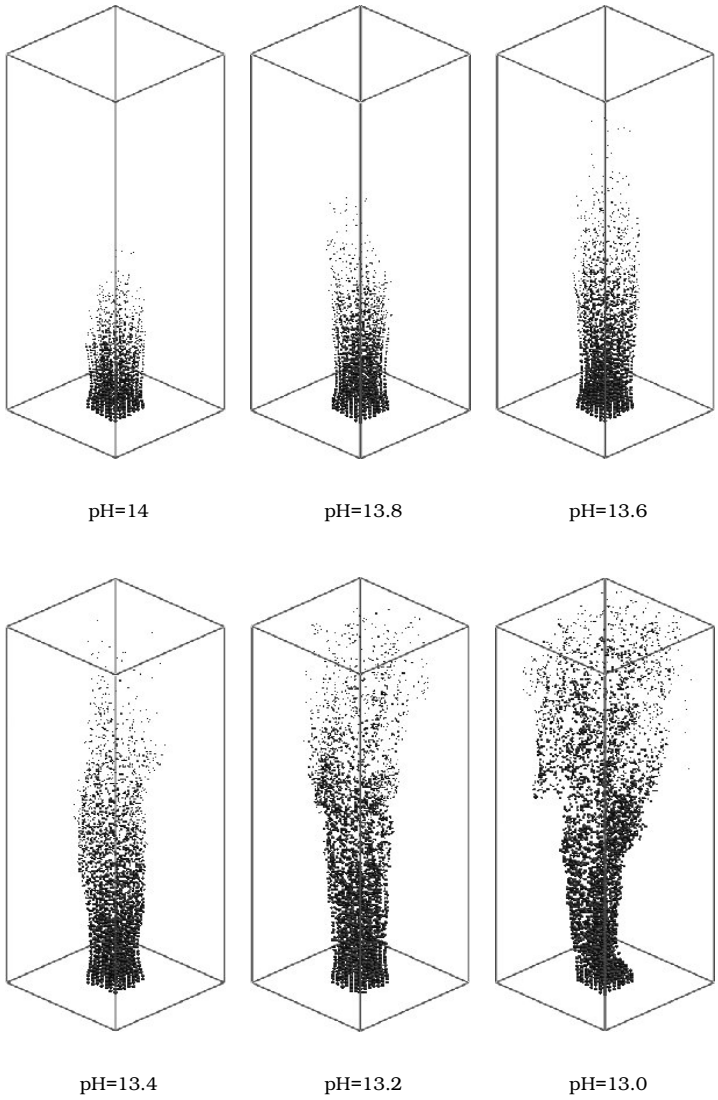


**Figure 3.23:** *Snapshot of bubble position at time* $t = 10\,\mathrm{s}$ *after the* $CO_2$ *gas was switched on with variation of initial liquid* $NaOH$ $pH$*.* $CO_2$ *gas superficial velocity=* $4.9\,\mathrm{mm/s}$.

the gas inlet. Only very small traces of dissolved $CO_2$ can be found in the vicinity of the bubbles while the hydroxide ion that have been consumed and newly formed carbonate ions is transported through all the column region. In time the pH is decreasing while the carbonate ions is increasing. The model is also able to predict the position of completely dissolved bubbles due to chemically enhanced mass transfer. Variation of initial pH shows that this position shifts upward in the column as the pH decreases.
Due to the complexity and detailed information that the present model provides, calculation time is still the bottleneck especially for problems which involve a large number of bubbles and chemical species. In the current work, coalescence and break up were not considered. However, appropriate coalescence and break up models can readily be implemented due to the lagrangian treatment of the bubble phase.

## Acknowledgements

The author would like to thank Prof. B.H. Hjertager (Chemical Fluid Flow Processes, Aalborg University Esbjerg) for giving inspiration on solving the chemical species balance.

## Notation

| | |
|---|---|
| $A$ | interfacial area, $\mathrm{m}^2$ |
| $C$ | model coefficient, dimensionless |
| $d$ | diameter, $\mathrm{m}$ |
| $D$ | diffusivity $\mathrm{m}^2\,\mathrm{s}^{-1}$, depth $\mathrm{m}$ |
| $E$ | enhancement factor, dimensionless |
| $E\ddot{o}$ | Eötvös number, $E\ddot{o} = (\rho_l - \rho_b)\,\mathrm{g}d_b^2/\sigma$, dimensionless |
| $\mathbf{F}$ | force vector, $\mathrm{N}$ |
| $\mathbf{g}$ | gravity acceleration, $\mathrm{m}\,\mathrm{s}^{-2}$ |
| $H$ | Henry constant (aqueous-concentration / gas-concentration), dimensionless |
| $\mathrm{Ha}$ | Hatta number, dimensionless |
| $k_{1,1}$ | forward reaction rate constant, $\mathrm{m}^3\,\mathrm{kmol}^{-1}\,\mathrm{s}^{-1}$ |
| $k_{1,2}$ | backward reaction rate constant, $\mathrm{s}^{-1}$ |
| $k_l$ | mass transfer coefficient, $\mathrm{m}\,\mathrm{s}^{-1}$ |
| $\mathbf{I}$ | unit tensor, dimensionless |
| $m$ | mass, $\mathrm{kg}$ |
| $\dot{m}$ | mass transfer from individual bubble, $\mathrm{kg}\,\mathrm{s}^{-1}$ |
| $\dot{M}$ | liquid side volume averaged mass transfer, $\mathrm{kg}\,\mathrm{s}^{-1}\,\mathrm{m}^{-3}$ |
| $M_w$ | molecular weight, $\mathrm{kg}\,\mathrm{kmol}^{-1}$ |
| $P$ | pressure, $\mathrm{N}\,\mathrm{m}^{-2}$ |
| $R$ | radius $\mathrm{m}$, reaction rate, $\mathrm{kmol}\,\mathrm{m}^{-3}\,\mathrm{s}^{-1}$ |

| | |
|---|---|
| Re | Reynolds number, $\mathrm{Re} = \rho_l \left\|\mathbf{v} - \mathbf{u}\right\| d_b/\mu_l$, dimensionless |
| $S$ | source term in the species balance equation, $\mathrm{kg\,m^{-3}\,s^{-1}}$ |
| $\mathbf{S}$ | characteristic filtered strain rate, $\mathrm{s^{-1}}$ |
| Sc | Schmidt number, $\mathrm{Sc} = \mu_l/(\rho_l D)$, dimensionless |
| Sh | Sherwood number, $\mathrm{Sh} = k_l d_b/D$, dimensionless |
| $t$ | time, s |
| $\mathbf{u}$ | liquid velocity vector, $\mathrm{m\,s^{-1}}$ |
| $\overline{\mathbf{u}}$ | liquid mean velocity, $\mathrm{m\,s^{-1}}$ |
| $\mathbf{u}'$ | liquid velocity fluctuation vector, $\mathrm{m\,s^{-1}}$ |
| $\mathbf{v}$ | bubble velocity vector, $\mathrm{m\,s^{-1}}$ |
| $V$ | volume, $\mathrm{m^3}$ |
| $W$ | width, m |
| $Y$ | mass fraction, dimensionless |
| $[.]$ | concentration, $\mathrm{kmol\,m^{-3}}$ |

## Greek letters

| | |
|---|---|
| $\delta_b$ | distance between two consecutive bubble, m |
| $\triangle$ | subgrid length scale, m |
| $\varepsilon$ | volume fraction, dimensionless |
| $\Gamma$ | species diffusion coefficient, $\mathrm{m^2\,s^{-1}}$ |
| $\mu$ | viscosity, $\mathrm{kg\,m^{-1}\,s^{-1}}$ |
| $\omega$ | lagrangian quantity |
| $\Omega$ | eulerian quantity |
| $\Phi$ | volume averaged momentum transfer due to interphase forces, $\mathrm{N\,m^{-3}}$ |
| $\rho$ | density, $\mathrm{kg\,m^{-3}}$ |
| $\sigma$ | interfacial tension, $\mathrm{N\,m^{-1}}$ |
| $\tau$ | stress tensor, $\mathrm{N\,m^{-2}}$ |
| $\zeta$ | volume fraction of a bubble included in a cell, dimensionless |

## Indices

| | |
|---|---|
| $aq$ | aqueous |
| $b$ | bubble |
| $cell$ | computational cell |
| $D$ | drag |
| eff | effective |
| $G$ | gravity |
| $j$ | $j^{th}$ species |
| $l$ | liquid |
| $L$ | lift |
| $P$ | pressure |
| $s$ | superficial |
| $S$ | subgrid |
| $T$ | turbulent |

$VM$ virtual mass
$*$ interfacial equilibrium value

## References

[1] D. Darmana, N. G. Deen, and J. A. M. Kuipers. Detailed modeling of hydrodynamics, mass transfer and chemical reactions in a bubble column using a discrete bubble model. *Chemical Engineering Science*, 12:3383–3404, 2005.

[2] D. Darmana, N. G. Deen, and J. A. M. Kuipers. Modeling of mass transfer and chemical reactions in a bubble column reactor using a discrete bubble model. Yokohama, Japan, May 30-June 4 2004. 5th International Conference on Multiphase Flow, ICMF'04. Paper No. 328.

[3] A. H. G. Cents, D. W. F. Brilman, P. J. Wijnstra, P. P. L. Regtien, and G. F. Versteeg. Measurement of bubble, drop and particle size distribution in multi-phase systems using ultrasonic spectroscopy. *Canadian Journal of Chemical Engineering*, 2003.

[4] N. G. Deen, T. Solberg, and B. H. Hjertager. Large eddy simulation of the gas-liquid flow in a square cross-sectioned bubble column. *Chemical Engineering Science*, 56:6341–6349, 2001.

[5] Y. Pan and M. P. Dudukovic. Numerical investigation of gas-driven flow in 2-d bubble columns. *AIChE Journal*, 46:434–449, 2000.

[6] A. Sokolichin and G. Eigenberger. Gas-liquid flow in buble columns and loop reactors: Part I. detailed modelling and numerical simulation. *Chemical Engineering Science*, 49:5735–5746, 1994.

[7] A. Tomiyama, H. Higaki I. Zun, Y. Makino, and T. Sakaguchi. A three-dimensional particle tracking method for bubbly flow simulation. *Nuclear Engineering and Design*, 175:77–86, 1997.

[8] E. Delnoij, F. A. Lammers, J. A. M. Kuipers, and W. P. M. van Swaaij. Dynamic simulation of dispersed gas-liquid two-phase flow using a discrete bubble model. *Chemical Engineering Science*, 52:1429–1458, 1997.

[9] C. Fleischer, S. Becker, and G. Eigenberger. Detailed modeling of the chemisorption of $CO_2$ into $NaOH$ in a bubble column. *Chemical Engineering Science*, 51:1715–1724, 1996.

[10] M. A. Márquez, R. J. Amend, R. G. Carbonell, A. E. Sáez, and G. W. Roberts. Hydrodynamics of gas-lift reactors with a fast, liquid-phase reaction. *Chemical Engineering Science*, 54:2263–2271, 1999.

[11] M. A. Márquez, A. E. Sáez, R. G. Carbonell, and G. W. Roberts. Coupling of hydrodynamics and chemical reaction in gas-lift reactors. *AIChE Journal*, 45(2):410–423, 1999.

[12] M. H. Al-Rashed and A. G. Jones. CFD modelling of gas-liquid reactive precipitation. *Chemical Engineering Science*, 54:4779–4784, 1999.

[13] V. V. Buwa and V. V. Ranade. Dynamics of gas-liquid flow in a rectangular bubble column: experimental and single/multi-group CFD simulations. *Chemical Engineering Science*, 57:4715–4736, 2002.

[14] V. V. Ranade and Y. Tayalia. Modelling of fluid dynamics and mixing in shallow bubble column reactors: influence of sparge design. *Chemical Engineering Science*, 56:1667–1675, 2001.

[15] S. Becker, A. Sokolichin, and G. Eigenberger. Gas-liquid flow in bubble columns and loop reactors: Part II. comparison of detailed experiments and flow simulations. *Chemical Engineering Science*, 49:5747–5762, 1994.

[16] R. C. Chen, J. Reese, and L. S. Fan. Flow structure in a three-dimensional bubble column and three-dimensional fluidized bed. *AIChE Journal*, 40:1093–1104, 1994.

[17] E. Delnoij, J. A. M. Kuipers, and W. P. M. van Swaaij. A three-dimensional CFD model for gas-liquid bubble columns. *Chemical Engineering Science*, 54:2217–2226, 1999.

[18] E. I. V. van den Hengel, D. Darmana, N. G. Deen, and J. A. M. Kuipers. Large eddy simulation of a bubble column reactor using the Euler-Lagrange approach. Davos, Switzerland, May 25-30 2003. Computational Fluid Dynamics in Chemical Reaction Engineering III.

[19] S. Láin and M. Sommerfeld. LES of gas-liquid flow in a cylindrical laboratory bubble column. Yokohama, Japan, May 30-June 4 2004. 5th International Conference on Multiphase Flow, ICMF'04. Paper No. 337.

[20] J. Smagorinsky. General circulation experiment with the primitive equations. *Monthly Weather Review*, 91:99–165, 1963.

[21] R. B. Bird, W. E. Stewart, and E. N. Lightfoot. *Transport Phenomena*. John Wiley and Sons, second edition, 2002.

[22] B. P. B. Hoomans, J. A. M. Kuipers, W. J. Briels, and W. P. M. Van Swaaij. Discrete particle simulation of bubble and slug formation in a two-dimensional gas-fluidised bed: A hard-sphere approach. *Chemical Engineering Science*, 51(1):99–118, 1996.

[23] M. P. Allen and D. J. Tildesley. *Computer Simulation of Liquids*. Oxford Science Publications, 1987.

[24] J. Centrella and J. R. Wilson. Planar numerical cosmology. II. the difference equations and numerical tests. *Astronomy & Astrophysics Journal Supplement Series*, 54:229–249, 1984.

[25] S. Balay, K. Buschelman, W. D. Gropp, D. Kaushik, M. Knepley,

L. C. McInnes, B. F. Smith, and H. Zhang. PETSc home page. http://www.mcs.anl.gov/petsc, 2001.

[26] J. H. Ferziger and M. Peric. *Computational Methods for Fluid Dynamics*. Springer, 1999.

[27] B. H. Hjertager. Computational fluid dynamics (CFD) analysis of multiphase chemical reactors. *Trends in Chemical Engineering*, 4:44–92, 1998.

[28] J. A. M. Kuipers, K. J. van Duin, F. P. H. van Beckum, and W. P. M. van Swaaij. Computer simulation of the hydrodynamics of a two dimensional gas-fluidized bed. *Computational Chemical Engineering*, 17:839, 1993.

[29] K. R. Westerterp, W. P. M. van Swaaij, and A. A. C. M. Beenackers. *Chemical Reactor Design and Operation*. John Wiley & Sons, 1998.

# 4

# Chemisorption of $CO_2$ in $NaOH$: a numerical and experimental study[§]

*"The meeting of two personalities is like the contact of two chemical substances: if there is any reaction, both are transformed."* - Carl Jung


## Abstract

*This chapter describes simulations that were performed with an Euler-Lagrange model that takes into account mass transfer and chemical reaction reported by Darmana et al. [3] (see chapter 3). The model is used to simulate the reversible two-step reactions found in the chemisorption process of $CO_2$ in an aqueous $NaOH$ solution in a lab-scale pseudo-2D bubble column reactor. The computational results are compared with experimental data of bubble velocities, which were obtained with the use of Particle Image Velocimetry. Furthermore, the influence of the mass transfer and chemical reaction on the hydrodynamics, bubble size distribution and gas hold-up is also studied and compared with the experiment. It is found that the present model is able to predict the entire reaction process. The prediction of the hydrodynamics without mass transfer is found to be accurate. The model however seems to underpredict the overall mass transfer process, which we believe, can be attributed to the inaccuracy of the mass transfer closure being used in the present study. Nevertheless, the trends of the influence of the mass transfer rate on the hydrodynamics have been successfully captured by the present model.*


[§]Based on: Darmana et al. [1, 2]

## 4.1 Introduction

Bubble columns reactors constitute one of the most significant reactor types for gas-liquid reactions. In order to improve the performance of this type of reactor detailed information on fluid flow, mass transfer and chemical reaction rates as well as the mutual interactions is crucial. However, due to its complexity the bubble column reactor is not yet well understood despite extensive research effort given in this area.
In the past decade, the reaction engineering community has been active in exploring the possibilities to utilize Computational Fluid Dynamics (CFD) in the modelling of multiphase reactors. However in most of the studies, mass transfer and chemical reaction are ignored amongst others due to excessive memory and computational power requirements. Research of multiphase CFD thus mainly focused on the modelling of the hydrodynamics of the reactors and improving the closures required by the model to achieve a better prediction of the hydrodynamics [4–10].
A few authors have tried to make a shortcut to the expensive CFD modelling of the multiphase reactors by reducing the degree of complexity into a steady state problem or solving the problem using a 1D or 2D model [11–13]. However, it has meanwhile become clear that the two-phase hydrodynamics of bubble column reactors can only be simulated with sufficient accuracy if a fully dynamic (transient) 3D model is used [4, 6, 10]. Hence steady state 1D or even 2D modelling will not be sufficient to properly capture the necessary details of the flow required to provide a basis for the incorporation of mass transfer and chemical reaction.
By employing a so called hybrid method, some authors tried to solve the problem by decoupling the interaction between hydrodynamics, mass transfer, chemical reactions and solve each sub-problem with a separate model. In those models, CFD is employed only for the hydrodynamic simulation, while the chemical reactions are accounted for in a custom-build compartmental model [14–17]. Since these methods essentially offer a compromise to cope with the necessity to get information on the mass transfer and chemical reaction process and the prohibitively expensive direct CFD calculation, it does not necessarily account for the interaction between hydrodynamics, mass transfer and chemical reactions. For example, the method does not incorporate back coupling from the mass transfer and chemical reaction phenomena to the hydrodynamics. This means a.o., that a fixed mean bubble size is used to calculate the specific surface area for mass transfer calculation. Due to an incorrect bubble size, the CFD prediction of other parameters needed in hybrid methods such as the integral gas hold-up and the slip velocity would not be accurate either, which eventually will deteriorate the overall predictive capabilities of the model for accounting for the mass transfer and chemical reaction process.
A full three-dimensional modelling, by accounting for all relevant phenomena such as hydrodynamics, mass transfer and chemical reaction in a single

model so far is only limited to a study of the effect of mass transfer on hydrodynamics during a limited time interval [18]. Recently Darmana et al. [3, 19] developed a method that can handle the hydrodynamics, mass transfer and chemical reactions prevailing in a bubble column based on the Euler-Lagrange model developed previously by Delnoij et al. [4,5] (see Chapter 3). The authors demonstrated that the fully transient, three-dimensional model is able to simulate a full process of $CO_2$ absorption in water for a lab-scale bubble column until saturation of the liquid prevails using a single state-of-the-art personal computer. Furthermore, they also used the model to simulate the chemisorption process of $CO_2$ in an aqueous $NaOH$ solution. However due to prohibitively long calculation time required to follow the complete reaction progress, the simulations were only carried out for a short time interval to get an impression of the effect of the reaction on the bubble size and hydrodynamics.
Darmana et al. [20] proposed a new algorithm to solve the Euler-Lagrange model in parallel (see chapter 5), which offers the possibility to perform calculations in a fraction of the time required for a serial calculation. In this chapter we use the new parallel algorithm to simulate a reversible two-step reaction system encountered in the chemisorption process of $CO_2$ gas in aqueous sodium hydroxide $(NaOH)$ solutions in a pseudo-2D lab-scale bubble column reactor. Specifically we investigate the applicability of the developed model to predict the full evolution of the hydrodynamics and all of the chemical species involved in the reaction. The simulation is carried out starting from a solution with a pH of $12.5$ until pH $\approx 7$. The influence of the reaction process on the hydrodynamics behavior is studied by comparing the simulation results with another simulation with the same geometry without mass transfer and chemical reactions. Furthermore, to validate the model the simulation results are compared with dedicated experimental measurements.

## 4.2 Chemisorption reaction

The chemisorption of $CO_2$ in aqueous alkaline solutions takes place via two reactions. Before these reactions can take place, $CO_2$ gas first has to absorb in water physically:

$$CO_2(g) \rightarrow CO_2(aq) \tag{4.1}$$

The elementary reactions than proceed as follows:

$$CO_2\,(aq) + OH^- \underset{k_{1,2}}{\overset{k_{1,1}}{\rightleftharpoons}} HCO_3^- \tag{4.2}$$

$$HCO_3^- + OH^- \underset{k_{2,2}}{\overset{k_{2,1}}{\rightleftharpoons}} CO_3^{2-} \tag{4.3}$$

where $k_{1,1}$ and $k_{1,2}$ respectively are the forward and backward rate constants for the first reaction while $k_{2,1}$ and $k_{2,2}$ represent the forward and backward rate constants for the second reaction. The reaction rates are consequently written as follows:

$$R_{1,1} = k_{1,1}\left[CO_2(aq)\right]\left[OH^-\right] \tag{4.4}$$
$$R_{1,2} = k_{1,2}\left[HCO_3^-\right] \tag{4.5}$$
$$R_{2,1} = k_{2,1}\left[HCO_3^-\right]\left[OH^-\right] \tag{4.6}$$
$$R_{2,2} = k_{2,2}\left[CO_3^{2-}\right] \tag{4.7}$$

The physico-chemical parameters that describe the chemisorption process used in this study are given in Appendix A.

## 4.3 Experiments

### 4.3.1 Experimental setup

The experiments are carried out in a laboratory scale bubble column (see Fig. 4.1). A pseudo-2D geometry is chosen to enable visualization of the flow structures and permit the determination of the bubble size distribution. The column has a width of $200\,\mathrm{mm}$, depth of $30\,\mathrm{mm}$ and height of $1500\,\mathrm{mm}$. The front, back and both side walls are made of $10\,\mathrm{mm}$ thick glass plates, while the top and bottom part are made of stainless steel. During the experiment the column is filled with liquid up to a level of $1000\,\mathrm{mm}$.
The bubbles are introduced into the column using a gas needle distributor system to ensure uniform bubble size and gas flow rate following the work of Harteveld et al. [21]. The gas phase is fed into the column via three different channels, which are individually controlled by mass flow controllers. Each channel is connected to a gas distributor, which is connected to seven gas needles. The gas distributor system has a total of $21$ needles located at the center of the bottom plate of the column with a square pitch of $5\,\mathrm{mm}$. At the top part of the column a pH meter, temperature sensor and gas flow meter are available to measure all relevant quantities during the experiment.
To investigate the influence of chemical reaction on the hydrodynamics, two types of experiments were carried out: with and without reaction. For further reference these cases are simply refer as E1 (experiment without reaction) and E2 (experiment with reaction). For E1, twice distilled water is used as the liquid phase, while pure nitrogen gas $(N_2)$ (purity $\geq 99.9\,\%vol$) is used as the gas phase. Furthermore for E2, a $NaOH$ solution with an initial pH of $12.5$ is used as the liquid phase with pure $CO_2$ (purity $\geq 99.7\,\%vol$) as the gas phase. The $NaOH$ solution was prepared by mixing twice distilled water with $NaOH$ grains in a separate stirred tank. Both the column and

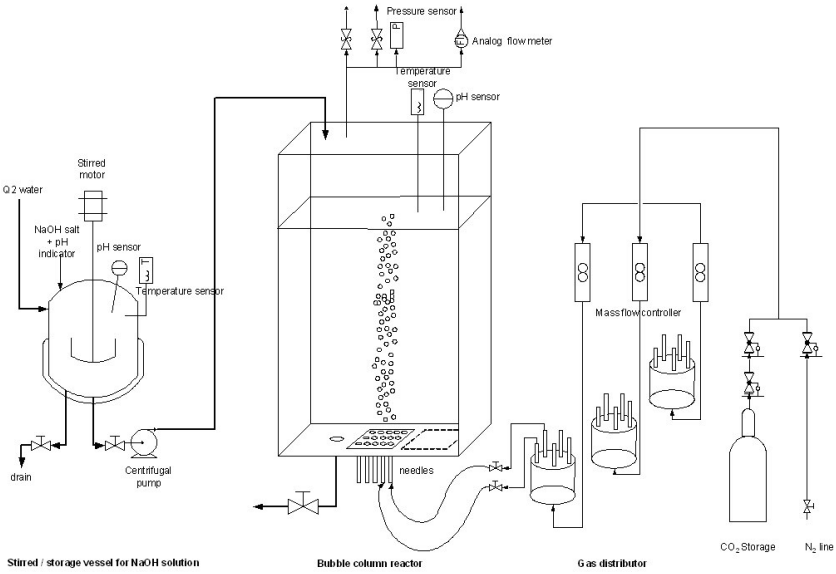


Schematic representation of the experimental setup.

Photo of (part of) the experimental setup.

**Figure 4.1:** *Experimental setup used in the present study.*

the stirred tank are completely isolated to prevent unwanted absorption of $CO_2$ from the atmosphere.
All experiments were carried out after the flow pattern was fully developed marked by the presence of a bubble plume meandering in a periodic fashion. For case E2 the experiment was started up by first using $N_2$ gas until the flow pattern was fully developed. The gas supply is then switched to $CO_2$. A new fully developed condition will be reached approximately $30\mathrm{s}$ after the gas supply was switched. This procedure was carried out during each start up since each gas needle channel required fine tuning to produce the desired (uniform) flow rate. The time needed for fine tuning is approximately $5\,\mathrm{min}$, which is of the same order of magnitude as the overall reaction process.

### 4.3.2 Particle image velocimetry (PIV)

The bubble velocity is measured by means of the Particle Image Velocimetry (PIV). With PIV, the column is illuminated from behind to obtain high contrast images of shadows of the bubbles against a bright liquid background (see Fig. 4.2). A high speed CMOS camera is then used to record images of the bubbles in the illuminated column.
Two subsequent images of the flow, separated by a short time delay, $\Delta t$, are divided into small interrogation areas. The volume-averaged displacement $\mathbf{s}_D(\mathbf{x},t)$ of the bubble images between the interrogation areas in the first and the second image is determined by means of a cross-correlation analysis. When the interrogation areas contain a sufficient number of bubble images, the cross-correlation consists of a dominant correlation peak embedded in a background of noise peaks.
The location of the tall peak, referred to as the displacement-correlation peak, corresponds to the bubble-image displacement. Provided that $\Delta t$ is sufficiently small, the velocity in the interrogation area, $\mathbf{v}(\mathbf{x},t)$ is then determined by dividing the measurement displacement by the image magnification $M$ and the time delay:

$$\mathbf{v}(\mathbf{x},t) = \frac{\mathbf{s}_D(\mathbf{x},t)}{M\Delta t} \tag{4.8}$$

The PIV camera used in the present study is a LaVision ImagePro 1200 HS camera equipped with a Nikkor $50\,\mathrm{mm}$ $1.8\,AF$ lens capable of recording up to $625\,\mathrm{Hz}$ at full frame resolution. The time delay $\Delta t$ is set to $5\,\mathrm{ms}$ while the magnification factor is $1360\,\mathrm{pix/m}$. A total of $2440$ pairs of images with a sampling frequency of $25\,\mathrm{Hz}$, which corresponds to $97.6\,\mathrm{s}$, is recorded in one measurement. The images are processed using the PIV software developed by Westerweel [22]. A $32 \times 32\,\mathrm{pix}^2$ interrogation area was used for the cross-correlation analysis in combination with a window shifting technique. A post processing step is carried out afterwards using a median test to remove

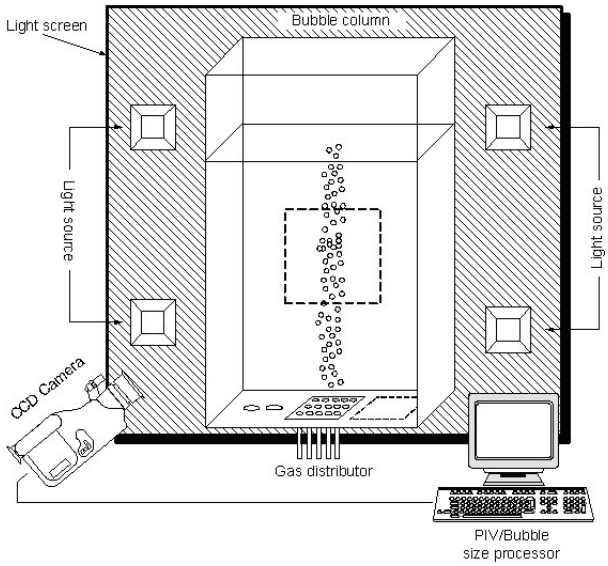


**Figure 4.2:** *Schematic representation of the experimental setup for the bubble velocity and size measurement.*

spurious vectors. Finally for the entire set of pictures, an ensemble average is calculated.

### 4.3.3 Integral gas hold-up and bubble size measurement

The integral gas hold-up, $(\varepsilon_I)$, is determined by measuring the difference between the height of the liquid level in the column with and without bubbles as follows:

$$\varepsilon_I = \frac{h - h_0}{h} \tag{4.9}$$

where $h$ and $h_0$ respectively are the height of the liquid surface with and without aeration.

The bubble size is measured by means of an image analysis technique. The experimental setup for the bubble measurement is shown in Fig. 4.2. Series of bubble images are recorded with a CCD camera (Dalsa Motion Vision CA-D6-0512W) with a resolution of $544 \times 516$ pix. To maximize the bubble contrast, the column is illuminated from behind (as for the bubble velocity measurement using PIV). The images are then analyzed offline by the Visi-Size Solo software (AEA Technology, England).

The bubble measurement software uses an algorithm to identify and measure the bubble size based on the intensity map of the image. A gray scale threshold is set to distinguish bubbles from the background liquid. The

threshold value is obtained manually by evaluating a sample image intensity histogram.
In order to identify the bubbles, the image is scanned from top to bottom, identifying dark segments on each line and associating them with segments from the previous line. When the bubble detection is completed, calculations are performed on each bubble to determine its diameter based on two different definitions, namely the area diameter $d_A$ and the perimeter diameter $d_P$. These diameters are respectively calculated as:

$$d_A = \frac{1}{M}\sqrt{\frac{4A_{pix}}{\pi}} \tag{4.10}$$

$$d_P = \frac{1}{M}\frac{P_{pix}}{\pi} \tag{4.11}$$

with $M$, $A_{pix}$ and $P_{pix}$ respectively are the magnification factor, the pixel area and the pixel perimeter.
The ratio $d_A/d_P$ measures the sphericity of the bubble with $d_A/d_P = 1$ reflecting a perfect circle. The VisiSize Solo software uses these parameters to distinguish clusters from individual bubbles. In the present study a magnification factor of $2350\,\mathrm{pix/m}$ is used, while a sphericity value of $0.675$ is used based on several data analysis, which pointed out that a large population of bubbles has a sphericity between $0.675$ and $0.75$. Finally, the Sauter mean diameter is determined as:

$$d_{32} = \frac{\Sigma_{k=1}^{n_b} d_k^3}{\Sigma_{k=1}^{n_b} d_k^2} \tag{4.12}$$

### 4.3.4 pH measurement

To measure the amount of hydroxyl ions being consumed during the chemisorption process, pH measurements were conducted. The pH electrode was positioned in the center of the column top in such a way that the electrode tip is $2\,\mathrm{cm}$ submerged. A pH glass electrode (Metrohm 6.0219.110) has been used in combination with a Metrohm 691 pH meter. Before usage, the electrodes were cleaned and filled with a $3\,\mathrm{M}$ KCl buffer solution and calibrated with buffer solutions of pH $7$, $9$ and $13$. The pH meter is connected to a computer via NI-DAQ data acquisition software from National Instruments where the pH evolution during the reaction is recorded in real time.

## 4.4 Discrete bubble model

A parallel version of the three-dimensional discrete bubble model (DBM) developed by Darmana et al. [3, 19, 20] (see chapter 3 and 5) is used to model the pseudo-2D bubble column. The liquid phase hydrodynamics are represented by the volume-averaged Navier-Stokes equation while the motion of

each individual bubble is tracked in a Lagrangian fashion. The interphase mass transfer is calculated for each bubble using the surface renewal theory, which takes into account chemically enhanced mass transfer through the enhancement factor $E$. The spatial distributions of chemical species residing in the liquid phase are computed from the (coupled) species conservation equations formulated in the Eulerian framework.

### 4.4.1 Bubble dynamics

The motion of each individual bubble is computed from the bubble mass and momentum equations while accounting for bubble-bubble and bubble-wall interactions via an encounter model similar in spirit to the model of Hoomans et al. [23]. The liquid phase contributions are taken into account by the interphase mass transfer rate $\dot{m}$ and the net force $\Sigma\mathbf{F}$ experienced by each individual bubble. For an incompressible bubble, the equations can be written as:

$$\rho_b \frac{dV_b}{dt} = \dot{m}_{\ell\to b} - \dot{m}_{b\to\ell} \tag{4.13}$$

$$\rho_b V_b \frac{d\mathbf{v}}{dt} = \Sigma\mathbf{F} - \left(\rho_b \frac{dV_b}{dt}\right)\mathbf{v} \tag{4.14}$$

where $\rho_b$, $V_b$ and $\mathbf{v}$ respectively represent the density, volume and velocity of the bubble. The interphase mass transfer rate $\dot{m}$ is calculated using a method, which will be described in section 4.4.4. The net force acting on each individual bubble is calculated by considering all the relevant fluid dynamical forces and modelled via separate, uncoupled contributions originating from gravity, pressure, drag, lift, virtual mass and wall forces:

$$\Sigma\mathbf{F} = \mathbf{F}_G + \mathbf{F}_P + \mathbf{F}_D + \mathbf{F}_L + \mathbf{F}_{VM} + \mathbf{F}_W \tag{4.15}$$

Expressions for each of these forces used in the present study can be found in Table 4.1. Note that the drag, lift and wall force closures used in the present study are obtained from Tomiyama et al. [24, 25]

### 4.4.2 Liquid phase hydrodynamics

The liquid phase hydrodynamics is represented by the volume-averaged Navier-Stokes equation system, which consists of the continuity and momentum equations. The presence of bubbles is reflected by the liquid phase volume fraction $\varepsilon_\ell$, the source term that accounts for the interphase mass transfer $\dot{M}$, and the interphase momentum transfer $\Phi$ :

$$\frac{\partial}{\partial t}\left(\varepsilon_\ell \rho_\ell\right) + \nabla\cdot\varepsilon_\ell\rho_\ell\mathbf{u} = \left(\dot{M}_{b\to\ell} - \dot{M}_{\ell\to b}\right) \tag{4.16}$$

**Table 4.1:** *Overview of forces acting on bubble*

| **Force** | **Closure** |
|---|---|
| $\mathbf{F}_G = \rho_b V_b \mathbf{g}$ | $-$ |
| $\mathbf{F}_P = -V_b \nabla P$ | $-$ |
| $\mathbf{F}_D = -\frac{1}{2} C_D \rho_l \pi R_b^2 \left\|\mathbf{v}-\mathbf{u}\right\| (\mathbf{v}-\mathbf{u})$ | $C_D = \max\left[\min\left[\frac{16}{\mathrm{Re}}\left(1+0.15\mathrm{Re}^{0.687}\right), \frac{48}{\mathrm{Re}}\right], \frac{8}{3}\frac{\mathrm{E\ddot{o}}}{\mathrm{E\ddot{o}}+4}\right]$ |
| $\mathbf{F}_L = -C_L \rho_\ell V_b (\mathbf{v}-\mathbf{u}) \times \nabla \times \mathbf{u}$ | $C_L = \begin{cases} \min\left[0.288\tanh\left(0.121\mathrm{Re}\right), f(\mathrm{E\ddot{o}}_d)\right]; \mathrm{E\ddot{o}}_d < 4 \\ f(\mathrm{E\ddot{o}}_d); 4 < \mathrm{E\ddot{o}}_d \leq 10 \\ -0.29; \mathrm{E\ddot{o}}_d > 10 \end{cases}$ |
| | $f(\mathrm{E\ddot{o}}_d) = 0.00105\mathrm{E\ddot{o}}_d^3 - 0.0159\mathrm{E\ddot{o}}_d^2 - 0.0204\mathrm{E\ddot{o}}_d + 0.474$ |
| | $\mathrm{E\ddot{o}}_d = \frac{\mathrm{E\ddot{o}}}{E^{2/3}}\ ;\ E = \frac{1}{1+0.163\mathrm{E\ddot{o}}^{0.757}}$ |
| $\mathbf{F}_{VM} = -C_{VM}\rho_\ell V_b \left(\frac{D_b \mathbf{v}}{D_b t} - \frac{D_b \mathbf{u}}{D_b t}\right)$ | $C_{VM} = 0.5$ |
| $\mathbf{F}_W = C_W R_b \rho_\ell \frac{1}{D_{bw}^2} \left\|\mathbf{u}-\mathbf{v}\right\|^2 \cdot \mathbf{n}$ | $C_W = \begin{cases} \mathrm{e}^{(-0.933\mathrm{Eo}+0.179)} & 1 < \mathrm{Eo} < 5 \\ 0.0007\mathrm{Eo}+0.04 & \mathrm{Eo} \geq 5 \end{cases}$ |

$$\frac{\partial}{\partial t}\left(\varepsilon_\ell \rho_\ell \mathbf{u}\right) + \nabla \cdot \varepsilon_\ell \rho_\ell \mathbf{u}\mathbf{u} = -\varepsilon_\ell \nabla P - \nabla \cdot \varepsilon_\ell \tau_\ell + \varepsilon_\ell \rho_\ell \mathbf{g} + \Phi \tag{4.17}$$

where $\mathbf{g}$ is the gravity constant, $\rho_\ell$, $\mathbf{u}$ and $P$ respectively the density, velocity and pressure for the liquid phase. Both phases are assumed to be incompressible, which is a reasonable assumption considering the limited height of the simulated systems. The liquid phase stress tensor $\tau_\ell$ is assumed to obey the general Newtonian form given by:

$$\tau_\ell = -\mu_{\mathrm{eff},\ell}\left[\left(\left(\nabla \mathbf{u}\right) + \left(\nabla \mathbf{u}\right)^T\right) - \frac{2}{3}\mathbf{I}\left(\nabla \cdot \mathbf{u}\right)\right] \tag{4.18}$$

where $\mu_{\mathrm{eff},\ell}$ is the effective viscosity. In the present model the effective viscosity is composed of two contributions, the molecular viscosity and the turbulent viscosity:

$$\mu_{\mathrm{eff},\ell} = \mu_{\mathrm{L},\ell} + \mu_{\mathrm{T},\ell} \tag{4.19}$$

where the turbulent viscosity $\mu_{\mathrm{T},\ell}$ is calculated using the sub-grid scale (SGS) model of Vreman [26]:

$$\mu_{\mathrm{T},\ell} = 2.5\rho_\ell C_S^2 \sqrt{\frac{B_\beta}{\alpha_{ij}\alpha_{ij}}} \tag{4.20}$$

where $C_s$ is a model constant with a typical value of 0.1, $\alpha_{ij} = \partial u_j / \partial x_i$, $\beta_{ij} = \Delta_m^2 \alpha_{mi}\alpha_{mj}$ and $B_\beta = \beta_{11}\beta_{22} - \beta_{12}^2 + \beta_{11}\beta_{33} - \beta_{13}^2 + \beta_{22}\beta_{33} - \beta_{23}^2$. $\Delta_i$ is the filter width in the $i$ direction.

It was decided to use the turbulent model proposed by Vreman rather than the standard Smagorinsky model introduced in Chapter 3, as it inherently accounts for reduced energy dissipation in near-wall regions. In case of a pseudo-2D column, the entire column can be considered to be a near-wall

region. It was found that the model of Vreman outperforms the Smagorinsky model in this case.

### 4.4.3 Chemical species

The fraction of a chemical species $j$ in the liquid mixture is represented by mass fraction $Y_\ell^j$ . The presence of various chemical species is accounted for through a transport equation for each species given by:

$$\frac{\partial}{\partial t}\left(\varepsilon_\ell \rho_\ell Y_\ell^j\right) + \nabla \cdot \left(\varepsilon_\ell \left(\rho_\ell \mathbf{u} Y_\ell^j - \Gamma_{\text{eff}}^j \nabla Y_\ell^j\right)\right) = \left(\dot{M}_{b\to\ell}^j - \dot{M}_{\ell\to b}^j\right) + \varepsilon_\ell S^j \tag{4.21}$$

where $S^j$ is the source term accounting for production or consumption of species $j$ due to homogenous chemical reactions and $\Gamma_{\text{eff}}^j$ a transport coefficient defined by:

$$\Gamma_{\text{eff}}^j = \frac{\mu_{\text{eff},\ell}}{\text{Sc}^j} \tag{4.22}$$

where $\text{Sc}^j$ is the Schmidt number of species $j$ defined as:

$$\text{Sc}^j = \frac{\mu_{L,\ell}}{\rho_\ell D^j} \tag{4.23}$$

where $D^j$ is the diffusivity of species $j$.
Changes in temperature as a result of the chemical reactions are not included in the current model, since no changes in the recorded temperature were observed during the experiment starting with pH$= 12.5$. Furthermore by using the method presented by Vas Bath [27], temperature rise at the bubble interface due to absorption and reaction during the residence time of $10\,\text{s}$ is estimated around $0.07\,\text{K}$ which confirms that the influence of temperature during the reaction can safely be ruled out.

### 4.4.4 Mass transfer

The interphase mass transfer of a bubble with radius $R_b$ is considered to be driven by the mass fraction gradient. The mass fraction of a chemical species $j$ in the liquid bulk and bubble are represented by $Y_\ell^j$ and $Y_b^j$ respectively, while the value of both quantities at each side of the bubble-liquid interface is given by $Y_\ell^{j*}$ and $Y_b^{j*}$.
The mass transfer rate of a bubble due to a mass fraction gradient of species $j$ is represented as:

$$\dot{m}_b^j = E k_l^j A_b \rho_\ell \left(Y_\ell^{j*} - Y_l^j\right) \tag{4.24}$$

where $E$ is the mass transfer enhancement factor due to chemical reactions, $A_b$ is the interfacial area of the bubble and $k_l^j$ is the mass transfer coefficient

for chemical species $j$.
The mass fraction on the liquid side of the interface can be determined using Henry's law:

$$Y_l^{j*} = H^j Y_b^{j*} \frac{\rho_b}{\rho_\ell} \tag{4.25}$$

where $H^j$ is the Henry constant for species $j$.
The mass transfer enhancement factor can be calculated numerically by solving the (coupled) diffusion equations in the boundary layer surrounding the bubbles. The coupled diffusion equations should be solved for each individual bubble; hence, in the case where a large number of bubbles are present, this method becomes impractical. In the present study, an approximate solution for the enhancement factor, in the form of a simple algebraic equation as a function of Hatta number, is therefore used instead (see Appendix A.4).

## 4.5 Simulations

Both of the E1 and E2 cases explained in section 4.3 are modeled using the DBM which we refer to as case S1 and S2 respectively. The applied computational grid consists of $80 \times 12 \times 400$ cells and the time steps, $(\delta t_{flow}, \delta t_{spec})$ are set to $1 \times 10^{-3}$ s while for bubble tracking $(\delta t_{bub})$ a time step of $1 \times 10^{-4}$ s is used. The bubbles are introduced into the column at $21$ positions according to the geometry of the experimental setup using an initial bubble size of $5.5$ mm. The boundary conditions are imposed using the flag matrix concept of Kuipers et al. [28] as is shown in Fig. 4.3. The definition of each boundary condition is given in Table 4.2.
To ensure that the simulations have exactly the same initial condition with respect to the hydrodynamics, case S2 was started from the solution of case S1 at $t = 10$ s. Five species transport equations are used to compute the mass fractions of $CO_2(aq)$, $OH^-$, $HCO_3^-$, $CO_3^{2-}$ and $H_2O$ as the background species. The initial mass fraction of each species involved in the reactions was set to $1 \times 10^{-50}$ except for $OH^-$ which is computed from the initial pH of $12.5$, and $H_2O$ which is calculated as:

$$Y_{H_2O} = 1 - \left( Y_{CO_2} + Y_{OH^-} + Y_{HCO_3^-} + Y_{CO_3^{2-}} \right) \tag{4.26}$$

The simulations were carried out in parallel using $16$ processors on an in-house Linux cluster (AMD opteron dual core 1.8GHz with 2GB of RAM for each core). In general, the simulation with reaction required $24$ h of calculation time for every $4$ s simulation.

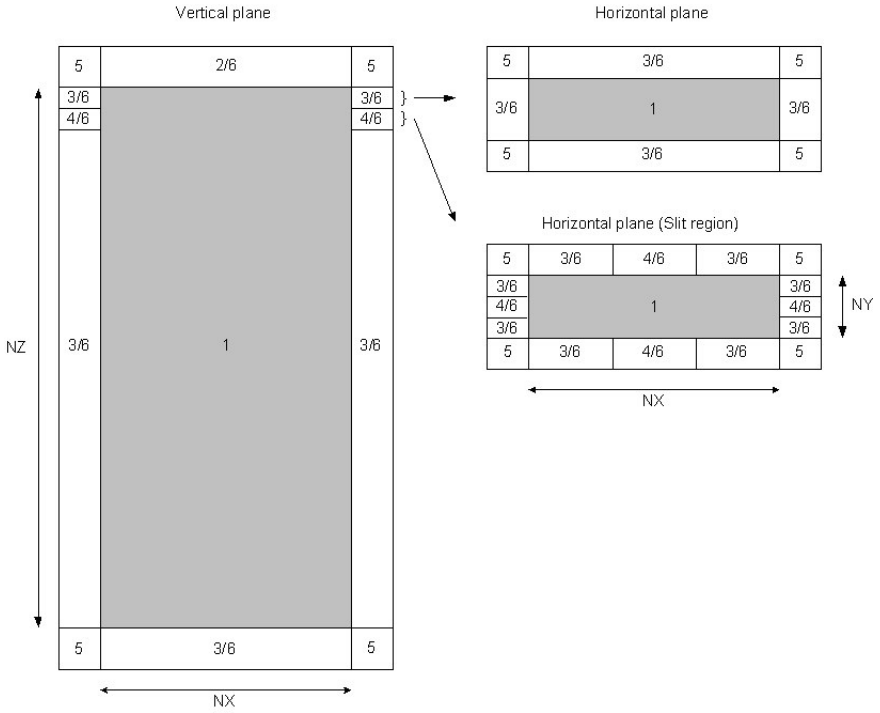


**Figure 4.3:** *Boundary conditions imposed in the discrete bubble model. The vertical plane is at $j = NY/2$ while the slits are defined at $k = NZ - 1$.*

**Table 4.2:** *Cell flags and corresponding cell types used in defining boundary conditions for the Navier-Stokes equations.*

| Flag | Boundary conditions |
|---|---|
| 1 | Interior cell, no boundary conditions specified |
| 2 | Impermeable wall, free slip boundary |
| 3 | Impermeable wall, no slip boundary |
| 4 | Prescribed pressure cell, free slip boundary |
| 5 | Corner cell, no boundary conditions specified |
| 6 | Neumann boundary for species transport $(\nabla Y^j = 0)$ |

## 4.6 Results and discussion

In this section the results obtained from the DBM model will be presented and compared with the experimental data. First, the overall reaction progress will be given. Then the influence of the mass transfer and chemical reaction on respectively the hydrodynamics, gas holdup, bubble meandering behavior and averaged velocities will be addressed.

### 4.6.1 Reaction progress

The chemisorption process is simulated using the DBM model (i.e. case S2). Pure $CO_2$ gas is fed at a superficial velocity of $7 \times 10^{-3}$ m/s into the column filled with a $NaOH$ solution with an initial pH of $12.5$. During their journey from the gas inlet to the liquid surface, the bubbles will transfer some of the $CO_2$ gas to the liquid through the interphase mass transfer mechanism which subsequently initiates the reversible two-step reactions as given in Eqs. 4.2 and 4.3.

Figure 4.4 (top) shows the evolution of the species concentrations during the chemisorption process predicted by DBM while Fig. 4.4 (bottom) shows the corresponding pH evolution. In the beginning of the process, all the dissolved $CO_2$ gas immediately reacts with hydroxide ions $(OH^-)$ and is converted into carbonate $(CO_3^{2-})$. Hence, only small traces of dissolved $CO_2$ gas located near the bubbles are observed while the concentration of bicarbonate $(HCO_3^-)$ in the entire column is negligible. Figure 4.5 shows typical snapshots resulting from DBM simulations for the chemisorption process at this stage consisting of the bubble size (and positions), gas velocity, liquid velocity field, and concentration field of the dissolved $CO_2$ gas, hydroxide, carbonate and bicarbonate. As can be seen from this figure, only a very small amount of $CO_2$ gas is found in the vicinity of the bubbles. The resulting reaction products are immediately transported by the convective flow field to the entire region of the column. As all of the species are transported with the same liquid velocity field, the concentration profiles of the hydroxide, carbonate and bicarbonate are similar.

At about $80$ s after the start of the reaction, the carbonate concentration reaches a maximum and subsequently starts to decrease. Meanwhile, the bicarbonate concentration starts to increase. This event is reflected in the pH curve by a change in the slope, which is caused by the shift of equilibrium of the first reaction (Eq. 4.3) which happens around pH $11$ in favor of bicarbonate. After about $200$ s, bicarbonate reaches the initial $OH^-$ concentration while carbonate is almost entirely consumed. At this moment, the first reaction (eq. 4.2) is shifted towards dissolved $CO_2$ and another obvious change in pH slope is observed, which happens around pH $7.5$. After this stage, the chemical reaction rates diminish and the dissolved $CO_2$ gas starts to accumulate in the entire column (see typical snapshots in Fig. 4.6).

By comparing the pH evolution predicted by the present model and the experimental measurement shown in Fig. 4.4 (bottom) we can conclude that the present model is able to predict the chemical evolution quite well. Qualitatively speaking, the predicted pH evolution resulting from the present model shows a similar trend and change in slope as observed in the experiment. Quantitatively however, the pH evolution predicted by the present model is somewhat lagging behind compared to the experimental one by about $15\%$. We believe that it can be attributed to the inaccuracy in the mass transfer correlation that is used in the present study, which under-

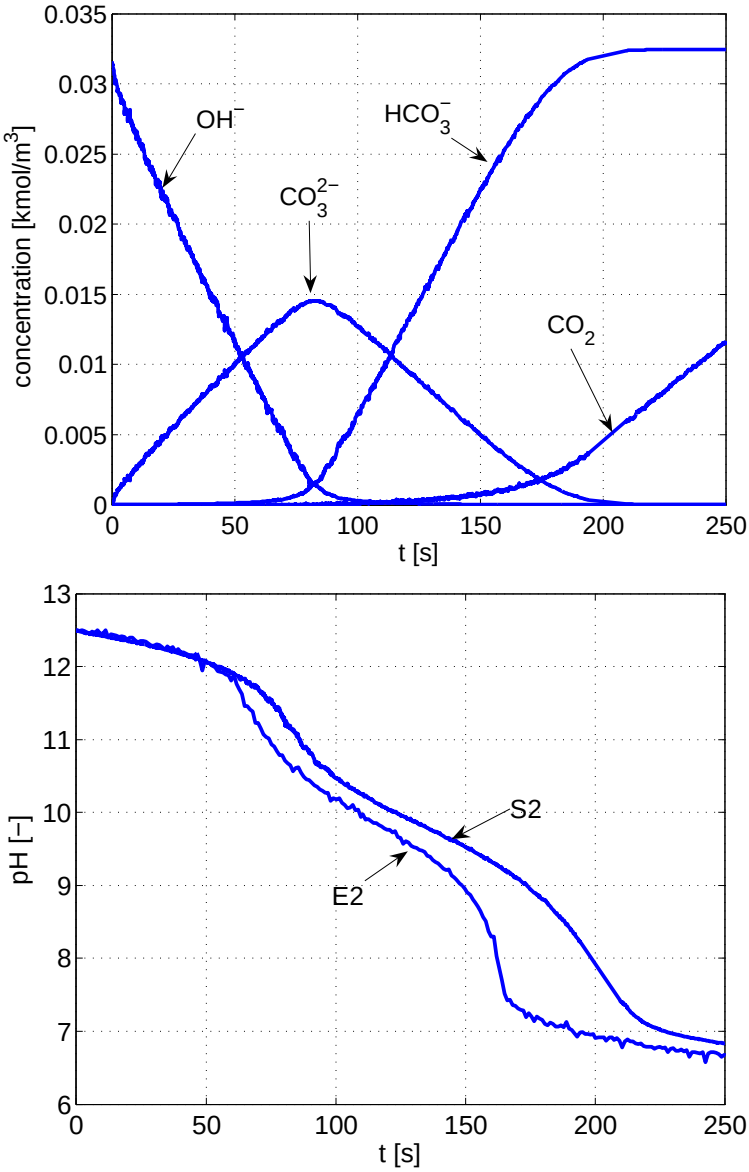


**Figure 4.4:** *Concentration history of each chemical species involved in the chemisorption process resulting from the DBM simulation (top) and the corresponding pH evolution (bottom) at width* $x/W = 0.5$*, depth* $y/D = 0.5$ *and height* $z/H = 0.95$*.*

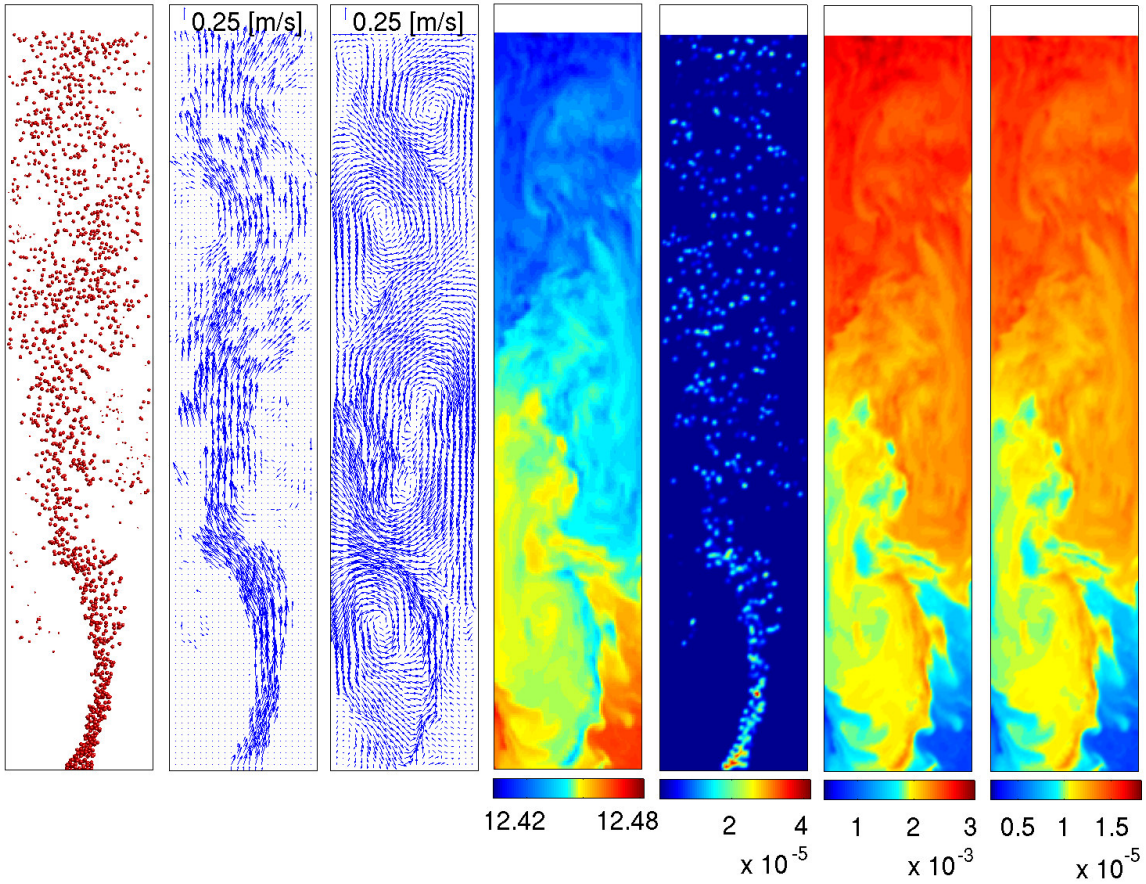


**Figure 4.5:** *Instantaneous solution* $10\ \mathrm{s}$ *after the* $CO_2$ *gas is introduced. From left to right: bubble positions, gas velocity, liquid velocity, pH, respectively concentration of dissolved* $CO_2$, $HCO_3^-$, $CO_3^{2-}$ $[\mathrm{kmol/m^3}]$.

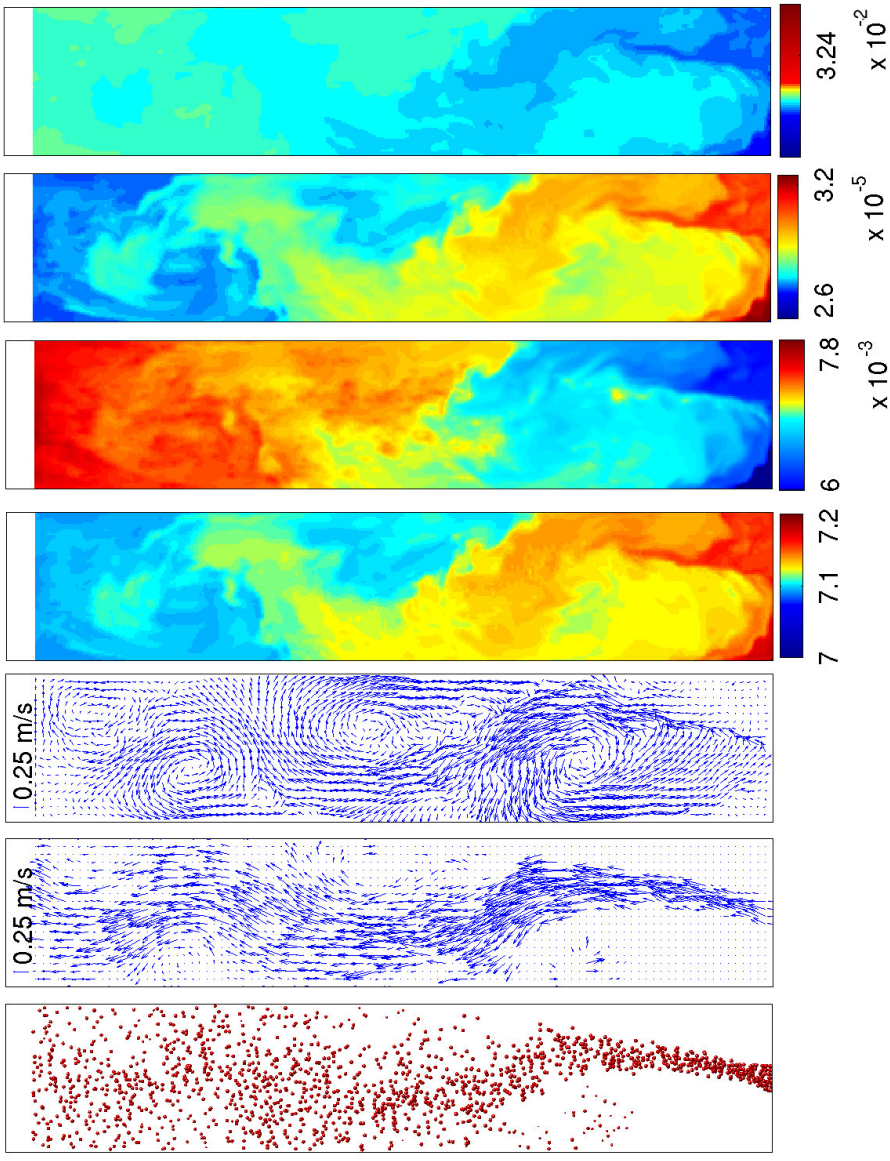


**Figure 4.6:** *Instantaneous solution* 220 s *after the* $CO_2$ *gas is introduced. From left to right: bubble positions, gas velocity, liquid velocity, pH, respectively concentration of dissolved* $CO_2$, $HCO_3^-$, $CO_3^{2-}$ $[\mathrm{kmol/m^3}]$.

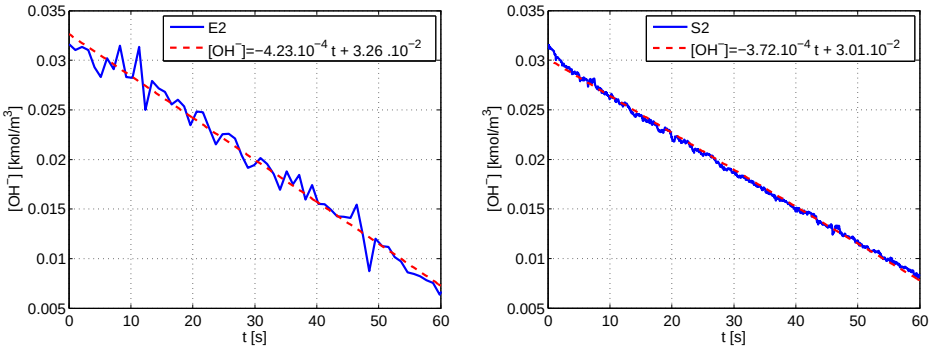


Experiment DBM simulation

**Figure 4.7:** *Evolution of $OH^-$ concentration during the early stage of the reaction. The slope is estimated using linear regression showing the rate of $OH^-$ consumption which proportional with total mass transfer rate from all bubble to the liquid.*

predicts the overall mass transfer rate.
To support this argument, the overall mass transfer rate for both simulation and experimental data is compared. By assuming that the enhancement correlation used in the present study is accurate (Westerterp et al. [29] suggests an accuracy within $10\%$), we can estimate the total mass transfer rate of $CO_2$ gas from the rate of consumption of the hydroxide during the early stages of the reaction. At this stage the dissolved $CO_2$ immediately reacts with $OH^-$ to produce carbonate; thus the rate of the $CO_2$ gas transferred to the liquid is proportional to the rate of $OH^-$ being consumed. Figure 4.7 shows the estimation of the mass transfer rate from the experimental measurement (top) and simulation result (bottom). As can be seen, the total mass transfer rate estimated by the present model underpredicts the experimental data by about $14\%$, which is close to the time delay of the reaction between the present model and experimental observation.

### 4.6.2 Flow structures

Some experimentally recorded images along with the corresponding instantaneous and time averaged gas velocity maps for case E1 and E2 are shown in Fig. 4.8. As can be seen, the bubbles travel from the inlet to the top region in a snake-like motion. However, as the bubbles approach the column surface, they move in the lateral direction. Several large vortical structures are present in the column at any given time. The vortices are stacked in the axial direction separated by the bubble plume. Some of the bubbles are dragged along leaving the main bubble plume and are trapped in the vor-

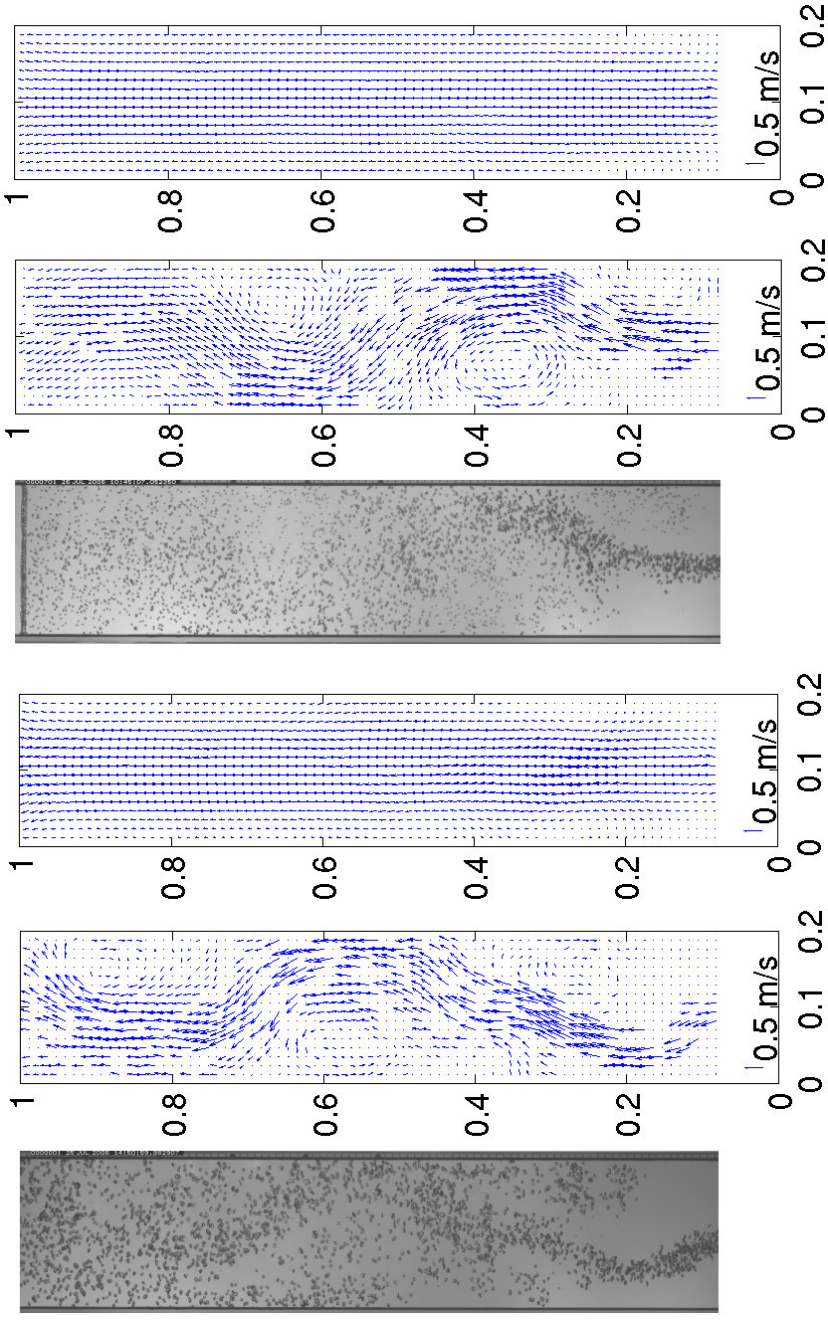


**Figure 4.8:** *Instantaneous bubbles position showing the flow structures observed in the experiment, the corresponding instantaneous gas velocity resulting from PIV and time-averaged gas velocity. Left: Nitrogen gas in water (E1); Right: Carbon dioxide gas in sodium hydroxide solution (E2),* $40\,\mathrm{s}$ *after gas was switched from* $N_2$ *to* $CO_2$.

tices for some time until they rejoin the plume. The direction of the vortices is clockwise when the the plume is on their left side or counter clockwise otherwise. The vortices start to form close to the surface region in a alternating fashion on each side of the column. The vortices are getting stronger as they travel to about halfway the column and start to loose their energy as they approach the column base until they finally disapear.
Using PIV, the bubbles velocities have been measured. The instantaneous velocity maps clearly reveal the meandering behavior of the bubble plume with high upward velocities present in the core of the bubble plume while other bubbles move along with the vortices with a tendency to move downward. The corresponding ensemble averaged bubble velocity map shows different structures compared to the instantaneous ones. Here, the meandering bubble behavior is no longer visible, instead the bubbles averaged velocities display a uniform upward profile with the central region showing higher velocities than the wall region.
A variation in flow structures is observed in case E2. Here due to (chemically enhanced) mass transfer, the bubble size rapidly decreases as the bubbles ascend toward the liquid surface. Bubbles that are trapped in the vortices have a longer residence time compared to those that travel in the core of the plume. This makes that the bubbles in the vortices have even smaller sizes and for some bubbles the contact time is long enough to achieve complete absorption.
The mass transfer also affects the rise velocity of the bubbles. From the instantaneous bubble velocities we can clearly see that compared to case E1 where bubbles are rising at relatively constant velocities, in case E2 the bubble rise velocities are initially high after leaving the inlet and gradually slow down as the bubbles approach the liquid surface. The corresponding ensemble averaged bubbles velocities show a similar pattern where the velocities are significantly lower compared to case E1. Furthermore the averaged velocity profiles are slightly different; here the upward velocity in the middle of the column is less pronounced compared to case E1.
As the reaction continues, the mass transfer rate from the bubbles to the liquid is decreasing. The bubble size distribution along with the bubble rise velocity gradually increases again. At the end of the reaction, similar flow fields like in case E1 are observed. If we continue the process until the liquid is saturated with dissolved $CO_2$, bubble coalescence starts to take place producing big bubbles with an observed diameter up to $2\,\mathrm{cm}$. In this situation the bubble column regime has transformed from the homogeneous to the heterogeneous regime.
Fig. 4.9 shows the instantaneous simulation results for case S1. Nitrogen gas at a superficial velocity of $7\times10^{-3}\mathrm{m/s}$ was injected into initially quiescent water. Shortly after the bubbles are introduced into the column, a bubble plume rises through the column and forms a typical mushroom like shape. The motion of the bubbles induces the bulk liquid to move in the upward direction at the center of the column and in the downward direction close

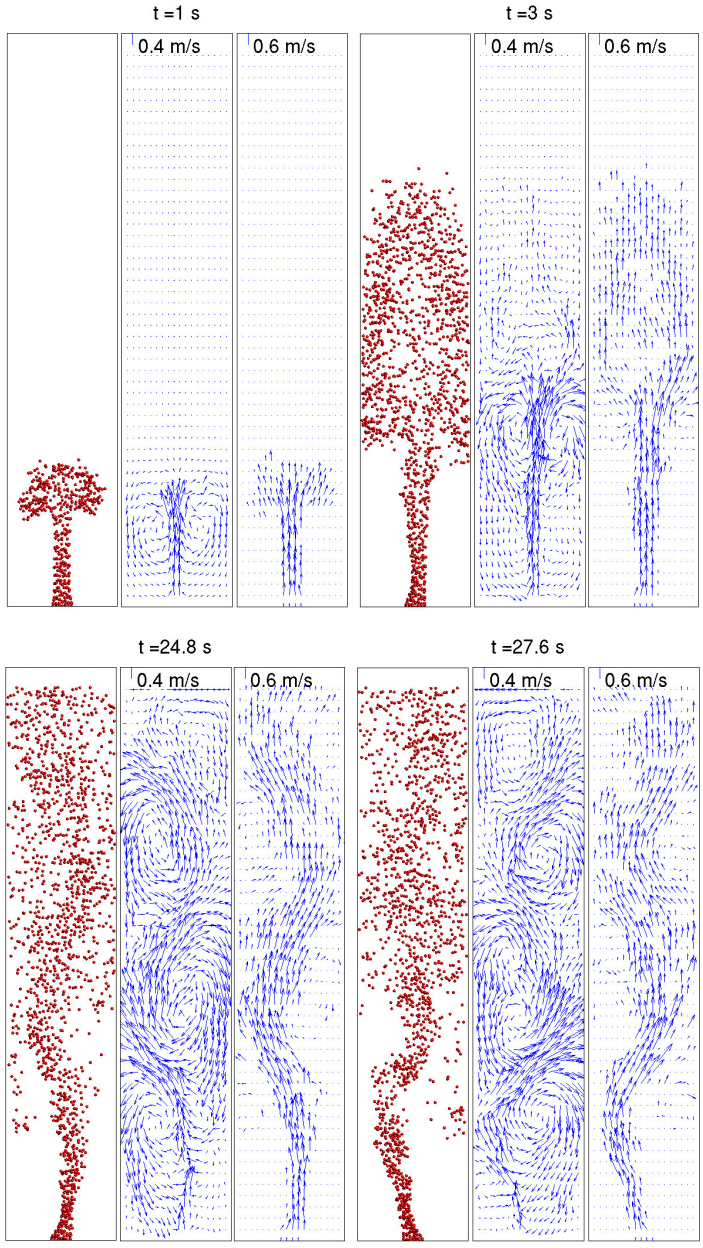


**Figure 4.9:** *Series of snapshots showing bubble position (left), liquid velocity (center) and gas velocity (right) obtained from case S1. The first row shows the structures during the startup period while the second row shows the flow structures that are half a bubble plume meandering period apart. The velocity plots are in the plane of* $y/D = 0.5$.

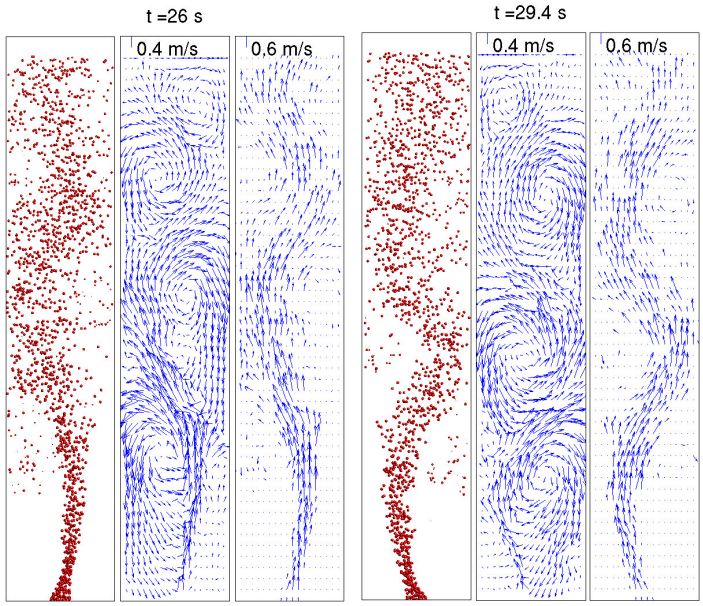


**Figure 4.10:** *Series of snapshots showing bubble position (left), liquid velocity (center) and gas velocity (right) obtained from simulation case S2. The time difference between the two snapshots corresponds to half a bubble plume meandering period. The velocity plots are in the plane of* $y/D = 0.5$.

to the sidewalls. The liquid motion interacts with the bubbles and thereby disturbs the movement of the bubble plume.
The interaction between liquid and bubbles eventually results in a meandering bubble plume that moves periodically and multiple vortices stacked in the vertical direction of the column are developed. Just like in case E1, these vortices are generated close to the liquid surface alternatingly on each side of the column and move downward until they disappear near the bottom of the column. Bubbles are mainly moving in the core of the plume, however some of the bubbles are randomly trapped in the liquid vortices for quite some time until they are dragged back to the core of the plume. Comparing with the snapshots obtained from the experiment, we can conclude that the flow structures obtained from the simulations resemble the experimental observation very well.
Fig. 4.10 shows the instantaneous solution of case S2 during the early stage of the reaction process. As can be seen, the flow structures for the simulation with mass transfer and chemical reaction are similar to the case S1 (and also E1). Just like in the Case E2, the bubbles in case S2 also show a bubble sizes reduction due to the (chemically enhanced) mass transfer where bubbles at the top region are relatively smaller in size compared to the inlet

region. Furthermore, bubbles that are trapped in the vortices are smaller than those that move in the bubble plume core. Comparison with case E2 however, reveals a discrepancy in the bubble size distribution predicted by the model. The bubbles in the top region of the column seem to be bigger than the ones observed in the experiment.

### 4.6.3 Bubble sizes and Integral gas holdup

In the present model the size change for each bubble due to the mass transfer process can be tracked. By mapping the bubble size to a Eulerian grid we can investigate the spatial distribution of the bubble sizes. Figure 4.11 shows a typical instantaneous bubble size distribution and the corresponding bubble size map in the Eulerian frame. As can be seen from the figure, the bubble size is decreasing as a function of distance from the distributor. Furthermore we can also notice that the bubbles trapped in the vortices are significantly smaller compared to the ones inside the core of the bubble plume as has been observed in the experiment.
A more qualitative comparison between simulation results and experimental data is shown in Fig. 4.12. Here we can clearly see that the Sauter mean diameter resulting from the present model is decreasing with distance from the gas distributor. In the measurement, the bubbles are moving very closely up to the height of $z/H \approx 0.4$. The bubble size measurement for this region therefore becomes less reliable as most of bubbles are identified as clusters and thereby being rejected, resulting in a mean bubble size much smaller than it should be. However above $z/H = 0.4$ the measured bubble size is more reliable. Comparison between simulations and experimental data clearly shows that the present model overpredicts the bubble sizes. Furthermore, the slope of the bubble size reveals that the present model underpredicts the mass transfer rate compared to the experimental measurement.
Comparison of the integral gas holdup between the experimental measurement and prediction by the present model is shown in Table 4.3. As can be seen, the integral gas holdup is reduced when mass transfer is taken into account. The reduction is a direct consequence of the decrease in bubble volume resulting from the mass transfer. Hence, for higher mass transfer rate, the bubble volume is smaller and consequently the gas holdup. Comparison between simulation results and experimental measurement data shows that in the case without reaction, the present model is able to predict the gas holdup quite accurately. However when mass transfer is taken into account, the gas holdup is overpredicted, which is consistent with the overprediction of the bubble size distribution.

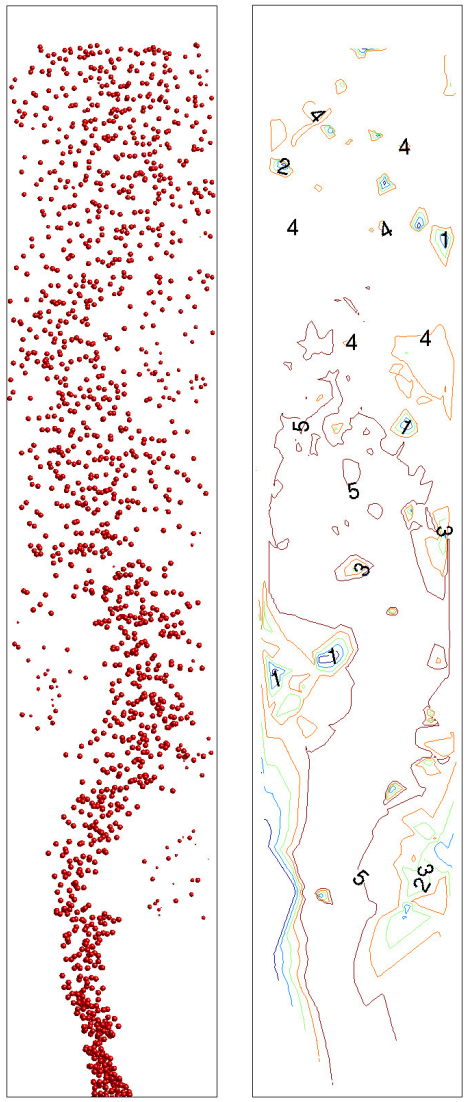


**Figure 4.11:** *Instantaneous bubble sizes distribution for case S2 (in* mm*),* 19.4 s *after the reactions begin; gas holdup=*1.6%*.*

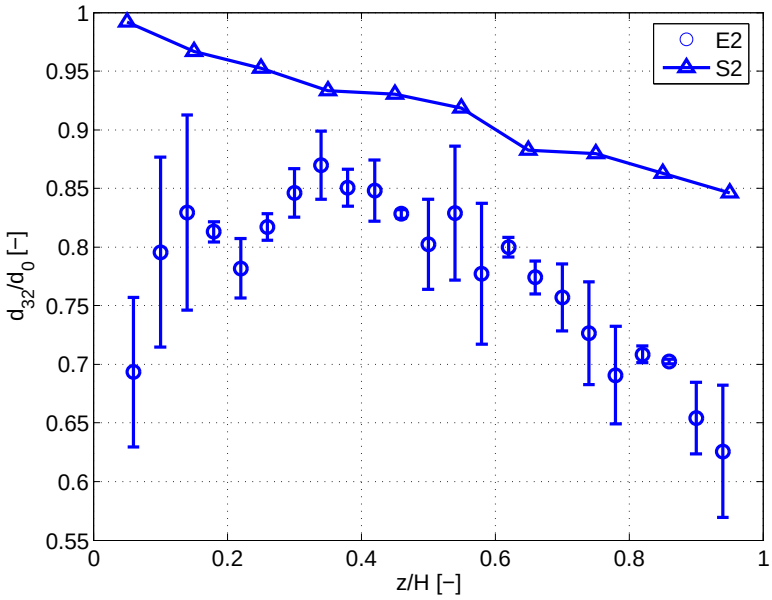


**Figure 4.12:** *Comparison of the Sauter mean diameter $d_{32}$ between measurement and current model prediction.*

**Table 4.3:** *Integral gas holdup, comparison between experiment and simulations*

| Case | Experiment (%) | Simulation (%) |
|---|---|---|
| 1 | 2.3 | 2.2 |
| 2 | 1.2 | 1.6 |

### 4.6.4 Bubble plume dynamics

The meandering behavior of the bubble plume is an important characteristic of a partially aerated pseudo-2D bubble column. This behavior however is difficult to reproduce in a numerical simulation and has become one of the key validation steps for a multiphase CFD model. In the previous section we have shown that the simulations indicate the existance of alternating vortical structures which are produced periodically, which induces the bubble plume meandering behavior. In this section this behavior will be quantified and compared with experimental data.
A time series of experimentally determined bubble velocity is presented in Fig. 4.13. The periodic meandering behavior is clearly visible. By comparing case E1 and E2 it is obvious that due to the mass transfer, the meandering period has become longer. Using Fast Fourier Transformations (FFT) we found that the meandering period for case E1 and E2 respectively amount $5.8\,\mathrm{s}$ and $10.2\,\mathrm{s}$.
The periodic meandering behavior is reproduced nicely by the present nu-

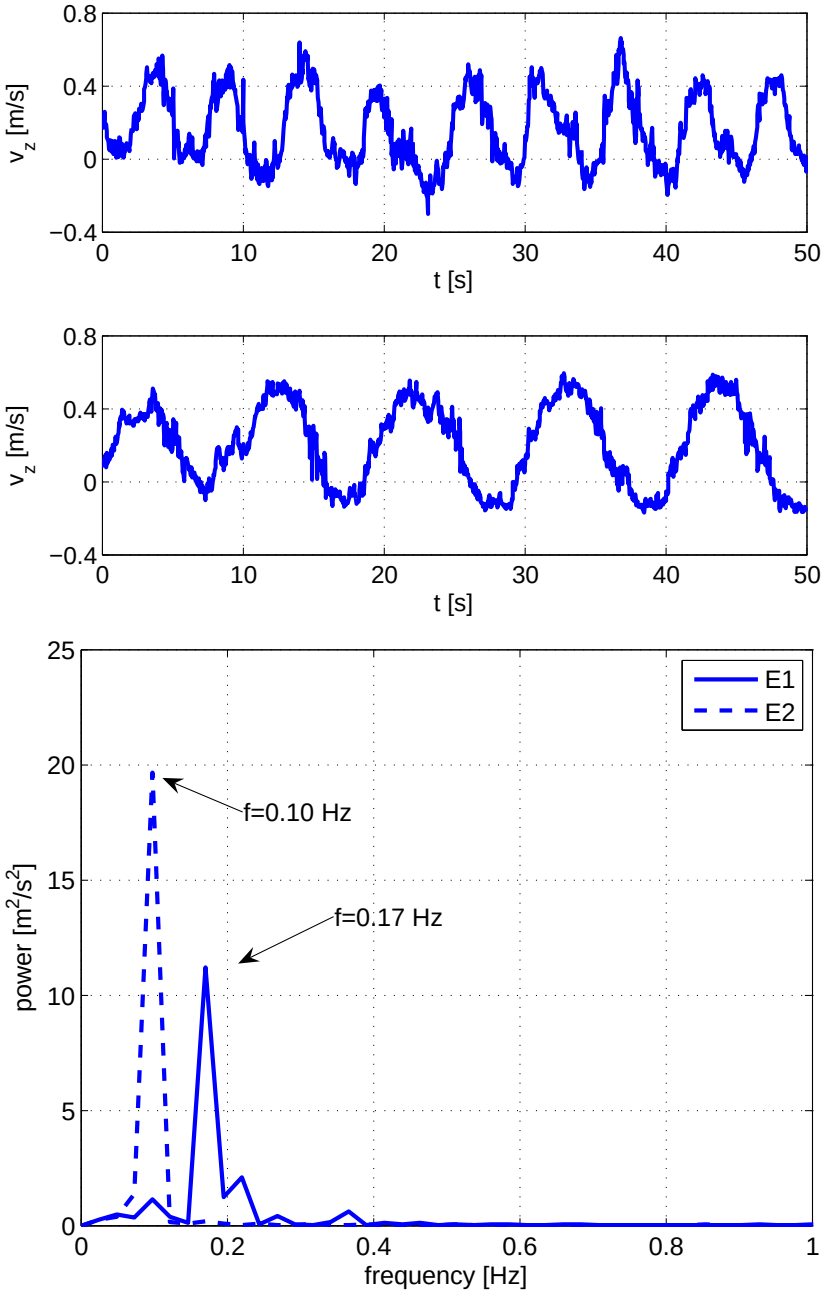


**Figure 4.13:** *Time history of the axial bubble velocity at* $x/W = 0.25; y/D = 0.5; z/L = 0.5$ *for case E1 (top) and E2 (middle). Bottom figure: the corresponding frequency domain for both cases showing the meandering frequency.*

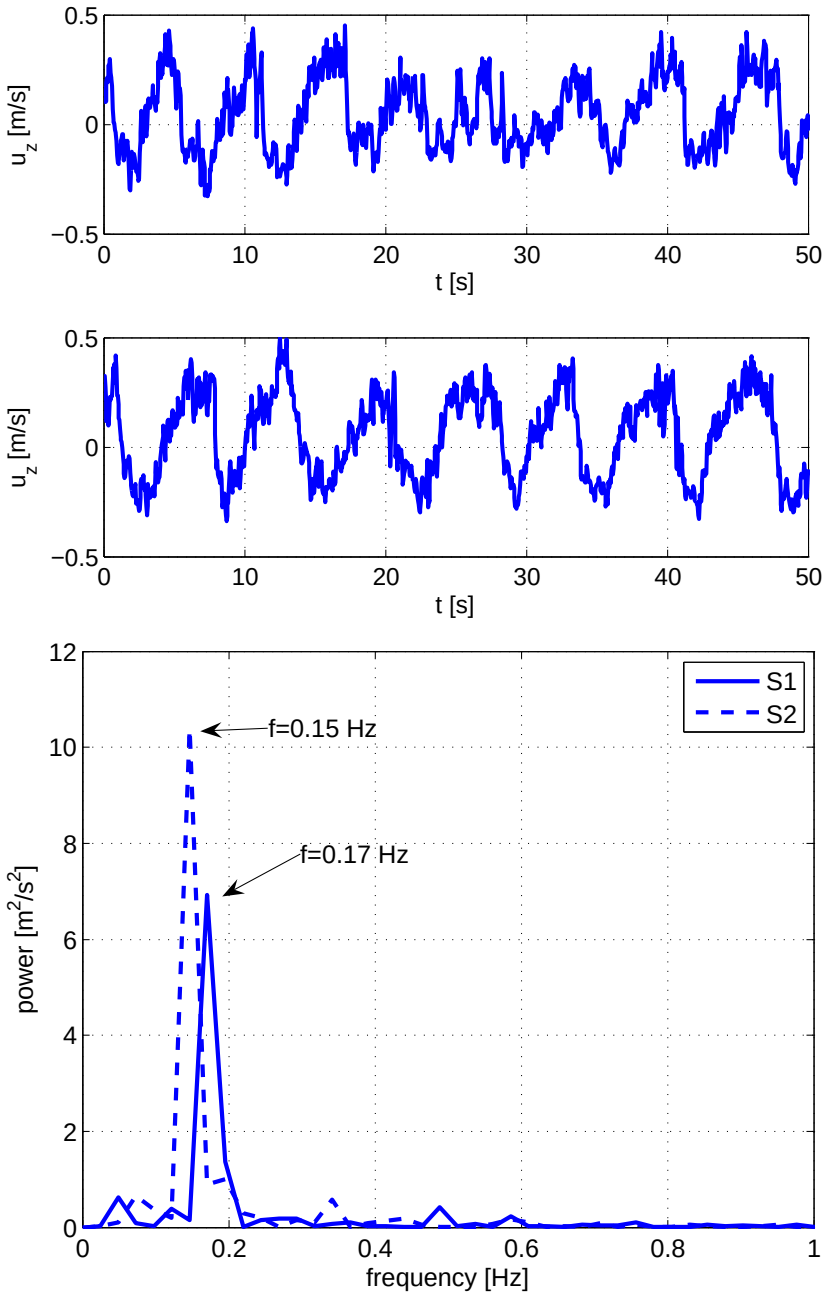


**Figure 4.14:** *Time history of the axial liquid velocity at $x/W = 0.25; y/D = 0.5; z/L = 0.5$ for case S1 (top) and S2 (middle). Bottom figure: the corresponding frequency domain for both cases showing the meandering frequency.*

merical simulations as can be seen in Fig. 4.14. Here we found that for case S1 and S2 the meandering period respectively are $5.8\,\mathrm{s}$ and $6.8\,\mathrm{s}$. Note that the period for case E1 and S1 is exactly the same which shows that the dynamic behavior for the case without mass transfer has been successfully captured. Just like in the experimental observation, the meandering period predicted by the simulation also decreases when the mass transfer is taken into account. However, here the period of case S2 is underestimated.
Buwa and Ranade [30] and Buwa et al. [7] investigated the influence of gas superficial velocities to the meandering period, they found that the meandering period is increased as the superficial gas velocity decreased. When mass transfer from bubbles to the liquid is accounted for, the effective superficial velocity is reduced. Thus, one can expect that the meandering period will increase as the mass transfer rate increases. In our case the underprediction of the meandering period can be related to the underprediction of the overall mass transfer rate.

### 4.6.5 Average velocity profile

Further quantitative comparison with the experimental data is carried out through the long term (i.e. the statistical averaged) quantities. In the present study the time-averaged mean velocity and velocity fluctuations of the simulation are calculated during a $t = 20 - 80\,\mathrm{s}$ interval and a $t = 20 - 95\,\mathrm{s}$ interval. The mean velocity is calculated as follows:

$$\overline{\mathbf{u}} = \frac{1}{N_t} \sum_{i=1}^{N_t} \mathbf{u}_i \tag{4.27}$$

where $N_t$ is the number of time steps used in the averaging.
The time-averaged mean bubble and liquid velocities profile as well as gas holdup for case S1 and S2 can be seen respectively in Figs. 4.15 and 4.16. As can be seen, the time-averaged quantities are completely different compared to the instantaneous data. The meandering flow profile has completely dissappeared and is replaced by a typical circulation pattern where the flow is going up in the center region of the column and going down near the walls. The averaged bubble velocity profile reveals that on average the bubbles are moving up in the entire column. However, the averaged bubble velocities are significantly higher in the center region of the column and lower close to the walls. The time-averaged gas holdup shows that statistically the bubbles are present in the entire top region of the column (i.e. at $z/H > 0.3$) while for the lower part of the column, the bubbles are more concentrated towards the central region of the column. In case S2, a similar situation is found. However, here the averaged bubbles velocities is more uniform (i.e. the bubble velocities in the middle are less dominant in comparison with case S1).
The comparison of the time-averaged velocity profiles is shown in Fig. 4.17.

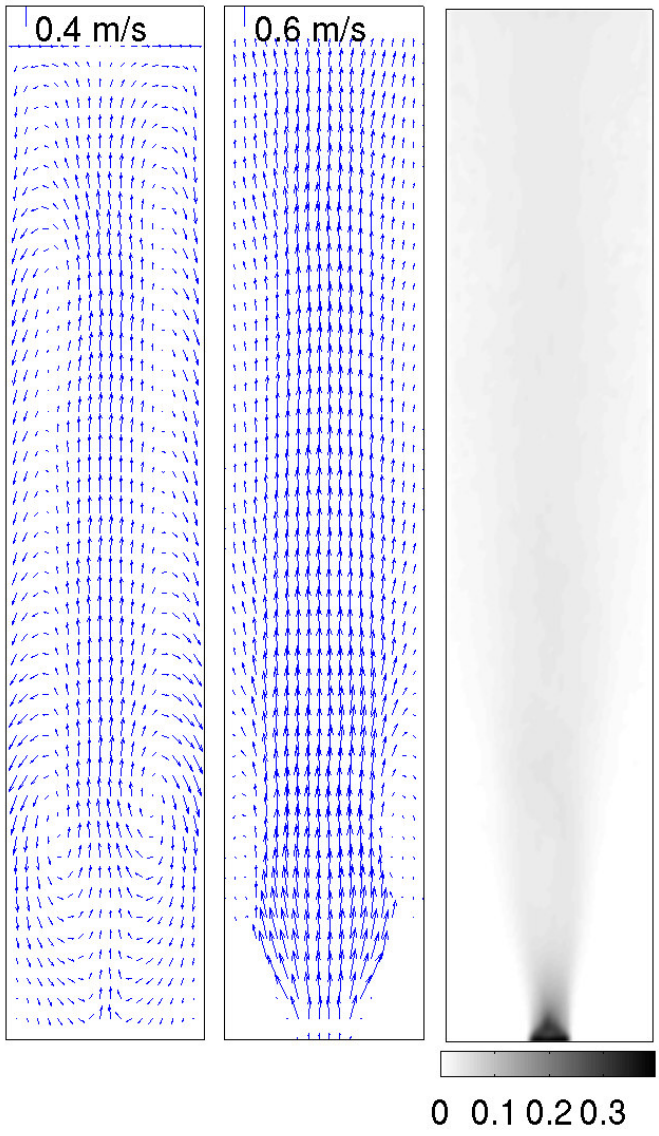


**Figure 4.15:** *Time-averaged liquid velocity (left), bubble velocity (center) and gas porosity (right) at* $y/D = 0.5$*. Case S1, averaging was carried out from* $t = 20 - 80\,\mathrm{s}$

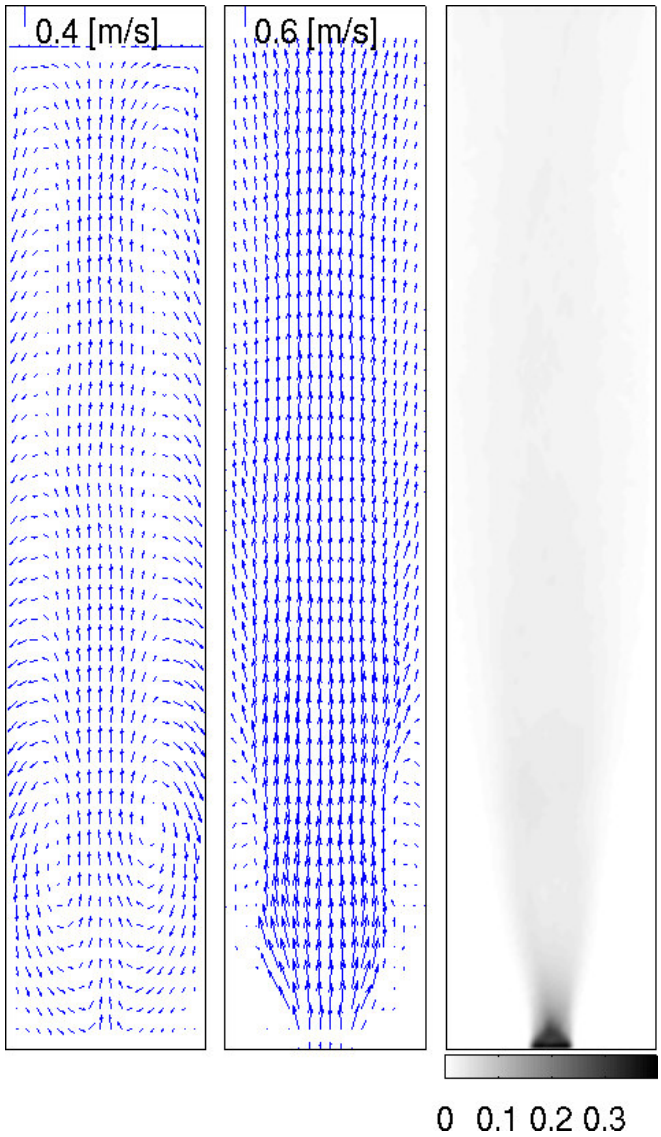


**Figure 4.16:** *Time-averaged liquid velocity (left), bubble velocity (center) and gas porosity (right) at* $y/D = 0.5$*. Case S2, averaging was carried out from* $t = 20 - 95\,\mathrm{s}$

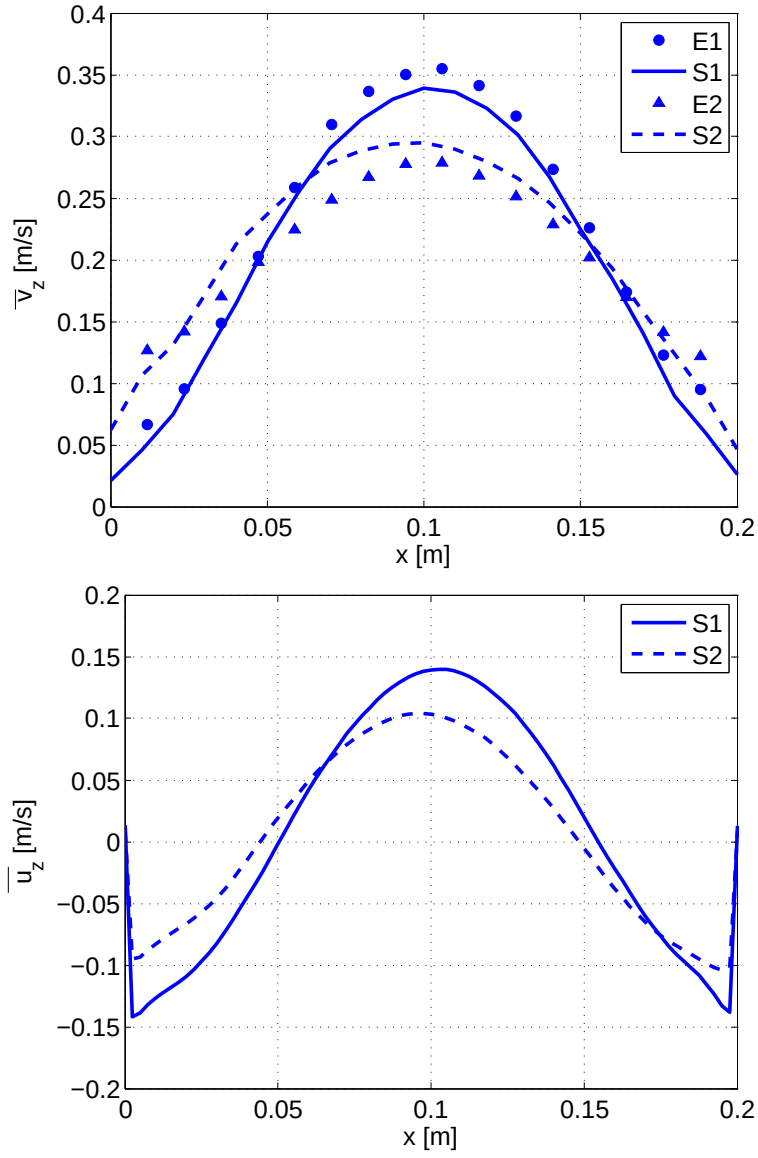


**Figure 4.17:** *Time-averaged bubble velocity profile (top) and time-averaged liquid velocity profile (bottom) at* $z/H = 0.75$.

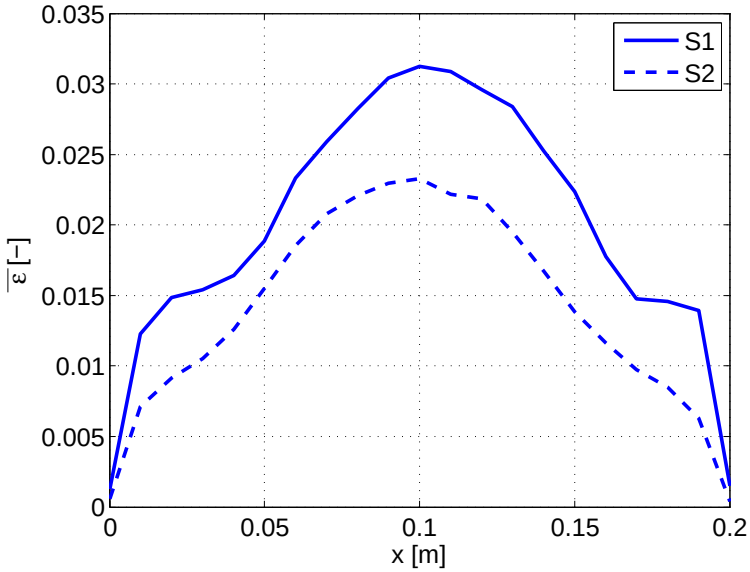


**Figure 4.18:** *Time-averaged gas porosity profile at* $z/H = 0.75$.

As can be seen, in the case without mass transfer, the bubble liquid velocity profile predicted by the present model (case S1) matches nicely with the experimental data (case E1). A very mild overprediction in the bubble velocity is observed in the center region of the column. For both the experimental data and simulation, the averaged bubble velocity is decreased when mass transfer is taken into account. Comparison between case S2 and E2 reveals that the averaged velocity profile predicted by the present model is slightly too high in the center region of the column.
The averaged liquid velocity profile shows similar trends with the averaged bubble counterpart. The profile shows that the liquid velocity has maximum upflow in the center of the column while downflow velocities is observed close to the wall region. Just like with the bubble velocity, the mass transfer also decreases the liquid velocities. Comparison between the liquid and bubble velocity profiles infers that the slip velocity is approximately constant in the lateral direction with a value of about $0.2\,\mathrm{m/s}$.
The averaged gas holdup profile at $z/H = 0.75$ can be seen in Fig. 4.18. It is found that the profile is symmetric in the lateral direction with a maximum value in the center of the column. This reflects that on a time-averaged basis, more bubbles are traveling in the central area of the column then in the wall region. Furthermore, the mass transfer also decreases the averaged gas holdup profile.

## 4.7 Conclusions

Detailed modeling results for a chemisorption process in a thin (pseudo-2D) bubble column reactor have been presented. Our model is based on the Euler-Lagrange approach and combines hydrodynamics, mass transfer and chemical reaction. The model results have been compared with experimental data and revealed close similarity between the computational and experimental results: a bubble plume with periodic meandering between the side walls of the column. A quantitative comparison in terms of averaged velocities, meandering period and gas holdup shows that for the case without mass transfer taken into account, the present model is able to capture all of the detailed characteristics accurately. When the mass transfer is taken into account however, we found that the overall mass transfer rate is lower compared to its experimental counterpart, which we believe can be attributed to innaccuracy of the mass transfer closure used in the present study. In this case the average bubble size predicted by the present model is higher than found experimentally, which leads to a higher gas hold up, higher flow field velocities and shorter meandering period compared to the experimental data. Nevertheless, the trends of the influence of mass transfer on the detailed characteristics mentioned above agrees very well with the experimental investigation. It is worth to mention here that the closure for the mass transfer is not as mature as the closures used for the hydrodynamics. However we are confident that when a more accurate closure for the mass transfer is available, the present model will give a closer comparison with the experimental investigation as has been shown here for the case without mass transfer. For this purpose, the front tracking model developed in Chapter 2 can lead to a promising computational tools to obtain a more reliable closures of both hydrodynamics and mass transfer that can be used in the discrete bubble model.

## Acknowledgements

This chapter could not have been realized without the help of many people. In particular the author would like to thank Robert Bouwer who built the setup with help from Ing. Robert Meijer and Dr. Mousa Al-Tarazi for the electronics and data acquisition part. The author also thanks Dr. ir. Wouter Harteveld (currently at Shell Global Solution, Amsterdam) for the discussion about the bubble inlet during the early development of the setup and Prof. Jerry Westerweel (Lab for Aero and Hydrodynamics, TU Delft) for the PIV software used in the present study. Help from Wim Leppink and Gerrit Schorfhaar during the rush hours is also acknowledged. Finally the experimental part would be completely empty without help from the authors' one and only apprentice, Ir. Roy Henket who worked on his final master assignment within the scope of this project.

## Notation

| | |
|---|---|
| $A$ | interfacial area, $\mathrm{m}^2$ |
| $c_i$ | concentration of species $i$, $\mathrm{kmol\,m}^{-3}$ |
| $C$ | model coefficient, dimensionless |
| $d$ | diameter, $\mathrm{m}$ |
| $D$ | diffusivity, $\mathrm{m}^2\,\mathrm{s}^{-1}$, depth, $\mathrm{m}$ |
| $E$ | enhancement factor, dimensionless |
| $E_\infty$ | enhancement factor at infinity, dimensionless |
| Eö | Eötvös number, dimensionless |
| $\mathbf{F}$ | force vector, $\mathrm{N}$ |
| $\mathbf{g}$ | gravity acceleration, $\mathrm{m\,s}^{-2}$ |
| $H$ | Henry constant (aqueous-concentration / gas-concentration), dimensionless |
| $Ha$ | Hatta number, dimensionless |
| $I$ | ionic concentration, $\mathrm{kmol\,m}^{-3}$ |
| $k_{\mathrm{sub},1}$ | reaction rate constant, sub: reaction number, forward, $\mathrm{m}^3\,\mathrm{kmol}^{-1}\,\mathrm{s}^{-1}$ |
| $k_{\mathrm{sub},2}$ | reaction rate constant, sub: reaction number, backward, $\mathrm{s}^{-1}$ |
| $k_l$ | mass transfer transfer coefficient, $\mathrm{m\,s}^{-1}$ |
| $K_1$ | equilibrium constant for reaction 1, $\mathrm{kmol}^{-1}\,\mathrm{m}^3$ |
| $K_2$ | equilibrium constant for reaction 2, $\mathrm{kmol}^{-1}\,\mathrm{m}^3$ |
| $K_w$ | solubility product, $\mathrm{kmol}^3\,\mathrm{m}^{-6}$ |
| $\mathbf{I}$ | unit tensor, dimensionless |
| $M$ | magnification factor, $\mathrm{pix\,m}^{-1}$ |
| $\dot{m}$ | mass transfer from individual bubble, $\mathrm{kg\,s}^{-1}$ |
| $\dot{M}$ | liquid side volume averaged mass transfer, $\mathrm{kg\,s}^{-1}\,\mathrm{m}^{-3}$ |
| $P$ | pressure, $\mathrm{N\,m}^{-2}$ |
| $R$ | radius, $\mathrm{m}$ |
| Re | Reynolds number, dimensionless |
| $S$ | source term in the species balance equation, $\mathrm{kg\,m}^{-3}\,\mathrm{s}^{-1}$ |
| $\mathbf{S}$ | characteristic filtered strain rate, $\mathrm{s}^{-1}$ |
| Sc | Schmidt number, dimensionless |
| Sh | Sherwood number, dimensionless |
| $t$ | time, $\mathrm{s}$ |
| $T$ | temperature, $\mathrm{K}$ |
| $\mathbf{u}$ | liquid velocity vector, $\mathrm{m\,s}^{-1}$ |
| $\mathbf{v}$ | bubble velocity vector, $\mathrm{m\,s}^{-1}$ |
| $V$ | volume, $\mathrm{m}^3$ |
| $Y$ | mass fraction, dimensionless |
| $z$ | ionic charge, dimensionless |
| $[\ldots]$ | concentration, $\mathrm{kmol\,m}^{-3}$ |

### Greek letters

| | |
|---|---|
| $\triangle$ | subgrid length scale, $\mathrm{m}$ |
| $\varepsilon$ | volume fraction, dimensionless |
| $\Gamma$ | species diffusion coefficient, $\mathrm{m^2\,s^{-1}}$ |
| $\mu$ | viscosity, $\mathrm{kg\,m^{-1}\,s^{-1}}$ |
| $\Phi$ | volume averaged momentum transfer due to interphase forces, $\mathrm{N\,m^{-3}}$ |
| $\rho$ | density, $\mathrm{kg\,m^{-3}}$ |
| $\sigma$ | interfacial tension, $\mathrm{N\,m^{-1}}$ |
| $\tau$ | stress tensor, $\mathrm{N\,m^{-2}}$ |

### Indices

| | |
|---|---|
| $aq$ | aqueous |
| $b$ | bubble |
| $cell$ | computational cell |
| $D$ | drag |
| $\mathrm{eff}$ | effective |
| $G$ | gravity |
| $j$ | $j^{th}$ species |
| $\ell$ | liquid |
| $L$ | lift |
| $P$ | pressure |
| $S$ | subgrid |
| $T$ | turbulent |
| $VM$ | virtual mass |
| $W$ | wall |
| $*$ | interfacial equilibrium value |

# Appendix A: Physico-chemical parameters

## A.1 Solubility

The solubility of $CO_2$ in aqueous electrolytic solutions was estimated using the method presented by Weisenberger and Schumpe [31]:

$$\log\left(\frac{H_w}{H}\right) = \Sigma\left(h_i + h_g\right) c_i \tag{A.1}$$

where the solubility coefficient of $CO_2$ in pure water, $H_w$, was taken from Versteeg and van Swaaij [32] as:

$$H_w = 3.59 \times 10^{-7}\, RT \exp\left(\frac{2044}{T}\right) \tag{A.2}$$

The expression for the solubility is valid at $298\ \mathrm{K}$ but can be used without loss of accuracy in a temperature range of $293 - 303\ \mathrm{K}$.

## A.2 Diffusivity

The diffusivity of $CO_2$ in pure water, $D_{w,CO_2}$ was taken from Versteeg and van Swaaij [32]:

$$D_{w,CO_2} = 2.35 \times 10^{-6} \exp\left(\frac{-2119}{T}\right) \tag{A.3}$$

The diffusion coefficients of gases into aqueous electrolyte solutions were estimated by the method suggested by Ratcliff and Holdcroft [33]:

$$\frac{D}{D_w} = 1 - 1.29 \times 10^{-4} \left[OH^-\right] \tag{A.4}$$

## A.3 Mass transfer rate

The mass transfer rate is determined using the following Sherwood relation [34]:

$$\mathrm{Sh} = \frac{k_l^j d_b}{D^j} = 2 + 0.015 \mathrm{Re}^{0.89} \mathrm{Sc}^{0.7} \tag{A.5}$$

where $d_b$ and $\mathrm{Re}$ are the diameter and Reynolds number of the bubble respectively. The correlation is derived for non-spherical bubbles by taking into account the stochastic deformations of the interface induced by turbulent motion in the surrounding fluid.
With this Sherwood relation, using a typical Schmidt number of $462$ and a Reynolds number of $1100$, one finds a typical Sherwood number of $562$.

## A.4 Enhancement factor

The enhancement factor is calculated using the relation given by Westerterp et al. [29]:

$$E = \begin{cases} -\frac{\mathrm{Ha}^2}{2(E_\infty - 1)} + \sqrt{\frac{\mathrm{Ha}^4}{4(E_\infty - 1)^2} + E_\infty \frac{\mathrm{Ha}^2}{E_\infty - 1} + 1} & ; \quad E_\infty > 1 \\ 1 & ; \quad E_\infty \leq 1 \end{cases} \tag{A.6}$$

**Table A.1:** *Parameters suggested by Weisenberger and Schumpe [31] for Eq. A.1*

| Ion | $h_i$ ($\mathrm{m^3 kmol^{-1}}$) | Gas | $h_g$ ($\mathrm{m^3 kmol^{-1}}$) |
|---|---|---|---|
| $Na^+$ | 0.1171 | $CO_2$ | $-0.0183$ |
| $OH^-$ | 0.756 | | |
| $HCO_3^-$ | 0.1372 | | |
| $CO_3^{2-}$ | 0.1666 | | |

where

$$E_\infty = \left(1 + \frac{D_{OH^-}\left[OH^-\right]}{2D_{CO_2}H\left[CO_2\left(g\right)\right]}\right)\sqrt{\frac{D_{CO_2}}{D_{OH^-}}} \tag{A.7}$$

$$\mathrm{Ha} = \frac{\sqrt{k_{1,1}D_{CO_2}\left[OH^-\right]}}{k_l} \tag{A.8}$$

This approximate enhancement factor has an accuracy within $10\%$ and provides a relatively cheap solution for the calculation of the enhancement factor for each individual bubble.

## A.5 Reaction rate

### First reaction

The forward rate constant $k_{1,1}$ $(\mathrm{m^3\,kmol^{-1}\,s^{-1}})$ of reaction 4.2 is calculated via the relation presented by Pohorecki and Moniuk [35] as:

$$\log\left(\frac{k_{1,1}}{k_{1,1}^\infty}\right) = 0.221I - 0.016I^2 \tag{A.9}$$

where the reaction rate constant at infinitely diluted solution, $k_{1,1}^\infty$ $(\mathrm{m^3\,kmol^{-1}\,s^{-1}})$, is given by:

$$\log k_{1,1}^\infty = 11.895 - \frac{2382}{T} \tag{A.10}$$

This equation is valid in the temperature range of $291 - 314\,\mathrm{K}$.
The ionic strength, $I$, is calculated as:

$$I = \frac{1}{2}\left(\left[Na^+\right]z_{Na^+}^2 + \left[OH^-\right]z_{OH^-}^2 + \left[HCO_3^-\right]z_{HCO_3^1}^2 + \left[CO_3^{2-}\right]z_{CO_3^{2-}}^2\right) \tag{A.11}$$

The backward rate constant $k_{1,2}$ $(\mathrm{s^{-1}})$ is calculated via the equilibrium constant $K_3$ and $K_w$ , and is derived for the following reaction:

$$CO_2 + H_2O \quad \rightleftharpoons \quad HCO_3^- + H^+ \tag{A.12}$$

$$H^+ + OH^- \quad \rightleftharpoons \quad H_2O \tag{A.13}$$

with $K_3$ $(\mathrm{kmol\,m^{-3}})$ is calculated according to Edwards et al. [36]:

$$K_3 = \frac{\left[HCO_3^-\right]\left[H^+\right]}{\left[CO_2\right]} = \exp\left(\frac{-12092.1}{T} - 36.786\ln(T) + 235.482\right) \tag{A.14}$$

and the solubility product, $K_w$ $(\mathrm{kmol^2\,m^{-6}})$, was taken from Tsonopolous et al. [37]:

$$K_w = \left[H^+\right]\left[OH^-\right] = 10^{-(5839.5/T + 22.4773\log(T) - 61.2062)} \tag{A.15}$$

The backward reaction $k_{1,2}$ is then obtained using the following relation:

$$K_1 = \frac{k_{1,1}}{k_{1,2}} = \frac{K_3}{K_w} \tag{A.16}$$

### Second reaction

Since the second reaction involves a proton transfer, it is very rapid. Eigen [38] determined the rates of reactions involving protons or hydroxyl ions in aqueous solutions to be in the order of $10^{10} - 10^{11}$ $\mathrm{m^3\ kmol^{-1}\ s^{-1}}$. The backward reaction rate $k_{2,2}$ $(\mathrm{s^{-1}})$ is calculated using the equilibrium constant $K_2$ $(\mathrm{m^3\ kmol^{-1}})$ as suggested by Hikita et al. [39]:

$$K_2 = \frac{k_{2,1}}{k_{2,2}} \tag{A.17}$$

with

$$\log K_2 = \log K_2^{\infty} + \frac{1.01\sqrt{[Na^+]}}{1 + 1.27\sqrt{[Na^+]}} + 0.125\left[Na^+\right] \tag{A.18}$$

$$\log K_2^{\infty} = \frac{1568.94}{T} + 0.4134 - 0.00673T \tag{A.19}$$

**Remark:** In the discrete bubble model, a value of $k_{2,1}$ of $10^6$ $\mathrm{m^3\ kmol^{-1}\ s^{-1}}$ is used to allow simulations to be performed with a larger time step. Several precalculations have been performed to test this assumption and it is found that using this value the second forward reaction is still much faster than the first forward reaction. At the end of the simulation the difference in the concentrations using the two value of $k_{2,1}$ is $0.0273\%$ which confirms that using a smaller value for $k_{2,1}$ does not yield any significant errors.

## References

[1] D. Darmana, R. L. B. Henket, N. G. Deen, and J. A. M. Kuipers. Experimental and numerical investigations of a chemisorption process in a bubble column reactor. In *Proceedings of the 7th World Congress of Chemical Engineering*, Glasgow, Scotland, UK, 10-14 July 2005.

[2] D. Darmana, R. L. B. Henket, N. G. Deen, and J. A. M. Kuipers. Detailed modelling of hydrodynamics, mass transfer and chemical reactions in a bubble column using a discrete bubble model: Chemisorption of $CO_2$ into $NaOH$ solution, numerical and experimental study. *to be submitted to Chemical Engineering Science*, 2006.

[3] D. Darmana, N. G. Deen, and J. A. M. Kuipers. Detailed modelling of hydrodynamics, mass transfer and chemical reactions in a bubble column using a discrete bubble model. *Chemical Engineering Science*, 60(12):3383–3404, June 2005.

[4] E. Delnoij, F. A. Lammers, J. A. M. Kuipers, and W. P. M. Van Swaaij. Dynamic simulation of dispersed gas-liquid two-phase flow using a discrete bubble model. *Chemical Engineering Science*, 52:1429–1458, 1997.

[5] E. Delnoij, J. A. M. Kuipers, and W. P. M. Van Swaaij. A three-simensional cfd model for gas-liquid bubble columns. *Chemical Engineering Science*, 54:2217–2226, 1999.

[6] N. G. Deen, T. Solberg, and B. H. Hjertager. Large eddy simulation of the gas-liquid flow in a square cross-sectioned bubble column. *Chemical Engineering Science*, 56:6341–6449, 2001.

[7] V. V. Buwa, D. S. Deo, and V. V. Ranade. Eulerian-lagrangian simulations of unsteady gas-liquid flows in bubble columns. *International Journal of Multiphase Flow*, 32:864885, 2006.

[8] A. Tomiyama, H. H. I. Zun, Y. Makino, and T. Sakaguchi. A three-dimensional particle tracking method for bubbly flow simulation. *Nuclear Engineering and Design*, 175:77–86, 1997.

[9] Y. Pan and M. P. Dudukovic. Numerical investigation of gas-driven flow in 2-d bubble columns. *AIChE Journal*, 46:434–449, 2000.

[10] A. Sokolichin and G. Eigenberger. Gas-liquid flow in bubble columns and loop reactors: Part i. detailed modeling and numerical simulation. *Chemical Engineering Science*, 49:5735–5746, 1994.

[11] C. Fleischer, S. Becker, and G. Eigenberger. Detailed modeling of the chemisorption of $CO_2$ into NaOH in a bubble column. *Chemical Engineering Science*, 51:1715–1724, 1996.

[12] M. A. Márquez, R. J. Amend, R. G. Carbonell, A. E. Sáez, and G. W. Roberts. Hydrodynamics of gas-lift reactors with a fast, liquid-phase reaction. *Chemical Engineering Science*, 54:2263–2271, 1999.

[13] M. A. Márquez, A. E. Sáez, R. G. Carbonell, and G. W. Roberts. Coupling of hydrodynamics and chemical reaction in gas-lift reactors. *AIChE Journal*, 45(2):410–423, 1999.

[14] M. Bauer and G. Eigenberger. A concept for multi-scale modeling of bubble columns and loop reactors. *Chemical Engineering Science*, 54:5109–5117, 1999.

[15] M. Bauer. *On the multiscale modeling of bubble column reactors*. PhD thesis, University of Stuttgart, Germany, 2001.

[16] M. Bauer and G. Eigenberger. Multiscale modeling of hydrodynamics, mass transfer and reaction in bubble column reactors. *Chemical Engineering Science*, 56:1067–1074, 2001.

[17] S. Rigopoulos and A. Jones. A hybrid cfd-reaction engineering framework for multiphase reactor modeling: basic concept and application to bubble column reactors. *Chemical Engineering Science*, 58:3077–3089, 2003.

[18] D. Mewes and D. Wiemann. Two-phase flow with mass transfer in bubble columns. *Chemical Engineering & Technology*, 26:862–868, 2004.

[19] D. Darmana, N. G. Deen, and J. A. M. Kuipers. Modelling of mass transfer and chemical reactions in a bubble column reactor using a discrete bubble model. In *Proceedings of the 5th International Conference on Multiphase Flow*, Yokohama, Japan, may 30 - June 4 2004. Paper No. 328.

[20] D. Darmana, N. G. Deen, and J. A. M. Kuipers. Parallelization of an Euler-Lagrange model using mixed domain decomposition and mirror domain technique: application to dispersed gas-liquid two-phase flow. *Journal of Computational Physics*, 2006. In Press, Corrected Proof, Available online 7 July 2006.

[21] W. K. Harteveld, R. F. Mudde, and H. E. A. Van den Akker. Dynamics of a bubble column: Influence of gas distribution on coherent structures. *The Canadian Journal of Chemical Engineering*, 81:389–394, 2003.

[22] J. Westerweel. *Digital particle image velocimetry - theory and application*. PhD thesis, Delft University of Technology, The Netherlands, 1993.

[23] B. P. B. Hoomans, J. A. M. Kuipers, W. J. Briels, and W. P. M. Van Swaaij. Discrete particle simulation of bubble and slug formation in a two-dimensional gas-fluidized bed: a hard-sphere approach. *Chemical Engineering Science*, 51:99–118, 1996.

[24] A. Tomiyama, H. Tamai, I. Zun, and S. Hosokawa. Transverse migration of single bubbles in simple shear flows. *Chemical Engineering Science*, 57:1849–1858, 2002.

[25] A. Tomiyama, T. Matsuoka, T. Fukuda, and T. Sakaguchi. A simple numerical method for solving an incompressible two-fluid model in a general curvilinear coordinate system. In A. Serizawa, T. Fukano, and J. Bataille, editors, *Advances in Multiphase Flow*, pages 241–252, Amsterdam, November 1995. Society of Petroleum Engineers, Inc., Elsevier.

[26] A. W. Vreman. An eddy-viscosity subrid-scale model for turbulent shear flow: algebraic theory and applications. *Physics of Fluids*, 16(10):3670–3681, 2004.

[27] R. V. Bhat. *Mass Transfer Accompanied by Multi-step Reactions and its Application to Gas-Liquid Reactor Design*. PhD thesis, University of Twente, Enschede, The Netherlands, 1998.

[28] J. A. M. Kuipers, K. J. Van Duin, F. P. H. Van Beckum, and W. P. M. Van Swaaij. Computer simulation of the hydrodynamics of a two dimensional gas-fluidized bed. *Computational Chemical Engineering*, 17:839, 1993.

[29] K. R. Westerterp, W. P. M. Van Swaaij, and A. A. C. M. Beenackers. *Chemical Reactor Design and Operation*. John Wiley & Sons Ltd, 411, 1984.

[30] V. V. Buwa and V. V. Ranade. Mixing in bubble columns reactors: role

of unsteady flow structures. *Canadian Journal of Chemical Engineering*, 81:402, 2003.

[31] S. Weisenberger and A. Schumpe. Estimation of gas solubility in salt solutions at temperatures from 273k to 363 k. *AIChE Journal*, 42:298–300, 1996.

[32] G. F. Versteeg and W. P. M. Van Swaaij. Solubility and diffusivity of acid gases ($CO_2$ and $N_2O$) in aqueous alkaloamine solutions. *Journal of Chemical & Engineering Data*, 33:29–34, 1988.

[33] G. A. Ratcliff and J. G. Holdcroft. Diffusivities of gases in aqueous electrolyte solutions. *Transactions of the Institution of Chemical Engineers and the Chemical Engineer*, 41:315319, 1963.

[34] H. Brauer. Particle/fluid transport processes. *Progress in Chemical Engineering*, 19:81–111, 1981.

[35] R. Pohorecki and W. Moniuk. Kinetics of reaction between carbon dioxide and hydroxyl ions in aqueous electrolytic solutions. *Chemical Engineering Science*, 43:1677–1684, 1988.

[36] T. J. Edwards, G. Maurer, J. Newman, and J. M. Prausnitz. Vapor-Liquid equilibria in multicomponent aqueous solutions of volatile weak electrolytes. *AIChE Journal*, 24:966–976, 1978.

[37] C. Tsonopolous, D. M. Coulson, and L. W. Inman. Ionization constants of water pollutants. *Journal of Chemical & Engineering Data*, pages 190–193, 1976.

[38] M. Eigen. Method for investigation of ionic reactions in aqueous solutions with half times as short as $10^{-9}$ sec. *Discussions of the Faraday Society*, 17:194–205, 1954.

[39] H. Hikita, S. Asai, and T. Takatsuka. Absorption of carbon dioxide into aqueous sodium hydroxide and sodium carbonate-bicarbonate solutions. *Chemical Engineering Journal*, 11:131–141, 1976.

# 5

# Toward modelling of large scale bubble column reactors: implementation of the parallel calculation strategy for the discrete bubble model[§§]

*"The future is here. It's just not widely distributed yet."* - William Gibson

## Abstract

*In this chapter, we report a parallel algorithm applicable to a Euler-Lagrange model embedding four-way coupling. The model describing the dispersed phase dynamics accounts for bubble-bubble collisions and is parallelized using a mirror domain technique while the pressure Poisson equation for the continuous phase is solved using a domain decomposition technique implemented in the PETSc library [S. Balay, K. Buschelman, W. D. Gropp, D. Kaushik, M. G. Knepley, L. C. McInneds, B. F. Smith and H. Zhang. PETSC Web page: http://www.msc.anl.gov/petsc, 2001]. The parallel algorithm is verified and it is found that it gives the same results for both phases as compared to the serial algorithm. Furthermore the algorithm shows good scalability up to 32 processors. Using the proposed method, a homogeneous bubbly flow in a laboratory scale bubble column can be simulated at very high gas hold-up (37%) while consuming a reasonable amount of calculation wall time.*

[§§]Based on: Darmana et al. [1, 2]

## 5.1 Introduction

Bubble columns are encountered in a wide range of applications such as the Fischer-Tropsch process for hydrocarbon synthesis, hydrogenation of unsaturated oil, oxidation of hydrocarbons, fermentation and (biological) wastewater treatment. Due to the simplicity in operation, low operating cost and the good mass, as well as heat transfer characteristics, bubble columns are often preferred over other types of reactors. The determination of global parameters such as the integral gas hold-up is of primary importance for scale-up and design purposes. Unfortunately the global parameters are strongly influenced by the local flow phenomena. The behavior of bubble columns is quite complex and detailed understanding of its dynamics is lacking. As the local properties in the two phase flow have proven to be difficult to measure in industrial equipment, there is a growing interest during the last decades to develop models which can accurately predict the detailed characteristics of bubble columns.

Due to advances in computer hardware and numerical solution methods Computational Fluid Dynamics (CFD) has emerged as a powerful tool for both scientists and engineers. Two models are widely used for describing hydrodynamics of bubble columns, i.e. the Euler-Euler (E-E) model and Euler-Lagrange (E-L) model. The E-E model employs the volume or ensemble averaged mass and momentum conservation equations to describe the time dependent motion of both phases [3–5]. The number of bubbles present in a computational cell is represented by a volume fraction and the information on the bubble size distribution is often obtained by incorporating population balance equations, which take into account break-up and coalescence of bubbles as well as growth or shrinkage of bubbles as a result of mass transfer.

The E-L model on the other hand adopts a continuum description for the liquid phase and additionally tracks each individual bubble using Newtonian equations of motion taking into account the four way interaction i.e., the mutual bubble-liquid and the mutual bubble-bubble or bubble-wall interaction. This allows for a direct consideration of additional effects related to bubble-bubble and bubble-liquid interaction. Mass transfer with and without chemical reaction, bubble coalescence and re-dispersion can be incorporated directly [4, 6–8]. Unlike the E-E model, the E-L model does not require additional models to predict the bubble size distribution since this information is already part of the solution.

One main limitation of the E-L model is the number of bubbles that can be treated since for each individual bubble one equation of motion needs to be solved. Without taking into account direct bubble-bubble interaction Kitagawa et al. [9] and Sommerfeld et al. [10] have succeeded to simulate bubble columns with about $10^5$ bubbles simultaneously present in the column. By neglecting the bubble-bubble interaction, however, bubbles could overlap with each other. As a consequence, in dense swarms,

considerable overlap between the bubbles can prevail. If the superficial gas velocity is sufficiently high, the local gas fraction can approach unity leading to numerical problems. Sommerfeld [11] claims that if the volume fraction of the gas exceeds $1 \times 10^{-3}$, the bubble-bubble interaction becomes so important in describing the fluid dynamics in the bubble column that four way coupling is needed. Furthermore, the bubble interaction is also required as a first step if bubble coalescence needs to be considered.
By introducing direct bubble-bubble interaction into the model, the computational effort is dramatically increased since the algorithm to solve the collision sequence is both CPU and memory intensive. Furthermore the time step required in the bubble tracking algorithm is no longer determined by the numerical stability criteria but by the time scale of the collision events, which normally are an order of magnitude smaller than the bubble tracking time scale. With a collision model Darmana et al. [8] reported that typically only $10^4$ bubbles can be simulated using a state of the art PC. In combination with the necessity to perform simulations in three dimensions with sufficiently fine spatial and temporal resolution, the method proves to be computationally very demanding and time consuming. On top of that, the model should be able to perform simulations over a sufficiently long time to obtain reasonable statistics, as needed for proper analysis of the column dynamics. This leads to the conclusion that this method is less attractive in handling large scale bubble columns.
Recently parallelization strategies have received considerable attention in the multiphase CFD community [12, 13]. By solving a problem in parallel, not only the time required to solve the problem can be reduced significantly, also the problem size that can be handled is increased, since the memory requirements can be distributed. From a numerical point of view, the Eulerian part of the model is easier to solve in parallel since the discretized form of the governing equations will lead to a large linear system of the form $Ax = b$ where the coefficient matrix $A$ is usually sparse. This matrix problem can be solved in parallel efficiently using a domain decomposition technique. Parallelization of the discrete part on the other hand is not straightforward due to the serial nature of the event driven algorithm implemented for tracking bubble-bubble and bubble-wall collisions [14].
In this chapter a detailed parallelization strategy is presented for solving a 3D transient Euler-Lagrange model taking into account the four way interaction. The continuous phase is described using the volume-averaged Navier-Stokes equations, whereas the dispersed phase is described by the Newtonian equations of motion for each individual bubble. The exchange of momentum between the gas and the liquid as well as the momentum exchange between the bubbles (four way coupling) will be accounted for. The equations describing the bubble motion will be presented in detail, incorporating all relevant forces acting on the bubble. In order to prevent, physically impossible, bubble-bubble overlap, the highly optimized direct bubble-bubble collision algorithm of Hoomans et al. [14] is implemented.

The Eulerian part of the model is parallelized using the well-known domain decomposition technique, whereas a so called *mirror domain technique* is employed to solve the Lagrangian part in a parallel fashion. To allow the parallel code to run in both distributed as well as shared memory architecture, the Massage Passing Interface (MPI) [15, 16] paradigm is used.

## 5.2 Model formulation

The transient, three-dimensional Euler-Lagrange model described in this chapter consists of two coupled parts: a part describing the bubble motion and a part describing the liquid phase motion. The model requires constitutive equations for the forces acting on a bubble. The interaction between the gas and the liquid phase is incorporated via the liquid volume fraction and a source term in the liquid phase momentum equation. The interaction between the bubbles is modeled via a collision model, including bubble bouncing and coalescence.

### 5.2.1 Bubble dynamics

The motion of for each individual bubble is computed from the bubble force balance. The liquid phase contributions are taken into account by the interphase momentum transfer experienced by each individual bubble. For an incompressible bubble, the equations can be written as:

$$m_b \frac{d\mathbf{v}}{dt} = \sum \mathbf{F} \tag{5.1}$$

$$\frac{d\mathbf{r}}{dt} = \mathbf{v} \tag{5.2}$$

The net force acting on each individual bubble is calculated by considering all the relevant forces. It is assumed that the net force is composed of separate, uncoupled contributions due to respectively gravity, pressure, drag, lift, virtual mass and wall forces:

$$\sum \mathbf{F} = \mathbf{F}_G + \mathbf{F}_P + \mathbf{F}_D + \mathbf{F}_L + \mathbf{F}_{VM} + \mathbf{F}_W \tag{5.3}$$

A brief introduction of these forces will be given here. A more detailed discussion of these forces can be found in the review papers of Magnaudet and Eames [17] and Jakobsen et al. [18, 19].
The gravity force acting on a bubble in a liquid is given by:

$$\mathbf{F}_G = \rho_b V_b \mathbf{g} \tag{5.4}$$

The far field pressure force incorporates contributions of the Archimedes buoyancy force, inertial forces and viscous strain and is given by:

$$\mathbf{F}_P = -V_b \nabla p \tag{5.5}$$

The drag exerted on a bubble rising through a liquid is expressed as:

$$\mathbf{F}_D = -\frac{1}{2} C_D \rho_l \pi R_b^2 \left|\mathbf{v} - \mathbf{u}\right| (\mathbf{v} - \mathbf{u}) \tag{5.6}$$

where the drag coefficient is given by the following relation

$$C_D = \max\left[\min\left[\frac{16}{\mathrm{Re}}\left(1 + 0.15\mathrm{Re}^{0.687}\right), \frac{48}{\mathrm{Re}}\right], \frac{8}{3}\frac{\mathrm{Eö}}{\mathrm{Eö}+4}\right] \tag{5.7}$$

This drag relation is based on an extensive number of bubble rise velocity measurements and was derived for $10^{-2} < \mathrm{Eö} < 10^3$; $10^{-14} < \mathrm{Mo} < 10^7$ and $10^{-3} < \mathrm{Re} < 10^5$, where the Eötvös number, $\mathrm{Eö} = (\rho_l - \rho_b)\,\mathbf{g} d_b^2/\sigma$ represents the dimensionless size, the Morton number, $\mathrm{Mo} = g\mu_l^4(\rho_l - \rho_b)/(\rho_l^2\sigma^3)$ is a dimensionless parameter describing the system properties, and the Reynolds number, $\mathrm{Re} = \rho_l \left|\mathbf{v} - \mathbf{u}\right| d_b/\mu_l$ represents the dimensionless velocity. In this work we use an air-water system, i.e. $\mathrm{Mo} = 2.52 \times 10^{-11}$ and bubble sizes ranging from $4$ to $10\,\mathrm{mm}$, i.e. $2.1 < \mathrm{Eö} < 13.4$. The steady relative velocity, $v_{rel} = |\mathbf{v} - \mathbf{u}|$ can straightforwardly be obtained, when only the gravity, pressure force and drag force are considered, leading to:

$$C_D \frac{1}{2}\rho_l v_{rel}^2 \frac{\pi d_b^2}{4} = (\rho_l - \rho_b) g_z \frac{\pi d_b^3}{6} \tag{5.8}$$

For air bubbles of this size rising in water, the drag coefficient given in Eq. 5.7 reduces to:

$$C_D = \frac{8}{3}\frac{\mathrm{Eö}}{\mathrm{Eö}+4} \tag{5.9}$$

When Eq. 5.9 is substituted in Eq. 5.8, the following relation for the rise velocity is obtained:

$$v_{rel} = \sqrt{\frac{2\sigma}{d\rho_l} + \frac{(\rho_l - \rho_b) g_z d_b}{2\rho_l}} \tag{5.10}$$

For an air-water system and bubble sizes as indicated earlier, rise velocities of $v_{rel} \approx 0.25\,\mathrm{m/s}$ are obtained, corresponding to Reynolds numbers in the range of $1000$ to $2500$. Note that the influence of shape deformations for large bubbles is implicitly accounted for through the drag relation.
A bubble rising in a non-uniform, liquid flow field experiences a lift force due to vorticity or shear in this flow field. The shear induced lift force acting on a bubble is usually written as [20]:

$$\mathbf{F}_L = -C_L \rho_l V_b (\mathbf{v} - \mathbf{u}) \times \nabla \times \mathbf{u} \tag{5.11}$$

In this work we use the lift coefficient $C_L$ that was derived for $1.39 \leq \mathrm{Eö} \leq 5.74$; $5.5 \leq \log_{10}\mathrm{Mo} \leq -2.8$; and shear rates $\gamma < 8.3\ \mathrm{s}^{-1}$ by Tomiyama et al. [21]:

$$C_L = \begin{cases} \min\left[0.288\tanh\left(0.121\mathrm{Re}\right), f(\mathrm{Eö}_d)\right]; \mathrm{Eö}_d < 4 \\ f(\mathrm{Eö}_d); 4 < \mathrm{Eö}_d \leq 10 \\ -0.29; \mathrm{Eö}_d > 10 \end{cases} \tag{5.12}$$

with

$$f(\mathrm{E\ddot{o}}_d) = 0.00105\mathrm{E\ddot{o}}_d^3 - 0.0159\mathrm{E\ddot{o}}_d^2 - 0.0204\mathrm{E\ddot{o}}_d + 0.474 \tag{5.13}$$

and

$$\mathrm{E\ddot{o}}_d = \frac{\mathrm{E\ddot{o}}}{E^{2/3}}\ ;\ E = \frac{1}{1 + 0.163\mathrm{E\ddot{o}}^{0.757}} \tag{5.14}$$

where $\mathrm{E\ddot{o}}_d$ is a modified Eötvös number using the horizontal diameter of the bubble that is obtained from the bubble aspect ratio $E$, which was determined experimentally by Wellek et al. [22] for $\mathrm{E\ddot{o}} < 40$ and $\mathrm{Mo} \leq 10^{-6}$. It is stressed here that small bubbles will tend to move towards the side of low liquid velocities, i.e. wall peaking, whereas large bubbles deform and due to wake effects tend to laterally move in the opposite direction, i.e. core peaking. It is noted here that although Eq. 5.12 is not strictly valid for the Morton numbers studied in this work, it is considered the best available closure for relatively large bubbles.
Accelerating bubbles experience a resistance, which is described as the virtual mass force [20]:

$$\mathbf{F}_{VM} = -C_{VM}\rho_l V_b \left( \frac{D_b\mathbf{v}}{D_b t} - \frac{D_l\mathbf{u}}{D_l t} \right) \tag{5.15}$$

where the $D/D_t$ operators denote the substantive derivatives pertaining to the respective phases. In this work it is assumed that the virtual mass force does not depend on the local void fraction and a virtual mass coefficient of $C_{VM} = 0.5$ is used.
Bubbles in the vicinity of a solid wall experience a force referred to as the wall force [23]:

$$\mathbf{F}_W = -C_W \frac{d}{2} \left[ \frac{1}{y^2} - \frac{1}{(L-y)^2} \right] \rho_l \left| (\mathbf{v} - \mathbf{u}) \cdot \mathbf{n}_z \right|^2 \mathbf{n}_w \tag{5.16}$$

where $\mathbf{n}_z$ and $\mathbf{n}_w$ respectively are the normal unit vectors in the vertical and wall normal direction, $L$ is the dimension of the system in the wall normal direction, and $y$ is the distance to the wall in that direction. Finally, the wall force coefficient $C_W$ is given by:

$$C_W = \begin{cases} \exp(-0.933\mathrm{E\ddot{o}} + 0.179); & 1 \leq \mathrm{E\ddot{o}} \leq 5 \\ 0.007\mathrm{E\ddot{o}} + 0.04; & 5 < \mathrm{E\ddot{o}} \leq 33 \end{cases} \tag{5.17}$$

### 5.2.2 Liquid phase hydrodynamics

The liquid phase hydrodynamics is described by the volume-averaged Navier-Stokes equations, which consist of continuity and momentum equations. The presence of the bubbles is reflected by the liquid phase volume fraction $\varepsilon_l$ and the interphase momentum transfer rate $\Phi$:

$$\frac{\partial}{\partial t}\left(\varepsilon_l \rho_l\right) + \nabla \cdot \varepsilon_l \rho_l \mathbf{u} = 0 \tag{5.18}$$

$$\frac{\partial}{\partial t}\left(\varepsilon_l \rho_l \mathbf{u}\right) + \nabla \cdot \varepsilon_l \rho_l \mathbf{u}\mathbf{u} = -\varepsilon_l \nabla p - \nabla \cdot \varepsilon_l \tau_l + \varepsilon_l \rho_l \mathbf{g} + \Phi \tag{5.19}$$

The liquid phase is assumed to be Newtonian, thus the stress tensor $\tau_l$ can be represented as:

$$\tau_l = -\mu_{\mathrm{eff},l}\left[\left(\left(\nabla \mathbf{u}\right) + \left(\nabla \mathbf{u}\right)^T\right) - \frac{2}{3}\mathbf{I}\left(\nabla \cdot \mathbf{u}\right)\right] \tag{5.20}$$

where $\mu_{\mathrm{eff},l}$ is the effective viscosity. In the present model the effective viscosity is composed of two contributions, the molecular viscosity and the turbulent viscosity:

$$\mu_{\mathrm{eff},l} = \mu_{L,l} + \mu_{T,l} \tag{5.21}$$

where the turbulent viscosity $\mu_{T,l}$ is calculated using the sub-grid scale (SGS) model of Smagorinsky [24]:

$$\mu_{T,l} = \rho_l \left(C_S \triangle\right)^2 |\mathbf{S}| \tag{5.22}$$

where $C_S$ represents a model constant with a typical value of $0.1$, $\mathbf{S}$ the characteristic filtered strain rate and $\triangle = \left(V_{cell}\right)^{1/3}$ the SGS length scale.

### 5.2.3 Collision model

In this work a hard sphere collision model resembling the model developed by Hoomans et al. [14] is used to process the sequence of collisions between bubbles or between bubble and both internal and external obstacles (i.e. walls) in the computational domain. This model can be illustrated as follows: consider a set of bubbles consisting of $N_b$ bubbles in total with index $\mathcal{B} = \{0, 1..N_b - 1\}$ and a set of obstacles $\mathcal{O}$. For every bubble $\ell \in \mathcal{B}$ we can define a set of possible collision partners $\mathcal{N}(\ell)$ as:

$$\mathcal{N}(\ell) := \left(\mathcal{B} \cup \mathcal{O}\right) \setminus \{\ell\} \tag{5.23}$$

Using the relation reported by Allen and Tildesley [25], we can determined the time required for a bubble $\ell$ to collide with a collision partner $m \in \mathcal{N}(\ell)$ from their initial positions and velocities (i.e. the collision time):

$$\delta t_{\ell,m} = \frac{-\mathbf{r}_{\ell m} \cdot \mathbf{v}_{\ell m} - \sqrt{\left(\mathbf{r}_{\ell m} \cdot \mathbf{v}_{\ell m}\right)^2 - \mathbf{v}_{\ell m}^2\left(-\mathbf{r}_{\ell m}^2 - \left(R_\ell + R_m\right)^2\right)}}{\mathbf{v}_{\ell m}^2} \tag{5.24}$$

where $\mathbf{r}_{\ell m} = \mathbf{r}_\ell - \mathbf{r}_m$ and $\mathbf{v}_{\ell m} = \mathbf{v}_\ell - \mathbf{v}_m$. Note that if $\mathbf{r}_{\ell m} \cdot \mathbf{v}_{\ell m} > 0$ the bubbles are moving away from each other and will not collide. Furthermore it is assumed that the relative velocity is constant during $\delta t_{\ell,m}$.
For each bubble $\ell$ the *individual* minimum collision time with other partners

$$\delta t_{\ell,n}^{\mathcal{N}} = \min(\delta t_{\ell,m}),\ \forall m \in \mathcal{N}(\ell) \tag{5.25}$$

is determined, where $n$ is the corresponding partner. Subsequently the *global* minimum collision time $\delta t^e_{a,b}$ is determined from all individual minimum collision times:

$$\delta t^e_{a,b} = \min(\delta t^{\mathcal{N}}_{\ell,n}),\ \forall \ell \in \mathcal{B} \tag{5.26}$$

where $\delta t^e_{a,b}$ represents the time to the next collision event $e$. First, all bubble positions will be updated to the instant of the collision, using a simple first order integration:

$$\mathbf{r}_\ell(t + \delta t^e_{a,b}) = \mathbf{r}_\ell(t) + \mathbf{v}_\ell \delta t^e_{a,b} \tag{5.27}$$

Following the movement of all bubbles, collision partners $a$ and $b$ are touching and the corresponding collision event is treated subsequently. Two types of collision events can take place: the collision partners can bounce or they can coalesce. The former process will be explained in this section while the latter will be explained in section 5.2.4. When the bubbles bounce, the momentum is exchanged based on conservation of momentum. In this case, the velocities of both bubbles are divided into a normal and a tangential component with respect to the line connecting the centres of mass of both bubbles (see Fig. 5.1). The tangential component does not change due to a collision while the normal component is changed according to the following relation (elastic bouncing):

$$\mathbf{v}^*_a = 2\frac{m_a\mathbf{v}_a + m_b\mathbf{v}_b}{m_a + m_b} - \mathbf{v}_a \tag{5.28}$$

Updating the velocities of the pair $a, b$ following a collision concludes one cycle of a collision event.

### 5.2.4 Coalescence model

Incorporation of the bubble coalescence mechanism into Euler-Lagrange modeling has been undertaken by Sommerfeld et al. [10] and Van den Hengel et al. [26]. Sommerfeld et al. [10] predicted the collision using a stochastic inter-bubble collision model. Coalescence is incorporated directly by comparing the contact time with the film drainage time. In the approach adopted by Van den Hengel et al. [26] bubble collisions are directly calculated using the method given in the previous section while the coalescence process is predicted using a stochastic approach based on the model of Chesters [27] and Lee et al. [28].

In the present study Sommerfeld's approach to determine coalescence in combination with direct calculation of collision is used. The implementation is straightforward: for a given bubble collision pair $a$ and $b$ predicted by the collision mechanism explained in the previous section the film-drainage time for coalescence to occur is calculated based on the model of Prince and Blanch [29] as follows:

$$\tau_{ab} = \sqrt{\frac{R^3_{ab}\rho_l}{16\sigma}} ln\left(\frac{h_0}{h_f}\right) \tag{5.29}$$

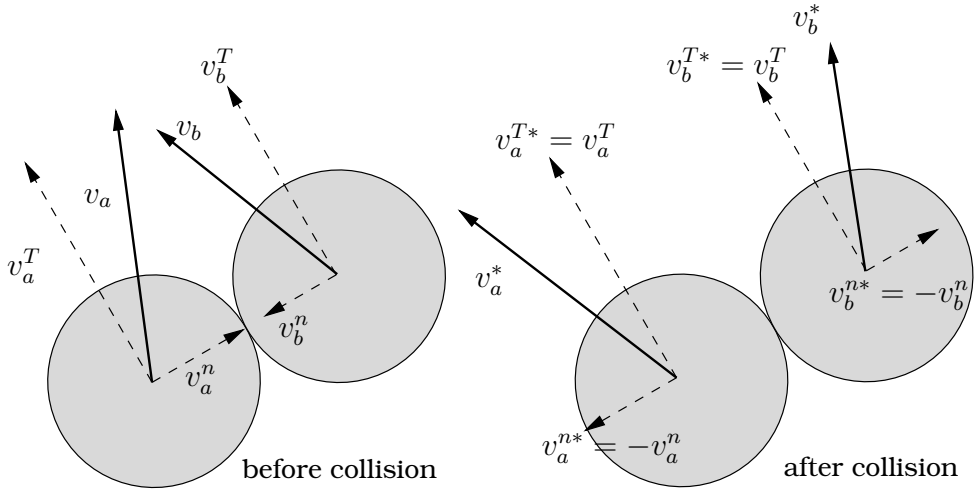


**Figure 5.1:** *Configuration of bubble bounce following a collision event.*

where the initial film thickness for an air-water system was taken as $h_0 = 10^{-4}$ m [30] and the final film thickness just before film breakage was taken as $h_f = 10^{-8}$ m [29, 30]. The equivalent bubble radius for a system of two different sized bubbles is obtained from [31]:

$$R_{ab} = 2.0 \left( \frac{1}{R_a} + \frac{1}{R_b} \right)^{-1} \tag{5.30}$$

The contact time between two bubbles is calculated by assuming that it is proportional to a deformation distance divided by the normal component of the collision velocity [10] (See illustration in Fig. 5.2):

$$t_{ab}^c = \frac{C_c R_{ab}}{|v_a^n - v_b^n|} \tag{5.31}$$

where $C_c$ represents the deformation distance normalized by the effective bubble radius and should be considered as a (calibration) factor. When the contact time is less than the film breakage time ($t_{ab}^c < \tau_{ab}$) coalescence will not occur and the bubbles will bounce. In all other cases ($t_{ab}^c \geq \tau_{ab}$) coalescence will commence and the properties of the new bubble are obtained from the encounter rules summarized in table 5.1.

It is noted that despite a vast amount of literature on this topic, there is still no consensus on the exact formulation of such model. In this work we have made a modest attempt to put together a coalescence model that includes the most important aspects of the coalescence process (i.e. film drainage) employing as much as possible information available from the model (i.e. bubble sizes and approach velocity). The simulations presented in this work

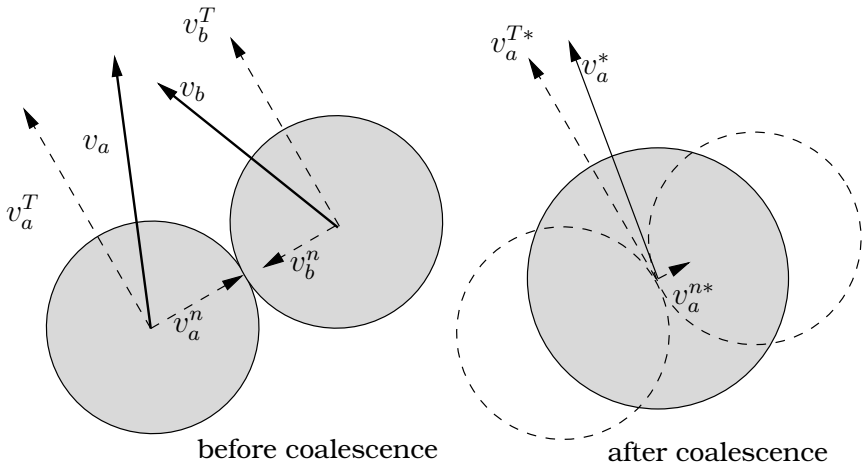


**Figure 5.2:** *Configuration of bubble collision and deformation uses in coalescence model (adapted from [10]).*

should therefore be considered as a demonstration of the possibilities a discrete bubble model offers to study coalescing flows and to demonstrate the impact the inclusion of a coalescence model has on the resulting hydrodynamics. Further research on the closure model for coalescence is still required.

## 5.3 Numerical solution method

In this section the numerical technique employed to solve the model presented in sect. 5.2 is described.

### 5.3.1 Time step

To resolve the time-dependent motion of the gas and the liquid phases, the discrete bubble model employs three different time scales (see Fig. 5.3). The

**Table 5.1:** *Change of bubble properties in a coalescence event*

| Parameter | Before coalescence | After coalescence |
|---|---|---|
| Index | $a$ , $b$ $(a < b)$ | $a$ |
| Mass | $m_a$ , $m_b$ | $m_a^* = m_a + m_b$ |
| Volume | $V_a$ , $V_b$ | $V_a^* = V_a + V_b$ |
| Position | $\mathbf{r}_a$, $\mathbf{r}_b$ | $\mathbf{r}_a^* = \frac{\mathbf{r}_a m_a + \mathbf{r}_b m_b}{m_a^*}$ |
| Velocity | $\mathbf{v}_a$, $\mathbf{v}_b$ | $\mathbf{v}_a^* = \frac{\mathbf{v}_a m_a + \mathbf{v}_b m_b}{m_a^*}$ |

biggest time step $\delta t_{flow}$ is used to solve the Navier-Stokes equations to obtain the liquid phase flow field taking into account the interphase coupling. The flow time step is divided into a fixed number of smaller bubble time steps, $\delta t_{bub}$. During this time step the forces experienced by each individual bubble are determined. Based on the net force, Eq. 5.2 is used to determine the bubble acceleration, which is required to obtain the bubble velocity at the end of the bubble time step. Within each bubble time step, the velocity of the bubbles is assumed to change only due to binary collisions between bubbles. Subsequently, an even smaller collision time step $\delta t_{a,b}$ is used to resolve the direct bubble-bubble and bubble-wall interaction. The size of this time step is not fixed and is determined by the sequence of collision events explained in sect. 5.3.3.

### 5.3.2 Interphase Coupling

The coupling between the gas and the liquid phases appears through the liquid volume fraction $\varepsilon_l$ and the interphase momentum transfer $\Phi$. Since the liquid phase and the bubbles are defined in different reference frames (i.e. respectively Eulerian and Lagrangian), a mapping technique which couples the two reference frames is required. This mapping technique translates the Lagrangian bubble quantities to the Eulerian grid, which are required as closure for the liquid phase equations and vice versa (Euler to Lagrange and Lagrange to Euler).
Kitagawa et al. [9] give the following criteria for the mapping function:

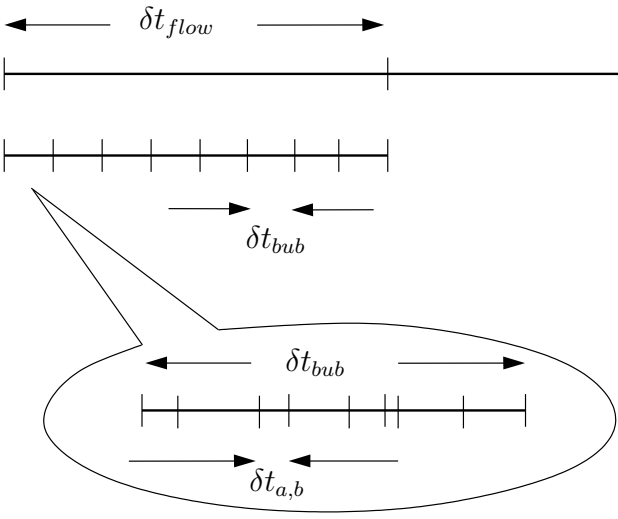


**Figure 5.3:** *Schematic representation of the three time steps employed in the Euler-Lagrange discrete bubble model.*

1. It should be a smooth function, i.e. the first derivatives should be continuous.
2. It should have an absolute maximum around the position where the variable is transferred.
3. For practical reasons it should have a finite domain. At the boundaries of the domain, the function should be zero.
4. The integral of the function over the entire domain should equal to unity to ensure the conservation of variable being transferred.

Kitagawa et al. [9] propose to use a Lagrangian template function which converts the dispersed phase volume fraction to a spatially differentiable distribution. Using Gaussian and goniometric functions they found that false numerical velocity fluctuations can be removed and the velocity fluctuation of the continuous phase due to the migration of dispersed elements (bubbles) through the Eulerian frame can be accurately captured. Using the same line of thought, Deen et al. [32] proposed to use a fourth-order polynomial function to obtain liquid quantities at the bubble position since the integration of this function is cheaper compared to a Gaussian function or the function proposed by Peskin [33]. They found that by employing this technique, a grid independent solution can be obtained.
Following the successful application of the Lagrangian template technique in the Euler-Lagrange framework, we adopt this technique for our model in the present study as well. The template function used is a clipped fourth-order polynomial function following the work of Deen et al. [32]:

$$\omega\left(\ell\right)=\omega\left(x-r_{\ell}\right)=\begin{cases}\frac{15}{16}\left[\frac{\left(x-r_{\ell}\right)^{4}}{n^{5}}-2\frac{\left(x-r_{\ell}\right)^{2}}{n^{3}}+\frac{1}{n}\right]\ ;\ -n\leq\left(x-r_{\ell}\right)\leq n\\ 0\ ;\ \text{otherwise}\end{cases} \tag{5.32}$$

where $2n$ is the width of the mapping window.
Fig. 5.4 schematically shows how the Euler-Lagrange two-way coupling is carried out. The template function is constructed at the center mass of a bubble $\ell$. This template is moving along with the bubble. In any computational cell $j$ the integral of this function, $\int_{\Omega_j}\omega(\ell)\mathrm{d}\Omega$ represents the influence of bubble $\ell$ on cell $j$ or the influence of the Eulerian value in cell $j$ on bubble $\ell$. Note that in 3D space the integral is evaluated as follows:

$$\int_{\Omega_j}\omega(\ell)\mathrm{d}\Omega=\int_{\Omega_{j,z}}\int_{\Omega_{j,y}}\int_{\Omega_{j,x}}\omega\left(x-r_{\ell,x}\right)\omega\left(y-r_{\ell,y}\right)\omega\left(z-r_{\ell,z}\right)\mathrm{d}x\mathrm{d}y\mathrm{d}z \tag{5.33}$$

Given bubble $\ell$ and the width of the mapping window $2n$, the liquid volume fraction in computational cell $j$ is calculated using the following formula:

$$\varepsilon_{l}(j)=1-\frac{\sum_{\forall\ell\in\mathcal{B}}V_{b}(\ell)\int_{\Omega_j}\omega(\ell)\mathrm{d}\Omega}{V_{cell}} \tag{5.34}$$

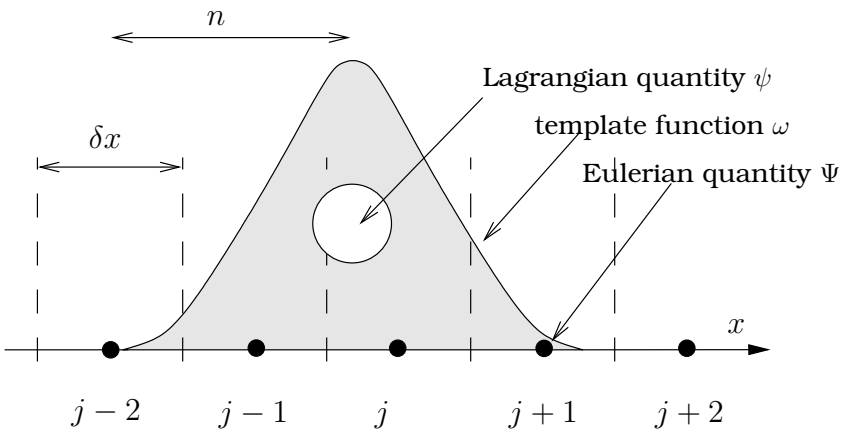


**Figure 5.4:** *Lagrangian and Eulerian two-way coupling using a template window function.*

The momentum transfer rate from the bubbles to the liquid in a computational cell $j$, $\Phi(j)$, can be calculated as:

$$\Phi(j) = \frac{\sum_{\forall \ell \in \mathcal{B}} \phi(\ell) \int_{\Omega_j} \omega(\ell) \mathrm{d}\Omega}{V_{cell}} \tag{5.35}$$

where $\phi$ is the reaction of the momentum transfer exerted on the bubbles, $\phi = -\sum \mathbf{F}$.
The calculation of the force exerted on the bubbles requires Eulerian quantities such as the liquid pressure and velocity to be defined at the position of the bubbles. However, since these quantities are stored in the Eulerian computational cell, again a mapping function should be defined. Using the Lagrangian template function, the Eulerian quantity $\Psi$ at a bubble $\ell$ position, $\psi(\ell)$ is calculated as:

$$\psi(\ell) = \sum_{\forall j \in \mathcal{C}} \Psi(j) \int_{\Omega_j} \omega(\ell) \mathrm{d}\Omega \tag{5.36}$$

### 5.3.3 Bubble dynamics

Solving for the bubble dynamics requires the calculation of the force closures given in section 5.2.1. The liquid quantities at the position of bubbles required to calculate this force are determined using the Euler to Lagrange mapping function defined in Eq. 5.36. Using an explicit first order scheme, the bubble velocity at the new time level is calculated as follows:

$$\mathbf{v}^{n+1} = \frac{\Sigma \mathbf{F}^n}{m_b} \delta t_{bub} + \mathbf{v}^n \tag{5.37}$$

Next, the bubble volume as well as the interphase force for each bubble is mapped to the Eulerian grid using the relation given in Eqs. 5.34 and 5.35 respectively to obtain the liquid phase volume fraction $\varepsilon_l$ and the volumetric interphase momentum transfer rate $\Phi$.
Subsequently bubbles are moved by taking into account the interactions between bubbles or between bubbles and confining walls. The method as explained in sect. 5.2.3 is sufficient for this task, however it is (unnecessarily) expensive for three reasons:

- The set of possible collision partners $\mathcal{N}(\ell)$ consists of all bubbles and obstacles in the entire domain, however partners which are located far away from the bubble $\ell$ are unlikely to collide in an immediate event.
- According to Eq. 5.26 $\delta t_{\ell,m}$ is determined twice since $\delta t_{\ell,m}$ is equal to $\delta t_{m,\ell}$.
- Given $N_e$ collision events during bubble time step $\delta t_{bub}$, using the method described in sect. 5.2.3 one should perform $N_e \times N_b$ bubble movements as given by Eq. 5.27 and evaluate $N_e$ times the new global minimum collision time $\delta t^e_{a,b}$. This procedure also implies that bubbles that are not involved in collisions will (unnecessarily) be moved $N_e$ times on a straight line.

To increase the algorithm efficiency in finding $\delta t^e_{a,b}$ for every collision event, we used the concept of a neighbor list window. Using this concept a dynamic set of $\mathcal{W}(\ell) \subset \mathcal{N}(\ell)$ is introduced, which consists of the neighboring possible collision partners of bubble $\ell$ that are located within a finite region close to the bubble:

$$\mathcal{W}(\ell) := \mathcal{W}(\ell) \subset \mathcal{N}(\ell) \mid \forall m \in \mathcal{N}(\ell), \parallel \mathbf{r}_{\ell m} \parallel < R_w \tag{5.38}$$

To ensure that $\delta t_{\ell,m}$ is not calculated twice, we use a simple restriction rule that bubbles with lower index will only "see" neighboring bubbles or obstacles with higher index but not the other way around. Using this rule, $\mathcal{W}(\ell)$ is divided into two unique subsets, namely $\mathcal{W}(\ell)^+$ and $\mathcal{W}(\ell)^-$ where neighbors with index less and greater than index of bubble $\ell$ are respectively stored (see Fig. 5.5 for illustration of the neighbor list window concept).
Using the concept of neighbor list window, we redefine the global minimum collision time given by Eq. 5.25 as follows:

$$\delta t^{\mathcal{N}}_{\ell,n} = \min(\delta t_{\ell,m}),\ \forall m \in \mathcal{W}(\ell)^+ \tag{5.39}$$

From this point the definition given in Eq. 5.39 is used instead of Eq. 5.26 to calculate the individual minimal collision time $\delta t^{\mathcal{N}}_{l,n}$ unless mentioned otherwise.
Next, the procedure to move bubbles can be optimized by only moving the bubbles which are actually involved in a collision event and recalculate the individual minimum collision times for the partners that just collided as

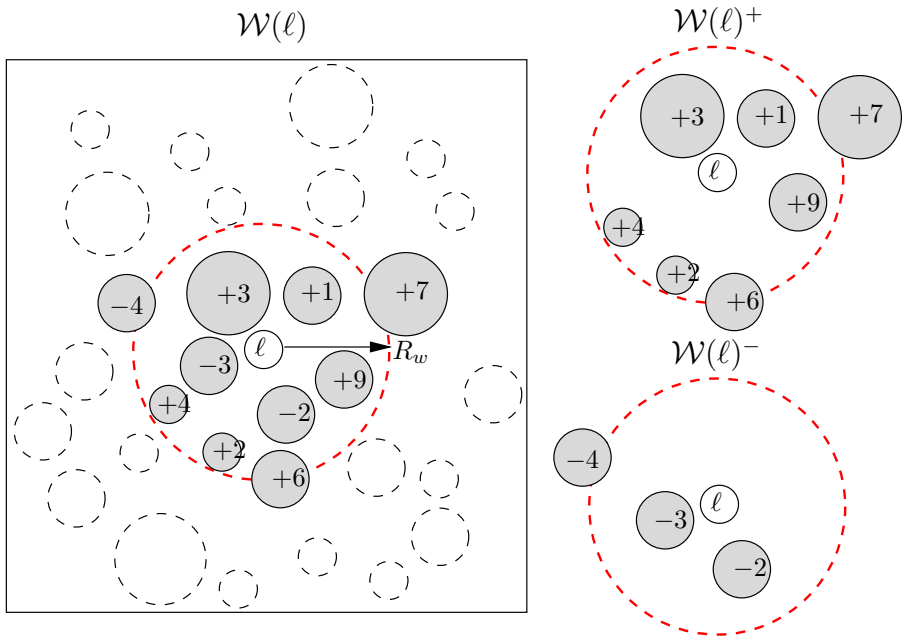


**Figure 5.5:** *The neighbor list of bubble $\ell$, $\mathcal{W}(\ell)$ (shown as grey bubble) consists of all bubbles (or obstacles) within radius $R_w$ from bubble $\ell$. The number represents the index of the bubble relative to bubble $\ell$. In the right picture, the neighbor list is divided based on the index higher or lower then the index $\ell$.*

well as all members of their neighbor list. Using this technique, bubbles will have different timeframes, as the ones which take part in a collision will be moved and their time will be advanced to the present time whereas the other bubbles remain at their original times and positions.
To keep track of the timeframe for each individual bubble, we introduce a variable $t_\ell; 0 \leq t_\ell < \delta t_{bub}; \forall \ell \in \mathcal{B}$ while $t^e; 0 \leq t^e < \delta t_{bub}$ is used to account for the accumulation of the global minimum collision time for the whole sequence of collision events $e$ occurred in the time interval $\delta t_{bub}$. Furthermore the individual minimum collision time given in Eq. 5.25 is modified accordingly by taking into account the latest time and positions of the bubbles to calculate the new individual minimum collision time following collision event $e$:

$$\delta t_{\ell,n}^{\mathcal{N}*} = t^e + \min\left(\delta t_{\ell,m}^*\right), \forall m \in \mathcal{W}(\ell)^+ \tag{5.40}$$

where $\delta t_{\ell,m}^*$ is the collision time between bubbles $\ell$ and $m$ evaluated for the bubble position at time $t^e$.
After all the collisions have been resolved, the time and positions for all bubbles are updated to the time level $\delta t_{bub}$, which concludes the calculation procedure for the bubbles dynamics. For the sake of clarity the reader

**Algorithm 1** Optimized bubble dynamics.

Initialize by setting $t^e = 0$, $t_\ell = 0; \forall \ell \in \mathcal{B}$
Calculate interphase force, velocity and up list neighbor:
$\forall \ell \in \mathcal{B} \Rightarrow \Sigma \mathbf{F}(\ell), \mathbf{v}(\ell), \mathcal{W}(\ell)^+$
Map bubble volume and interphase momentum to Eulerian cell:
$\forall \ell \in \mathcal{B} \Rightarrow V_b(\ell) \rightarrow \varepsilon_l; \mathbf{F}(\ell) \rightarrow \Phi$
Calculate *individual* collision time: $\forall \ell \in \mathcal{B} \Rightarrow \delta t^{\mathcal{N}}_{\ell,n}$
Determine *global* minimum collision time: $\delta t^e_{a,b}$
**while** $\left(t^e + \delta t^e_{a,b}\right) < \delta t_{bub}$ **do**
  Advance time: $t^e = t^e + \delta t^e_{a,b}$
  Update position and time for the collision pair:
  $\forall \ell \in \{a, b\} \Rightarrow \mathbf{r}_\ell(t^e) = \mathbf{r}_\ell(t_\ell) + \mathbf{v}_\ell \cdot (t^e - t_\ell); t_\ell = t^e$
  Process collision between pair $a$ and $b$
  Calculate new *individual* collision time:
  $\forall \ell \in \left\{a, b, \mathcal{W}(a)^-, \mathcal{W}(b)^-\right\} \Rightarrow \delta t^{\mathcal{N}*}_{\ell,n}$
  Determine new *global* minimum collision time: $\delta t^e_{a,b}$
**end while**
Move all bubbles: $\forall \ell \in \mathcal{B}$ calculate $\mathbf{r}_\ell(\delta t_{bub}) = \mathbf{r}_\ell(t_\ell) + \mathbf{v}_\ell \cdot (\delta t_{bub} - t_\ell)$

can refer to Algorithm 1 for the complete procedure of the optimized bubble dynamics.

### 5.3.4 Liquid phase numerical scheme

The numerical solution of the liquid phase conservation equations is based on the SIMPLE algorithm [34] and applied to solve the volume averaged Navier-Stokes equation. The computational cells are labelled by indices $(i, j, k)$ which are located at the cell center and a staggered grid is employed to prevent numerical instability. Using this arrangement the scalar variables are defined at the cell centres whereas the velocities are defined at the cell faces.
Applying first-order time differencing and fully implicit treatment of the convective fluxes, the discretized form of the continuity equation for the continuous phase (Eq. 5.18) becomes:

$$\begin{aligned}(\varepsilon_l \rho_l)^{n+1}_{i,j,k} - (\varepsilon_l \rho_l)^n_{i,j,k} \quad &+ \quad \frac{\delta t}{\delta x}\left\{\langle \varepsilon_l \rho_l u_x\rangle^{n+1}_{i+\frac{1}{2},j,k} - \langle \varepsilon_l \rho_l u_x\rangle^{n+1}_{i-\frac{1}{2},j,k}\right\} \\ &+ \quad \frac{\delta t}{\delta y}\left\{\langle \varepsilon_l \rho_l u_y\rangle^{n+1}_{i,j+\frac{1}{2},k} - \langle \varepsilon_l \rho_l u_y\rangle^{n+1}_{i,j-\frac{1}{2},k}\right\} \\ &+ \quad \frac{\delta t}{\delta z}\left\{\langle \varepsilon_l \rho_l u_z\rangle^{n+1}_{i,j,k+\frac{1}{2}} - \langle \varepsilon_l \rho_l u_z\rangle^{n+1}_{i,j,k-\frac{1}{2}}\right\} = 0\end{aligned} \tag{5.41}$$

where the superscripts $n$ and $n+1$ indicate the old and the new time level respectively. For the discretization of mass and momentum convection terms, the second order accurate Barton scheme [35] is applied.
In the discretization of the momentum equation (Eq. 5.19) the terms associated with the continuous phase pressure gradients are treated fully implicitly while the interphase momentum transfer and other terms are treated

explicitly. The discretization of the continuous phase momentum equation (Eq. 5.19) in each direction is respectively given by:

$$(\varepsilon_l \rho_l u_x)^{n+1}_{i+\frac{1}{2},j,k} = A^n_{i+\frac{1}{2},j,k} - (\varepsilon_l)^{n+1}_{i+\frac{1}{2},j,k} \frac{\delta t}{\delta x} \left\{ (p)^{n+1}_{i+1,j,k} - (p)^{n+1}_{i,j,k} \right\} \tag{5.42}$$

$$(\varepsilon_l \rho_l u_y)^{n+1}_{i,j+\frac{1}{2},k} = B^n_{i,j+\frac{1}{2},k} - (\varepsilon_l)^{n+1}_{i,j+\frac{1}{2},k} \frac{\delta t}{\delta y} \left\{ (p)^{n+1}_{i,j+1,k} - (p)^{n+1}_{i,j,k} \right\} \tag{5.43}$$

$$(\varepsilon_l \rho_l u_z)^{n+1}_{i,j,k+\frac{1}{2}} = C^n_{i,j,k+\frac{1}{2}} - (\varepsilon_l)^{n+1}_{i,j,k+\frac{1}{2}} \frac{\delta t}{\delta z} \left\{ (p)^{n+1}_{i,j,k+1} - (p)^{n+1}_{i,j,k} \right\} \tag{5.44}$$

where momentum convection, viscous interaction, gravity and interphase momentum transfer have been collected in the explicit terms $A^n$, $B^n$ and $C^n$.

The numerical solution of the discretized model equations evolves through a sequence of computational cycles, or time steps, with a duration $\delta t$. For each computational cycle the advanced $(n+1)$-level values at time $t + \delta t$ of all key variables have to be calculated through the entire computational domain. This calculation requires the old $n-$level values at time $t$, which are known from either the previous computational cycle or the specified initial conditions. Then each computational cycle consists of two distinct phases:

- calculation of the explicit terms $A^n$, $B^n$ and $C^n$ in the momentum equation for all interior cells,
- implicit computation of the pressure for the entire computational mesh with an iterative procedure. This implicit procedure consists of several steps.

The first step involves the calculation of the mass residuals for the liquid phase $D_{i,j,k}$ from the continuity equations (Eq. 5.18), for each interior cell:

$$\begin{aligned} D^*_{i,j,k} = (\varepsilon_l \rho_l)^*_{i,j,k} - (\varepsilon_l \rho_l)^n_{i,j,k} \quad &+ \quad \tfrac{\delta t}{\delta x} \left\{ \langle \varepsilon_l \rho_l u_x \rangle^*_{i+\frac{1}{2},j,k} - \langle \varepsilon_l \rho_l u_x \rangle^*_{i-\frac{1}{2},j,k} \right\} \\ &+ \quad \tfrac{\delta t}{\delta y} \left\{ \langle \varepsilon_l \rho_l u_y \rangle^*_{i,j+\frac{1}{2},k} - \langle \varepsilon_l \rho_l u_y \rangle^*_{i,j-\frac{1}{2},k} \right\} \\ &+ \quad \tfrac{\delta t}{\delta z} \left\{ \langle \varepsilon_l \rho_l u_z \rangle^*_{i,j,k+\frac{1}{2}} - \langle \varepsilon_l \rho_l u_z \rangle^*_{i,j,k-\frac{1}{2}} \right\} \end{aligned} \tag{5.45}$$

where the superscript $(*)$ refers to the most recently obtained values. If the convergence criterion:

$$D^*_{i,j,k} < \mathrm{eps}\, (\varepsilon_l \rho_l)^*_{i,j,k} \tag{5.46}$$

is not satisfied simultaneously for all internal computational cells, then a whole field pressure correction is calculated using the following relation:

$$\begin{aligned} &J^n_{i-1,j,k} \delta p^{\mathrm{new}}_{i-1,j,k} + J^n_{i+1,j,k} \delta p^{\mathrm{new}}_{i+1,j,k} + J^n_{i,j-1,k} \delta p^{\mathrm{new}}_{i,j-1,k} + J^n_{i,j+1,k} \delta p^{\mathrm{new}}_{i,j+1,k} + \\ &J^n_{i,j,k-1} \delta p^{\mathrm{new}}_{i,j,k-1} + J^n_{i,j,k+1} \delta p^{\mathrm{new}}_{i,j,k+1} + J^n_{i,j,k} \delta p^{\mathrm{new}}_{i,j,k} = -D^*_{i,j,k} \end{aligned} \tag{5.47}$$

where $J^n$ represents the Jacobi matrix which contains the derivative of defect $D$ with respect to the liquid pressure at time level $n$ and has been obtained analytically from the continuity equation for the liquid phase in combination with the momentum equations. Applying Eq. (5.47) for all internal computational cells results in a set of linear equations that can be assembled in matrix form as:

$$\mathbf{J}^n \cdot \delta \mathbf{p}^{\text{new}} = -\mathbf{D}^* \tag{5.48}$$

To save computational effort the elements of the Jacobi matrix are evaluated at the old time level. By solving Eq. 5.48, a pressure correction term is obtained and new pressure is subsequently calculated followed by calculation of the new velocity field.
Provided that the corresponding estimates of the mass residual (Eq. (5.45)) do not meet the convergence criteria simultaneously for all interior computational cells, the pressure correction equation (Eq. (5.47)) is again calculated using the updated velocity field to compute the mass residual **D** for all cells. This iterative process is repeated until the convergence criteria are satisfied or the specified maximum allowable number of iterations reached.

## 5.4 Parallelization strategy

The dynamic nature of bubbles makes their spatial distribution non-uniform. This implies that the number of collisions is considerably higher in more dense regions when compared with dilute regions [36] which implies that partitioning of the model based on bubble position (i.e. the domain decomposition) cannot give a high parallel efficiency.
In the present model, parallelization for the disperse phase is carried out using a so called *mirror domain technique*. Unlike domain decomposition technique where each processor hold unique computational subdomain and synchronized the data only at the subdomain boundary, each processors in mirror domain technique hold identical complete computational data (i.e. data is mirrored through all processors). Unique data subset is determined for each processors and calculation is conducted by each processors only for this subset of data. Since calculation in each processor is done only for unique portion of data, the data is no longer identical throughout the processors set hence synchronization by interchanging data between processors is required after each calculation step.
This section describes the parallelization strategy of the numerical method explained in sect. 5.3. The model is partitioned and distributed over a set of processors $\mathcal{P} = \{0.1..N_P - 1\}$ using mirror domain technique for the disperse phase while a domain decomposition technique is adopted in solving the continuous phase. The interprocessor communications is carried out using Message Passing Interface (MPI).

**Algorithm 2** The parallel algorithm executed on each processor $\mathcal{P}$ for the optimized bubble dynamics using the mirror domain concept.

Initialize by setting: $t^e = 0$, $t_\ell = 0; \forall \ell \in \mathcal{B}$
Determine *local* bubble set: $\mathcal{B}^{\mathcal{P}} \subseteq \mathcal{B}$
Calculate *local* interphase force, velocity and up list neighbor: $\forall \ell \in \mathcal{B}^{\mathcal{P}} \Rightarrow \Sigma \mathbf{F}(\ell), \mathbf{v}(\ell), \mathcal{W}(\ell)^+$
$\forall \ell \in \mathcal{B}^P$ gather and scatter $\mathbf{v}(\ell)$
Map *local* bubble volume and *local* interphase momentum to the Eulerian cell:
$\forall \ell \in \mathcal{B}^P \Rightarrow V_b(\ell) \rightarrow \varepsilon_l; \mathbf{F}(\ell) \rightarrow \Phi$
Gather (with sum operator) and scatter: $\varepsilon_l$ and $\Phi$
Calculate *local* individual collision time: $\forall \ell \in \mathcal{B}^{\mathcal{P}} \Rightarrow \delta t^{\mathcal{N}}_{\ell,n}$
Determine *local* minimum collision time: $\delta t^e_{a,b}$
Gather (with minimal operator) and scatter to obtain *global* minimum collision time: $\delta t^e_{a,b}$
**while** $\left(t^e + \delta t^e_{a,b}\right) < \delta t_{bub}$ **do**
  Advance time: $t^e = t^e + \delta t^e_{a,b}$
  Update position and time for the collision pair:
  $\forall \ell \in \{a, b\} \Rightarrow \mathbf{r}_\ell(t^e) = \mathbf{r}_\ell(t_\ell) + \mathbf{v}_\ell \cdot (t^e - t_\ell); t_\ell = t^e$
  Process collision between pair $a$ and $b$
  Calculate new *local* individual collision time:
  $\forall \ell \in \left\{\left\{a, b, \mathcal{W}(a)^-, \mathcal{W}(b)^-\right\} \bigcap \mathcal{B}^{\mathcal{P}}\right\} \Rightarrow \delta t^{\mathcal{N}*}_{\ell,n}$
  Determine new *local* minimum collision time: $\delta t^e_{a,b}$
  Gather (with minimal operator) and scatter to obtain new *global* minimum collision time: $\delta t^e_{a,b}$
**end while**
*Locally* move all bubbles: $\forall \ell \in \mathcal{B}^{\mathcal{P}} \Rightarrow \mathbf{r}_\ell(\delta t_{bub}) = \mathbf{r}_\ell(t_\ell) + \mathbf{v}_\ell \cdot (\delta t_{bub} - t_\ell)$
$\forall \ell \in \mathcal{B}^P$ gather and scatter $\mathbf{r}(\ell)$

### 5.4.1 Discrete phase

Using the mirror domain technique for the disperse phase, we exploit the fact that for a given identical initial data set of bubble positions and velocities as well as the continuous phase flow field across the processors, the calculation of the bubble dynamics can be performed independently for each individual bubble in a effective parallel fashion. Data uniformity throughout processors is maintained by either calculating part of the data locally and interchange between processors or execute an identical procedure on identical data locally on each processor.
The serial algorithm shown in Algorithm 1 is modified using the mirror domain concept. The resulting parallel algorithm executed on each processor $\mathcal{P}$ is given in Algorithm 2. First the initialization procedure is executed. Subsequently a local bubble list $\mathcal{B}^{\mathcal{P}} \subseteq \mathcal{B}$ is determined. Two types of bubble partitioning are used: based on memory location and based on bubble index using a round-robin rule. To calculate the interphase force and velocity, the first partitioning technique is used in view of the fact that the message passing interface can transfer continuous data in memory much faster than repeatedly transferring single data. The bubble partitioning using round-robin is used in determining the collision time, since bubbles only *see* other bubbles with a higher index, thus partitioning based on the memory loca-

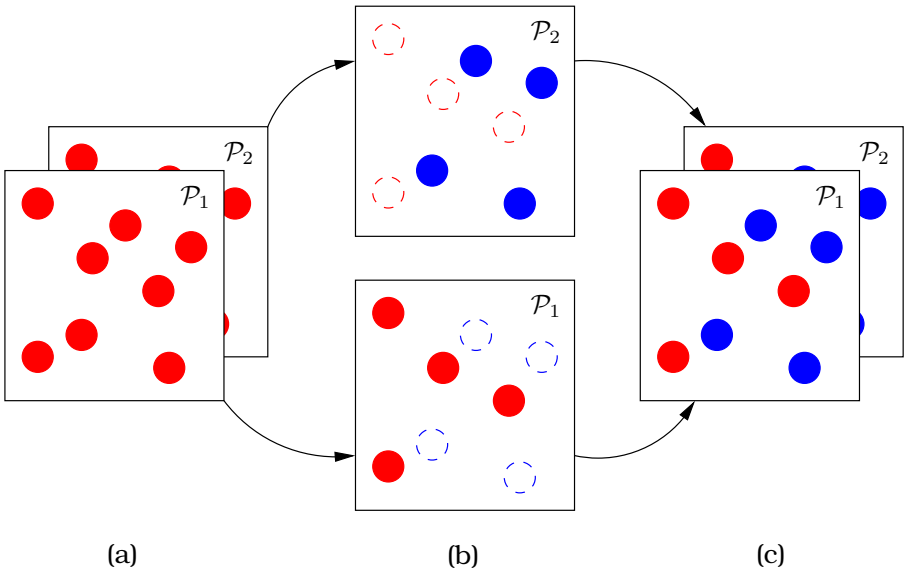


**Figure 5.6:** *Illustration of parallel strategy for bubble force calculation, Euler to Lagrange mapping and Lagrange to Euler mapping. (a) mirrored bubble data at all processors $\mathcal{P}_n$. (b) new data for unique subset of bubble is calculated in parallel on each processors $\mathcal{P}_n$. (c) updated local data is gathered and mirror through all processors.*

tion would only result in poor parallel performance as the processors with a higher index will calculate bubbles with a higher index with less associated possible bubble neighbors, while processors with a lower index will calculate bubbles with a lower index with more bubble associated neighbors.
For all local bubbles, the interphase forces, velocities and up-list neighbors are calculated next (see illustration in Fig. 5.6). The bubble velocities previously calculated locally are combined to obtaine a complete set of bubble velocities in all processors. Subsequently the local interphase forces and the bubble volume are mapped to the local Eulerian grid to obtained local liquid volume fraction and interphase momentum transfer. Using the sum operator available in MPI, these local quantities are combined and redistributed to all processors to obtain the global liquid volume fraction and interphase momentum transfer rate.
Next the collision sequence is determined (see illustration in Fig. 5.7). First the individual collision time is calculated for all local bubbles partitioned in a round-robin manner. For all local individual collision times previously calculated, the local minimum collision time is determined. By making use of the minimum operator available in MPI, the local minimum collision times of all processors are compared to determine the global minimum collision time and distribute the result to all processors. While the accumulated event time

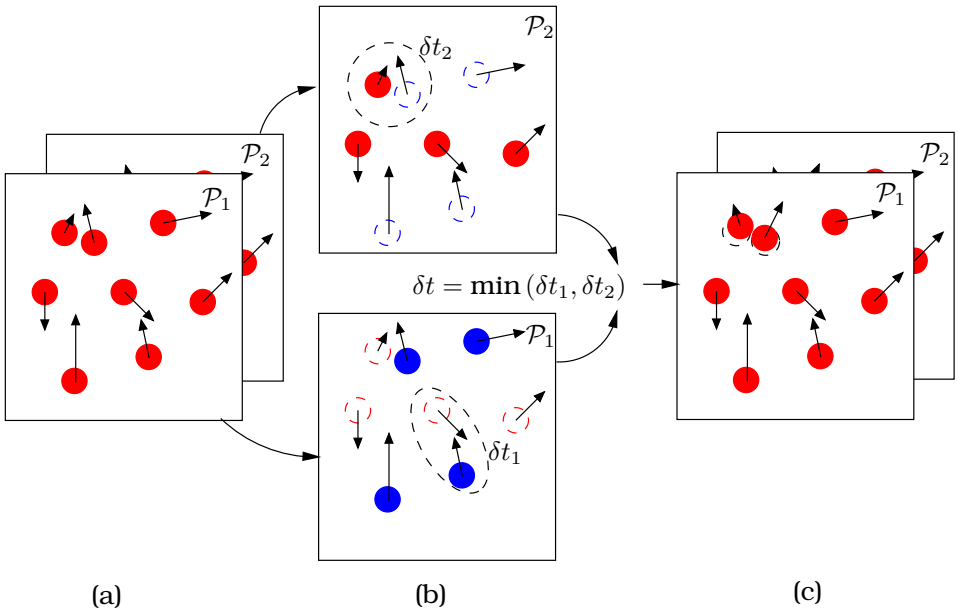


**Figure 5.7:** *Illustration of parallel strategy for bubble encounter detection. (a) mirrored bubble velocity and position at all processors $\mathcal{P}_n$. (b) each processors $\mathcal{P}_n$ calculate processor global minimum encounter time $\delta t_n$ for a unique subset of bubbles. (c) processor global minimum encounter times are compared to find global minimum encounter time $\delta t$ followed by updating the bubble position in all processors by $\delta t$.*

$t^e$ is smaller than the bubble time step, all processors execute an identical procedure which consecutively consists of updating the accumulated event time, updating the positions and individual times for the collision partners, and process the collision between partners $a$ and $b$.
Subsequently, the new local individual collision times are determined for the collision pair and all their down-list neighbors. The calculations however, are carried out only on the processors associated with the considered bubbles. Based on all local individual collision times a new local minimum collision time is determined. Again, using the MPI minimum operator the global minimum collision time is determined and distributed to all processors. These steps are repeated until the next accumulated event time is exceeding the bubble time step. Finally all processors locally move the bubbles to time level $\delta t_{bub}$ and gather the bubble positions from other processors to obtain a complete set of bubbles positions.
Using the present approach, a total of $4 \times N_v$ variables defined on the Eulerian grid ($\Phi$ in three directions + $\varepsilon_l$) and $6 \times N_b$ variables defined on the Lagrangian bubble positions (velocities and positions in three directions) have to be interchanged between processors outside the while loop for ev-

ery $\delta t_{bub}$, while for every collision event 3 variables consisting of the local minimum collision time and collision partners have to be interchanged. All communications except the ones inside the while loop are carried out in a non-blocking fashion (i.e. overlapping with the calculation) to reduce the effective communication time. The amount of data that has to be communicated for every collision event is very small hence cannot benefit from overlapping communication with calculation.
It is noted that there is no memory reduction for the main bubble variables such as positions and velocities, as these variable have to be known on each processor, however significant memory reduction arises from the up-list neighbor requirements. For a maximum number of $N_{\mathcal{W}}^{+}$ up-list neighbors per bubble, a total of $N_b \times N_{\mathcal{W}}^{+}$ memory blocks should be allocated in a serial calculation. Whereas for a number of $N_b^{\mathcal{P}}$ local bubbles, only $N_b^{\mathcal{P}} \times N_{\mathcal{W}}^{+}$ memory blocks are required on each processors for the parallel calculation. As the number of main bubble variables is much less than $N_{\mathcal{W}}^{+}$, one might expect to have a memory reduction factor of $\approx N_P$ by running a simulation in parallel with $N_P$ number of processors.

### 5.4.2 Continuous phase

The continuous phase calculation is parallelized by making use of the PETSc library version 2.3.0 [37–39]. PETSc is a suite of data structures and routines for the scalable (parallel) solution of scientific applications modeled by partial differential equations. It employs the MPI standard for all message-passing communication. PETSc has been used for a wide variety of applications, including computational fluid dynamics, structural dynamics, materials modeling and econometrics. Many of the solvers are appropriate for problems discretized using either structured grids or unstructured grids. In the present study we consider PETSc as a black box hence it will only briefly be discussed. Interested readers are referred to the PETSc user manual or publications on application simulations developed by PETSc users [40–43].
The discrete bubble model uses the linear solver component of PETSc to solve the pressure correction equation given in Eq. 5.48 and uses the efficient parallel data formats provided by PETSc to store the Jacobian matrix and the defect vector. As the parallel calculation for the discrete phase requires that complete data sets of the liquid velocity and pressure are known on all of the processors, solving the pressure correction matrix using PETSc is straightforward. For instance, one can divide the hepta-diagonal matrix in several block rows according to the number of processors involved in the calculation and fill the corresponding blocks locally as shown in Fig. 5.8. By calling the PETSc linear solver command in each processor the matrix is solved iteratively in parallel by taking into account coupling with other matrix elements which reside on the other processors. After convergence is reached, the solution block of the linear equations (i.e. the pressure correction terms) are available locally. Subsequently each processor can in-

terchange their local pressure correction terms to obtain a complete set of pressure corrections followed by the calculation of new pressure and velocities for the whole domain.
PETSc provides interfaces to various Krylov methods, such as conjugate gradient (CG), generalized minimal residual (GMRES), biconjugate gradient (BCG), etc. It also provides access to various preconditioners such as Jacobi, block Jacobi, additive Schwartz, etc. Several tests have been conducted using various combinations of the Krylov methods and the associated preconditioners. It was found that the combination of the conjugate gradient Krylov method with the block Jacobi preconditioner gives the best performance for the present model. The number of subdomain blocks for the block Jacobi is set to one (default value) so that each processor gets a complete subdomain of the problem and does a single local incomplete factorization on the Jacobian corresponding to this subdomain [43]. To increase convergence rate, elements in the off diagonal block matrix which are responsible for the coupling terms between processors should be minimized. Therefore in the present study the matrix is arranged in such way that each block rows correspond with the physical domain partition which gives fewest elements in off-diagonal blocks. By rearranging the matrix structures in this way, the solution is obtained about 20% faster compared to regular matrix partition

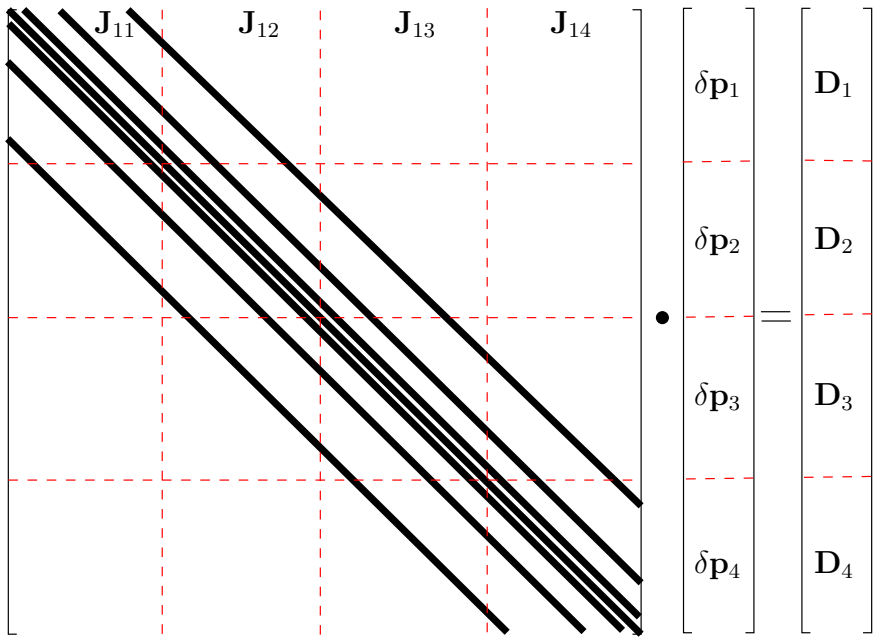


**Figure 5.8:** *Illustration of the decomposition of an hepta-diagonal matrix resembling the three dimensional pressure correction equations into 4 block rows.*

**Table 5.2:** *Simulation conditions for the simulation of homogeneous bubbly flow in a lab-scale bubble column.*

| Variable | Value |
|---|---|
| Physical domain | $0.2\ \mathrm{m} \times 0.2\ \mathrm{m} \times 0.6\ \mathrm{m}$ |
| Computational cell | $60 \times 60 \times 180$ |
| $\delta t_{flow}$ | $10^{-3}$ s |
| $\delta t_{bub}$ | $10^{-4}$ s |
| Liquid density | $10^3\ \mathrm{kg/m^3}$ |
| Liquid viscosity | $10^{-3}$ Pa s |
| Gas density | $1\ \mathrm{kg/m^3}$ |
| Surface tension | $0.073\ \mathrm{N/m}$ |
| Gravitational acceleration | $9.81\ \mathrm{m/s^2}$ |
| Initial bubble diameter | $4 \times 10^{-3}$ m |
| Size of window mapping | $3d_b$ m |
| Number of gas nozzle | 625 (uniformly arranged with $8\ \mathrm{mm^2}$ pitch distance) |

as shown in Fig. 5.8.

## 5.5 Parallel algorithm verification and benchmark

In this section the parallel algorithm is subject to verification and benchmarking. A homogeneous bubbly flow in a square lab-scale bubble column with medium to high gas hold-up is selected as a test case since it represent a previously "beyond reached" case to simulate with an Euler-Lagrange model. The simulation conditions are summarized in Table 5.2. Air is injected from 625 nozzles located at the bottom of the column into an initially quiescent liquid. The boundary conditions are imposed to the column using the flag matrix concept of Kuipers et al. [44] as illustrated in Fig. 5.9. The definition of each boundary condition is given in Table 5.3. The configuration of boundary conditions used in the simulations has been carefully investigated. The prescribed pressure cells close to the column surface wall are required as inlet as well as outlet channel to compensate for the change of liquid volume due to bubbles entering and leaving the column. The width of this pressure cell slit is one third of the total width of the column and located in the middle. It was found that this configuration avoids instabilities developing at the top surface of the column [8]. The simulation was conducted on an SGI Altix 3700 system, consisting of total 416 CPUs (Intel Itanium 2, 1,3 GHz, 3 Mbyte cache each). Every node in the Altix is a CC-NUMA machine (i.e. Cache-Coherent Non Uniform Memory Access). In the CC-NUMA model, the system runs one operating system and shows only a single memory image to the user even though the memory is physically distributed over the processors. Since processors can access their 'own' memory (i.e. memory on the same physical board as the processor) much faster than that of other processors, memory access is

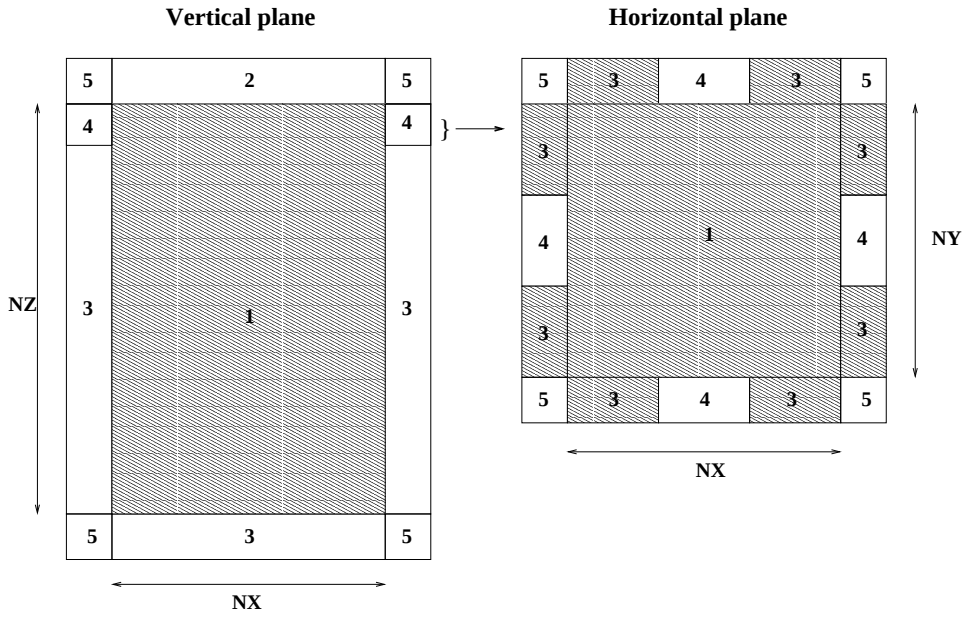


**Figure 5.9:** *Typical boundary conditions used in simulations with the discrete bubble model. The vertical plane is at $j = NY/2$ while the horizontal plane is at $k = NZ$.*

**Table 5.3:** *Cell flags and corresponding cell types used in defining boundary conditions.*

| Flag | Boundary conditions |
|---|---|
| 1 | Interior cell, no boundary conditions specified |
| 2 | Impermeable wall, free slip boundary |
| 3 | Impermeable wall, no slip boundary |
| 4 | Prescribed pressure cell, free slip boundary |
| 5 | Corner cell, no boundary conditions specified |

non uniform (NUMA).
In the present simulation, the domain partitioning in the continuous phase calculation was applied in the $z$ direction only as can be seen in Fig. 5.10. This partition configuration has been selected since it gives the smallest inter-domain connection, which minimizes data communication between processors.

### 5.5.1 Parallel verification

For verification and benchmarking purposes a superficial gas velocity of $3\,\mathrm{cm/s}$ is used. The verification is performed by comparing the simulation results obtained by the serial and parallel algorithms. The liquid phase

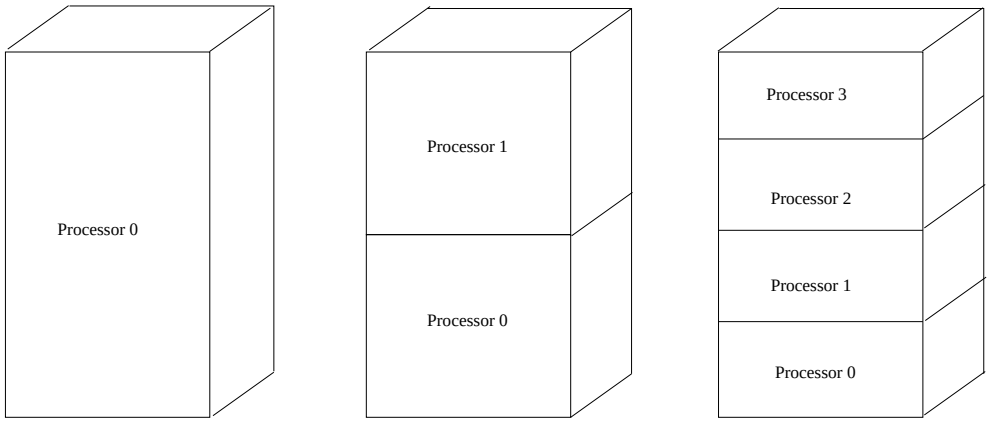


**Figure 5.10:** *Domain partitioning for parallel flow solver calculation using 1,2 and 4 processors.*

velocity in the vertical direction is compared, moreover we also compare the mapped bubble vertical velocity. For this comparison series of simulations were conducted from identical initial conditions. The comparison was made after the flow has evolved during 500 flow time steps. Figure 5.11 (top) shows the vertical liquid velocity along the vertical center-line of the column while Fig. 5.11 (bottom) shows the mapped bubble vertical velocity on the same line. As we can see, after 500 flow time steps, there are no significant differences between the serial and parallel solutions.
The parallelization of the parallel bubble solver algorithm is verified by comparing the time series of the $l_2$ norm of the consecutive event contact points. The event contact point between collision partners $a$ and $b$ is determined using the following relation:

$$\mathbf{x}_c = \mathbf{x}_a + \{R_a + 0.5\,(\mid \mathbf{x}_{ab} \mid - (R_a + R_b))\} \cdot \frac{\mathbf{x}_{ab}}{\mid \mathbf{x}_{ab} \mid} \tag{5.49}$$

with $\mathbf{x}_{ab} = \mathbf{x}_b - \mathbf{x}_a$ the translation vector between collision partners $a$ and $b$. Figure 5.12 shows the comparison of the event contact point between collision partners recorded in the simulation using the serial and parallel algorithms. As we can see, the differences between sequential and parallel solution are not observable, which implies that similar events are obtained using both algorithms.

## 5.5.2 Parallel performance

According to Ferziger and Peric [45], the analysis of the performance of parallel programs can be characterized by the *speed-up* factor and the *efficiency*

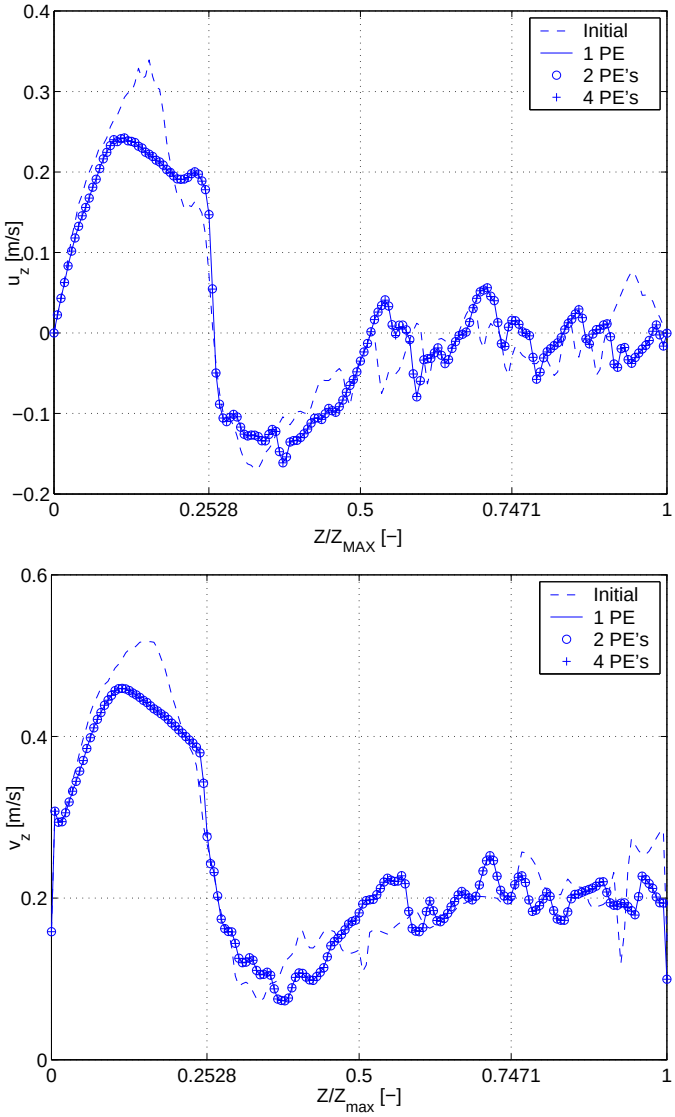


**Figure 5.11:** *Comparison of $u_z$ (top) and $v_z$ (bottom) at the vertical center-line of the column, the vertical lines in the figure represent the locations of the partition domains. The simulation is started from identical initial conditions for the serial and parallel cases. The comparison was made after the flow has evolved during 500 flow time steps from the initial condition.*

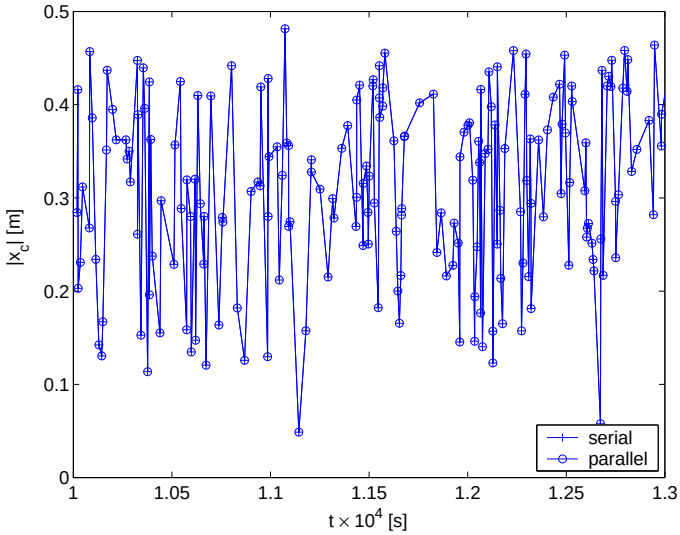


**Figure 5.12:** *Time series of the $l_2$ norm of a sequence of $200$ event contact points as obtained from the serial and parallel algorithms.*

defined respectively by:

$$S_n = \frac{T_s}{T_n} \tag{5.50}$$

and

$$E_n = \frac{T_s}{nT_n} \tag{5.51}$$

where $T_s$ is the execution time for the best serial algorithm on a single processor and $T_n$ is the execution time for the parallelized algorithm using $n$ processors.

In this study the measurement of calculation times was conducted after the flow was fully developed, which can be assessed by monitoring the number of bubbles present in the column. When the column reaches a steady state condition (in the terms of bubble hold-up) the number of bubbles entering and leaving the column is more or less similar. For the present study, the steady state is reached $10\,\mathrm{s}$ after the bubbles is enter the column.

Figure 5.13 (top) shows the speedup obtained with 1, 2, 4, 8, 16 and 32 processors while Fig. 5.13 (bottom) shows the corresponding efficiency. As can be seen from these figures, the proposed parallel algorithm demonstrates good scalability. Using 32 processors a speed-up of more than 20 can be reached while the corresponding efficiency is still relatively high. The performance of the total model in terms of speed-up and efficiency is a weighted average of the underlying dispersed and the continuum parts. For this reason, the curves for the total model always lie in between the curves for the

two separate parts.

## 5.6 Application to bubbly flow

In this section, the proposed method is applied to simulate the buoyancy driven flow in a square bubble column for an air-water system. The square bubble column introduced in sect. 5.5.1 is used as a base configuration. Two cases are simulated; a case with and without coalescence model, to investigate the influence of coalescence on the bubble size distribution and the hydrodynamic characteristics.

### 5.6.1 Hydrodynamics of homogeneous bubbly flow

Air is injected through 625 individual nozzles into an initially quiescent liquid as shown in Fig. 5.14. Shortly after the bubbles are released, they start to rise in the column and drag the liquid upwards. For the case that the nozzles are only present in the center area of the column, Darmana et al. [8] observed a mushroom-shaped bubble plume during the initial period of bubble injection. In the present simulation this shape is not observed due to the uniform aeration, which induces a uniform liquid flow. Instead of generating a mushroom-shaped bubble plume, the bubbles rise in a uniform fashion.
After about $3\,\mathrm{s}$ the first bubble escapes from the column. Liquid vortices are generated close the surface of the column with upward direction in the center region and downward direction close the corners of the column. This type of liquid vortices is normally responsible for creating large scale fluctuations as they will travel downwards in a region close to the wall and influence the bubbles close to the inlet region. However in the present configuration, the down flow which is developed near the wall region is counteracted by the bubbles moving upward in that region resulting in suppression of the liquid down flow and a local bubble velocity reduction.
A fully developed flow condition is reached after about $10\,\mathrm{s}$ of operation. A typical snapshot of the flow structures after the flow has become fully developed is shown in Fig. 5.15. The figure clearly depicts that the bubble trajectories are rectilinear in the small region close to the inlet region of the column. In this region, bubble velocities are mainly directed vertically resulting in a smooth path of bubbles. However as the bubbles move further from the inlet, interaction with the liquid as well as interaction with the other bubbles becomes more pronounced which turns the bubble trajectory into a non-smooth path. In this situation the horizontal components of the bubble velocities become more significant resulting in non-smooth bubble trajectories.
The pronounced liquid agitation which prevails during the first few seconds of the simulation has disappeared and is replaced by various small vortices,

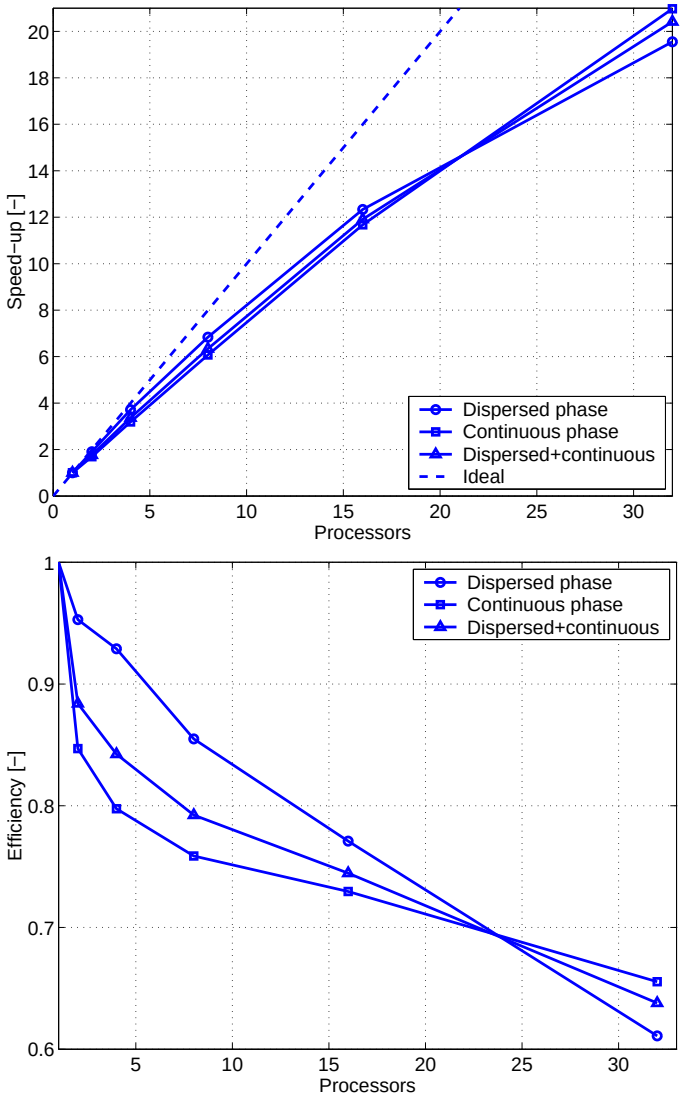


**Figure 5.13:** *Speed-up (top) and efficiency (bottom) of the dispersed and continuous phase solver for different number of processors to evaluate the performance of the parallel algorithm on a* $60 \times 60 \times 180$ *numerical grid containing* $\approx 10^5$ *bubbles. The measurement was conducted after the flow in the column is fully developed.*

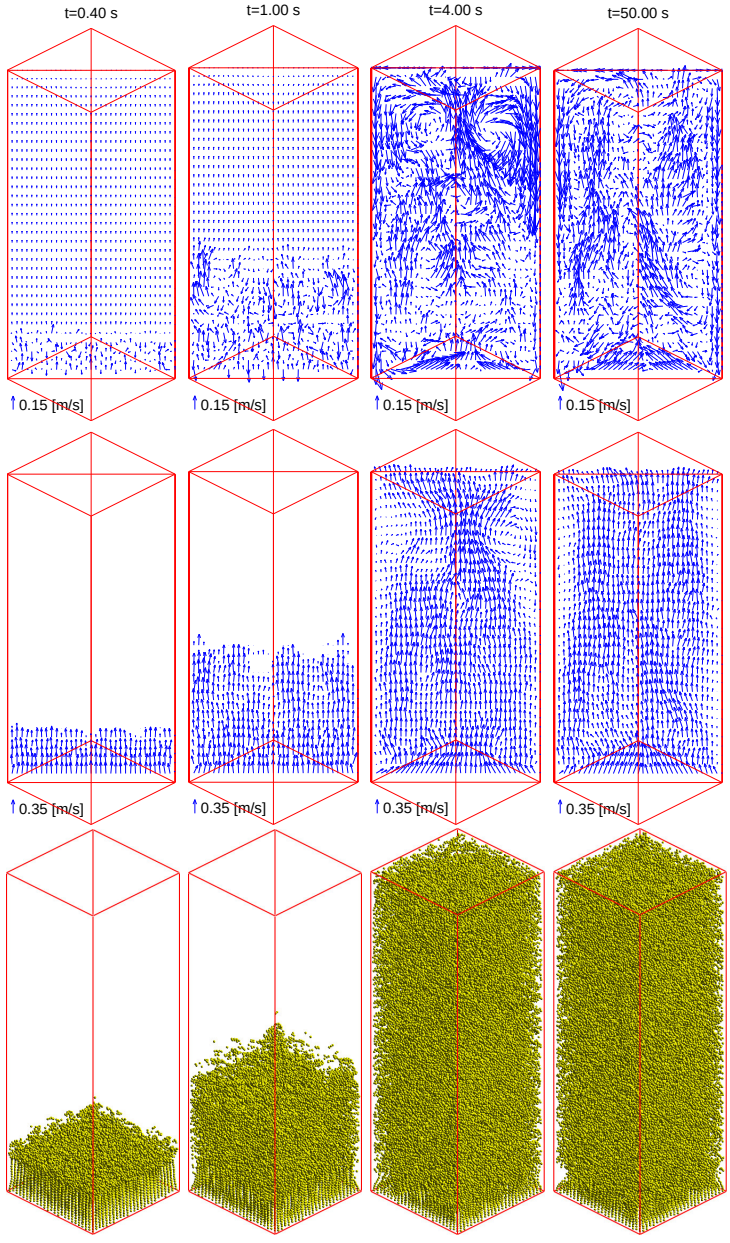


**Figure 5.14:** *Series of corresponding liquid velocity fields, bubble velocity fields and bubble positions obtained from the simulation of an non-coalescing air-water bubble column at different times after the air flow was switched on. Gas superficial velocity* = 3 cm/s.

which are distributed randomly in the liquid phase. These vortices are not strong enough to influence the bubbles trajectory in general as can be seen in the figure showing the bubble path-way. A weak down flow is observed in the vicinity of each corner of the column which slightly reduces the bubble velocities in these areas.
The time-averages of the gas phase volume fraction, bubbles velocity and the liquid velocity of the column are shown in Fig. 5.15. The time-average of quantity $\phi$ is calculated as:

$$\overline{\phi} = \frac{1}{N_t} \sum_{i=1}^{N_t} \phi_i \tag{5.52}$$

where $N_t$ is the number of time steps used in the averaging.
The time-averaged quantities clearly show that the column exhibits uniform behavior. The gas volume fraction is uniform almost everywhere except close to the corner regions where there are slightly less bubbles present. Variation of the gas volume fraction can also be observed close to the inlet region. In this region stripes corresponding to higher and lower volume fractions are discernible as a direct result of the rectilinear bubble motion in this region. On average the bubble velocity is relatively uniform except close to the corner area where the bubble velocity is lower than in the rest of the column. A very low average liquid velocity is observed in the entire column. A weak large scale circulation pattern is observed in the upper half region of the column where up-flow is located in the center region while down-flow is located in the corners. The down-flow however terminates to exist at about one third of the column height.

### 5.6.2 The effect of coalescence

Next, the influence of coalescence on the flow structures is investigated. A fully developed flow condition in the column which was obtained from the model without coalescence was used as the initial condition. After the coalescence model was turned on, the simulation was run for another $10\ \mathrm{s}$ to allow the column to reach its new fully developed condition. A typical snapshots of a fully developed flow structure when the bubble coalescence model is taken into account is given in Fig. 5.16a. It can be seen that the column exhibits different flow structures compared to the case without coalescence. First of all a non-uniform bubble size distribution is obtained as a direct result of the coalescence process. The variation of the bubble size automatically induces a variation of the bubble velocities as big bubbles tend to move faster than small bubbles. As the speed of a bubble increases, it will catch the smaller (i.e. slower) bubbles on its path. Another coalescence event might occur following the collision resulting in even bigger and faster moving bubbles, which leads to a continuous growth of the bubbles as they ascend.

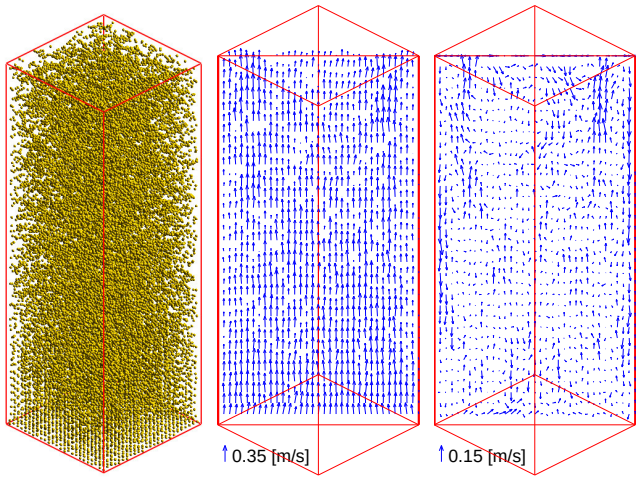


(a) Instantaneous snapshots

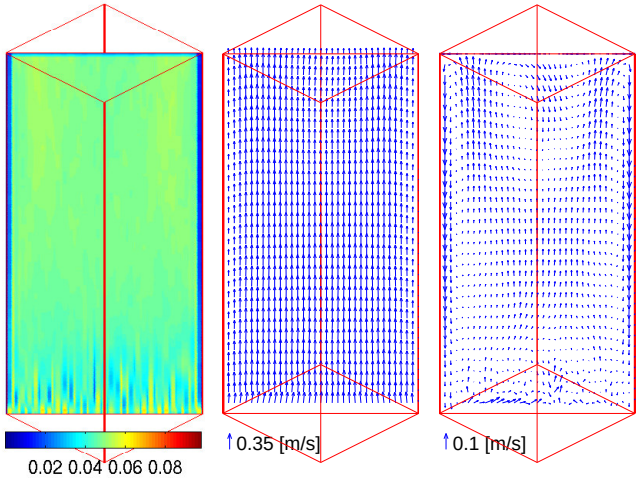


(b) Average quantities

**Figure 5.15:** *Snapshots of instantaneous bubble positions, bubble velocities and corresponding liquid velocities at* $t$=65 s *(a) and the corresponding averaged quantities of the gas phase volume fraction, bubble velocity and liquid velocity (b). Averaging is taking place for the last* 45 s*. Simulation results with a gas superficial velocity of* 1 cm/s *and the coalescence model turned off.*

The lift coefficient, which initially tends to disperse the bubbles towards the wall, changes sign as the bubbles are getting bigger and as a consequence cause to move the bubbles toward the center of the column instead. This behavior produces a narrowing of the bubble swarm near the top region of the column as can be observed in Fig.5.16a. The bubble size distribution also influences the liquid velocity as the fast moving bubbles will induce a higher liquid velocity as well. The snapshots clearly show that the liquid velocity gradually turns into a irregular pattern as the mean bubble size increases. In the corner regions where there are less bubbles, strong downward liquid flow is developed. This flow appears to push the bubble dispersion toward the center column even further.
The corresponding time-averaged flow field of the coalescence case is given in Fig. 5.16b. The average gas volume fraction clearly shows the narrowing behavior of the bubble dispersion. The average bubble velocity is higher compared to the case without coalescence and increases further with increasing height. Furthermore, the regions in the corners with low bubble velocity are wider compared to the non-coalescing case. The average liquid velocity clearly shows large scale circulation patterns with upward flow in the center of the column and downward flow in the corners.
A more quantitative comparison is obtained by comparing the time-average liquid and bubbles velocities along the horizontal axis at a height of $h = 0.45\,\mathrm{m}$. Figures 5.17a and 5.17b show the lateral profiles of the liquid and bubble velocity respectively. As can be seen from these figures, without coalescence model, the average liquid velocity is very small. In the central region of the column the averaged liquid velocity is $-1\,\mathrm{cm/s}$ while a maximal velocity of $4\,\mathrm{cm/s}$ is observed in the region close to the wall. When the coalescence model is turned on, the averaged liquid velocity is dramatically changed as the averaged liquid velocity now shows velocities of about $12.5\,\mathrm{cm/s}$ in the central part of the column. A similar picture emerges for the average bubble velocity as the velocity at the center of the column is increased from $20\,\mathrm{cm/s}$ for the case without coalescence to $35\,\mathrm{cm/s}$ for the case with coalescence.
The influence of coalescence on the average liquid velocity fluctuations is shown in Fig. 5.18. The average liquid velocity fluctuations are calculated as:

$$\mathbf{u}' = \frac{1}{N_t}\sqrt{\sum_{i=1}^{N_t}\left(\mathbf{u}_i - \overline{\mathbf{u}}\right)^2} \tag{5.53}$$

As can be see from Fig. 5.18, the coalescence model also amplifies the velocity fluctuations. The fluctuations in the vertical direction which was formerly uniform has doubled in the center region of the column and increased by a factor of three near the wall when the coalescence is taken into account. A similar result is obtained for the fluctuations in the horizontal direction where the fluctuations are increased four times over almost the entire width of the column. The amplification of the velocity fluctuations arises since the coalescence leads to the formation of regions with lower gas hold-up where

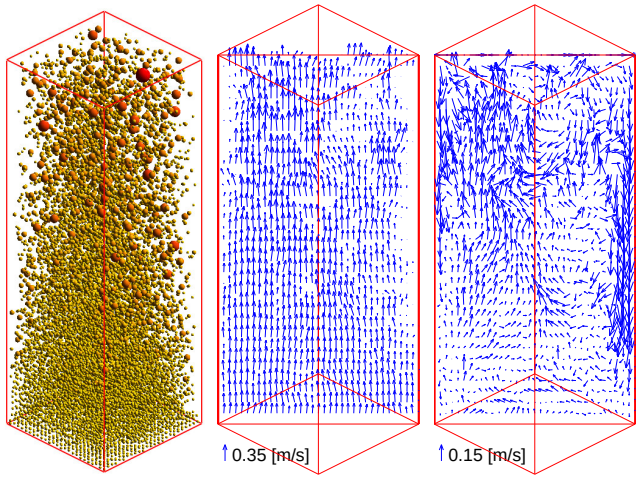


(a) Instantaneous snapshots

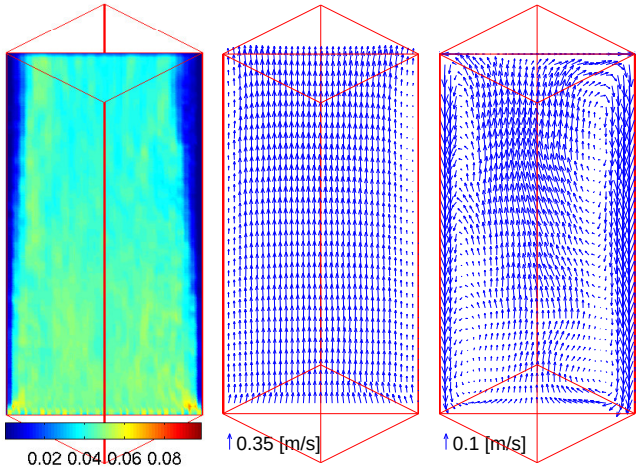


(b) Average quantities

**Figure 5.16:** *Snapshots of instantaneous bubble positions, bubbles velocities and corresponding liquid velocities (a) and the averaged quantities of the gas phase volume fraction, bubble velocity and liquid velocity (b). Simulation results with a gas superficial velocity of* $1\,\mathrm{cm/s}$ *and the coalescence model turned on.*

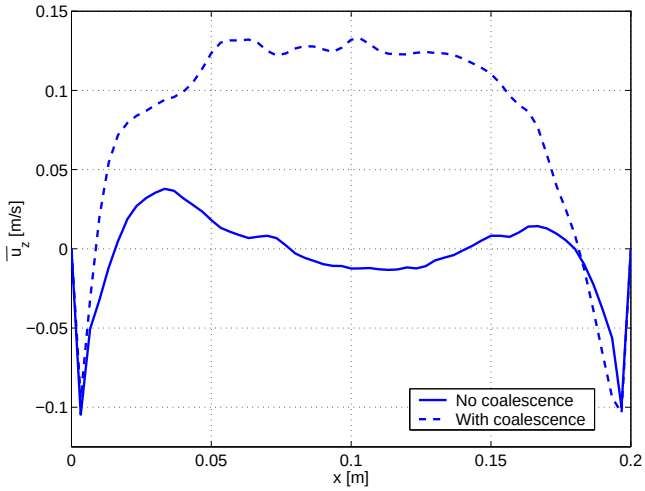


(a) Average liquid velocity in the vertical direction

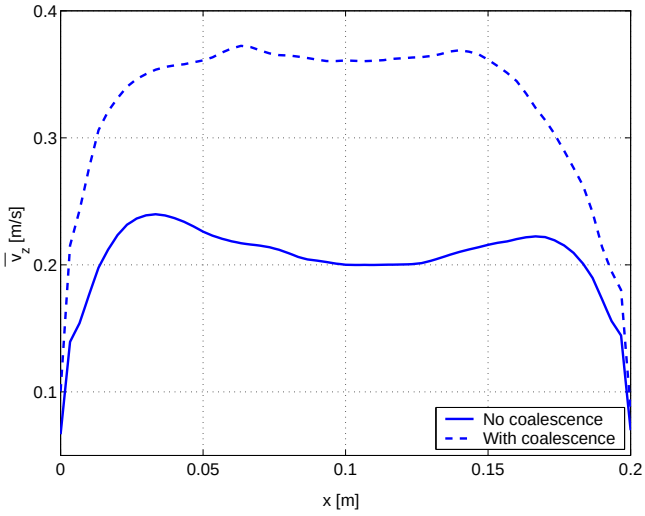


(b) Average bubble velocity in the vertical direction

**Figure 5.17**: *Comparison of the average liquid velocities (a) and average bubble velocities (b) between the cases with and without coalescence at a height of* $z = 0.45\,\mathrm{m}$ *and a depth of* $y = 0.1\,\mathrm{m}$*. The gas enters the column uniformly at a superficial velocity of* $1\,\mathrm{cm/s}$.

liquid vortices start to develop. These vortices in turn will influence the bubble motion and the induced velocity fluctuations.
Figure 5.19 (top) shows the bubble size distribution in four different vertical regions of the column. The regions are four non-overlapping, equally-sized compartments. All bubbles inside one particular compartment are grouped based on their volume resulting from binary coalescence events. Ten different bubble classes are used, resembling bubble sizes resulting from 1 to 9 coalescence events. Furthermore, the tenth class contains bubbles that experienced more than 9 coalescence events. The number of bubbles in each class is normalized by the total number of bubbles in the compartment.
In the lower part of the column, the bubble size appears to be homogeneous with $90\%$ of the bubbles having the initial size of $4\,\mathrm{mm}$, while about $10\%$ of the bubble population has experienced one coalescence event. A sudden change can be observed at $h = 0.225\,\mathrm{m}$ as more than $50\%$ of the bubbles in this region have already coalesced (i.e. about $30\%$ coalesced once while the rest of the bubbles coalesced more than once). At $h = 0.375\,\mathrm{m}$ only $30\%$ of the total bubble population did not experience coalescence. This number is more or less equal to the number of bubbles that already coalesced once while $15\%$ of the bubbles in this region coalesced twice. In this region we can also observe that about $5\%$ of the bubbles coalesced more than 8 times. In the two upper regions of the column the bubble distribution is more or less similar, however we can clearly see that the number of bubbles that coalesced more than 9 times has doubled in the upper region compared to the region below into more than $10\%$.
For each region the average of the bubble size distribution is represented by the Sauter mean diameter which reflects the mean bubble size for all bubbles in the region averaged on basis of specific area and is given as:

$$d_{32} = \Sigma_{i=1}^{N_b} \frac{d_i^3}{d_i^2} \tag{5.54}$$

Figure 5.19 (bottom) shows the Sauter mean diameter at six different locations measured from the bottom of the column shown in Fig. 5.16. As can be seen for this particular case, due to coalescence the volume mean diameter is increased almost linearly as a function of distance from the inlet. It also appears from this simulation that due to coalescence the bubbles have doubled in size during their residence in the column.

### 5.6.3 Integral gas hold-up as function of superficial velocity

With the present parallel algorithm, the limitation of the discrete bubble model on the gas hold-up that can be treated has virtually been eliminated. In this study we use the model to predict the integral gas hold-up as a function of the superficial gas velocity. Using a gas inlet consisting of multiple nozzles that are uniformly arranged at the base of the column, Harteveld et

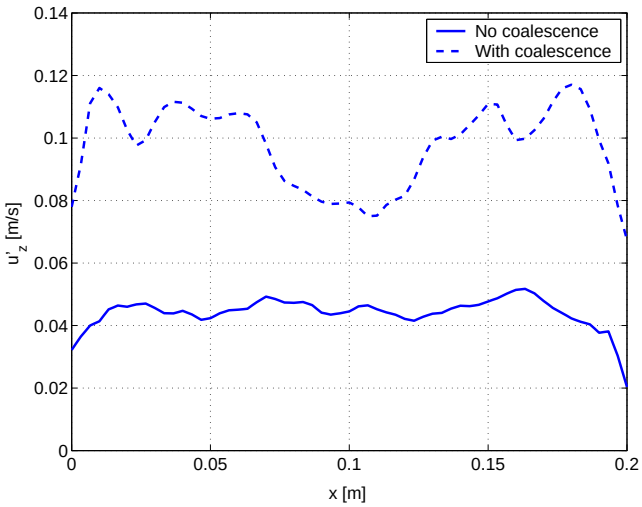


(a) Average liquid velocity fluctuations in the vertical z-direction

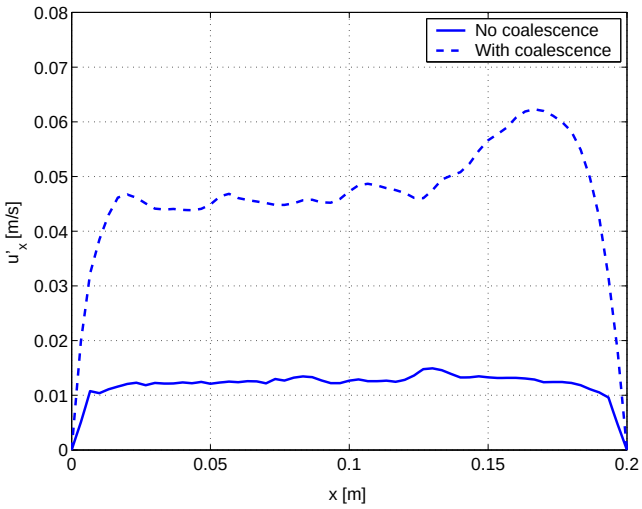


(b) Average liquid velocity fluctuations in the horizontal x-direction

**Figure 5.18:** *Comparison of the average liquid velocity fluctuations in the vertical (a) and horizontal direction (b) between cases with and without coalescence at a height of* $z = 0.45\,\mathrm{m}$ *and a depth of* $y = 0.1\,\mathrm{m}$*. The gas enters the column uniformly at a superficial velocity of* $1\,\mathrm{cm/s}$*.*

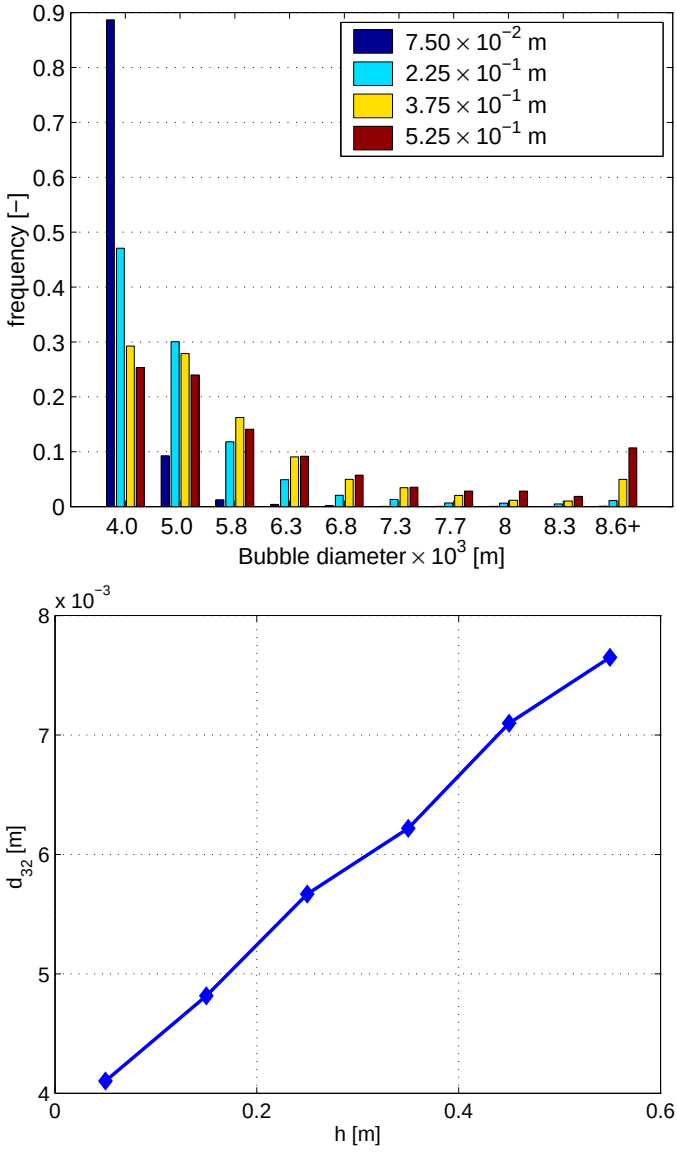


**Figure 5.19:** *Top: bubble size distribution in four regions along the vertical axis of the column ($x = 0.1\,\mathrm{m}$ ; $y = 0.1\,\mathrm{m}$). Bottom: Sauter mean diameter ($d_{32}$) along the vertical axis of the column. The gas enters the column uniformly at a superficial velocity of* $1\,\mathrm{cm/s}$.

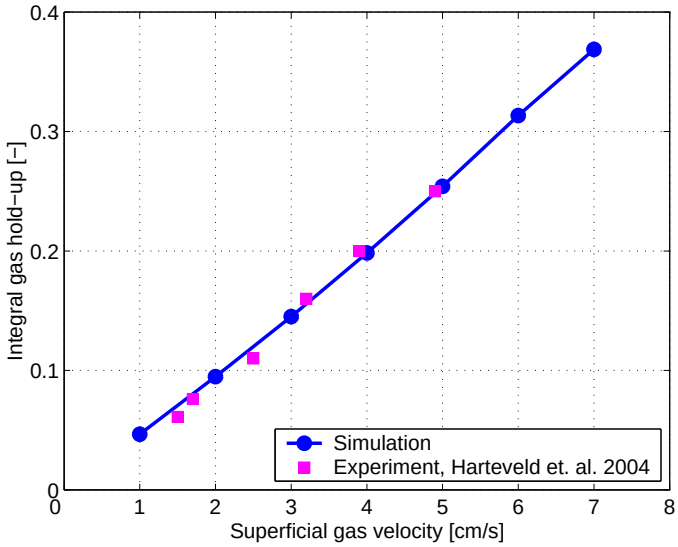


**Figure 5.20:** *Dependency of the integral gas hold-up in the bubble column predicted by the present model in comparison with the experimental measurement with similar superficial gas velocity by Harteveld et al. [46].*

al. [46] showed that a much higher gas hold-up can be obtained compared to other types of inlets such as sintered or porous plates.
The column geometry and the nozzle arrangement explained in Sect. 5.5 is used as a base model. Without the coalescence model taken into account, cases were run with superficial velocities ranging between $1\,\mathrm{cm/s}$ and $7\,\mathrm{cm/s}$ and the average integral gas hold-up under fully developed conditions is monitored and compared with experimental measurement data of Harteveld et al. [46]. It is noted that the column used in the work of Harteveld is cylindrical, whereas it is square in our work. This has an effect on the liquid down flow, which mostly takes place in the circumferential wall area and in the corners respectively. It is believed however that the flow in the core in the column is hardly affected by the geometry, which allows us to make a direct comparison.
Figure 5.20 shows the comparison between the simulation results and the experimental measurement data. As can be seen a gas hold-up up to $37\%$ can be obtained with the present model. The number of bubbles simultaneously present in the column ranges from about $3.3 \times 10^4$ at a superficial velocity of $1\,\mathrm{cm/s}$ to $2.7 \times 10^5$ at a superficial velocity of $7\,\mathrm{cm/s}$. The increase in gas hold-up with the superficial gas velocity is almost linear as can be inferred from Fig. 5.20. The simulation results show perfect agreement with the experimental measurements.

## 5.7 Conclusions

In this study, a parallelization strategy for a two-phase Euler-Lagrange model for bubbly flow has been successfully developed accounting for four way coupling. A new mapping technique based on the work of Kitagawa et al. [9] has implemented which relates data in the Eulerian and Lagrangian frame.
The implementation of the parallel algorithm was verified by comparing the computational results obtained from the serial and parallel algorithms. It was demonstrated that both algorithms give the same results. Speed-up and efficiency measurements were performed to investigate the performance of the parallel algorithm. A maximum speed-up up to 20 can be reached using 32 processors.
Subsequently the proposed model was used to investigate the influence of coalescence on the hydrodynamics of a bubble column. We found that the coalescence phenomenon changes the flow structures considerably, furthermore the average velocities and velocity fluctuations of both phases are changed considerably. In the present study break-up is not yet taken into account thus incorporation of coalescence in our calculations admittedly tends to give overprediction in bubble size distribution.
The model is used to predict the integral gas hold-up in a homogeneous bubble column as a function of the gas superficial velocity. A maximum gas hold-up of $37\%$ can be achieved with the present model. A perfect agreement of our computations with the experimental data by Harteveld et al. [46] was found for.
Using the present parallel algorithm, it becomes possible to simulate a relatively large scale bubble column. In addition to the work described in this chapter, we used the model to simulate a bubble column with twice the height of the column described in sect. 5.5 to investigate the different flow structures resulting from different coalescence models. Figure 5.21 shows example results obtained from the simulation. The figure on the left shows the typical result of homogeneous bubbly flow without coalescence taken into account, which gives similar flow structures like the case in a shorter column. When the coalescence model is switched on, some bubbles coalesce as they ascend toward the top surface. The mean size of the bubbles is larger further from the inlet. In reality, bubbles will experience breakage as they reach their critical size. As no breakage model is incorporated in the present model, the influence of breakage is mimicked by limiting the maximum bubble size in the column calculated based on the critical bubble size. The result from this approach is shown in the right of Fig. 5.21. It can be clearly seen that the structure of the bubbles in the case both breakage and coalescence are accounted for is different with the result where only coalescence is considered. Here, the bubble size increases up to about half of the height of the column and becomes constant, since the bubbles have reached their critical size. These results

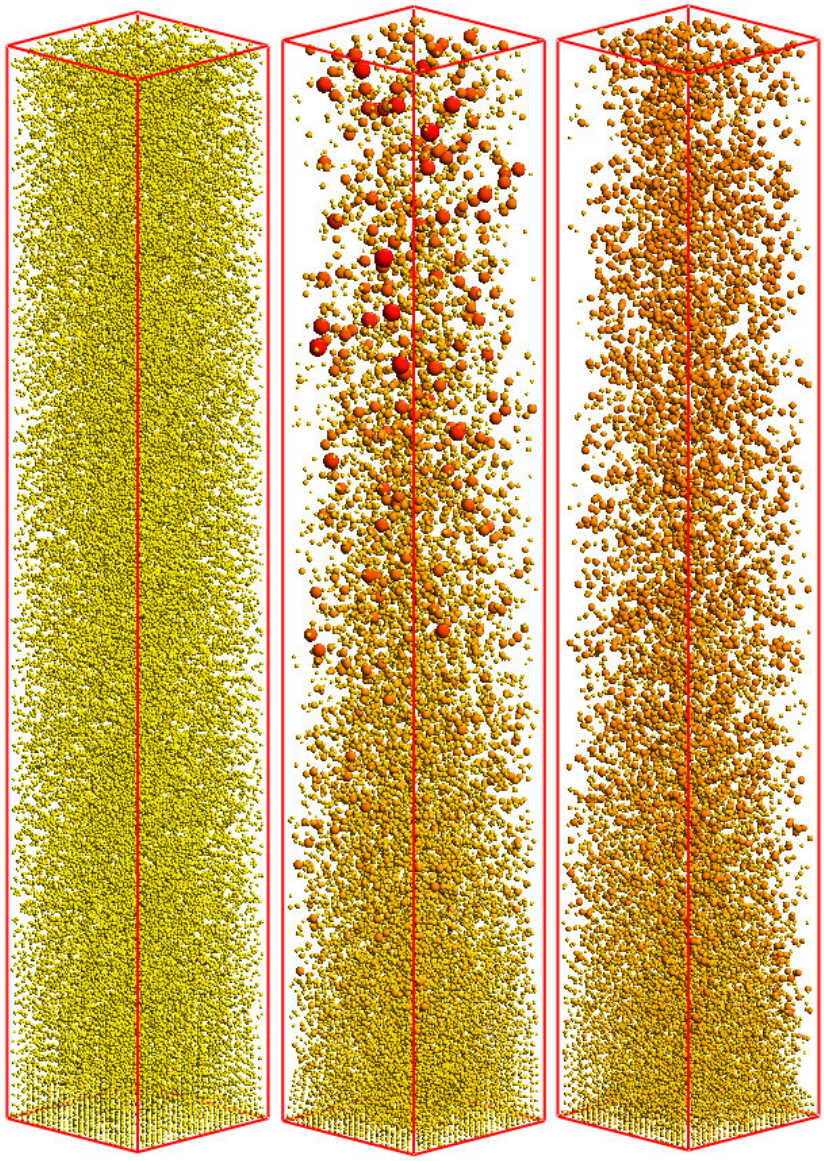

**Figure 5.21:** *Example of the application of the discrete bubble model to a large bubble column. The column dimensions are* $0.2\,\mathrm{m} \times 0.2\,\mathrm{m} \times 1.2\,\mathrm{m}$*; the grid size is similar to the case given in sect. 5.5. Left: simulation without coalescence taken into account; middle: with coalescence taken into account; right: coalescence accounted for, however a maximal bubble size is applied to mimic the balance between coalescence and break-up.*

indicate the importance of incorporating breakage in the discrete bubble model. A proper implementation of the breakage model however, still has to be investigated in the future.

## Acknowledgements

The author would like to thank Prof. dr. ir. B.J. Geurts (Multiscale Modeling and Simulation, Faculty of EEMCS, University of Twente) for discussions on the topic and for allowing the author to test the initial parallel version of the code from his account on the Aster system.

## Notation

| | |
|---|---|
| $\mathcal{B}$ | set of bubbles, dimensionless |
| $C$ | model coefficient, dimensionless |
| $d$ | diameter, $\mathrm{m}$ |
| $E$ | eccentricity, dimensionless; efficiency, dimensionless |
| Eö | Eötvös number, $\mathrm{Eö} = (\rho_l - \rho_b)\,\mathbf{g} d_b^2/\sigma$, dimensionless |
| $\mathbf{F}$ | force vector, $\mathrm{N}$ |
| $\mathbf{g}$ | gravity acceleration, $\mathrm{m\,s^{-2}}$ |
| $h$ | film thickness, $\mathrm{m}$ |
| $\mathbf{I}$ | unit tensor, dimensionless |
| $m$ | mass, $\mathrm{kg}$ |
| Mo | Morton number, $\mathrm{Mo} = g\mu_l^4(\rho_l - \rho_b)/(\rho_l^2\sigma^3)$, dimensionless |
| $\mathcal{N}$ | set of possible collision partners, dimensionless |
| $\mathcal{O}$ | set of obstacles, dimensionless |
| $p$ | pressure, $\mathrm{N\,m^{-2}}$ |
| $\mathcal{P}$ | set of processors, dimensionless |
| $R$ | radius, $\mathrm{m}$ |
| $\mathbf{r}$ | bubble position vector, $\mathrm{m}$ |
| Re | Reynolds number, $\mathrm{Re} = \rho_l\,\lvert\mathbf{v} - \mathbf{u}\rvert\,d_b/\mu_l$, dimensionless |
| $S$ | speed-up, dimensionless |
| $\mathbf{S}$ | characteristic filtered strain rate, $\mathrm{s^{-1}}$ |
| $t$ | time, $\mathrm{s}$ |
| $T$ | calculation time, $\mathrm{s}$ |
| $\mathbf{u}$ | liquid velocity vector, $\mathrm{m\,s^{-1}}$ |
| $\overline{\mathbf{u}}$ | liquid mean velocity, $\mathrm{m\,s^{-1}}$ |
| $\mathbf{u}'$ | liquid velocity fluctuation vector, $\mathrm{m\,s^{-1}}$ |
| $\mathbf{v}$ | bubble velocity vector, $\mathrm{m\,s^{-1}}$ |
| $v$ | bubble velocity component, $\mathrm{m\,s^{-1}}$ |
| $V$ | volume, $\mathrm{m^3}$ |
| $\mathcal{W}$ | set of neighbor list window, dimensionless |
| $y$ | distance to the wall, $\mathrm{m}$ |

### Greek letters

| | |
|---|---|
| $\varepsilon$ | volume fraction, dimensionless |
| $\delta t$ | time step, $\mathrm{s}$ |
| $\Delta$ | subgrid length scale, $\mathrm{m}$ |
| $\gamma$ | shear rate, $\mathrm{s}^{-1}$ |
| $\Phi$ | volume averaged momentum transfer due to interphase forces, $\mathrm{N\,m}^{-3}$ |
| $\mu$ | viscosity, $\mathrm{kg\,m}^{-1}\,\mathrm{s}^{-1}$ |
| $\psi$ | Lagrangian quantity |
| $\Psi$ | Eulerian quantity |
| $\rho$ | density, $\mathrm{kg\,m}^{-3}$ |
| $\sigma$ | interfacial tension, $\mathrm{N\,m}^{-1}$ |
| $\tau$ | stress tensor, $\mathrm{N\,m}^{-2}$; film drainage time, $\mathrm{s}$ |
| $\omega$ | mapping function, dimensionless |

### Indices

| | |
|---|---|
| $b$ | bubble |
| $c$ | coalescence |
| $D$ | drag |
| $e$ | event |
| $\mathrm{eff}$ | effective |
| $G$ | gravity |
| $l$ | liquid |
| $L$ | lift |
| $n$ | normal direction |
| $P$ | pressure |
| $\mathcal{P}$ | processor |
| $rel$ | relative |
| $s$ | serial |
| $S$ | subgrid |
| $T$ | turbulent |
| $VM$ | virtual mass |
| $W$ | wall |

## References

[1] D. Darmana, N. G. Deen, and J. A. M. Kuipers. Parallelization of an Euler-Lagrange model using mixed domain decomposition and mirror domain technique: application to dispersed gas-liquid two-phase flow. *Journal of Computational Physics*, 2006. In Press, Corrected Proof, Available online 7 July 2006.

[2] D. Darmana, N. G. Deen, and J. A. M. Kuipers. Parallelization of an Euler-Lagrange model using a mixed domain decomposition and mirror

domain technique: application to dispersed gas liquid two phase flow. In *Computational Fluid Dynamics in Chemical Reaction Engineering IV*, Barga, Italy, June 19-24 2005.

[3] N. G. Deen, T. Solberg, and B. H. Hjertager. Large eddy simulation of the gas-liquid flow in a square cross-sectioned bubble column. *Chemical Engineering Science*, 56:6341–6349, 2001.

[4] A. Sokolichin and G. Eigenberger. Gas-liquid flow in bubble columns and loop reactors: Part I. detailed modelling and numerical simulation. *Chemical Engineering Science*, 49:5735–5746, 1994.

[5] Y. Pan and M. P. Dudukovic. Numerical investigation of gas-driven flow in 2-d bubble columns. *AIChE Journal*, 46:434–449, 2000.

[6] A. Tomiyama, H. Higaki I. Zun, Y. Makino, and T. Sakaguchi. A three-dimensional particle tracking method for bubbly flow simulation. *Nuclear Engineering and Design*, 175:77–86, 1997.

[7] E. Delnoij, F. A. Lammers, J. A. M. Kuipers, and W. P. M. van Swaaij. Dynamic simulation of dispersed gas-liquid two-phase flow using a discrete bubble model. *Chemical Engineering Science*, 52:1429–1458, 1997.

[8] D. Darmana, N. G. Deen, and J. A. M. Kuipers. Detailed modeling of hydrodynamics, mass transfer and chemical reactions in a bubble column using a discrete bubble model. *Chemical Engineering Science*, 60:3383–3404, 2005.

[9] A. Kitagawa, Y. Murai, and F. Yamamoto. Two-way coupling of Eulerian-Lagrangian model for dispersed multiphase flows using filtering functions. *International Journal of Multiphase Flow*, 27:2129–2153, 2001.

[10] M. Sommerfeld, E. Bourloutski, and D. Bröder. Euler/Lagrange calculations of bubbly flows with consideration of bubble coalescence. *The Canadian Journal of Chemical Engineering*, 81:508–518, 2003.

[11] M. Sommerfeld. Overview and fundamentals. In Von Karman Institute for Fluid Mechanics, editor, *Theoretical and experimental modelling of particulate flow, Lecture Series No. 2000-6*, pages 1–62, April 2000.

[12] H. Enwald, E. Peirano, A. E. Almstedt, and B. Leckner. Simulation of the fluid dynamics of a bubbling fluidized bed. experimental validation of the two fluid model and evaluation of a parallel multiblock solver. *Chemical Engineering Science*, 54:311–328, 1999.

[13] H. Lindborg, V. Eide, S. Unger, S. T. Henriksen, and H. A. Jakobsen. Parallelization and performance optimization of a dynamic pde fixed bed reactor model for practical application. *Computers and Chemical Engineering*, 28:1585–1597, 2004.

[14] B. P. B. Hoomans, J. A. M. Kuipers, W. J. Briels, and W. P. M. van Swaaij. Discrete particle simulation of bubble and slug formation in a

two-dimensional gas-fluidised bed: A hard-sphere approach. *Chemical Engineering Science*, 51(1):99–118, 1996.

[15] G. Burns, R. Daoud, and J. Vaigl. LAM: An Open Cluster Environment for MPI. In *Proceedings of Supercomputing Symposium*, pages 379–386, 1994.

[16] J. M. Squyres and A. Lumsdaine. A Component Architecture for LAM/MPI. In *Proceedings, 10th European PVM/MPI Users' Group Meeting*, number 2840 in Lecture Notes in Computer Science, pages 379–387, Venice, Italy, September / October 2003. Springer-Verlag.

[17] J. Magnaudet and I. Eames. The motion of high-Reynolds-number bubbles in inhomogeneous flows. *Annual Reviews of Fluid Mechanics*, 32:659–708, 2000.

[18] H. A. Jakobsen, B. H. Sannæs, S. Grevskott, and H. F. Svendsen. Modeling of vertical bubble-driven flows. *Industrial and Engineering Chemistry Research*, 36:4052–4074, 1997.

[19] H. A. Jakobsen, H. Lindborg, and C. A. Dorao. Modeling of bubble column reactors: Progress and limitations. *Industrial and Engineering Chemistry Research*, 44:5107–5151, 2005.

[20] T. R. Auton. Lift force on a spherical body in a rotational flow. *Journal of Fluid Mechanics*, 183:199–218, 1987.

[21] A. Tomiyama, H. Tamai, I. Zun, and S. Hosokawa. Transverse migration of single bubbles in simple shear flows. *Chemical Engineering Science*, 57:1849–1858, 2002.

[22] R. M. Wellek, A. K. Agrawal, and A. H. P. Skelland. Shape of liquid drops moving in liquid media. *AIChE Journal*, 12:854–862, 1966.

[23] A. Tomiyama, T. Matsuoka, T. Fukuda, and T. Sakaguchi. A simple numerical method for solving an incompressible two-fluid model in a general curvilinear coordinate system. In A. Serizawa, T. Fukano, and J. Bataille, editors, *Advances in Multiphase Flow*, pages 241–252, Amsterdam, November 1995. Society of Petroleum Engineers, Inc., Elsevier.

[24] J. Smagorinsky. General circulation experiment with the primitive equations. *Monthly Weather Review*, 91:99–165, 1963.

[25] M. P. Allen and D. J. Tildesley. *Computer Simulation of Liquids*. Oxford Science Publications, 1987.

[26] E. I. V. van den Hengel, N. G. Deen, and J. A. M. Kuipers. Application of coalescence and breakup models in a discrete bubble model for bubble columns. *Industrial and Engineering Chemistry Research*, 44:5233–5245, 2005.

[27] A. K. Chesters. The modelling of coalescence processes in fluid-liquid dispersion: a review of current understanding. *Transactions of the In-*

*stitution of Chemical Engineers*, 69:259–270, 1991.

[28] C. H. Lee, L. E. Erickson, and L. A. Glasgow. Bubble breakup and coallescence in turbulent gas-liquid dispersion. *Chemical Engineering Communications*, 59:65–84, 1987.

[29] M. J. Prince and H. W. Blanch. Bubble coalescence and break-up in air-sparged bubble columns. *AIChE Journal*, 36:1485–1499, 1990.

[30] R. D. Kirkpatrick and M. J. Lockett. Influence of approach velocity on bubble coalescence. *Chemical Engineering Science*, 29:2362–2373, 1974.

[31] A. K. Chesters and G. Hofman. Bubble coalescence in pure liquids. *Applied Scientific Research*, 38:353–361, 1982.

[32] N. G. Deen, M. van Sint Annaland, and J. A. M. Kuipers. Multi-scale modeling of dispersed gas-liquid two-phase flow. *Chemical Engineering Science*, 59:1853–1861, 2004.

[33] C. S. Peskin. Numerical analysis of blood flow in the heart. *Journal of Computational Physics*, 25:220–252, 1977.

[34] S. V. Patankar and D. B. Spalding. A calculation procedure for heat, mass and momentum transfer in three-dimensional parabolic flows. *International Journal of Heat and Mass Transfer*, 15:1787–1806, 1972.

[35] J. Centrella and J. R. Wilson. Planar numerical cosmology. II. the difference equations and numerical tests. *Astronomy & Astrophysics Journal Supplement Series*, 54:229–249, 1984.

[36] B. P. B. Hoomans. *Granular Dynamic of Gas-Solid Two-Phase Flows*. PhD thesis, University of Twente, 1999.

[37] S. Balay, K. Buschelman, W. D. Gropp, D. Kaushik, M. G. Knepley, L. C. McInnes, B. F. Smith, and H. Zhang. PETSc Web page, 2001. http://www.mcs.anl.gov/petsc.

[38] S. Balay, K. Buschelman, V. Eijkhout, W. D. Gropp, D. Kaushik, M. G. Knepley, L. C. McInnes, B. F. Smith, and H. Zhang. PETSc users manual. Technical Report ANL-95/11 - Revision 2.1.5, Argonne National Laboratory, 2004.

[39] S. Balay, V. Eijkhout, W. D. Gropp, L. C. McInnes, and B. F. Smith. Efficient management of parallelism in object oriented numerical software libraries. In E. Arge, A. M. Bruaset, and H. P. Langtangen, editors, *Modern Software Tools in Scientific Computing*, pages 163–202. Birkhäuser Press, 1997.

[40] G. B. Deng, J. Piquet, X. Vasseur, and M. Visonneau. A new fully coupled method for computing turbulent flows. *Computers and Fluids*, 30:445–472, 2001.

[41] B. G. M. Van Wachem and J. C. Schouten. Experimental validation

of 3-D Lagrangian VOF model: Bubble shape and rise velocity. *AIChE Journal*, 48(12):2744–2753, December 2002.

[42] W. D. Gropp, D. K. Kaushik, D. E. Keyes, and B. F. Smith. High performance parallel implicit CFD. *Journal of Parallel Computing*, 27:337–362, 2001.

[43] P. Wang, S. Balay, K. Sepehmoori, J. Abate, B. Smith, and G. A. Pope. A fully implicit parallel EOS compositional simulator for large scale reservoir simulation. In *SPE $15^{th}$ Reservoir Simulation Symposium*, pages 63–71. Society of Petroleum Engineers, Inc., February 1999.

[44] J. A. M. Kuipers, K. J. van Duin, F. P. H. van Beckum, and W. P. M. van Swaaij. Computer simulation of the hydrodynamics of a two dimensional gas-fluidized bed. *Computer Chemical Engineering*, 17:839, 1993.

[45] J. H. Ferziger and M. Peric. *Computational Methods for Fluid Dynamics*. Springer, 1999.

[46] W. K. Harteveld, J. E. Julia, R. F. Mudde, and H. E. A. van den Akker. Large scale vortical structures in bubble columns for gas fraction in the range of 5%-25%. In *Proceedings of CHISA 2004 Conference*, pages 2963–2982, Prague - Czech Republic, Aug 22 - 26 2004.

# 6

# Numerical study of homogeneous bubbly flow: influence of the inlet conditions to the hydrodynamic behavior[§]

*"..and now for something completely different, a man with three noses."* - Monty Python's Flying Circus

## Abstract

*This chapter studies the role of the gas injection pattern on the large scale structures in a homogeneous pseudo-2D bubble column operated at relatively high gas hold-up. Seven cases with different inlet configuration have been studied experimentally by Harteveld et al. [2]. Each of these cases has been simulated using a (parallel) Euler-Lagrange model developed by Darmana et al. [3]. The presence of coherent structures for both uniform and non-uniform gas injection is studied. Furthermore, the influence of the gas injection pattern on the dynamics is investigated, while the statistical (average and fluctuating) quantities are compared with the PIV/PTV and LDA measurement data of Harteveld et al. [2]. The results show that the model resembles the observed experimental flow structures to a large extent.*

[§]Based on: Darmana et al. [1]

## 6.1 Introduction

In the chemical industry bubble columns are often used because of their simple construction and operation, good heat and mass transfer properties and isothermal conditions of operation. The flow in a bubble column is complex and not yet well understood despite the extensive research devoted to this topic. Based on the flow rates of the gas phase, two typical flow regimes can be distinguished. At low gas flow rates, the homogeneous regime is found, which is characterized by uniformly distributed bubbles and the absence of large scale liquid circulation. On the other hand, when high flow rates are utilized the heterogeneous regime is found, displaying non-uniformly distributed bubbles and large scale liquid circulation.
From a practical point of view a bubble column operated in the homogeneous regime with relatively high gas hold-up and a small uniform bubble size is desirable, since this configuration provides a large gas-liquid interface, which improves the mass and heat transfer performance of the column. It is relatively difficult however to generate a uniform flow especially at relatively high gas hold-ups, since the coalescence rate normally increases under these conditions. Due to coalescence a non uniform bubble size distribution will be generated, which will induce non uniformity of the flow behavior.
One of the key elements to obtain a homogeneous bubbly flow system is the employment of uniform injection as suggested by Harteveld et al. [2]. They showed experimentally that a uniform flow without large scale vortical structures and circulation patterns is obtained with very uniform injection; and additionally that the vortical structures and circulation can be re-obtained by introduction of non-aerated zones. Their experimental results provide valuable data that can be used to validate CFD models and improve our understanding of the role of the sparger with respect to the hydrodynamics and prevailing flow structures in bubble columns.
A significant amount of computational work has been performed over the last decade to reproduce the dynamics of the large scale circulation and vortical structures computationally. In numerical simulations typically lab-scale bubble columns are considered at relatively low superficial gas velocities with a localized gas distributor area at the base of the column [4–12]. This type of bubble column operation will create a bubble plume which is meandering irregularly and automatically implies non uniformity of the gas hold-up throughout the column.
Using either Euler-Euler or Euler-Lagrange models some authors like Deen et al. [7], Darmana et al. [8] and Buwa et al. [11, 12] reported that using the widely accepted closure correlations (a.o. closures proposed by Tomiyama et al. [13, 14]) both the dynamics and time-averaged behavior in a partially aerated bubble column at low gas hold-up can be reproduced very well. As most of the closures are empirically obtained from experiments involving single bubbles (or droplets), their applicability to systems with high gas

hold-ups is often questionable. On the other hand, hardly any correlation is available in literature which takes into account the effect of the local gas hold-up. One of the works in this research area (the simulation results by Behzadi et al. [15]) suggests that using drag and lift correlations, which account for the elevated dispersed phase fraction, does not yield satisfactory results.
In this chapter, the experimental cases studied by Harteveld et al. [2] are simulated by means of a CFD model. The CFD code used in the present study is the parallel version of the transient three-dimensional Euler-Lagrange model developed by Darmana et al. [3] (see Chapter 5) supplemented with the force closures proposed by Tomiyama et al. [13, 14, 16]. The presence of coherent structures for both uniform and non-uniform gas injectors is studied together with the influence of the gas injection pattern on the dynamics. In addition the statistical (average and fluctuating) quantities are compared with the PIV/PTV and LDA measurement data of Harteveld et al. [2]. The study in particular is meant to further validate the developed Euler-Lagrange model and investigate the applicability of both the model and the applied closures to simulate bubble columns that are operated in a (homogeneous) regime with high gas hold-up.

## 6.2 Experiments

The experimental data used in the present study are taken from the work of Harteveld et al. [2] and will be briefly explained here for the sake of clarity.

### 6.2.1 Experimental setup

The pseudo-2D bubble column used in the experiments was a $50\%$ down-scaled version of that used by Becker et al. [4]. A schematic overview of the experimental setup is given in Fig. 6.1 (a). The column has a width of $24.3\mathrm{cm}$, depth of $4.05\,\mathrm{cm}$ and a height of $99\,\mathrm{cm}$. The sparger for this column is made of $95$ needles arranged in a triangular pattern with a distance between the needles of $0.9\,\mathrm{cm}$ in the x-direction and $1.04\,\mathrm{cm}$ in the y-direction, as shown in Fig. 6.1 (b).
The nozzles are arranged in seven groups: one central group of $11$ needles and six groups of $14$ needles. The ungassed liquid height was $0.70\,\mathrm{m}$. The gas injection pattern was varied to study its influence on the hydrodynamics and flow structures. In total seven injection patterns were investigated by Harteveld et al. [2], which we refer to as case E1 to E7. The superficial velocity of $0.020\,\mathrm{m/s}$ was kept constant when the injection pattern was altered. The patterns are described in Table 6.1 and schematically depicted in Figure 6.2.

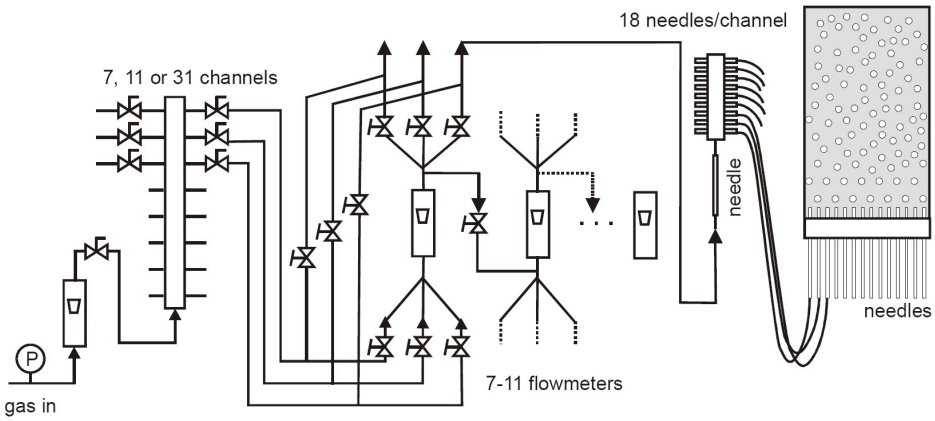


(a) Schematic overview of the experimental setup

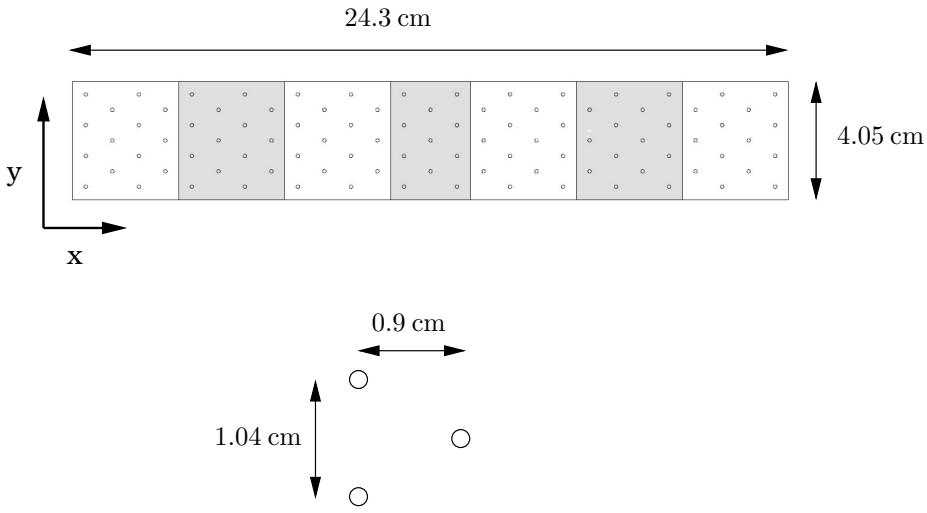


(b) Geometry of the nozzles.

**Figure 6.1:** *Experimental setup used by Harteveld et al. [2].*

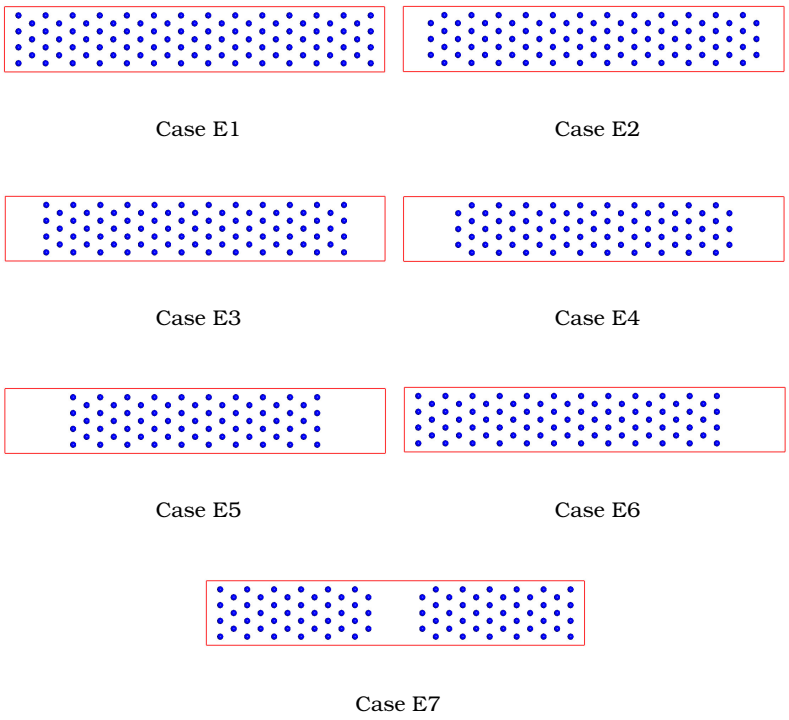


**Figure 6.2:** *Gas injection patterns for pseudo-2D column.*

Table 6.1: *Gas injection patterns for use in the pseudo-2D column*

| Pattern | Description gas injection | Needles used | Relative area aerated zone (%) | Aeration for : |
|---|---|---|---|---|
| E1 | Uniform | 95 | 100 | $0 \leqslant x/W \leqslant 1.00$ |
| E2 | Central, 1 wall row off | 87 | 93 | $0.035 \leqslant x/W \leqslant 0.965$ |
| E3 | Central, 2 wall row off | 81 | 85 | $0.075 \leqslant x/W \leqslant 0.925$ |
| E4 | Central, 3 wall row off | 73 | 78 | $0.11 \leqslant x/W \leqslant 0.89$ |
| E5 | Central, 4 wall row off | 67 | 70 | $0.15 \leqslant x/W \leqslant 0.85$ |
| E6 | Asymmetric, 4 wall rows off | 81 | 85 | $x/W \leqslant 0.85$ |
| E7 | Wall, 3 central rows off | 84 | 89 | $x/W < 0.445$ & $x/W > 0.555$ |

### 6.2.2 Instantaneous gas and liquid velocity

The large scale structures in the pseudo-2D column were studied with the aid of Particle Image Velocimetry (PIV) and Particle Tracking Velocimetry (PTV). A CCD camera (Dalsa Inc.) with a maximal resolution of $512 \times 512$ pix was used to record images of the flow. The lower area $(0 < z < 0.7\,\mathrm{m})$ of the column was recorded in two steps, each step imaging an area of $0.24 \times 0.35$ m, providing a resolution of $0.64$ mm/pix. Both the PIV and PTV analyses were performed with the use of DaVis PIV software from LaVision. Sequences of images of the bubble motion were recorded and PIV was used to determine the bubble velocities from these sequences. To obtain bubble shadows over a large area of the column the column is illuminated from the back. This leads to bubble velocities averaged in the depth direction of the column. Fifty pairs of bubble images were captured with a frame rate of $150$ Hz. The images were processed using interrogation areas of $32 \times 32$ pix with an overlap of $50\%$. The fifty subsequent velocity fields were then time-averaged to yield a quasi-instantaneous velocity field corresponding over a period of $0.33$ s.
The liquid flow was determined by putting tracers in the liquid. Relatively large particles were selected to provide sufficient contrast: polystyrene particles with a diameter of approximately $2.5$ mm. Due to the large inertia of the particles, only the largest structures were determined. For the PTV analysis, the images were recorded at a framerate of $30$ Hz over a period of $0.6$ s. Due to the presence of the bubbles, most tracer particles were only visible for short periods while some particles were visible for a longer period resulting in a wide variation of vector density. Since the particles were not neutrally buoyant (i.e. having a slip velocity of $0.09$ m/s), the results cannot be directly compared with the simulations, but should rather be used to obtain a qualitative impression of the large flow structures.
The PIV and PTV results were obtained from sets of experiments performed on different days, therefore the vector fields do not correspond to the same time instants and the large scale instantaneous structures are different.

### 6.2.3 Time-averaged liquid velocity

The average liquid velocity was measured by means of Laser Doppler Anemometry (LDA). For the LDA measurements, the flow was seeded with hollow glass particles, which were neutrally buoyant and were $10\ \mu\mathrm{m}$ in diameter. The equipment consisted of a 4W Spectra-Physics $Ar^+$ laser and a TSI 9201 colorburst multicolor beam separator. Beam pairs were focused using a backscatter probe with a lens of $0.122\ \mathrm{m}$ focal length. Detected light was sent to the TSI 9230 colorlink. The axial component was determined with green ($\lambda = 514.5\ \mu\mathrm{m}$) beams, the tangential component using blue ($\lambda = 488\ \mu\mathrm{m}$) beams. The fringe spacings were $1.28\ \mu\mathrm{m}$ (green channel) and $1.22\ \mu\mathrm{m}$ (blue channel). A preshift frequency of $500\ \mathrm{kHz}$ was used. Bursts were processed with the IFA-750 (TSI) processor. For each measurement point, a time series of $300\ \mathrm{s}$ was used.

### 6.2.4 Time averaged void fraction

The integral gas hold-up, ($\varepsilon_I$), was determined by measuring the difference between the height of the liquid level in the column with and without bubbles present as follows:

$$\varepsilon_I = \frac{h - h_0}{h} \tag{6.1}$$

where $h$ and $h_0$ respectively are the average height of the liquid surface with and without aeration.
The spatial distribution of the average gas hold-up is measured by using glass fiber probes. Light is emitted into one end of a glass fiber while the other end is put inside the bubble column facing downward. If the $200\ \mu\mathrm{m}$ diameter tip is located in the water phase, most of the light exits the tip of the probe. If the tip is located in the gas phase, most of the light is reflected backwards. The amount of reflected light is recorded and the relative occurrence of the phases is determined from this signal, which is done via direct sampling of the signal and offline software processing. Five fiber probes are used simultaneously to measure the void fraction over a line from the center of the column to the wall.
The technique generally underestimates the void fraction for the present experimental condition by $10 - 20\%$, depending on the type of signal processing that is used. The inacurracy is corrected by applying the so-called low level criterion and further improved by applying a correction factor which is determined by comparing the results from the glass fiber probes and the integral gas hold-up measurements (see Harteveld et al. [2] for further details). The time series in the experiments for the probes had a length of $1000\ \mathrm{s}$. During this time, typically some $15,000$ bubbles were collected per probe ($\varepsilon_I \approx 20\%$).

## 6.3 Discrete bubble model

A parallel version of the three-dimensional discrete bubble model (DBM) developed by Darmana et al. [3] (see Chapter 5) is used to model the pseudo-2D bubble column. The liquid phase hydrodynamics are represented by the volume-averaged Navier-Stokes equations while the motion of each individual bubble is tracked in a Lagrangian fashion.

### 6.3.1 Bubble dynamics

The motion of each individual bubble is computed from the bubble mass and momentum equations while accounting for bubble-bubble and bubble-wall interactions via an encounter model similar in spirit to the model of Hoomans et al. [17]. The liquid phase contributions are taken into account by the net force $\Sigma\mathbf{F}$ experienced by each individual bubble. For an incompressible bubble, the equations can be written as:

$$\rho_b V_b \frac{d\mathbf{v}}{dt} = \sum \mathbf{F} \tag{6.2}$$

where $\rho_b$, $V_b$ and $\mathbf{v}$ respectively represent the density, volume and velocity of the bubble. The net force acting on each individual bubble is calculated by considering all the relevant forces. It is composed of separate, uncoupled contributions which in the present study include: gravity, pressure, drag, lift, virtual mass and wall forces:

$$\sum \mathbf{F} = \mathbf{F}_G + \mathbf{F}_P + \mathbf{F}_D + \mathbf{F}_L + \mathbf{F}_{VM} + \mathbf{F}_W \tag{6.3}$$

Expressions for each of these forces used in the present study can be found in Table 6.2. Note that the drag, lift and wall force closures used in the present study are obtained from Tomiyama et al. [13, 14].

### 6.3.2 Liquid phase hydrodynamics

The liquid phase hydrodynamics are represented by the volume-averaged Navier-Stokes equations, which consist of the continuity and momentum equations. The presence of bubbles is reflected by the liquid phase volume fraction $\varepsilon_\ell$ and the interphase momentum transfer $\Phi$ :

$$\frac{\partial}{\partial t}\left(\varepsilon_\ell \rho_\ell\right) + \nabla \cdot \varepsilon_\ell \rho_\ell \mathbf{u} = 0 \tag{6.4}$$

$$\frac{\partial}{\partial t}\left(\varepsilon_\ell \rho_\ell \mathbf{u}\right) + \nabla \cdot \varepsilon_\ell \rho_\ell \mathbf{u}\mathbf{u} = -\varepsilon_\ell \nabla P - \nabla \cdot \varepsilon_\ell \tau_\ell + \varepsilon_\ell \rho_\ell \mathbf{g} + \Phi \tag{6.5}$$

where g is the gravity constant, $\rho_\ell$, $\mathbf{u}$ and $P$ respectively the density, velocity

Table 6.2: *Overview of forces acting on a bubble.*

| **Force** | **Closure** |
|---|---|
| $\mathbf{F}_G = \rho_b V_b \mathbf{g}$ | $-$ |
| $\mathbf{F}_P = -V_b \nabla P$ | $-$ |
| $\mathbf{F}_D = -\frac{1}{2} C_D \rho_l \pi R_b^2 \left\|\mathbf{v}-\mathbf{u}\right\| (\mathbf{v}-\mathbf{u})$ | $C_D = \max\left[\min\left[\frac{16}{\mathrm{Re}}\left(1+0.15\mathrm{Re}^{0.687}\right), \frac{48}{\mathrm{Re}}\right], \frac{8}{3}\frac{\mathrm{Eö}}{\mathrm{Eö}+4}\right]$ |
| $\mathbf{F}_L = -C_L \rho_\ell V_b (\mathbf{v}-\mathbf{u}) \times \nabla \times \mathbf{u}$ | $C_L = \begin{cases} \min\left[0.288\tanh\left(0.121\mathrm{Re}\right), f(\mathrm{Eö}_d)\right]; \mathrm{Eö}_d < 4 \\ f(\mathrm{Eö}_d); 4 < \mathrm{Eö}_d \leq 10 \\ -0.29; \mathrm{Eö}_d > 10 \end{cases}$ |
| | $f(\mathrm{Eö}_d) = 0.00105\mathrm{Eö}_d^3 - 0.0159\mathrm{Eö}_d^2 - 0.0204\mathrm{Eö}_d + 0.474$ |
| | $\mathrm{Eö}_d = \frac{\mathrm{Eö}}{E^{2/3}}\ ;\ E = \frac{1}{1+0.163\mathrm{Eö}^{0.757}}$ |
| $\mathbf{F}_{VM} = -C_{VM}\rho_\ell V_b \left(\frac{D_b \mathbf{v}}{D_b t} - \frac{D_b \mathbf{u}}{D_b t}\right)$ | $C_{VM} = 0.5$ |
| $\mathbf{F}_W = C_W R_b \rho_\ell \frac{1}{D_{bw}^2} \left\|\mathbf{u}-\mathbf{v}\right\|^2 \cdot \mathbf{n}$ | $C_W = \begin{cases} \mathrm{e}^{(-0.933\mathrm{Eo}+0.179)} & 1 < \mathrm{Eo} < 5 \\ 0.0007\mathrm{Eo}+0.04 & \mathrm{Eo} \geq 5 \end{cases}$ |

and pressure for the liquid phase. Both phases are assumed to be incompressible, which is a reasonable assumption considering the limited height of the simulated systems. The liquid phase stress tensor $\tau_\ell$ is assumed to obey the general Newtonian form given by:

$$\tau_\ell = -\mu_{\mathrm{eff},\ell}\left[\left(\left(\nabla\mathbf{u}\right)+\left(\nabla\mathbf{u}\right)^T\right) - \frac{2}{3}\mathbf{I}\left(\nabla\cdot\mathbf{u}\right)\right] \tag{6.6}$$

where $\mu_{\mathrm{eff},\ell}$ is the effective viscosity. In the present model the effective viscosity is composed of two contributions, the molecular viscosity and the turbulent viscosity:

$$\mu_{\mathrm{eff},\ell} = \mu_{\mathrm{L},\ell} + \mu_{\mathrm{T},\ell} \tag{6.7}$$

where the turbulent viscosity $\mu_{\mathrm{T},\ell}$ is calculated using the sub-grid scale (SGS) model of Vreman [18]:

$$\mu_{\mathrm{T},\ell} = 2.5\rho_\ell C_S^2 \sqrt{\frac{B_\beta}{\alpha_{ij}\alpha_{ij}}} \tag{6.8}$$

where $C_s$ is a model constant with a typical value of $0.1$, $\alpha_{ij} = \partial u_j/\partial x_i$, $\beta_{ij} = \Delta_m^2 \alpha_{mi}\alpha_{mj}$ and $B_\beta = \beta_{11}\beta_{22} - \beta_{12}^2 + \beta_{11}\beta_{33} - \beta_{13}^2 + \beta_{22}\beta_{33} - \beta_{23}^2$. $\Delta_i$ is the filter width in the $i$ direction.

## 6.4 Simulations

All of the experimental cases E1 to E7 explained in section 6.2 are modeled using the three dimensional DBM which we refer to as case S1 to S7 respectively. The applied computational grid consists of $101 \times 17 \times 290$ cells and

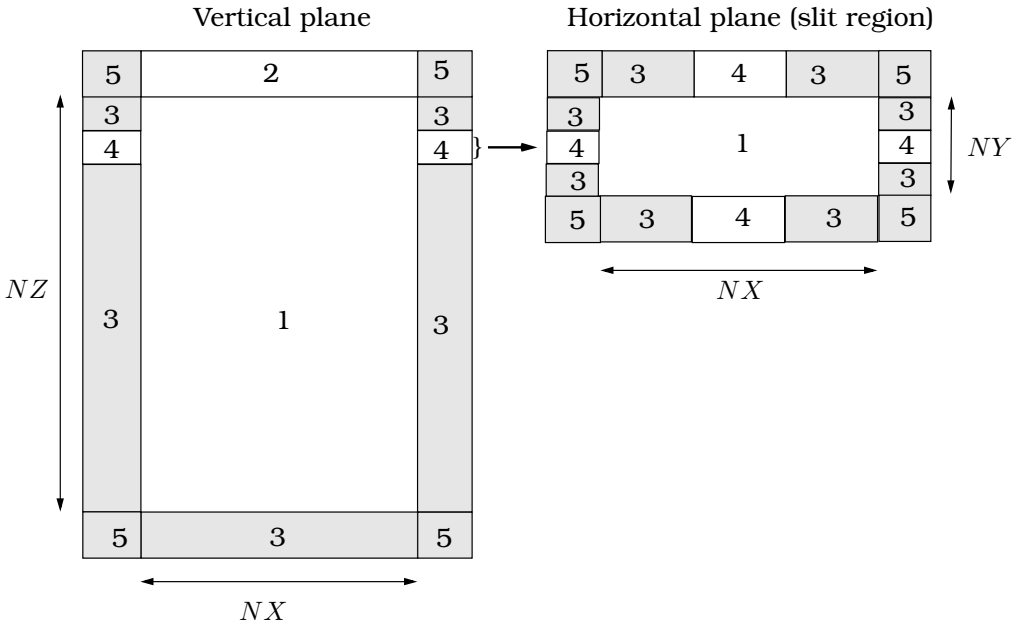


**Figure 6.3:** *Typical boundary conditions used in simulations with the discrete bubble model. The vertical plane is at $j = NY/2$ while a slit is defined at $k = NZ - 1$.*

**Table 6.3:** *Cell flags and corresponding cell types used in defining boundary conditions.*

| flag | boundary conditions |
|---|---|
| 1 | Interior cell, no boundary conditions specified |
| 2 | Impermeable wall, free slip boundary |
| 3 | Impermeable wall, no slip boundary |
| 4 | Prescribed pressure cell, free slip boundary |
| 5 | Corner cell, no boundary conditions specified |

the time step, $\delta t_{flow}$ is set to $1 \times 10^{-3}$ s while for the bubble tracking ($\delta t_{bub}$) a time step of $1 \times 10^{-4}$ s is used. The boundary conditions are imposed to the column using the flag matrix concept of Kuipers et al. [19] as is shown in Fig. 6.3. The definition of each boundary condition can be found in Table 6.3.

Each nozzle in the experimental setup is modeled as a position in the bottom of the column where bubbles with specific size enter the column with a fixed velocity. All the bubbles entering the column have a diameter of $4$ mm (Harteveld et al. [2] observed that the inlet bubbles may vary from $3.5 - 4.5$ mm). The distance between the center of two consecutive bubbles released from a single hole $\delta_b$ is set to $2.5 \times R_b$. This arrangement is made to

avoid unnecessary collisions between two consecutive bubbles immediately after they enter the column. The velocity of bubbles entering the column is determined from the superficial velocity through the following formula:

$$v_{z,enter} = \frac{v_s \delta_b W \times D}{N_h V_b} \tag{6.9}$$

with $v_s$ the superficial gas velocity, $W \times D$ the cross sectional area of the column and $N_h$ is number of holes.
For all of the nozzles, the vertical position of the bubbles underneath the bottom plate is generated in such way that none of the bubbles enter the column at the same time. This was implemented in order to prevent (artificial) pulsing behavior of the incoming bubbles, which would occur if bubbles enter the column through all holes simultaneously. By doing so, the occurrence of undesired pressure fluctuations at the top of the column was prevented.
During the simulation on average about $19,000$ computational bubbles are present in the calculation. This amount of bubbles is resulting from the balance between bubbles coming into the column through the nozzle and the bubbles leaving the column from the top surface. For every simulated second, it takes about $24\,\mathrm{h}$ calculation time using $8$ processors on a SGI Altix 3700 system with Intel Itanium 2, 1.3 GHz processors.

## 6.5 Result and discussion

In this section the results obtained from the DBM model will be presented and compared with experimental data. First, the flow structures during the start-up period resulting from simulation will be shown. Then, the flow structures present after the flow has fully developed will be compared with experimental observations. Finally, the comparison between simulation results and experimental data on the bases of averaged quantities will be addressed.

### 6.5.1 Flow structures during the startup period

All simulations were carried out by injecting bubbles into an initially quiescent liquid. Depending on the injection pattern, bubbles will rise through the liquid and occupy the column space with different patterns until a fully developed condition is reached. Figure 6.4 shows series of snapshots of the bubble structures during the startup period resulting from the DBM simulation for case S1 (fully aerated column). As can be seen, the bubbles are rising in a uniform fashion and filling the entire column in the lateral direction right from the start. In a later stage some bubbles are rising faster than others and split the bubble population into two groups. This situation however does not sustain for a long time as the bubbles in the lower part

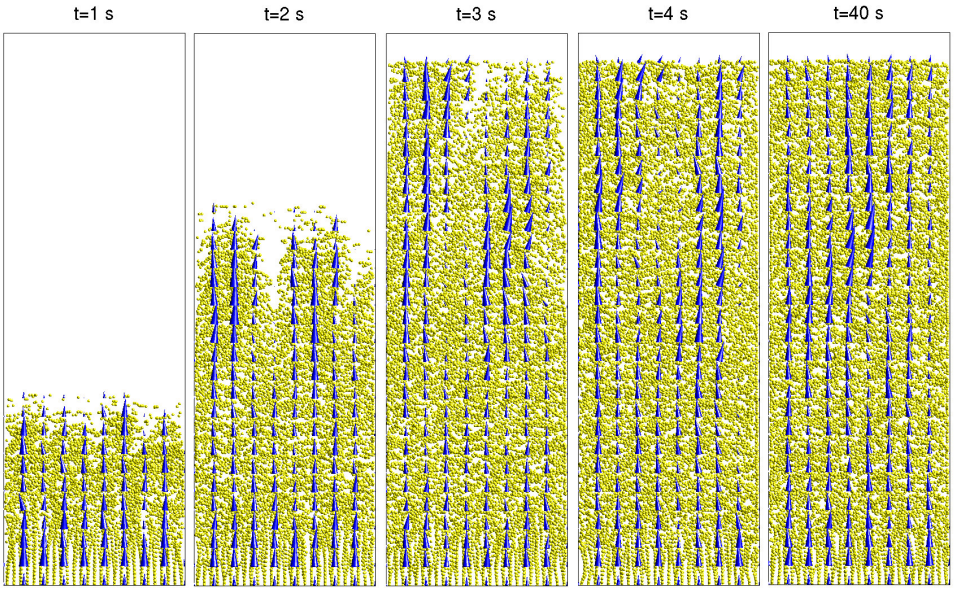


**Figure 6.4:** *Series of instantaneous solution for case S1 during the startup period showing the bubble structures and their velocities.*

of the column still move in a homogeneous fashion. At about $t = 3\,\mathrm{s}$ some bubbles start to leave the top surface and the column starts to exhibit a uniform flow pattern where bubbles are present everywhere and rising with relatively uniform velocity.

The results from the partially aerated cases (i.e. Cases S2-S5) can be seen in Figs. 6.5 and 6.6. Here, the non-aerated regions are introduced starting from the wall regions and continually increasing toward the center region of the column. As can be seen, by introducing non-aerated regions, vortices start to developed on both sides of the bottom corner. The two vortices push the bubbles toward the center region creating a necking zone that expands as the non-aerated zone increases. Outside the necking zone, the bubbles are pushed back toward the left and right wall filling up the entire column in the lateral direction. In the upper part of the flow, a typical mushroom shaped structure is found. The roof of the mushroom shape is relatively flat in case S2 and is gradually transformed showing a more sharp roof as the non-aerated zone is increased.

After the bubbles start to leave the top surface, the bubble pattern in cases S2 and S3 show a stable structure where all bubbles are uniformly distributed through out the entire column and uniformly move in the vertical direction (except for the bottom corner regions). In cases S4 and S5 however, the bubbles behave differently. Here, bubbles are moving upward as a

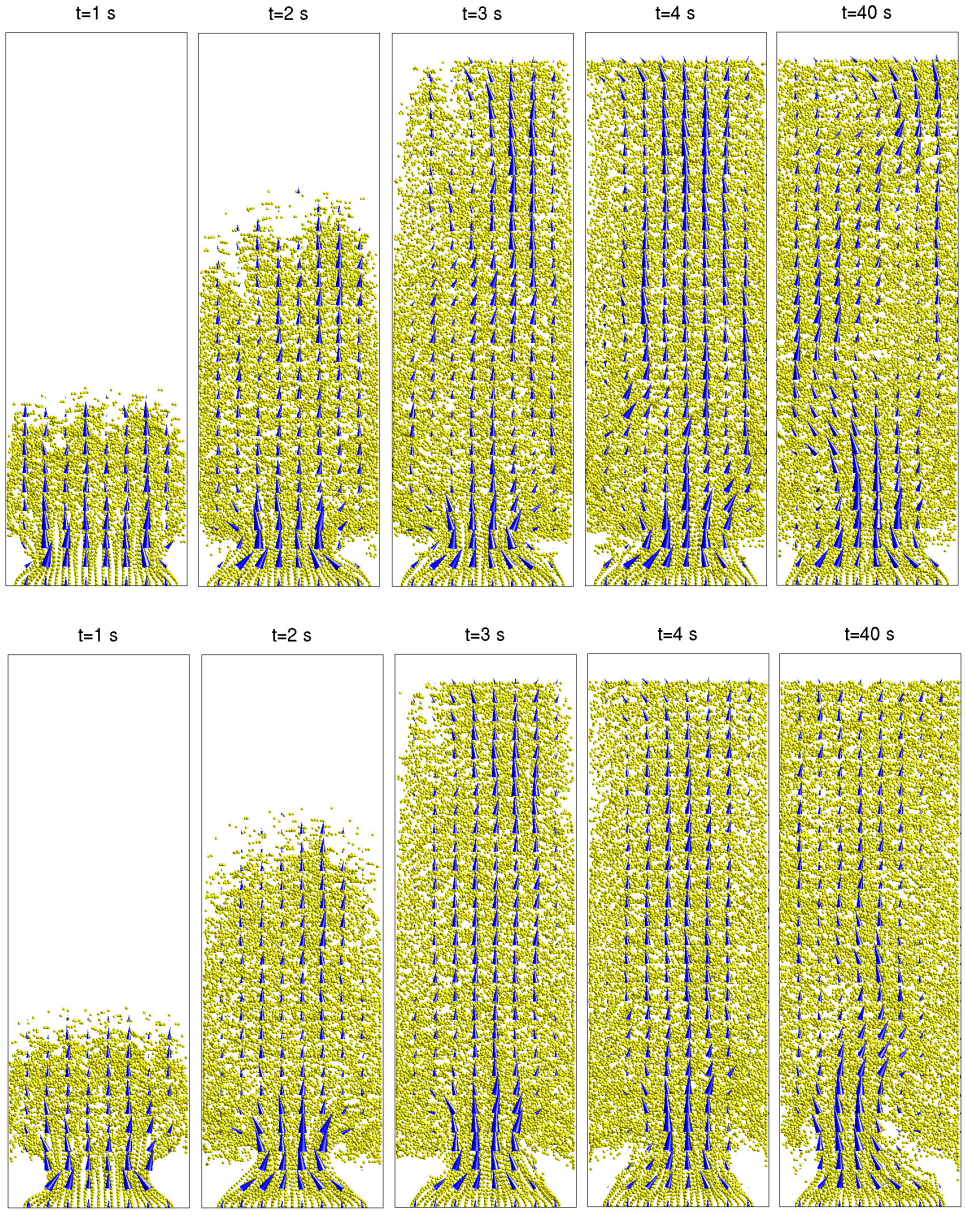


**Figure 6.5:** *Instantaneous solution for case S2 (top row) and S3 (bottom row) during the startup period.*

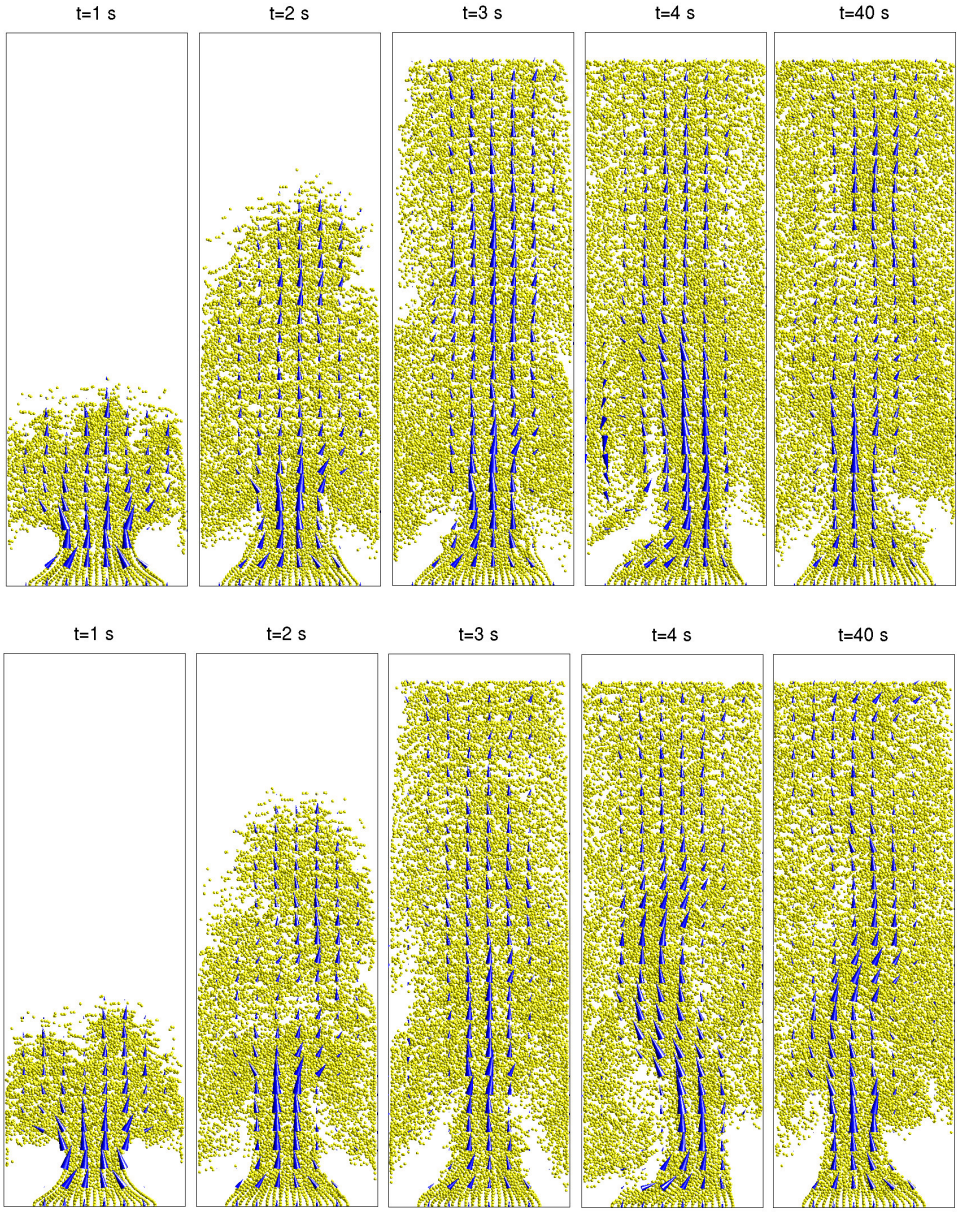


**Figure 6.6:** *Instantaneous solution for case S4 (top row) and S5 (bottom row) during the startup period.*

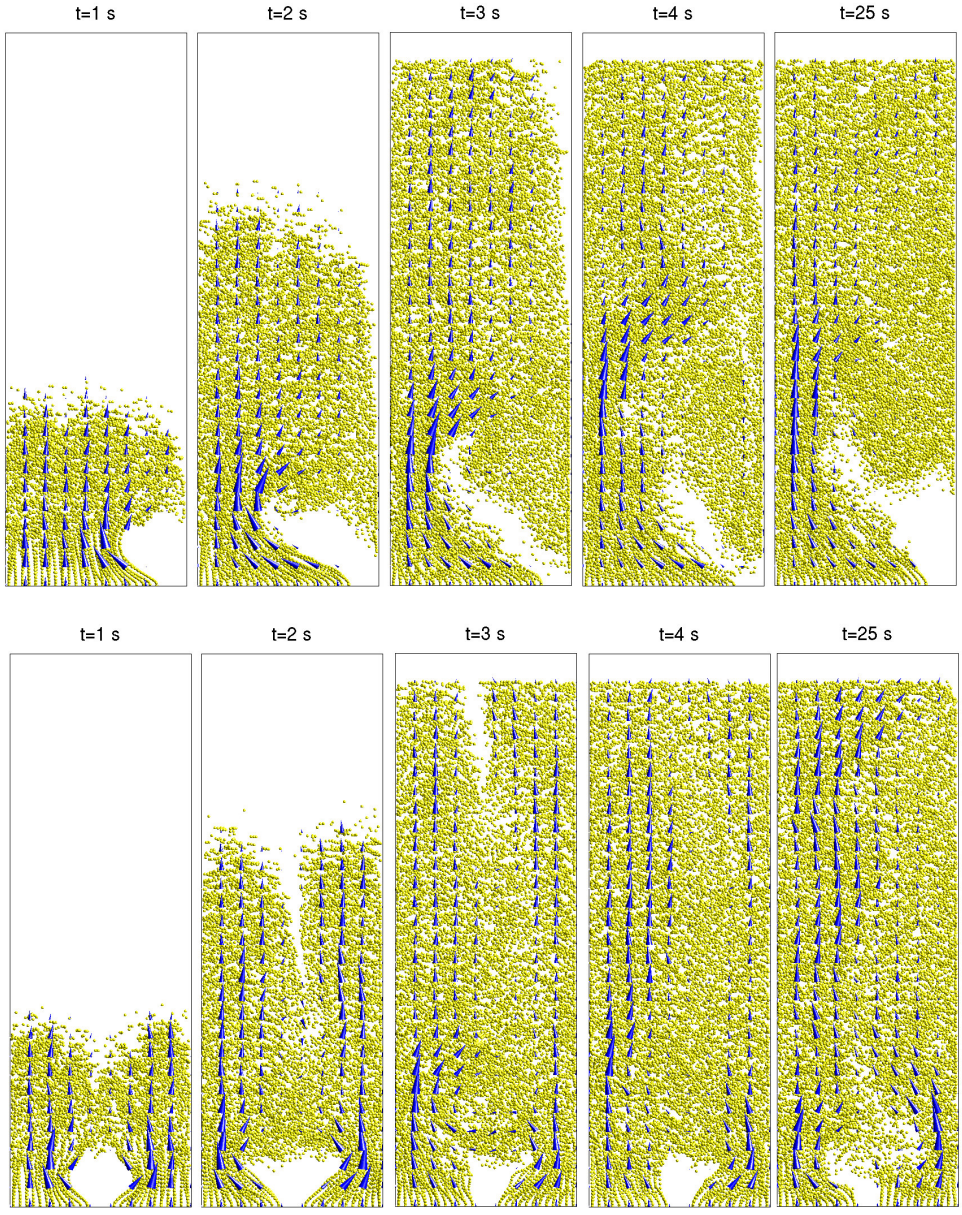


**Figure 6.7**: *Instantaneous solution for case S6 (top row) and S7 (bottom row) during the startup period.*

meandering plume in the center region of the column. The two vortices in the inlet region have become bigger and stronger. These vortices are strong enough to trap and drag along large portions of the bubbles for some times until they finally escape and rejoin the bubbles in the plume region. After a while however these structures are less pronounced; nevertheless the large circulation cells are still noticeable.
The startup period for the asymmetric injection pattern (case S6) is shown in Fig. 6.7 (top). For case S6 the non-aerated region is only near the right wall, creating vortices in that region. The vortices push the bubbles further toward the left wall generating a larger vortical zone. Higher up in the column the bubbles that were pushed aside by the vortices are moving back toward the right wall filling the column in the lateral direction. Later on, the same vortices trap large portions of bubbles and drag them down filling up the gap in the right corner. The top region of the structures is similar with half of the structures found on the partially aerated bubble columns (cases S2-S5), showing a mushroom shaped structure which moves in the vertical direction and later on fills up the entire column except the area close to the non-aerated inlet.
The flow structures appearing during the startup in the case that the center region is non-aerated (case S7) is shown in Fig. 6.7 (bottom). In this case, the bubbles initially rise in two groups separated by the non-aerated zone. At about $z > 10\,\mathrm{cm}$ the two groups rejoin, generating a liquid area enclosed by bubbles. At a higher position, the bubbles are again splitted into two groups as they ascend to the liquid surface. The two groups of bubbles are not present for long time and dissappear after about $t = 4\,\mathrm{s}$. Afterwards, the bubbles fill the entire top region of the column uniformly, while the void region close to the non-aerated area starts to meander irregularly from left to right.

### 6.5.2 Fully developed flow structures

Comparison between simulation results and experimental observations after the flow has fully developed can be seen in Figs. 6.8 to 6.14. Here the bubble velocity resulting from the DBM simulations is averaged in the depth direction to mimic the bubble velocity resulting from the PIV measurements, while the liquid velocity in a slice positioned at $y/D = 0.5$ is presented. The figures indicate that the flow structures found in the experiments and simulations are similar to a large degree. For uniform gas injection the patterns found in the experiment (case E1) and simulation (case S1) show a perfect resemblance (see 6.8). In both cases the bubbles are distributed uniformly over the entire region of the column. Furthermore, for both cases a rectilinear bubble path can be observed close to the inlet area before the interaction between bubbles and the liquid makes the bubble paths more irregular. The close resemblance can also be observed in the bubble velocity; i.e. the bubbles show a similar tendency to rise with more or less uniform velocity. In

the liquid velocity no large structures are observed for both cases, which further confirms the uniformity of the flow field. When small non-aerated regions are introduced in both lower corners of the column, a small discrepancy between experimental observation (case E2) and the simulation result (case S2) appears (see Fig. 6.9). In this case, vortices are present in both corners; however, the vortices predicted by the simulation are bigger in size than in the experimental counterpart. In the simulation, the bubble paths are more converged immediately after injection to the column, resulting in a tighter necking zone compared with the experiment. The bubble velocity field resulting from case S2 shows that the bubbles are accelerated in the necking zone, while the velocity in the circulation zone is very low. This situation is not observed in case E2. In the top of the column, similar structures are obtained for both cases where bubbles rise uniformly toward the column surface.

As the non-aerated zone is increased from $7\%$ to $15\%$, the vortices near both corners of the inlet region are growing, as is shown in Fig. 6.10. Here, the experimental result (case E3) shows a pronounced vortical zone on both sides of the inlet resulting in a necking zone. Comparing with case S3 however, these vortices are smaller and the necking zone is bigger. The upper part of the column shows relatively similar structures, where bubbles distribute almost uniformly in the lateral direction. The accelerated bubbles in the necking zone are now subsequently propagated to the surface of the column generating a snake-like bubble plume, where bubbles move faster compared to the bubbles outside the plume. This structure is observed in both experiment and simulation, which is also resembled in the liquid velocity field, where multiple circulation cells are stacked in the axial direction. A similar situation is also found when the nonaerated zone is further increased from $15\%$ to $22\%$, as is shown in Fig. 6.11.

Figure 6.12 shows that expanding the nonaerated zone from $22\%$ to $30\%$ results in a different flow pattern. Here, the simulation result (case S5) shows a pronounced bubble plume structure, where "piles of bubbles" are packed together starting from the inlet up to the column surface. Some of the bubbles are trapped in a circulation zone, which is strong enough to drag the bubbles down and fill up the region outside the bubble plume. This structure however is less pronounced in the experiment (case E5). Furthermore, a high bubble velocity in the bubble plume can be observed for both case E5 and S5, which is also reflected in the liquid velocity field.

In the case of the non-aerated zone on one side of the column (i.e. case E6/S6) the comparison between the simulation and the experiment shows good resemblance (see Fig. 6.13). Both cases show that the bubbles are pushed toward the left wall by the strong vortices, while some of the bubbles are dragged down by the same vortices. In the top region, bubbles fill the entire region of the column, however in case E6 the effect of the circulation pattern to the bubble structure is more pronounced compared to the experimental counterpart. The bubble velocity also shows good similarity

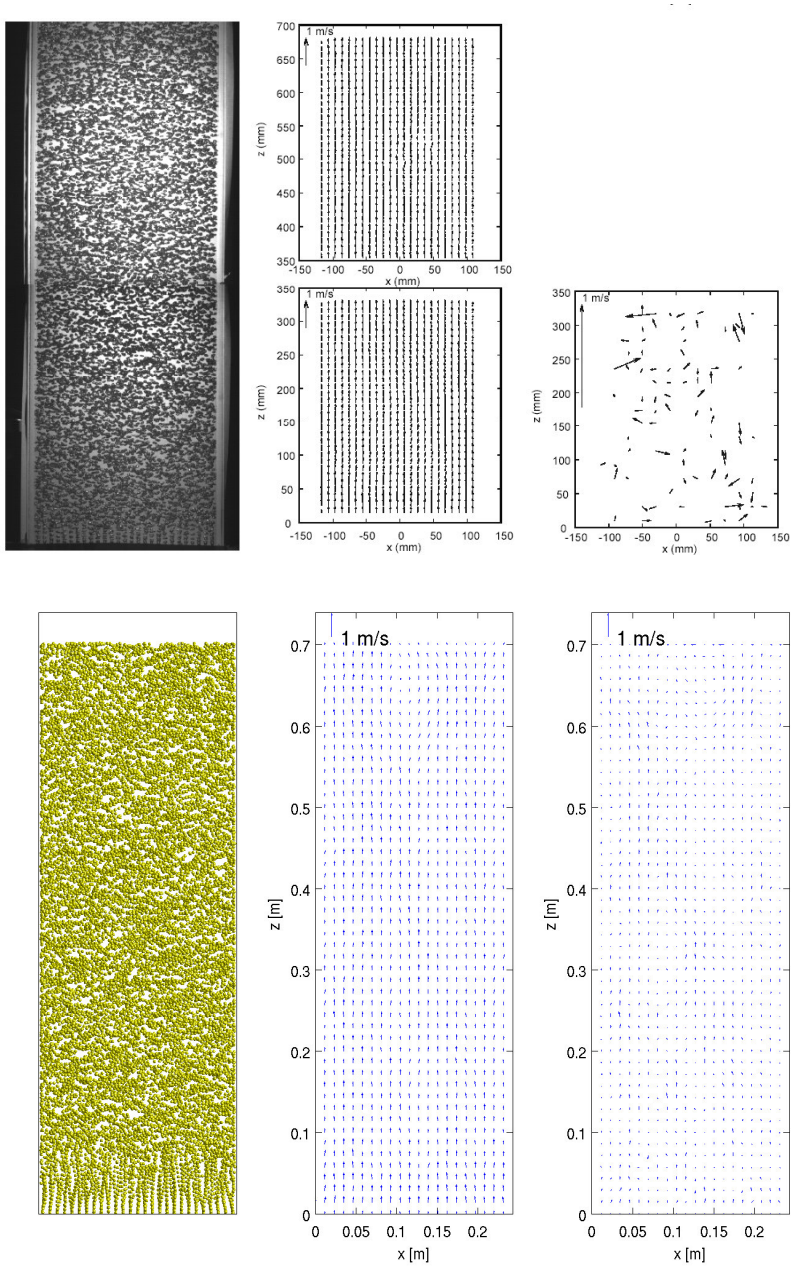


**Figure 6.8:** *Instantaneous flow structure comparison between case E1 (top row) and S1 (bottom row). From left to right: bubble positions, bubble velocity and liquid velocity.*

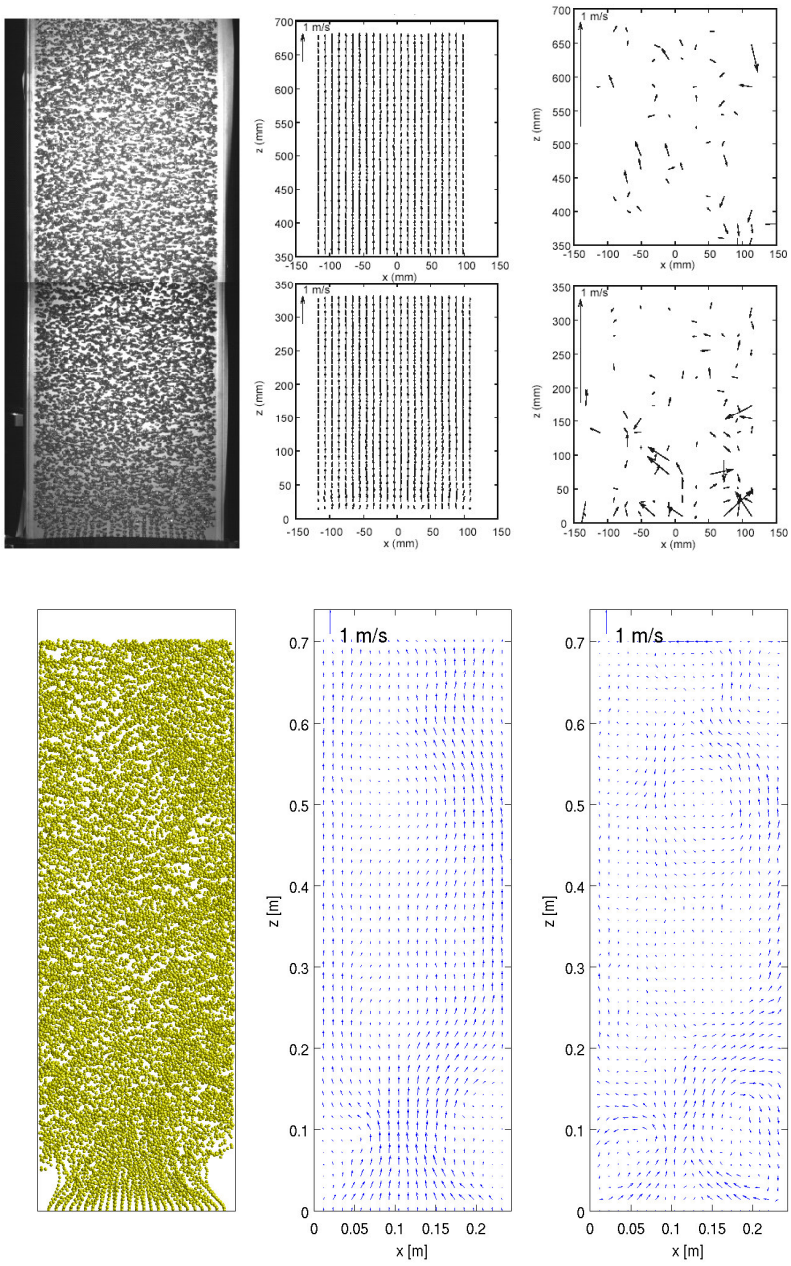


**Figure 6.9:** *Instantaneous flow structure comparison between case E2 (top row) and S2 (bottom row). From left to right: bubble positions, bubble velocity and liquid velocity.*

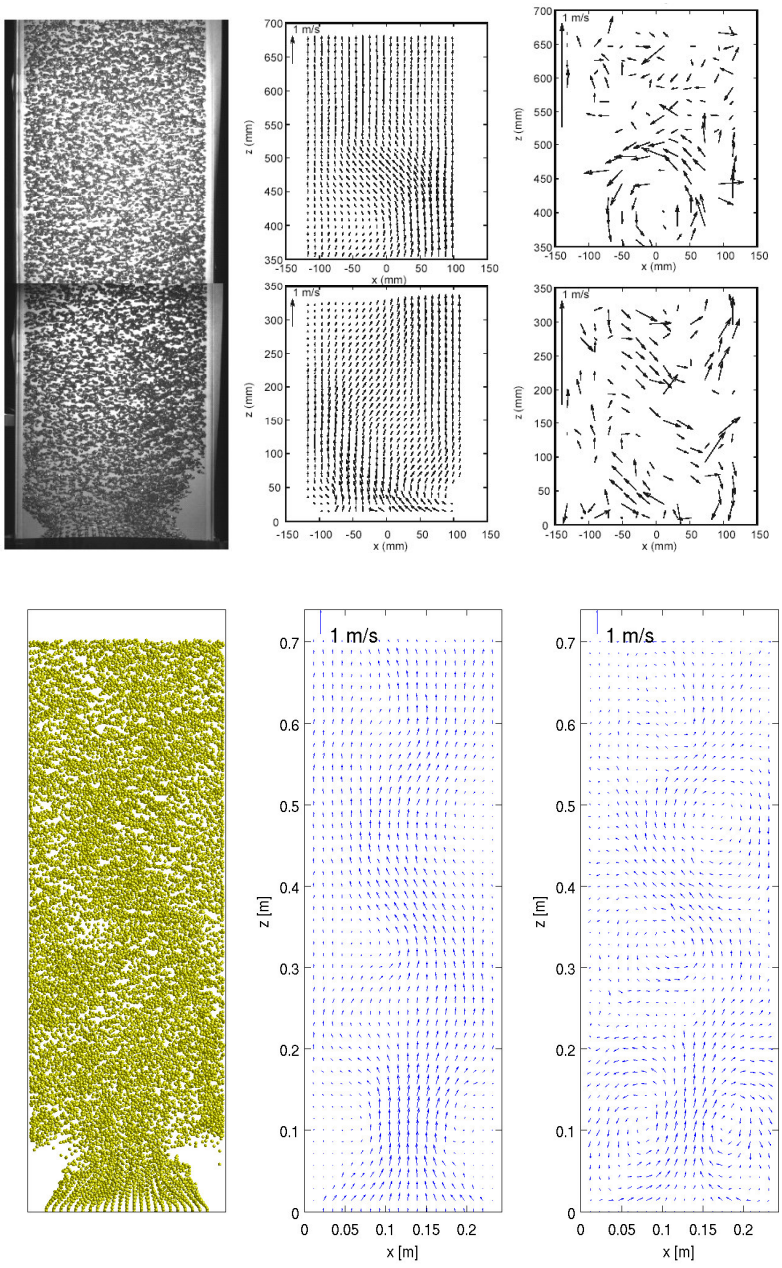


**Figure 6.10:** *Instantaneous flow structure comparison between case E3 (top row) and S3 (bottom row). From left to right: bubble positions, bubble velocity and liquid velocity.*

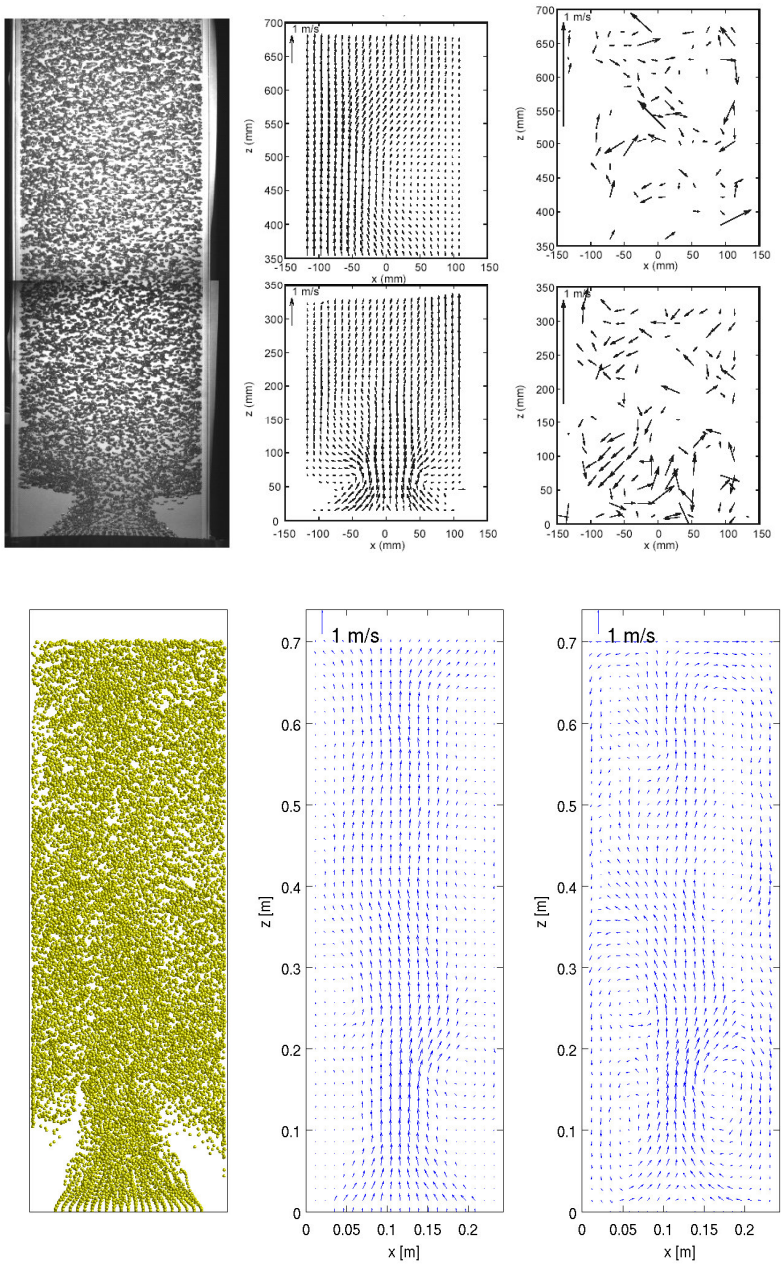


**Figure 6.11:** *Instantaneous flow structure comparison between case E4 (top row) and S4 (bottom row). From left to right: bubble positions, bubble velocity and liquid velocity.*

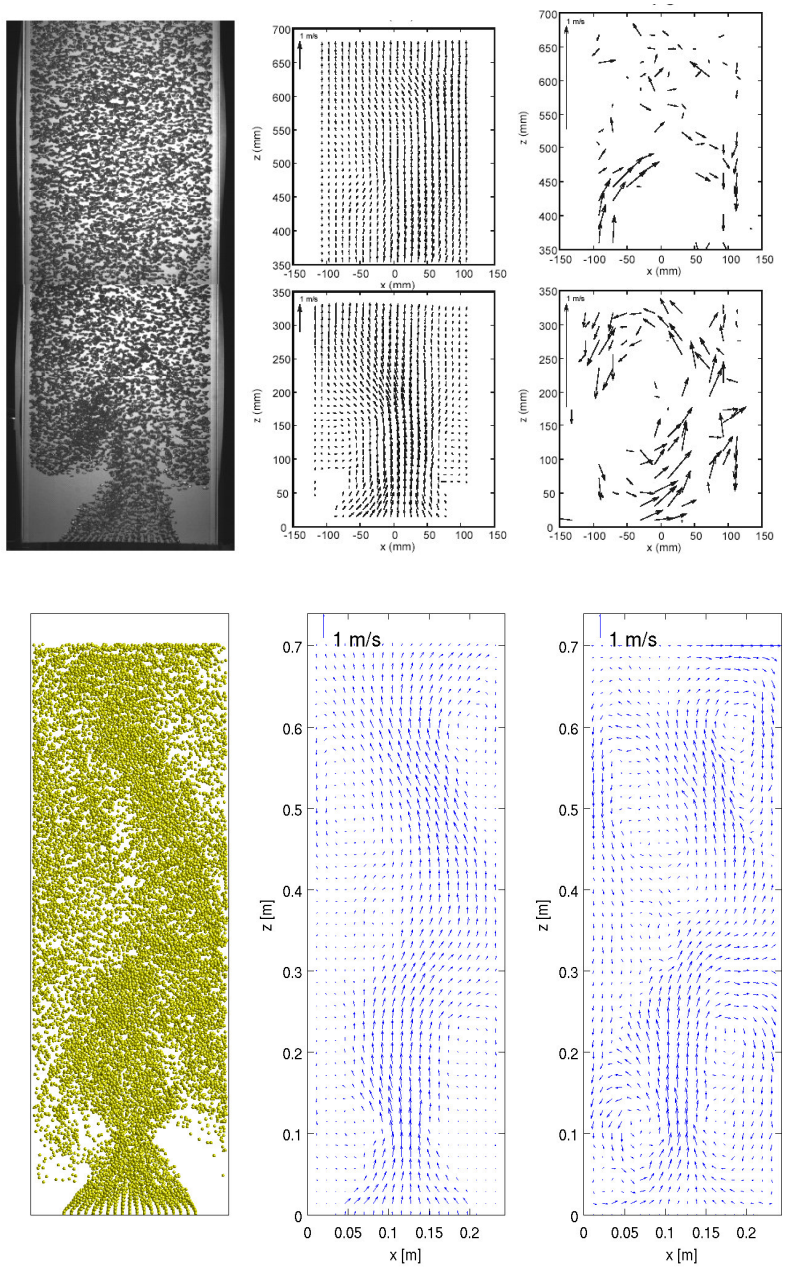


**Figure 6.12:** *Instantaneous flow structure comparison between case E5 (top row) and S5 (bottom row). From left to right: bubble positions, bubble velocity and liquid velocity.*

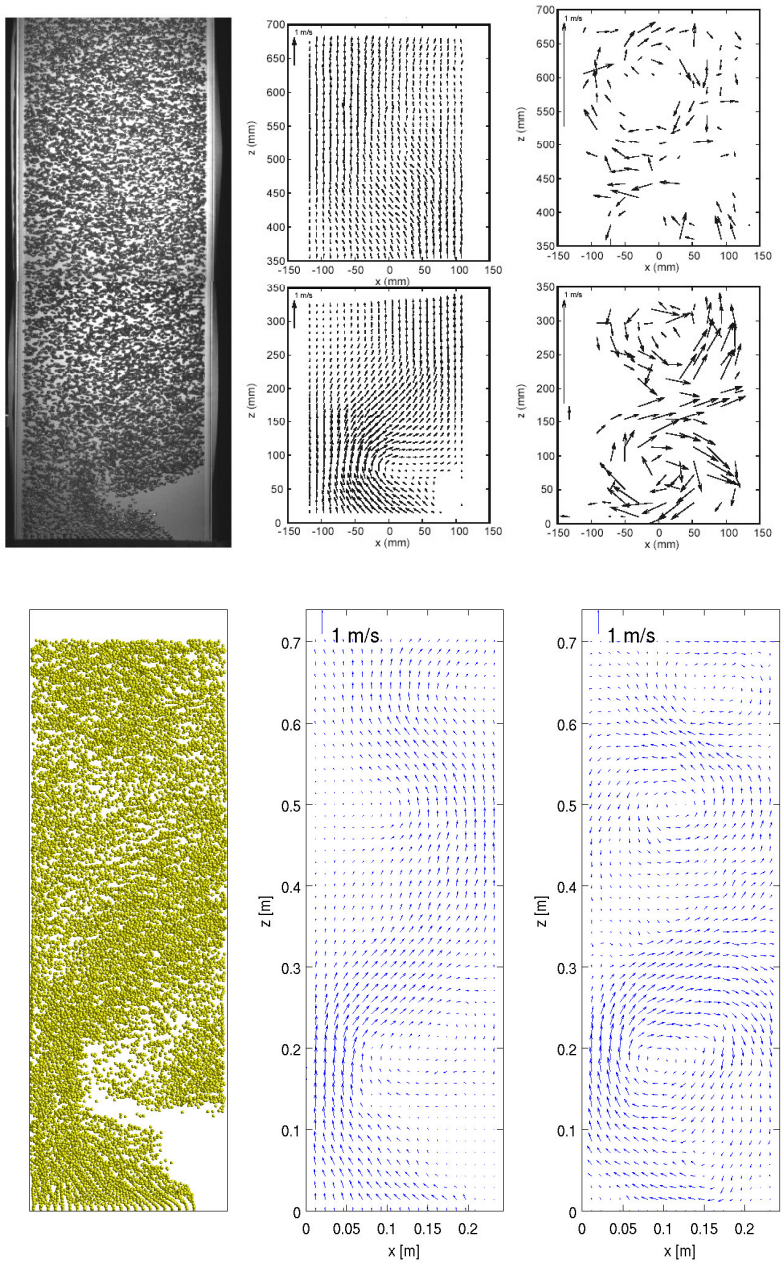


**Figure 6.13:** *Instantaneous flow structure comparison between case E6 (top row) and S6 (bottom row). From left to right: bubble positions, bubble velocity and liquid velocity.*

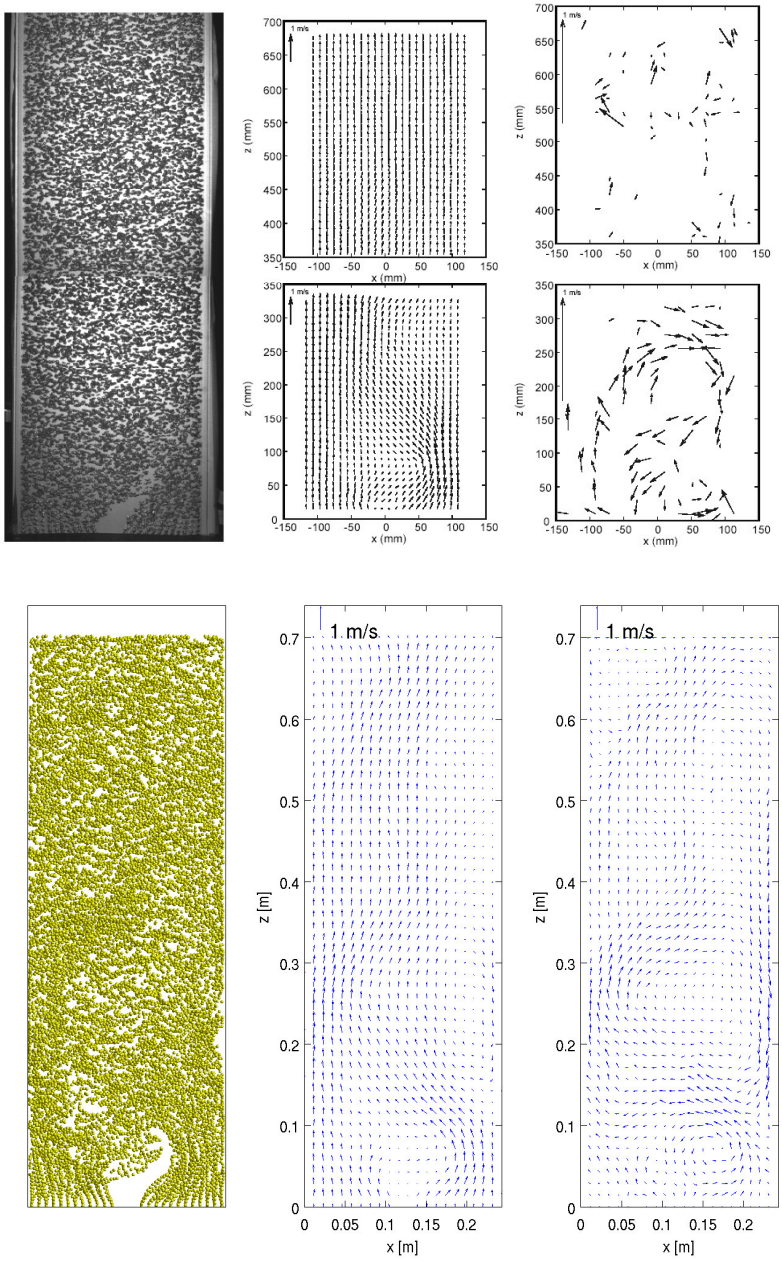


**Figure 6.14:** *Instantaneous flow structure comparison between case E7 (top row) and S7 (bottom row). From left to right: bubble positions, bubble velocity and liquid velocity.*

between the two cases, where bubbles moving in the plume have a high upflow velocity, while the bubbles inside the large vortices have a tendency to move along with it. In the liquid velocity field, several (fixed) circulation cells are found, which are stacked in the axial direction.
Finally for the cases where the gas is injected near the wall but not in the center (case E7/S7), again we find good resemblance as shown in Fig. 6.14. For both cases we find some vortical structure in the lower part of the column, which move around quite irregularly. These structures however are not found in the higher regions of the column ($z > 0.2\,\mathrm{m}$).

### 6.5.3 Integral gas hold-up

The comparison of the integral gas hold-up obtained from the simulations and experiments is given in Fig 6.15. The total gas hold-up in the simulations is obtained by calculating the total volume of all bubbles present in the column divided by the total volume of the column while the experimental gas hold-up is obtained by measuring the total expansion of the dispersion in the column. The figure shows that the simulation results reflect the same trend as observed in the experiments. By increasing the non-aerated zone in case 1 to 5 the integral gas hold-up is consistently decreasing despite the fact that the superficial velocity is kept constant. As the top part of the column is having a relatively similar bubble population, the decrease in the

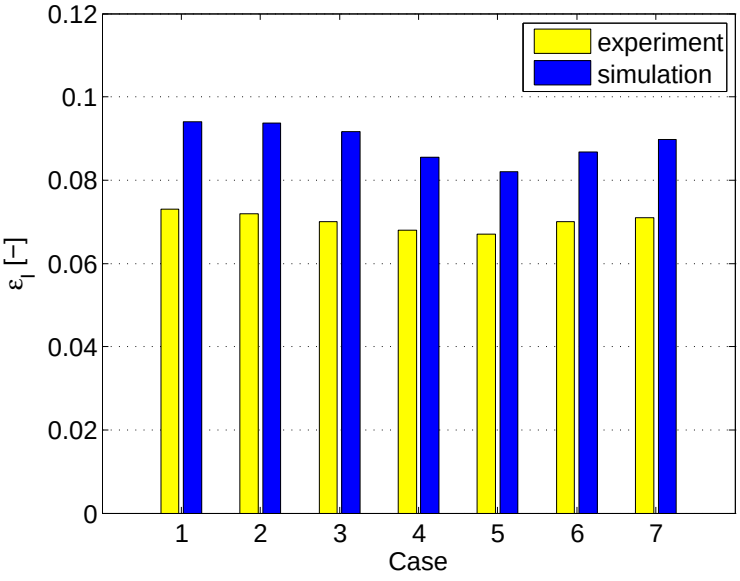


**Figure 6.15:** *Integral gas hold-up, comparison between simulation and experiment.*

gas hold-up can be attributed to the increasing size of vortices close to the non-aerated region. A similar situation occurs in cases 6 and 7. Quantitative comparison between experiment and simulation however shows that the simulations consistently overpredict the experimental data with about $25\,\%$.

### 6.5.4 Time-averaged quantities

The time-averaged quantities in the simulations are calculated using the following relation:

$$\overline{\phi} = \frac{1}{N_t} \sum_{i=1}^{N_t} \phi_i \tag{6.10}$$

where $\phi$ is the quantity at hand, $N_t$ is the number of time steps used in the averaging. While the RMS value of the quantity is calculated as:

$$\phi' = \frac{1}{N_t} \sqrt{\sum_{i=1}^{N_t} \left(\phi_i - \overline{\phi}\right)^2} \tag{6.11}$$

In the experiments the liquid velocity is measured using the LDA technique as described in sect. 6.2.3. For the uniform gas injection (case $1$) the comparison between the experimental and simulation results can be found in Fig. 6.16. As can be seen, the velocity profile resulting from the simulation shows similarity with the experimental results where upflow is present in the center region, while downflow is present close to the wall. At a height of $z = 0.05\,\mathrm{m}$ a discrepancy between simulation and experiment exists; here the simulation shows core a peaking velocity profile, while the experiment shows wall peaking which might be related to the adopted closure for the lift coefficient. At higher levels in the column the simulation agrees with the experiment, where the velocity shows upflow in the center of the column and downflow close to the walls. Further comparison shows that the velocity profile of the simulation has a higher value in the center compared to the experiment, while close to the wall the downflow predicted by the simulation is also stronger compared to the experiment. A similar situation can be seen in the velocity profile in the depth direction. We suspect that this discrepancy is resulting from the fact that in the experiment liquid is flowing in between bubbles generating a microscale circulation, generating a rather flat velocity profile. Meanwhile in the simulation due to the limitation of the spatial resolution presently used, the liquid tends to move in a large circulation pattern.
The averaged velocity profile in the lower part of the column (i.e. $z = 0.05\,\mathrm{m}$) for all cases is shown in Figs. 6.17 and 6.18. From these figures we can see that due to the different injection patterns applied in each case, different velocity profiles are obtained. In case $1$ a relatively flat velocity profile

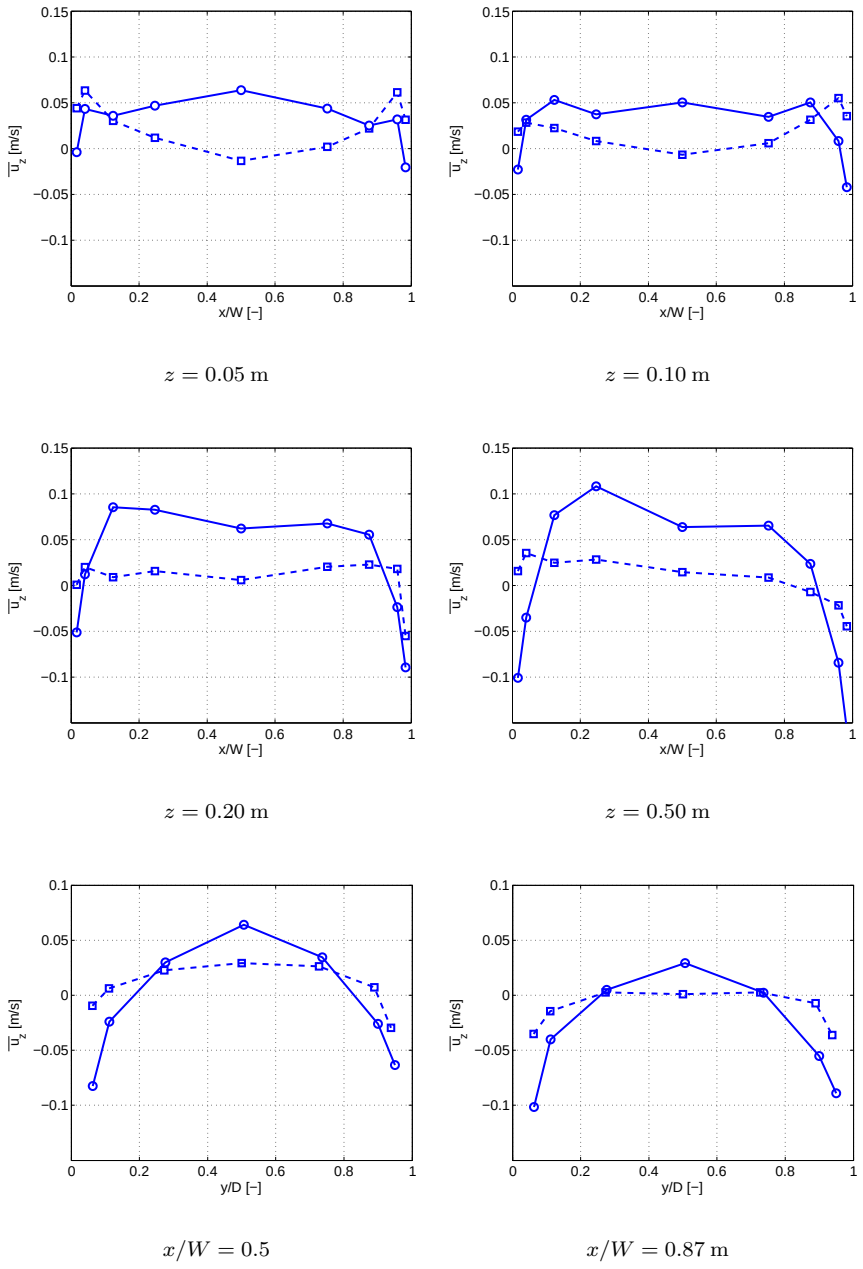


**Figure 6.16:** *Velocity profile for uniform gas injection (case 1) at the center line with $y/D = 0.5$ (first two rows) and over two lines in the $y-$direction ($z = 0.5$ m) (last row). Continuous line: simulation, dashed line: experiment.*

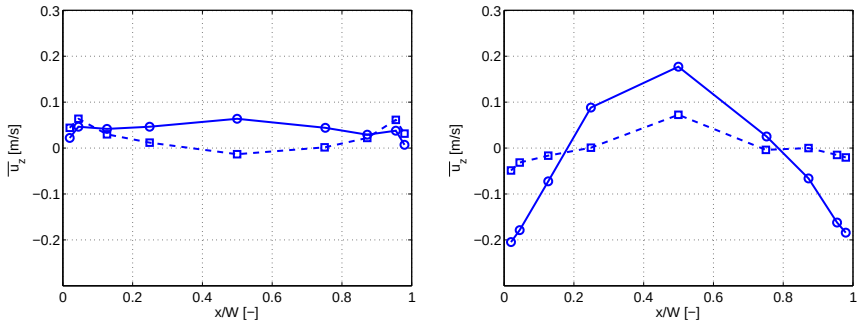


case 1 case 2

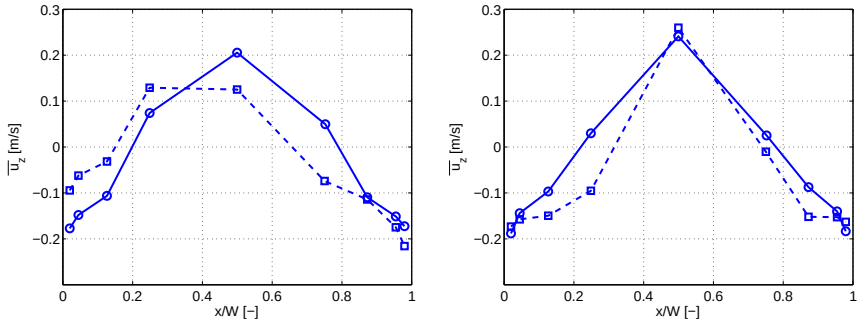


case 3 case 4

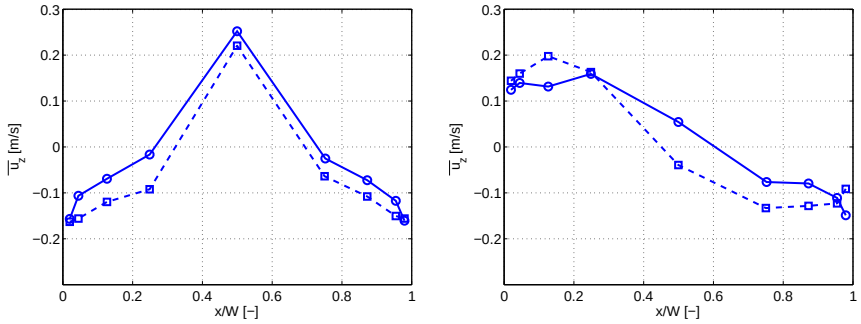


case 5 case 6

**Figure 6.17:** *Axial velocity profiles for various gas injection patterns at* $z = 0.05$ m. *Continuous line: simulation, dashed line: experiment.*

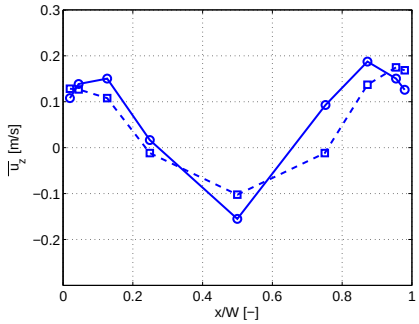


case 7

**Figure 6.18:** *Axial velocity profiles for various gas injection patterns at* $z = 0.05\,\mathrm{m}$ *(continued). Continuous line: simulation, dashed line: experiment.*

is found, while case $2$ to case $5$ show an upflow in the center region and downflow close to the walls. For case $6$ an asymmetric velocity profile is present due to the asymmetric aeration. Here, the left part of the column displays upflow, while the right part shows downflow. Finally, for case $7$ we found upflow on both sides of the wall and downflow in the center region. Comparison between experiment and simulation shows that for all cases the velocity profile has been correctly predicted by the present model. Some discrepancy is found in all cases, but the main patterns are the same. For case $2$ however we found that the discrepancy is relatively large compared with the other cases. This is due to the fact that the simulation overpredicts the vortices in the non-aerated zone as shown in Fig. 6.9.

For all cases velocity profiles in the higher region of the column (i.e. $z = 0.7\,\mathrm{s}$) are presented in Figs. 6.19 and 6.20. At this height we found that the averaged velocity profile is relatively flat for all cases. The strong upflow found at the lower height in cases $2$ to $5$ is no longer present, which indicates that the flow is moving rather uniformly close to the column surface. A similar situation is found in cases $6$ and $7$, where the assymmetric flow found in the bottom section of the column has disappeared. The results indicate that for all cases the predicted velocity profile agrees well with the experimental data.

Average void fraction profiles for cases $1$ and $5$ are shown in Fig. 6.21. In the top region (i.e. $z \geq 0.2\,\mathrm{m}$), almost no difference between cases $1$ and $5$ is found. However, closer to the bottom case $5$ shows that the gas hold-up is peaking in the center region and is close to zero on both sides close to the wall. Furthermore, we found that the transition from a bubble plume structure present in the lower part of the column to the homogeneous bubble structure predicted by the present model appears to develop in a higher

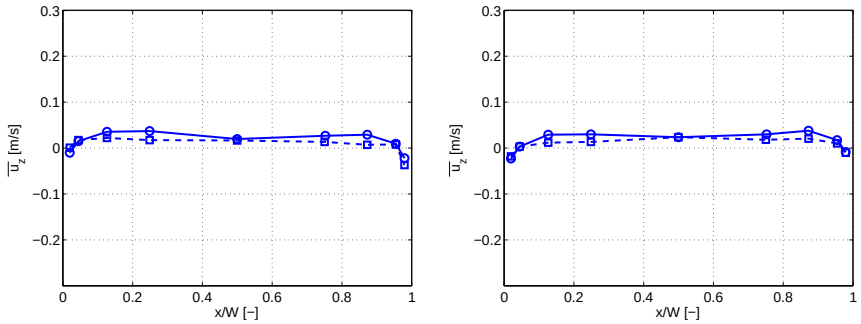


case 1 case 2

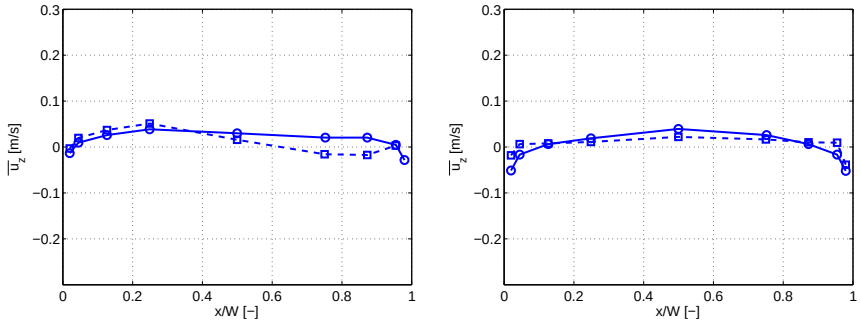


case 3 case 4

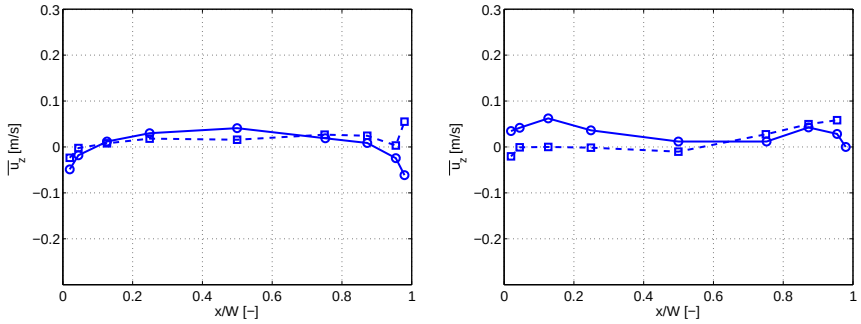


case 5 case 6

**Figure 6.19:** *Axial velocity profiles for various gas injection patterns at* $z = 0.7$ m. *Continuous line: simulation, dashed line: experiment.*

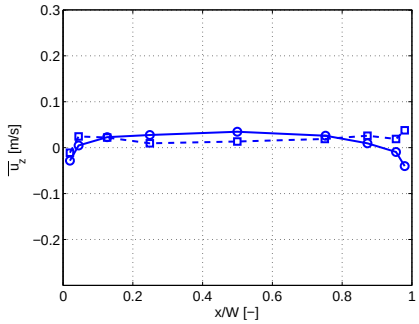


case 7

**Figure 6.20:** *Axial velocity profiles for various gas injection patterns at* $z = 0.7$ m *(continued). Continuous line: simulation, dashed line: experiment.*

region compared to the experimental data. When comparing the simulation and experimental results, we find that in general the simulation overpredicts the gas hold-up by about $20\%$, which is consistent with the integral gas hold-up overprediction described in sect. 6.5.3.
The dynamic behavior is studied via the axial normal stresses. Figures 6.22 and 6.23 shows these stresses at various heights and for various injection patterns. As can be seen in the experimental data, the stress level is relatively low for all cases except for case E5, where the flow becomes highly dynamic marked by high stress levels in almost the entire column. In the simulation the results are slightly different; here we found that for all cases the stress level is low, except for case S3, where a significant degree of fluctuation is present close to the inlet region. A high degree of fluctuation in the entire column is found in cases S4 and S5. Compared to case S4 however, case S5 shows a significantly higher stress level. These results show that the transition from a stable to a dynamic flow condition occurs earlier in the simulation compared with the experiment, which indicates that the present model overpredicts the dynamic behavior of the column. This might come from the turbulence model, which we suspect becomes less accurate as the local gas hold-up is increased.

## 6.6 Conclusions

In this chapter, the discrete bubble model is validated against the experimental data of Harteveld et al. [2] where seven injection patterns are studied to investigate their influence on the flow structure. We found that the model in general is able to reproduce the observed variations rather well. For all

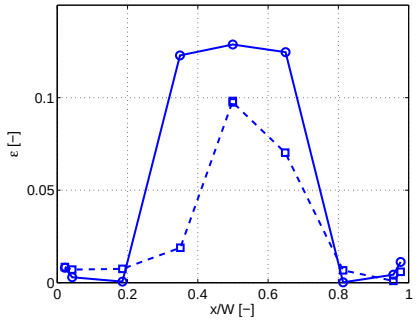


case 5, $z = 0.05$ m

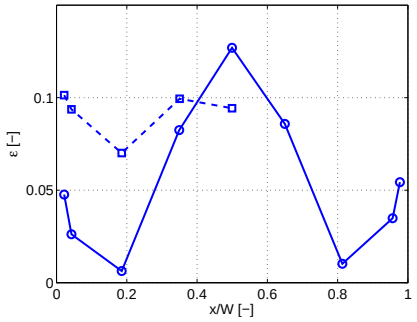


case 5, $z = 0.10$ m

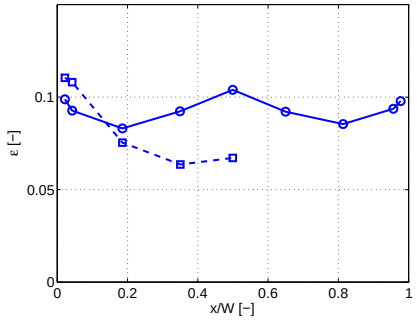


case 5, $z = 0.20$ m

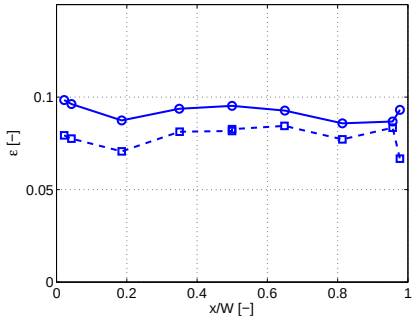


case 5, $z = 0.50$ m

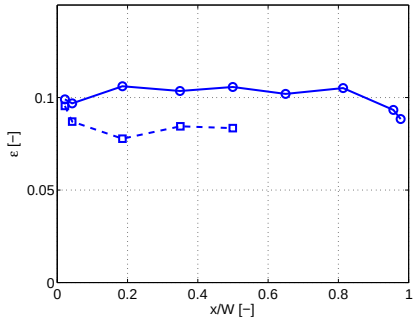


case 5, $z = 0.70$ m

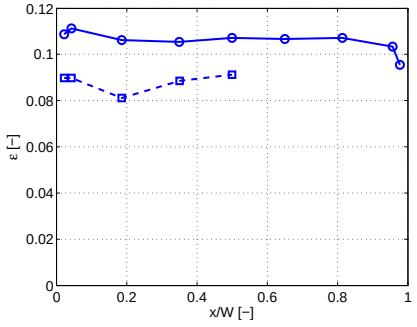


case 1, $z = 0.70$ m

**Figure 6.21:** *Void fraction profiles for case 1 and 5, over the line $y = 0$. Continuous line: simulation, dashed line: experiment.*

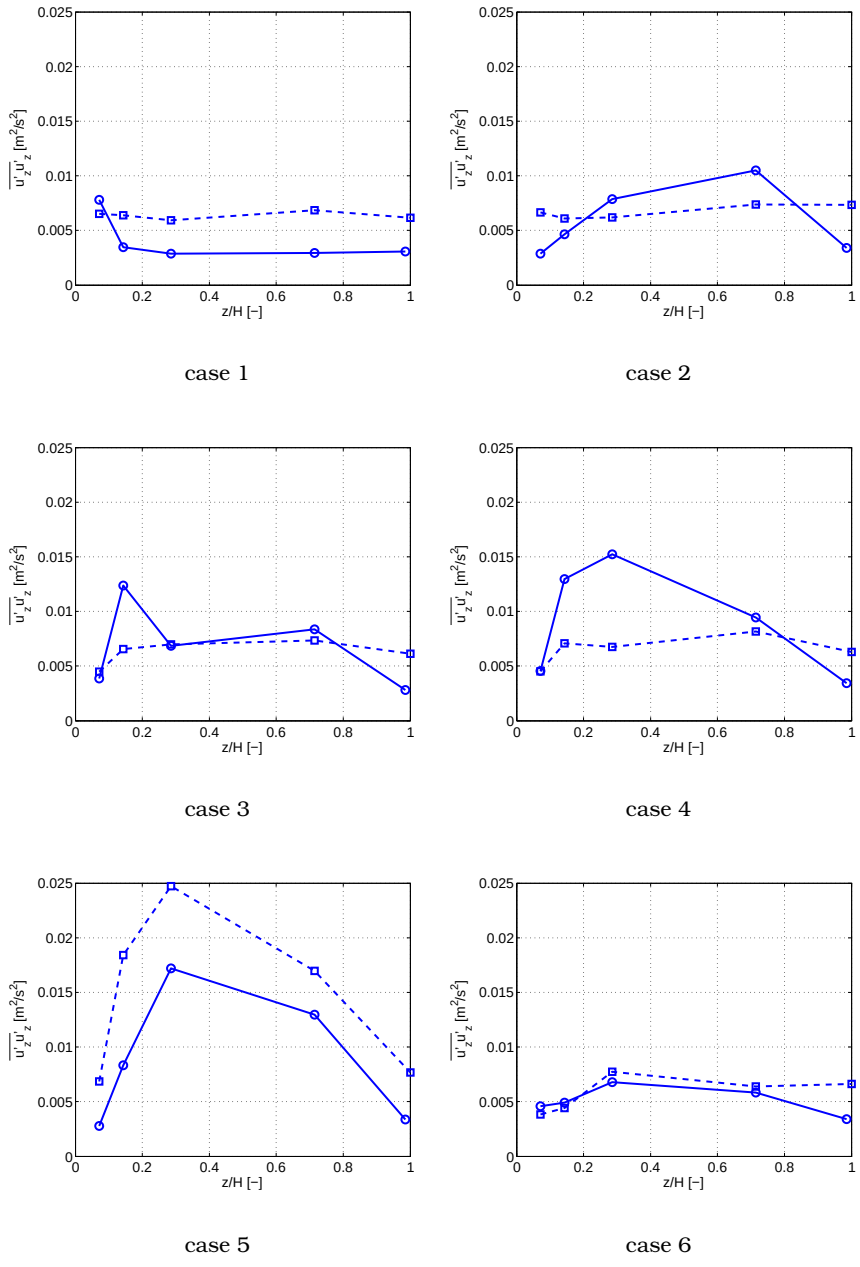


**Figure 6.22:** *Axial normal stresses for the various injection patterns. Continuous line: simulation, dashed line: experiment.*

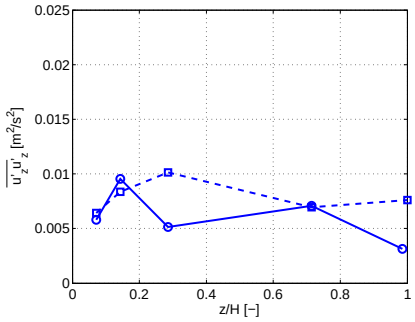


case 7

**Figure 6.23:** *Axial normal stresses for the various injection patterns (continued). Continuous line: simulation, dashed line: experiment.*

cases the integral gas hold-up is overpredicted by almost $25\%$ by the present model. The trends of the change in gas hold-up however agree with the experiment. The velocity profiles in general agree with the experiment, however we have noticed that the simulation results tends to produce stronger upflow in the center of the column and stronger downflow close the walls. We suspect that this behavior is due to the fact that in the experiments the liquid is moving in between the bubbles while in the simulation due to the limited spatial resolution the liquid moves in a large circulation pattern. Finally, the simulations display an earlier transition from the stable to the dynamic regime compared with the experimental data, which might result from an innacurracy of the turbulence model at high gas hold-ups. Further study to investigate the validity of the turbulence model at high gas hold-ups is necessary.

## Acknowledgements

The author would like to thank Dr. ir. Wouter Harteveld (currently at Shell Global Solutions, Amsterdam) and Prof. dr. R. F. Mudde (Department of Multi-Scale Physics, Faculty of Applied Sciences, Delft University of Technology) for providing the experimental data and valuable discussion on the topic.

## Notation

| | |
|---|---|
| $C$ | model coefficient, dimensionless |
| $d$ | diameter, $\mathrm{m}$ |
| Eö | Eötvös number, dimensionless |
| $\mathbf{F}$ | force vector, $\mathrm{N}$ |
| $\mathbf{g}$ | gravity acceleration, $\mathrm{m\,s^{-2}}$ |
| $\mathbf{I}$ | unit tensor, dimensionless |
| $P$ | pressure, $\mathrm{N\,m^{-2}}$ |
| $R$ | radius, $\mathrm{m}$ |
| Re | Reynolds number, dimensionless |
| $S$ | source term in the species balance equation, $\mathrm{kg\,m^{-3}\,s^{-1}}$ |
| $\mathbf{S}$ | characteristic filtered strain rate, $\mathrm{s^{-1}}$ |
| $t$ | time, $\mathrm{s}$ |
| $\mathbf{u}$ | liquid velocity vector, $\mathrm{m\,s^{-1}}$ |
| $\mathbf{v}$ | bubble velocity vector, $\mathrm{m\,s^{-1}}$ |
| $V$ | volume, $\mathrm{m^3}$ |

### Greek letters

| | |
|---|---|
| $\triangle$ | subgrid length scale, $\mathrm{m}$ |
| $\varepsilon$ | volume fraction, dimensionless |
| $\mu$ | viscosity, $\mathrm{kg\,m^{-1}\,s^{-1}}$ |
| $\Phi$ | volume averaged momentum transfer due to interphase forces, $\mathrm{N\,m^{-3}}$ |
| $\rho$ | density, $\mathrm{kg\,m^{-3}}$ |
| $\sigma$ | interfacial tension, $\mathrm{N\,m^{-1}}$ |
| $\tau$ | stress tensor, $\mathrm{N\,m^{-2}}$ |

### Indices

| | |
|---|---|
| $b$ | bubble |
| $cell$ | computational cell |
| $D$ | drag |
| eff | effective |
| $G$ | gravity |
| $\ell$ | liquid |
| $L$ | lift |
| $P$ | pressure |
| $S$ | subgrid |
| $T$ | turbulent |
| $VM$ | virtual mass |
| $W$ | wall |
| $*$ | interfacial equilibrium value |

## References

[1] D. Darmana, N. G. Deen, W. Harteveld, R. F. Mudde, and J. A. M. Kuipers. Numerical study of homogeneous bubbly flow: influence of the inlet conditions to the hydrodynamic behavior. *In preparation*, 2006.

[2] W. K. Harteveld, J. E. Julia, R. F. Mudde, and H. E. A. van den Akker. Large scale vortical structures in bubble columns for gas fractions in the range of 5%-25%. In *CHISA*, August 2004.

[3] D. Darmana, N. G. Deen, and J. A. M. Kuipers. Parallelization of an Euler-Lagrange model using mixed domain decomposition and mirror domain technique: application to dispersed gas-liquid two-phase flow. *Journal of Computational Physics*, 2006. In Press, Corrected Proof, Available online 7 July 2006.

[4] S. Becker, A. Sokolichin, and G. Eigenberger. Gas-liquid flow in bubble columns and loop reactors: Part II. comparison of detailed experiments and flow simulations. *Chemical Engineering Science*, 49:5747–5762, 1994.

[5] E. Delnoij, F. A. Lammers, J. A. M. Kuipers, and W. P. M. van Swaaij. Dynamic simulation of dispersed gas-liquid two-phase flow using a discrete bubble model. *Chemical Engineering Science*, 52:1429–1458, 1997.

[6] E. Delnoij, J. A. M. Kuipers, and W. P. M. Van Swaaij. A three-simensional cfd model for gas-liquid bubble columns. *Chemical Engineering Science*, 54:2217–2226, 1999.

[7] N. G. Deen, T. Solberg, and B. H. Hjertager. Large eddy simulation of the gas-liquid flow in a square cross-sectioned bubble column. *Chemical Engineering Science*, 56:6341–6349, 2001.

[8] D. Darmana, N. G. Deen, and J. A. M. Kuipers. Modelling of mass transfer and chemical reactions in a bubble column reactor using a discrete bubble model. In *Proceedings of the 5th International Conference on Multiphase Flow*, Yokohama, Japan, may 30 - June 4 2004. Paper No. 328.

[9] D. Darmana, N. G. Deen, and J. A. M. Kuipers. Detailed modelling of hydrodynamics, mass transfer and chemical reactions in a bubble column using a discrete bubble model. *Chemical Engineering Science*, 60(12):3383–3404, June 2005.

[10] D. Darmana, R. L. B. Henket, N. G. Deen, and J. A. M. Kuipers. Experimental and numerical investigations of a chemisorption process in a bubble column reactor. In *Proceedings of the 7th World Congress of Chemical Engineering*, Glasgow, Scotland, UK, 10-14 July 2005.

[11] V. V. Buwa, D. S. Deo, and V. V. Ranade. Eulerian-lagrangian simu-

lations of unsteady gas-liquid flows in bubble columns. *International Journal of Multiphase Flow*, 32:864885, 2006.

[12] V. V. Buwa and V. V. Ranade. Mixing in bubble columns reactors: role of unsteady flow structures. *Canadian Journal of Chemical Engineering*, 81:402, 2003.

[13] A. Tomiyama, H. Tamai, I. Zun, and S. Hosokawa. Transverse migration of single bubbles in simple shear flows. *Chemical Engineering Science*, 57:1849–1858, 2002.

[14] A. Tomiyama, T. Matsuoka, T. Fukuda, and T. Sakaguchi. A simple numerical method for solving an incompressible two-fluid model in a general curvilinear coordinate system. In A. Serizawa, T. Fukano, and J. Bataille, editors, *Advances in Multiphase Flow*, pages 241–252, Amsterdam, November 1995. Society of Petroleum Engineers, Inc., Elsevier.

[15] A. Behzadi, R. I. Issa, and H. Rusche. Modelling of dispersed bubble and droplet flow at high phase fractions. *Chemical Engineering Science*, 59:759–770, 2004.

[16] A. Tomiyama, H. Higaki I. Zun, Y. Makino, and T. Sakaguchi. A three-dimensional particle tracking method for bubbly flow simulation. *Nuclear Engineering and Design*, 175:77–86, 1997.

[17] B. P. B. Hoomans, J. A. M. Kuipers, W. J. Briels, and W. P. M. Van Swaaij. Discrete particle simulation of bubble and slug formation in a two-dimensional gas-fluidised bed: A hard-sphere approach. *Chemical Engineering Science*, 51(1):99–118, 1996.

[18] A. W. Vreman. An eddy-viscosity subrid-scale model for turbulent shear flow: algebraic theory and applications. *Physics of Fluids*, 16(10):3670–3681, 2004.

[19] J. A. M. Kuipers, K. J. van Duin, F. P. H. van Beckum, and W. P. M. van Swaaij. Computer simulation of the hydrodynamics of a two dimensional gas-fluidized bed. *Computational Chemical Engineering*, 17:839, 1993.

# List of publications

## Peer reviewed journal publications

1. D. Darmana, N.G. Deen, J.A.M. Kuipers. Detailed modeling of hydrodynamics, mass transfer and chemical reactions in a bubble column using a discrete bubble model. *Chemical Engineering Science*, 60(12):3383-3404, 2005.

2. D. Darmana, N.G. Deen, J.A.M. Kuipers. Parallelization of an Euler-Lagrange model using mixed domain decomposition and mirror domain technique: application to dispersed gas-liquid two-phase flow. *Journal of Computational Physics*, 2006. In press.

3. D. Darmana, N.G. Deen, J.A.M. Kuipers. Detailed 3D modelling of mass transfer processes in two phase flows with dynamics interfaces. *Chemical Engineering and Technology*, 29(9):1027-1033, 2006.

4. D. Darmana, R.L.B. Henket, N.G. Deen, J.A.M. Kuipers. Detailed modelling of hydrodynamics, mass transfer and chemical reactions in a bubble column using a discrete bubble model: Chemisorption of $CO_2$ into $NaOH$ solution, numerical and experimental study. Submitted to *Chemical Engineering Science*, 2006.

5. D. Darmana, N.G. Deen, W. Harteveld, R. F. Mudde, J.A.M. Kuipers. Numerical study of homogeneous bubbly flow: influence of the inlet conditions to the hydrodynamic behavior. *In preparation*, 2006.

6. D. Darmana, W. Dijkhuizen, N.G. Deen, M. van Sint Annaland, J.A.M. Kuipers. Direct numerical simulation of the mass transfer process in a swarm of deforming bubbles. *In preparation*, 2006.

## Proceedings and international conference presentations

1. E.I.V. Van den Hengel, D. Darmana, N.G. Deen, J.A.M. Kuipers, Large Eddy Simulation of a Bubble Column Reactor using the Euler-Lagrange Approach, In *Proceedings of Computational Fluid Dynamics in Chemical Reaction Engineering III*, Davos, Switzerland, 25-30 May 2003.

2. D. Darmana, N.G. Deen, J.A.M. Kuipers, Modelling of mass transfer and chemical reactions in a bubble column reactor using a discrete bubble model. In *Proceedings of the 5th International Conference on Multiphase Flow*, Yokohama, Japan, may 30 - June 4 2004. Paper No. 328 (oral presentation).

3. D. Darmana, R.L.B. Henket, N.G. Deen, J.A.M. Kuipers, Validation of a Discrete Bubble Model for Chemisorption in a Bubble Column Reactor. Oral presentation at the *43rd European Two-Phase Flow Group Meeting*, Prague, Czech Republic, 11-13 May 2005.

4. D. Darmana, W. Dijkhuizen, N.G. Deen, M. van Sint Annaland, J.A.M. Kuipers. Multi-scale modelling of bubbly flows. Oral presentaton at *Workshop of the Hydrodynamics of Bubbly Flows*, Leiden, The Netherlands, 6-16 June 2005.

5. D. Darmana, N.G. Deen, J.A.M. Kuipers, Parallelization of an Euler-Lagrange model using a mixed domain decomposition and mirror domain technique: application to dispersed gas liquid two phase flow. In *Proceedings of Computational Fluid Dynamics in Chemical Reaction Engineering IV*, Barga, Italy, June 19-24 2005 (oral presentation).

6. D. Darmana, R.L.B. Henket, N.G. Deen, J.A.M. Kuipers, Experimental and numerical investigations of a chemisorption process in a bubble column reactor. In *Proceedings of the 7th World Congress of Chemical Engineering*, Glasgow, Scotland, UK, 10-14 July 2005. Paper O140-002 (oral presentation).

7. D. Darmana, N.G. Deen, J.A.M. Kuipers, Detailed 3D modelling of mass transfer processes in two phase flows with dynamics interfaces. In *Proceedings of the 7th German-Japanese Symposium on bubble column*, Goslar, Germany, 20-23 May 2006 (oral presentation).

## Technical reports

1. D. Darmana, Aerodynamics inverse design by optimization (in Bahasa), BSc thesis, Institute Technology of Bandung, Indonesia, 1998.

2. D. Darmana and S. Pietrzko, Calculation of volumen velocity, radiation power and radiation efficiency for vibrating plate, Technical report, Dept. of acoustics and noise abatement EMPA, Dübendorf, Switzerland, 2001.

3. D. Darmana, Modelling of emulsification processes in shear flow, MSc thesis (executed at Akzo Nobel Chemical Research Center), University of Twente, The Netherlands, 2002.

4. D. Darmana, On the multiscale modelling of hydrodynamics, mass transfer and chemical reactions in bubble columns, PhD thesis (this book), University of Twente, The Netherlands, 2006.

# About the author

Dadan Darmana was born on July $24^{th}$, 1976 in Jakarta, Indonesia. After completing his secondary education at Sekolah Menengah Atas Negeri 68 (SMAN 68) Jakarta in 1994, he continued his study at the Institute Technology of Bandung, Indonesia, from which he obtained his bachelor's degree with cum laude in Aerospace Engineering in 1998 on the subject of "Aerodynamics inverse design by optimization" under supervision of Dr. B. I. Soemarwoto. In August 2000 he started to pursue his master degree with a full scholarship from EPAM at the Mathematical Physics and Computational Mechanics, Departement of Applied Mathematics, University of Twente, The Netherlands. During the summer holidays of 2001 he went to EMPA Dübendorf, Switzerland, where he conducted a small research in the field of sound propagation under supervision of Dr. Stanislaw Pietrzko. After finishing his master's thesis on "Modelling of emulsification processes in shear flow" which was executed at Akzo Nobel Chemical Research Center, Arnhem, The Netherlands under supervision of Dr. Joop Baltussen (Akzo Nobel) and Prof. Bernard Geurts (University of Twente), he received his Master's degree in Engineering Mathematics from the University of Twente in June 2002. In July of the same year he married Rini Farida Rosdiany whom he met three years earlier in Bandung. Afterwards, he started his PhD research in September 2002 at the group of Fundamentals of Chemical Reaction Engineering (FAP) at University of Twente, supervised by his promotor Prof. J.A.M. Kuipers and co-promotor Dr. Niels Deen. The results of this research are presented in this thesis. During his free time, the author likes to do outdoor activities, traveling, photography and computer technology especially in an open-source based software. After his PhD graduation he will return back to his wife in Indonesia and hopefully find an academic position as lecturer.